Dipl.-Ing. René Plasser

Numerical Computation of Nonlinear 3-Dimensional Time-Periodic Electromagnetic Field Problems by the Finite Element Method

DOCTORAL DISSERTATION

for obtaining the academic degree of
doctor of technical sciences
submitted to the

Graz University of Technology

Supervisor/First reviewer
Univ.-Prof. Dipl.-Ing. Dr.-techn. Oszkár Bíró
Institute of Fundamentals and Theory in Electrical Engineering

Second reviewer
Univ.-Prof. Dipl.-Ing. Dr.-techn. József Pávó
Budapest University of Technology and Economics

Graz, April 2018

Statutory Declaration

I declare that I have authored this thesis independently, that I have not used other than the declared sources / resources and that I have explicitly marked all material which has been quoted either literally or by content from the used sources. The document available on TUGRAZonline is identical to this thesis.

Eidesstattliche Erklärung

Ich erkläre an Eides statt, dass ich die vorliegende Arbeit selbstständig verfasst, andere als die angegebenen Quellen/Hilfsmittel nicht benutzt und die den benutzten Quellen wörtlich und inhaltlich entnommenen Stellen als solche kenntlich gemacht habe. Das in TUGRAZonline hochgeladene Textdokument ist mit der vorliegenden Dissertation identisch.

_____	_____	_____
Ort	Datum	Unterschrift

Acknowledgements

After two years gaining practical experience at Siemens AG Österreich–Transformers Weiz I decided to extend my knowledge by doing research in the field of electromagnetic field simulations at the Graz University of Technology. I would like to thank all supporters at Siemens for their valuable contributions and for respecting my inquisitiveness and my decision of doing research in this field of expertise at the University.

In first place, I would like to express my deep gratitude to my PhD supervisor Univ.-Prof. Dipl.-Ing. Dr.-techn. Oszkár Bíró for his excellent guidance and feedback during the last years. Additionally I have to remark that he was not only my mentor in the field of expertise but also a precious supporter in any kind of issues occurring in the past years.

Furthermore, it is a pleasure to thank my colleagues at the Institute of Fundamentals and Theory in Electrical Engineering at the Graz University of Technology. It has been a privilege exchanging ideas in scientific topics as well as in lecturing.

I am much obliged to my colleague Gergely Koczka from Siemens AG Österreich –Transformers Weiz. He provided for me the interface to industry and his contributions were milestones in the fundamentals of this thesis

Thanks to the industrial partner Trench Austria GmbH for providing measurement data on the additional losses of dry insulated air reactors for validation with computational results.

Finally, I would like to thank my family and friends for their continued care, support and encouragement.

This thesis is dedicated to my wonderful wife Marlene, who always inspired me with her faith and trust in me and my work, as well as to my son who delights me every single day with his unconditional love.

Abstract

Since the finite element method (FEM) has consolidated itself in the numerical computation of electro-magnetic fields as a fundamental tool for solving various kinds of complex problems, the demands in accuracy and quantity of the results obtained by this solution technique have steadily increased. Therefore, it is necessary to continuously improve and adapt the algorithms of finite element solvers.

This thesis contributes to the numerical computation of nonlinear, three-dimensional, time-periodic, eddy-current problems solved by the aid of the FEM by enhancing and adapting an existing FE-electromagnetic field analysis tool. The solution procedures treated focus on obtaining time-periodic, steady-state solutions by utilizing harmonic decomposition methods to bypass a time-consuming transient solution.

After an evaluation of the numerical results of the present solver by comparing to measurements to determine the impact of the number of considered higher harmonics in the computation, a nonlinear magnetic circuit model of a basic benchmark transformer was developed, based on FE solution algorithms. Hence it was possible to quickly assess the impact of modifications in the solution procedure of various potential formulations and nonlinear iteration strategies applied. With that knowledge gained, the FEM-solver was enhanced and validated by executing several numerical test problems as well as compared with solution approaches of external institutions.

In the final stage of this work, a static initialization procedure has been introduced to increase the efficiency in solving nonlinear eddy-current problems including a direct-current bias in the excitation. Two procedures to obtain an initial solution by first solving the problem without eddy-currents have been addressed in detail. This result provides the starting condition of the solution process with eddy-currents present.

Keywords: 3-dimensional, computational electromagnetics, DC-bias, eddy-currents, electro-magnetic field computations, electromagnetic modeling, finite element analysis, finite element methods, geomagnetism, nonlinear magnetics, nonlinear magnetic-circuit models, transformer problems

Kurzfassung

Da sich in der numerischen Berechnung elektromagnetischer Felder die Finite-Elemente-Methode (FEM) als grundlegendes Werkzeug zur Lösung verschiedenster komplexer Problemdomänen etabliert hat, sind die Anforderungen an die Genauigkeit und Quantität der Ergebnisse dieser Lösungsstrategie stetig gestiegen. Daher ist es notwendig, die Lösungsalgorithmen des Finite-Elemente-Solvers kontinuierlich zu verbessern und anzupassen.

Diese Arbeit leistet einen Beitrag zur numerischen Berechnung von nichtlinearen, dreidimensionalen, zeitperiodischen, Wirbelstromproblemen, die mit Hilfe der FEM gelöst werden, indem ein bestehendes FE-Elektro-Magnetfeldanalysewerkzeug erweitert und angepasst wird. Die untersuchten Lösungsverfahren sind darauf ausgerichtet, zeitperiodische, stationäre Lösungen zu erhalten, indem harmonische Diskretisierungs-Methoden verwendet werden, um einen zeitaufwändigen transienten Lösungsansatz zu umgehen.

Nach einer Auswertung der numerischen Ergebnisse des vorliegenden FE-Solvers durch Vergleich mit Messungen zur Bestimmung der Auswirkung der Anzahl der betrachteten höheren Harmonischen in der Berechnung, wurde ein nichtlineares Magnetkreismodell, basierend auf den FE-Lösungsalgorithmen, eines grundlegenden Benchmark-Transformators entwickelt. So war es möglich, die Auswirkungen von Modifikationen im Lösungsverfahren verschiedener Potenzial-Formulierungen und nichtlinearer Iterationsstrategien schnell abzuschätzen. Mit diesem Wissen wurde der FEM-Solver erweitert und validiert, indem mehrere numerische Testprobleme durchgeführt und mit Lösungsansätzen externer Institutionen verglichen wurden.

In der letzten Phase dieser Arbeit wurde ein Statisches-Initialisierungsverfahren eingeführt, um die Effizienz bei der Lösung nichtlinearer Wirbelstromprobleme mit Gleichstromanteil in der Erregung, zu erhöhen. Hierzu werden zwei Verfahren, in denen das Problem zunächst ohne Wirbelströme gelöst wird, um eine erste Lösung zu erhalten, detailliert behandelt. Dieses Ergebnis liefert dann die Anfangsbedingung des Lösungsprozesses für die Wirbelstromberechnung.

Schlagwörter: 3-dimensional, rechnergestützte Elektromagnetik, DC-Überlagerung, Wirbelströme, elektromagnetische Feldberechnung, elektromagnetische Modellierung, Finite Elemente Analyse, Finite Elemente Methoden, Geomagnetismus, nichtlinearer Magnetismus, nichtlineare Netzwerkmodelle, Transformatorprobleme

Contents

1 Introduction

1.1 Motivation

Electrical power is the most common energy source to energize and run a substantial number of devices in daily use. The steady progress in the development of electronics and power electronics has led to there being hardly any device we are using that is not powered by electricity. Due to this trend, our power consumption has increased exponentially in the past decades. On the one hand it is a very comfortable power source for consumers: on the other hand it is a quite challenging task for providers to guarantee a consistent flow of energy.

In the early days of electrification it was hardly imaginable that one day electrical energy would be this valuable and a shortage of this power source was inconceivable. The industry was powered up and machines and devices were developed without questioning their efficiency. It seemed that there were no restrictions in size and occurring losses at all to achieve the main goal – functionality. Even generating electrical energy was wasteful, dissipating crude materials not caring about the environment. This lavish evolution claims its toll. Pollution increased due to unclean thermal power plants and resources were rapidly harvested.

Due to limits in power generation and the rapid growth in the amount of electrical devices new policies in using electric energy emerged. Engineers started to investigate the efficiency of electrical devices. The new challenging focus was to increase functionality and efficiency. Furthermore, since especially in densely

populated areas the available space plays a significant role, a compact design has also become an object of great interest.

In increasing efficiency, the main focus was mostly on devices for power generation and distribution to avoid unnecessary losses. As a consequence, new design studies and sophisticated analyses of the behavior of electrically driven apparatuses gained importance. The most significant losses are the copper, iron and eddy current losses which lead to a substantial amount of electrical losses, dissipated thermal energy and highly affect the degree of efficiency. It was obvious that intensive research had to be done to correctly assess material properties and the effects of electromagnetic field distributions.

Especially in large power transformers [1, 2, 3] these new findings have shown that electromagnetically induced eddy currents are a dominant issue in generating additional losses influencing the efficiency. These losses occur in the windings of a transformer due to the skin-effect and are also due to eddy currents flowing in the iron core influencing the magnetic flux distribution and in other conductive materials used in the assembly of a transformer as e.g. clamping plates or the housing. To account for these losses, the mathematical models of transformers had to be adapted considering eddy currents. To handle the losses in the windings of the transformer new types of wires were designed to minimize the skin effect (see appendix A) and additionally to cut down material demands. Hence so called stranded litz-wires and continuously transposed conductors replaced massive conductors [4, 5, 6, 7, 8, 9, 10, 11].

A similar procedure was applied to the magnetically most relevant parts as the iron core. Due to proper design of the core material it turned out that using laminated steel sheets reduces the influence of eddy currents enormously. In order to achieve better flux distributions in the core, more suitable material types were developed and oriented material structures were applied for a better flux guidance [12, 13, 14, 15].

Due to the mentioned scarcity of available space, the dimensions of power transformers needed to be reduced and induced eddy currents in the transformer housing became relevant since the magnetic field decays with the distance. Due to reductions in the dimensions of the housing, the distances between the active parts and the highly permeable steel tank were scaled down hence the additional losses due to induced eddy currents in the steel tank increased. It is impossible to cover these additional losses with investigations based on analytical studies within such complex structures. However these losses are not negligible and are needed to be researched.

During the analysis of additional losses, environmental influences had also been investigated. It turned out that geo-magnetically induced currents [16] (GIC) are also

a decisive source for additional losses in transformers. These currents are caused by solar activity as e.g. sun flare [17, 18]. The interaction with the earth´s magnetic field can produce auroral currents disturbing the dormant magnetic field resulting in variations in the earth surface potential (ESP) and producing a current, known as geo-magnetically induced current flowing through the grounded neutral of transformers and along the transmission lines. These direct current (DC) components can cause adverse problems in power distribution infrastructures as power transformers by adding a DC bias to the magnetization current of the transformer. As a consequence, the core of the transformer gets saturated within the half-period in which the magnetization current and the DC bias are in the same direction resulting in increasing noise level, additional core losses as well as eddy current losses due to higher leakage flux [19, 20, 21].

As a consequence of the above demands, numerical methods have been developed to assess the characteristics of electrical devices with complex geometries by computer aided design. Since numerical investigations are needed, it is obvious that improving these computations is a main goal. In the very beginning, the available resources were poor and the functionality limited hence the computational costs were significant. Since then there has been a continuous progress in developing numerical solvers. The major issue is computational time. Determining the characteristics of an electrical device as accurately as possible is a complex task. It is not only a matter of hardware of a computational unit to save computational time. The algorithms implemented in the numerical solving procedure are dominant. Therefore it is necessary to investigate mathematical algorithms to speed up the computations by simultaneously increasing the accuracy of the results.

Due to the steady research there are still possibilities to improve numerical investigations and it is obvious that the motivation is present to decrease computational costs as it will be shown in this thesis.

1.2 State of the art

1.2.1 Finite Element Method

There is a huge amount of literature dealing with the Finite Element Method (FEM) and it is not the topic of this thesis to cover the entire history of FEM. This method has been well known for over 50 years and has been steadily developed since then. The basic idea of the finite element method is to subdivide a geometrical domain of a boundary-value problem into smaller subdomains, called the finite elements (FE), and expressing the governing differential equations to be solved computationally using linear algebra techniques. An extensive collection of FEM strategies has been compiled by O. Zienkiewicz [22] besides plenty of researchers as e.g. [23, 24, 25, 26, 27, 28]. This technique can be applied in many fields of interest as e.g. mechanical problems to determine mechanical stress or behavior of structures as well as in electromagnetic problems to determine electromagnetic field quantities as well as gaining information of local attributes as magnetic flux distributions or power losses. In this thesis we will focus on the application in electromagnetic field investigations. With the aid of FEM it is possible to observe the inside of problem domains and to visualize emerging physical processes for one dimensional (1D), two dimensional (2D) and of course three dimensional (3D) arrangements.

For solving a boundary-value problem with FEM one needs to define the problem domains and express the FE with continuity conditions and excitations to solve the relevant differential equation system. Due to the steady improvement of this technique, plenty of formulations to describe the problem domains have been researched [29, 30, 31, 32, 33, 34]. In the beginning of numerically solving electromagnetic field problems the main focus of investigations was related to 1D and 2D problems due to limited computational resources available. The most popular formulation developed uses a magnetic vector potential to describe non-conducting domains and an electric scalar potential as well as a magnetic vector potential covering the partial differential equations for conducting areas. This basic concept has its benefits as the magnetic flux density is directly expressed by a magnetic vector potential. Besides this approach another technique has been developed using a magnetic scalar potential to be used in non-conducting regions and a magnetic current vector potential in addition to a magnetic scalar potential to describe conducting domains [35, 36, 37, 38]. These formulations will be described in detail in sub-section 2.1.2. These techniques have been successfully applied to 2D

problems and later on been adapted to cover more complex and practically relevant 3D model domains. Pioneer work has been conducted e.g. in [39, 40, 41, 42, 43, 44, 45]. Since the basic idea of applying FEM emerged, a lot of effort has been given to improvement and development to achieve practically relevant simulation results. Due to limited access to computational resources and enormous computational costs FEM simulations were restricted to scientific research facilities as for example universities. Reducing the computational costs by finding more efficient solving algorithms and sustained availability of improved calculation machines it has now become possible to access FEM simulations in everyday procedures in research as well as in computer aided design (CAD) in commercial use. Hence nowadays almost every electromagnetic application can be specifically investigated with reasonable expense based on FEM.

1.2.2 Modelling by finite elements

As this thesis is essentially dealing with investigations of three dimensional problems, the given elaborations of terms and concepts will refer to this scope.

Nowadays there are hardly any restrictions in modelling a problem domain in conjunction with FEM. To subdivide a 3D problem domain into finite elements two approaches have become most popular beside others. On the one hand, tetrahedral edge based elements are used to mesh the domain of interest in finite elements and on the other hand hexahedral edge based elements are employed. In addition to several other parameters, the decision on the density as well on the polynomial order of the FEs (linear, quadratic or higher order basis functions) have major impact on the accuracy of the computational result. It depends on the problem of interest and the postulated accuracy how to select the most efficient FE-mesh. Several works validating the advantages and disadvantages of tetrahedral and hexahedral elements can be found, mostly proposing that both techniques are eligible with tendency to preferring the hexahedral construct due to robustness and providing more accurate results accompanied by less effort in optimizing the elements [46, 47, 48, 49, 50]. On the other hand, tetrahedral meshes are easier to be generated automatically. Also mixed formulations are appropriate, combining the features of tetrahedral, hexahedral and other volume structures to mesh model domains [51]. Furthermore, non-conforming meshing can also be applied to examine problems involving movement [52, 53, 54, 55, 56, 57]. Regarding this work, the FE structures implemented in the FEM solver used are 2^{nd} order edge based hexahedral finite elements. The governing differential equations in association with the boundary

conditions (boundary value problem, BVP) need to be set up in such discretized domains to yield an algebraic equation system (or a system of ordinary differential equations in time). The two widely spread approaches applied are either a variational method by minimizing a functional [58, 59] that represents the energy associated with the boundary value problem or a weighted-residual method such as the well-known Galerkin technique [60]. The latter one is based on generating a residual instantly from the BVP without having to resort to a functional at all. Therefore, the Galerkin approach has gained popularity and will also be followed in this thesis, see section 2.2.

1.2.3 Evolution of solving capabilities

The early three dimensional problems investigated by applying FEM were of simple geometry involving homogenous as well as linear materials due to limitations of the available computational resources and solving algorithms. In order to obtain practically applicable results and exploit the constantly improving hardware, the solvers had to be adapted. The magnetic materials used in a real world electromagnetic device have nonlinear characteristics and neglecting their hysteresis is not satisfactory when computing losses. The pioneering scientific findings considering hysteresis by C.P. Steinmetz [61, 62, 63, 64] were a major step forward in this respect. Besides nonlinearity, anisotropic properties have gained recognition in applications and are to be considered for meaningful investigations. Taking into account real world material specifications, FEM-solving algorithms have developed to highly powerful investigation tools not only to accurately compute electromagnetic field properties but also to predict additional losses hard to estimate by an analytical approach and occurring in parts of devices not essential for their operation [65].

The most common way to solve a nonlinear time varying problem is to perform a step by step computation with the time domain discretized into suitable time-steps and the unknown quantities predicted in each time-step. The quantities obtained are then used as initial values for the next time-step. This procedure is also known as transient solution and often called brute force method in the literature [66, 67, 68, 69, 70]. It is obvious that the characteristics of the problem highly affect the duration of the computation since the transient solution can take several time-periods before achieving steady-state. Thus the computational time increases dramatically. This procedure is indispensable when treating transient phenomena as for example inrush effects whether a periodic or non-periodic excitation is present. If steady-state

solutions due to periodic excitations are needed only, the solving algorithm can be adapted to skip the tremendous time consumption of the transient solution. Several approaches determining fast steady-state solutions have been investigated and well documented in the literature [71, 72, 73, 74, 75, 76]. Besides others, two established algorithms are, on the one hand, the ”time-periodic finite element method” taking advantage of the symmetry and periodicity of the excitation computing only one half of the time-period [77, 78, 79]. On the other hand, the solution can be predicted by applying the well-known harmonic balance technique often called “harmonic-balance finite element method” in the literature [80, 81, 82, 83], decomposing the time-periodic solution as the sum of its harmonic components. As these two formulations are quite dominant in contemporary solving procedures it is obvious that there is a focus on improvement. Thus this thesis deals with both formulations and they will be examined in detail in section 2.3.

The usual excitations in BVPs describing electromagnetic devices are coil currents. Since real world problems are frequently voltage driven, methods based on coupling the FEM-model with an electrical circuit model have been introduced to iteratively determine the unknown winding currents considering the skin-effect as well as nonlinear material characteristics [84, 85, 86, 87].

The prediction of losses is a major topic in state of the art analysis of real world problems. Plenty of books and research work are dealing with losses occurring in electrical devices including analytical approaches yielding a good estimation of the expected losses, experimental loss models using specific parameter studies well designed for the problem at hand or highly sophisticated evaluation strategies [88, 89, 90, 91, 92, 93, 94]. The spectrum of losses is a wide variety consisting among others of resistive losses of the wiring often called copper losses, iron losses mostly manifesting in hysteretic behavior due to nonlinearity of the materials as well as eddy current losses due to induced eddy currents in active materials as well as adjacent passive assembly parts of the construct. The spectrum of losses is well presented in literature [3] as well as specifically investigated in Ph.D. theses as e.g. [95].

Particularly high losses in a transformer construct can be observed if a direct current (DC) is accompanying the exciting alternating current (AC). Such DC components are a consequence of geo-magnetically induced currents GIC [16, 96] as mentioned earlier. These currents affect the operating conditions by evoking a bias of the magnetizing current. Hence the core material is saturated in one half-period leading to an increase of magnetization losses. These additional losses are not negligible, therefore this issue has gained recognition and many researchers have considered the appearance of DCs in FEM based solution strategies [97, 98, 99, 100,

101, 102, 103, 104, 105, 106]. Since the implementation in FEM is not straightforward and the computational costs are quite extensive, this thesis will validate different solution approaches dealing with DC components under voltage excitation.

Constructing a real world problem model with the aid of 3D-FEM considering issues as e.g. nonlinear material behavior, eddy-currents, DC bias and voltage excited coils in detail and aiming to obtain accurate and meaningful results, is seen to lead to equation systems involving a high numbers of degrees of freedom. This results in a dramatic increase of computational costs. As the recent development of computational resources has been fast and multiple core calculation units are now the rule rather than an exception, new approaches in analyzing FEM based models have become necessary. The solving algorithms of the equation system of a FEM analysis can now be adapted to make parallel computations executable, leading to a sustainable saving of computational time. The idea of clustering several computational units forming so called “super-computers” has been the next step in parallelization. Not only parallel CPUs are nowadays available but also many workstations can be connected. It has become possible to split up computable sections of the solution processes to several workstations in a parallel way carrying out independent computations with a superior process coordinating the communication between the computers. Finally, the solutions are merged to obtain the results. This technique is called parallel “Message Passing Interface” (MPI) and has been successfully implemented in FEM as demonstrated in [107, 108, 109, 110].

1.3 Scientific contributions

The contributions of this thesis to science are briefly summarized below including published work as well as some unpublished investigations.

- In order to validate existing FEM procedures to solve nonlinear, periodic eddy current problems, a dry insulated air reactor has been investigated. Additional eddy current losses in an adjacent steel grid used as reinforcement in concrete constructions have been determined. A reduced vector potential formulation was applied to different FEM strategies to compare the results to measured values. The findings of this work have first been presented at a PhD Symposium [111] as well as at a conference [112] and later on published in [113].

- To assess the competitiveness and efficiency of the FEM algorithms, a benchmark problem has been defined in cooperation with Professor Yasuhito Takahashi from the Doshisha University in Kyoto, Japan. A comparison of different techniques with those developed by the Japanese group has been done with the initial problem setup of a basic current driven single phase transformer. The findings have been presented at a symposium [114], and a version with voltage excitation of the primary coil at a conference [115]. In order to make the comparisons with the magnetic vector potential formulation used by the Japanese group more meaningful, this formulation with voltage excitation was then implemented, and a comparison presented at a conference [116] and later published in [117].
- In order to enable a fast evaluation of the advantages and disadvantages of FEM formulation to solve nonlinear, periodic problems, a simplified nonlinear magnetic circuit model has been designed based on the 3D transformer problem investigated in the works [114] - [117]. Initially, the main issue was to set up the solution algorithm of the magnetic circuit problem similarly to the one used in the 3D harmonic balance fixed-point technique with current vector potential formulation. Hence it was possible to quickly examine the procedures for solving the nonlinear equation system and their impact on the convergence of the nonlinear iterations. The outcome has first been presented at a conference [118] and published in [119]. Consequently, the magnetic vector potential formulation applied in the 3D FEM was introduced in the magnetic circuit model. It hence became possible to compare the magnetic vector potential and the current vector potential formulations using the harmonic balance fixed-point nonlinear iteration technique. Different load case scenarios were investigated for validation and presented at two symposia [120] and [121] and an enhanced version with voltage excitation at a conference [122].
- A novel solving strategy for improving the FEM analysis of 3D, nonlinear, periodic eddy current problems involving voltage driven coils under DC bias has been presented at a conference [123] and further published in IEEE Transaction on Magnetics [124].

1.4 Thesis outline

This thesis is subdivided into 8 chapters starting with the first chapter introducing the motivation of research and the improvements achieved in this field of expertise. Furthermore, a review of relevant literature representing a survey of the development in FEM-based problem analysis is given as well as the current state of the art procedures of currently applied techniques are briefly described. This establishes the starting point for the investigations.

Chapter 2 summarizes the mathematical background as well as technical fundamentals applied in this thesis. This chapter also includes the description of the investigated solution algorithms and possibilities for their improvement.

Chapter 3 examines an initial numerical FEM problem for the evaluation of additional eddy current losses in air reactors using different solution approaches.

In chapter 4 basic nonlinear magnetic-circuit models are designed representing different potential formulations to enable quick analyses of the FEM based solution algorithms. The circuit models are based on a 3D benchmark transformer problem which is investigated in more detail by a nonlinear 3D FEM approach in chapter 5, where the fixed-point solution procedures investigated on the thesis are compared to methods known from the literature and are hence validated.

Furthermore, in chapter 6, a detailed validation of the use of various potential formulations in the fixed-point context is given based on the transformer problem of the chapters 4 and 5.

In chapter 7, a nonlinear 3D FEM eddy current problem is investigated when a DC bias is present. The aim is to determine the benefit of an adapted solution algorithm for treating DC biased problems including the influence of a static initial solution for the nonlinear iteration approach to yield the dynamic steady state solution.

Finally the research will be summarized in chapter 8 with the scientific results recapitulated.

2 Fundamentals

2.1 Electromagnetism and physical background

The presence of electromagnetic phenomena influencing our lives has an astonishing history. The first known discovery is ascribed to the antique Greeks who detected a force interaction when scrubbing amber resulted in lifting a papyrus sheet. Furthermore, a stone with the ability to attract iron, now known as magnetite, was discovered. Since then intense investigations have led to more knowledge of electric and magnetic phenomena. Based on these experimental researches, scientists as Cavendish, Coulomb, Ampère and Faraday just to name a few, published their pioneering results. It was the work of Maxwell in 1864 who presented a set of equations completely describing electromagnetically coupled phenomena by enhancing Ampère´s law and gathering Faraday´s law of induction as well as Gauss´ laws of magnetism and electricity. Later on Hertz verified Maxwell´s theory with the discovery of electromagnetic waves. These findings are the basis of modern computational electrodynamics and can be found well detailed in literature as e.g. [125, 126, 127].

2.1.1 Maxwell´s equations

The so-called Maxwell´s equations use electromagnetic field quantities to fully describe electromagnetic phenomena. Since the main focus of this thesis is on low frequency time-periodic conditions, quasi static eddy current problems are treated. Hence, the influence of the displacement current density is assumed to be negligible. The resulting equations in the quasi-static limit [125] are

$$\nabla \times \mathbf{H} = \mathbf{J} \qquad \text{Ampère´s law,} \qquad (2.1)$$

$$\nabla \times \mathbf{E} = -\frac{\partial \mathbf{B}}{\partial t} \qquad \text{Faraday´s law,} \qquad (2.2)$$

$$\nabla \cdot \mathbf{B} = 0 \qquad \text{Gauss´ law of magnetism} \qquad (2.3)$$

where ∇ represents the Nabla operator, $\mathbf{H}$ is the vector of the magnetic field intensity, $\mathbf{J}$ is the current density vector, $\mathbf{E}$ is the electrical field intensity vector, the vector $\mathbf{B}$ is the magnetic flux density and t is time. Equation (2.1) implies the principle of charge conversation written as the law of continuity:

$$\nabla \cdot \mathbf{J} = 0\,. \qquad (2.4)$$

These equations can be written in integral form to explicitly show the physical relations. On the one hand, Gauss´ theorem can be applied to yield a conversion of a volume integral of the divergence of a vector into a surface integral over the surface delimiting the volume. On the other hand, Stokes´ theorem states the equivalence of a surface integral of the curl of a vector field to a closed line integral over the curve delimiting the surface [128]. Taking advantage of these theorems, one can obtain the integral form of Ampère´s, of Faraday´s law and of Gauss´ law of magnetism. Hence (2.1)-(2.3) can be written as

$$\oint_{\partial\Gamma} \mathbf{H} \cdot d\mathbf{l} = \int_{\Gamma} \mathbf{J} \cdot d\boldsymbol{\Gamma}\,, \qquad (2.5)$$

$$\oint_{\partial\Gamma} \mathbf{E} \cdot d\mathbf{l} = -\int_{\Gamma} \frac{\partial \mathbf{B}}{\partial t} \cdot d\boldsymbol{\Gamma}\,, \qquad (2.6)$$

$$\oint_{\partial\Omega} \mathbf{B} \cdot d\boldsymbol{\Gamma} = 0\,, \qquad (2.7)$$

where $\partial\Gamma$ is the boundary of the surface Γ and $\partial\Omega$ denotes the bounding surface of the volume Ω. Fig. 2.1 and Fig. 2.3 illustrate the physical interpretation of the first Maxwell equation showing that the whirls of the magnetic field intensity are equivalent to the conductive current. The physical content of the second Maxwell equation drawn in Fig. 2.2 and Fig. 2.4 is that a time varying magnetic field density causes whirls of the electrical field intensity.

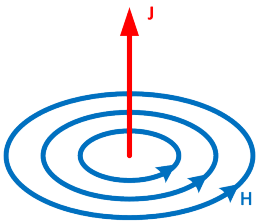

Fig. 2.1: Physical interpretation of (2.1).

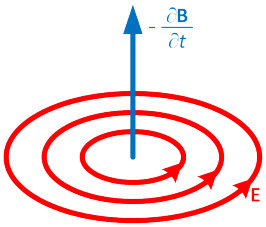

Fig. 2.2: Physical interpretation of (2.2).

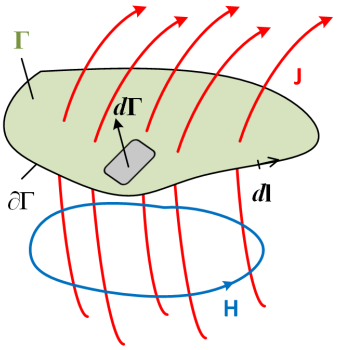

Fig. 2.3: Physical interpretation of (2.5).

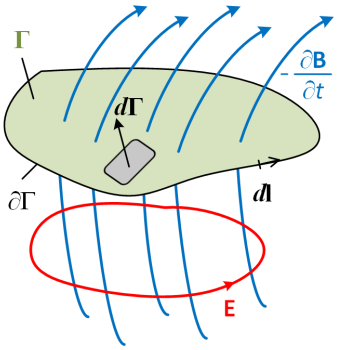

Fig. 2.4: Physical interpretation of (2.6).

The field quantities appearing in Maxwell´s equations are coupled by material relations:

$$\mathbf{B} = \mu \mathbf{H}, \quad \mathbf{H} = \nu \mathbf{B}, \tag{2.8}$$

$$\mathbf{J} = \sigma \mathbf{E}, \quad \mathbf{E} = \rho \mathbf{J}, \tag{2.9}$$

$$\mu = \mu_r \mu_0; \quad \mu_0 = 4\pi \cdot 10^{-7} \left(\frac{\mathrm{Vs}}{\mathrm{Am}} \right). \tag{2.10}$$

The magnetic permeability μ is the product of the relative permeability μ_r and the permeability of free space μ_0. The magnetic reluctivity ν is the inverse of μ. σ represents the electrical conductivity of a material with its inverse ρ, the electrical resistivity. These materials may vary in space and with temperature, frequency or the field quantities and are in general described by tensors. In case of isotropic materials, these tensors become scalars as assumed in this thesis.

2.1.2 Potential Formulations

To ensure an efficient treatment of electromagnetic field problems, it is advantageous to describe the field quantities appearing in Maxwell´s equations by means of potential functions. With the aid of adjunct scalar and vector potentials, certain Maxwell's equations can be automatically satisfied.

Since this thesis deals with nonlinear eddy-current problems and utilizes potential functions, one has to classify the relevant domains with respect to their conductivity. Hence, two geometric regions are distinguished as illustrated in Fig. 2.5. The conductivity of the coils with given current density in Ω_n is irrelevant.

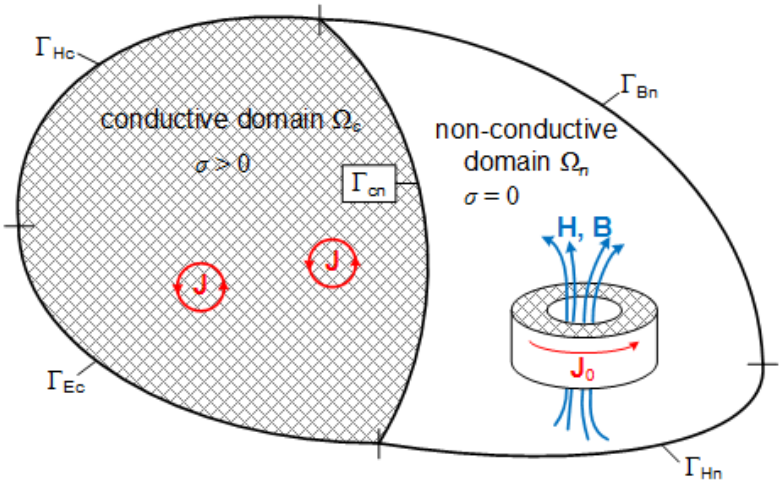

Fig. 2.5: Basic topology of an eddy-current problem domain.

Initially it is assumed that the source coils are current driven as indicated in Fig. 2.5 with an impressed current density $\mathbf{J}_0$. Later on in this thesis the case of voltage driven coils will be examined as well. The exciting coils are included in the non-conductive domain Ω_n where the field quantities are static but time-dependent. In the conductive region Ω_c eddy currents are to be additionally considered. Hence, the governing differential equations to be solved in the non-conducting domain are

$$\left.\begin{aligned} \nabla \times \mathbf{H} &= \mathbf{J}_0 \\ \nabla \cdot \mathbf{B} &= 0 \end{aligned}\right\} \text{ in } \Omega_n , \tag{2.11}$$

and for the conducting domain we have

$$\left.\begin{aligned} \nabla \times \mathbf{H} &= \mathbf{J} \\ \nabla \times \mathbf{E} &= -\frac{\partial \mathbf{B}}{\partial t} \\ \nabla \cdot \mathbf{B} &= 0 \end{aligned}\right\} \text{ in } \Omega_c \ . \tag{2.12}$$

The material relations have been written in (2.8)-(2.10) with the nonlinearity of the magnetic permeability considered by a suitable *B*-*H* curve in this thesis. In the exciting coils, an impressed total current density or a given voltage source inevitably leads to skin effect. This effect will be explained in appendix A, but will be assumed to be negligible in this work due to the proper design of the wiring.

In general, 3D eddy-current problems are formulated as boundary value problems (BVP) to allow a FEM investigation. The outer boundaries illustrated in Fig. 2.5 prescribe either the tangential or the normal component of the relevant field quantity. TABLE 2.1 summarizes the possible boundary conditions where **n** represents the surface normal vector.

TABLE 2.1: Boundary conditions for the problem domain in Fig. 2.5

Boundary	Condition
Γ_{Hc}	$\mathbf{H} \times \mathbf{n} = 0$
Γ_{Ec}	$\mathbf{E} \times \mathbf{n} = 0$
Γ_{Hn}	$\mathbf{H} \times \mathbf{n} = \mathbf{K}$
Γ_{Bn}	$\mathbf{B} \cdot \mathbf{n} = -b$
Γ_{cn}	$\mathbf{H} \times \mathbf{n}$ and $\mathbf{B} \cdot \mathbf{n}$ are continuous

Note that the symbol **K** represents a surface current density as an impressed vector field and *b* denotes a scalar field representing a magnetic surface charge density.

The tangential component of the magnetic field intensity is prescribed on the boundaries Γ_{Hc} and Γ_{Hn}, whereas the tangential component of the electrical field intensity is defined on Γ_{Ec}, and the normal component of the magnetic flux density is given on Γ_{Bn}. To couple the formulations of the conducting domain Ω_c and the non-conducting area Ω_n, the continuity of the tangential component of the magnetic field intensity and the normal component of the magnetic flux intensity are prescribed on the interface Γ_{cn}. Utilizing these conditions along with the set of differential equations of (2.11) and (2.12) ensures a unique solution [43].

Based on the above division of the topology of eddy current problems and in accordance with the formulations used in this work, three commonly used potential formulations will be introduced to transform Maxwell´s equations to second order

elliptic or parabolic partial differential equations. The so called **A**,V-**A**-formulation and its modified form, the $\mathbf{A}_r$,V-$\mathbf{A}_r$-formulation as well as the **T**,ϕ-ϕ-formulation are introduced in the following sub-sections [129].

2.1.2.1 A,V-A-formulation

This formulation is widely used in FEM based computational problems due to the simplicity of introducing a magnetic vector potential **A** to describe the magnetic flux density in the entire problem domain and an additional electrical scalar potential V to represent the electric field intensity in the conducting regions Ω_c.

Since the magnetic flux density is source free, i.e. it obeys Gauss´ law for magnetism (2.3) and the divergence of the curl of any vector field **F** is identically zero $\left(\nabla\cdot\left(\nabla\times\mathbf{F}\right)\equiv 0\right)$,

$$\mathbf{B}=\nabla\times\mathbf{A} \tag{2.13}$$

can be written. Since the divergence of **A** is not defined, this equation has infinitely many solutions. The uniqueness of **A** can be achieved by appropriate gauging but this is not necessary to describe the field quantities uniquely. Substituting (2.13) into Maxwell´s equations, Faraday´s law in the quasi static limit can be written as

$$\nabla\times\mathbf{E}=-\nabla\times\frac{\partial\mathbf{A}}{\partial t}. \tag{2.14}$$

Utilizing the fact that the curl of the gradient of any scalar function F is identically zero $\left(\nabla\times\left(\nabla F\right)\equiv 0\right)$ one can introduce a modified electrical scalar potential v to guarantee a symmetric equation system when applying Galerkin techniques (see sub-section 2.2.2), hence one can obtain the electrical field intensity as

$$\mathbf{E}=-\frac{\partial\mathbf{A}}{\partial t}-\nabla V=-\frac{\partial}{\partial t}\left(\mathbf{A}+\nabla v\right), \tag{2.15}$$

as well as the current density using the material relations:

$$\mathbf{J}=-\sigma\left(\frac{\partial\mathbf{A}}{\partial t}+\nabla V\right)=-\sigma\frac{\partial}{\partial t}\left(\mathbf{A}+\nabla v\right). \tag{2.16}$$

Furthermore, Ampère´s law can be rewritten as:

$$\nabla \times \left(\nu \nabla \times \mathbf{A} \right) = \mathbf{J} \,. \tag{2.17}$$

Having introduced the magnetic vector potential and the modified electric scalar potential, one obtains a set of partial differential equations expressing Ampère´s law and the continuity law in the conducting domain as:

$$\left.\begin{aligned} \nabla \times \left(\nu \nabla \times \mathbf{A} \right) + \sigma \frac{\partial \mathbf{A}}{\partial t} + \sigma \frac{\partial}{\partial t} \nabla v = \mathbf{0}, \\ -\nabla \cdot \left(\sigma \frac{\partial \mathbf{A}}{\partial t} + \sigma \frac{\partial}{\partial t} \nabla v \right) = 0 \end{aligned}\right\} \text{in } \Omega_c \,, \tag{2.18}$$

and Ampère´s law in the non-conducting domain as

$$\nabla \times \left(\nu \nabla \times \mathbf{A} \right) = \mathbf{J}_0 \text{ in } \Omega_n \,. \tag{2.19}$$

The Dirichlet and Neumann boundary conditions on the potentials are summarized in TABLE 2.2.

TABLE 2.2: Valid boundary conditions for the **A**,*V*-**A**-formulation

Boundary	Condition
Γ_{Hc}	$\left(\nu \nabla \times \mathbf{A} \right) \times \mathbf{n} = \mathbf{0}$ and $\left(-\sigma \frac{\partial \mathbf{A}}{\partial t} - \sigma \frac{\partial}{\partial t} \nabla \mathrm{v} \right) \cdot \mathbf{n} = 0$
Γ_{Ec}	$\mathbf{A} \times \mathbf{n} = \mathbf{0}$ and $v = v_D = \text{constant}$
Γ_{Hn}	$\left(\nu \nabla \times \mathbf{A} \right) \times \mathbf{n} = \mathbf{K}$
Γ_{Bn}	$\left(\nabla \times \mathbf{A} \right) \cdot \mathbf{n} = -b$
Γ_{cn}	$\left(\nu_c \nabla \times \mathbf{A}_c \right) \times \mathbf{n}_c + \left(\nu_n \nabla \times \mathbf{A}_n \right) \times \mathbf{n}_n = \mathbf{0}$ and $\left(\nabla \times \mathbf{A}_c \right) \cdot \mathbf{n}_c + \left(\nabla \times \mathbf{A}_n \right) \cdot \mathbf{n}_n = 0$

Note that the subscript c indicates quantities of the conducting domain and n those of the non-conductive regions. The relationship between the outer normal vectors is $\mathbf{n}_c = -\mathbf{n}_n$

The tangential component of the vector potential **A** is continuous on the interfacing boundary Γ_{cn} between the two regions implying the continuity of the

normal component of the magnetic flux density on Γ_{cn}, whereas the condition of the tangential component of the field intensity being continuous is still to be fulfilled. On the Dirichlet-boundary Γ_{Ec} the tangential component of the vector potential is zero and a constant scalar potential value v_D is introduced enabling skin effect problems with voltage excitation with the scalar potential given as the time-integral of the voltage on the boundary:

$$v_D = \int_0^t U(\tau) d\tau \quad \text{on } \Gamma_{Ec} \,. \tag{2.20}$$

In case of skin effect problems with current excitation, v_D is an unknown constant satisfying the integral condition

$$\int_{\Gamma_{Ec}} \sigma \left(\frac{\partial \mathbf{A}}{\partial t} + \nabla \frac{\partial v}{\partial t} \right) \cdot \mathbf{n} d\Gamma = i \,, \tag{2.21}$$

where i represents the given current.

For effectively treating time-harmonic problems the equations can be transformed into the frequency domain by the conversion $\frac{\partial}{\partial t} \Rightarrow j\omega$ where $j = \sqrt{-1}$ is the imaginary unit and ω is the angular frequency $\omega = 2\pi f$ with respect to the frequency f. Hence the equations for the $\mathbf{A},V$-$\mathbf{A}$-formulation (2.13)-(2.19) can be rewritten as

$$\mathbf{B} = \nabla \times \mathbf{A} \,, \tag{2.22}$$

$$\nabla \times \mathbf{E} = -\nabla \times j\omega \mathbf{A} \,, \tag{2.23}$$

$$\mathbf{E} = -j\omega \mathbf{A} - \nabla V = -j\omega \mathbf{A} - j\omega \nabla v \,, \tag{2.24}$$

$$\mathbf{J} = -\sigma \left(j\omega \mathbf{A} + \nabla V \right) = -\sigma j\omega \left(\mathbf{A} + \nabla v \right) , \tag{2.25}$$

$$\nabla \times \left(\nu \nabla \times \mathbf{A} \right) = \mathbf{J} \tag{2.26}$$

and written for the two domains:

$$\left.\begin{aligned}\nabla\times\left(\nu\nabla\times\mathbf{A}\right)+\sigma j\omega\mathbf{A}+\sigma j\omega\nabla V=\mathbf{0},\\ -\nabla\cdot\left(\sigma j\omega\mathbf{A}+\sigma j\omega\nabla V\right)=0\end{aligned}\right\}\ \text{in}\ \ \Omega_c\,, \tag{2.27}$$

and

$$\nabla\times\left(\nu\nabla\times\mathbf{A}\right)=\mathbf{J}_0\ \ \text{in}\ \ \Omega_n\,. \tag{2.28}$$

2.1.2.2 $\mathbf{A}_r$,V-$\mathbf{A}_r$-formulation

The so-called reduced vector potential formulation is commonly used for current excited problems. The major advantage in comparison to the $\mathbf{A}$,V-$\mathbf{A}$-formulation is that the field quantities of an exciting coil can be expressed by utilizing Biot-Savart´s law in free space and thus it is not necessary to discretize the coils by the finite element structure [35, 130, 131, 132]. Hence, the vector potential can be split in two parts, a known Biot-Savart source vector potential $\mathbf{A}_s$ and a reduced vector potential part $\mathbf{A}_r$ as

$$\mathbf{A}=\mathbf{A}_s+\mathbf{A}_r\ \ \text{with}\ \ \mathbf{A}_s=\frac{\mu_0}{4\pi}\int_{\Omega_s}\frac{\mathbf{J}_0}{r_{QA}}d\Omega\,, \tag{2.29}$$

where $\mathbf{A}_s$ denotes the vector potential due to the source currents in free space with the Coulomb gauge used to ensure the uniqueness of $\mathbf{A}_s$, r_{QA} is the distance between the reference point and the source point. To compute $\mathbf{A}_s$, the integration domain Ω_s has to include all regions where $\mathbf{J}_0$ is nonzero. The relationship to the Biot-Savart magnetic field is

$$\begin{aligned}&\nabla\times\mathbf{A}_s=\mathbf{B}_s=\mu_0\mathbf{H}_s\ \ \text{and}\\ &\nabla\times\mathbf{H}_s=\nabla\times\left(\nu_0\nabla\times\mathbf{A}_s\right)=\mathbf{J}_0.\end{aligned} \tag{2.30}$$

According to (2.13) the resulting magnetic flux density is obtained as

$$\mathbf{B}=\mu_0\mathbf{H}_s+\nabla\times\mathbf{A}_r\,, \tag{2.31}$$

and the electrical field intensity is

$$\mathbf{E} = -\frac{\partial}{\partial t}\mathbf{A}_s - \frac{\partial}{\partial t}\mathbf{A}_r - \frac{\partial}{\partial t}\nabla v \,. \tag{2.32}$$

The differential equations derived from Maxwell's equations in the conducting domain are:

$$\left.\begin{aligned} \nabla\times\left(\nu\nabla\times\mathbf{A}_r\right)+\sigma\frac{\partial\mathbf{A}_r}{\partial t}+\sigma\frac{\partial}{\partial t}\nabla v &= -\sigma\frac{\partial\mathbf{A}_s}{\partial t}-\nabla\times\left(\nu\nabla\times\mathbf{A}_s\right), \\ -\nabla\cdot\left(\sigma\frac{\partial\mathbf{A}_r}{\partial t}+\sigma\frac{\partial}{\partial t}\nabla v\right) &= \nabla\cdot\left(\sigma\frac{\partial\mathbf{A}_s}{\partial t}\right) \end{aligned}\right\} \text{in } \Omega_c \tag{2.33}$$

and in the non-conducting domain

$$\nabla\times\left(\nu\nabla\times\mathbf{A}_r\right)=\nabla\times\left(\nu_0\nabla\times\mathbf{A}_s-\nu\nabla\times\mathbf{A}_s\right)=\nabla\times\mathbf{H}_s-\nabla\times\nu\mu_0\mathbf{H}_s \text{ in } \Omega_n. \tag{2.34}$$

Transforming the obtained set of partial differential equations into the frequency domain results in

$$\left.\begin{aligned} \nabla\times\left(\nu\nabla\times\mathbf{A}_r\right)+\sigma j\omega\mathbf{A}_r+\sigma j\omega\nabla v &= -\sigma j\omega\mathbf{A}_s-\nabla\times\nu\mu_0\mathbf{H}_s, \\ -\nabla\cdot\left(\sigma j\omega\mathbf{A}_r+\sigma j\omega\nabla v\right) &= \nabla\cdot\left(\sigma j\omega\mathbf{A}_s\right) \end{aligned}\right\} \text{in } \Omega_c, \tag{2.35}$$

and

$$\nabla\times\left(\nu\nabla\times\mathbf{A}_r\right)=\nabla\times\mathbf{H}_s-\nabla\times\nu\mu_0\mathbf{H}_s \text{ in } \Omega_n. \tag{2.36}$$

The boundary conditions are defined similarly to the **A**,*V*-**A**-formulation and summarized in TABLE 2.3.

TABLE 2.3: Boundary conditions using the reduced magnetic vector potential formulation

Boundary	Condition
Γ_{Hc}	$\left(\nu\nabla\times\mathbf{A}_r+\nu\nabla\times\mathbf{A}_s\right)\times\mathbf{n}=\mathbf{0}$ and $\left(-\sigma\frac{\partial}{\partial t}\left(\mathbf{A}_r+\mathbf{A}_s\right)-\sigma\frac{\partial}{\partial t}\nabla v\right)\cdot\mathbf{n}=0$
Γ_{Ec}	$\left(-\frac{\partial}{\partial t}\left(\mathbf{A}_r+\mathbf{A}_s\right)-\nabla v\right)\times\mathbf{n}=\mathbf{0}$
Γ_{Hn}	$\mathbf{A}_r\times\mathbf{n}=-\mathbf{A}_s\times\mathbf{n}$ and $v=v_D=\text{constant}$ $\left(\nu\nabla\times\mathbf{A}_r+\nu\nabla\times\mathbf{A}_s\right)\times\mathbf{n}=\mathbf{K}$
Γ_{Bn}	$\left(\nabla\times\left(\mathbf{A}_r+\mathbf{A}_s\right)\right)\cdot\mathbf{n}=-b$
Γ_{cn}	$\left(\nu_c\nabla\times\left(\mathbf{A}_r+\mathbf{A}_s\right)\right)\times\mathbf{n}_c+\left(\nu_n\nabla\times\left(\mathbf{A}_r+\mathbf{A}_s\right)\right)\times\mathbf{n}_n=\mathbf{0}$ and $\left(\nabla\times\left(\mathbf{A}_r+\mathbf{A}_s\right)\right)\cdot\mathbf{n}_c+\left(\nabla\times\left(\mathbf{A}_r+\mathbf{A}_s\right)\right)\cdot\mathbf{n}_n=0$

It is assumed that the source vector potential $\mathbf{A}_s$ satisfies the boundary conditions on Γ_{Hc} and Γ_{Bn} as given for the $\mathbf{A},V$-$\mathbf{A}$-formulation in TABLE 2.2 which may not be exact on the far-boundary but for practical reasons it is accepted that the reaction field is negligible.

Regarding symmetry planes of the model domain in case of the $\mathbf{A},V$-$\mathbf{A}$-formulation it is possible to only model a part of the given problem as well as of the implemented FEM-structure of the excitations. In case of the $\mathbf{A}_r,V$-$\mathbf{A}_r$-formulation it is necessary to determine the source quantities by integrating over the entire source-volume. Hence, it is sufficient to define the symmetry boundary conditions for the reduced vector potential $\mathbf{A}_r$ and the scalar potential v only.

2.1.2.3 T,ϕ-ϕ -formulation

A very efficient method for quasi-static field problems is the so-called $\mathbf{T},\phi$-ϕ-formulation. Since the displacement current density is neglected in the quasi-static case, the current density is source-free resulting in the benefit that, in non-conductive regions Ω_n, a magnetic scalar potential ϕ can be used instead of a magnetic vector potential $\mathbf{A}$. This results in the major advantage of reducing the number of scalar unknown functions to one instead of three.

Since the current density $\mathbf{J}$ is source free (see (2.4)) in the quasi-static limit, the current vector potential $\mathbf{T}$ is introduced in the conductive domain Ω_c as

$$\mathbf{J} = \nabla \times \mathbf{T} . \tag{2.37}$$

Substituting (2.37) into Ampère´s law (2.1) and introducing a known current vector potential $\mathbf{T}_0$

$$\nabla \times \mathbf{T}_0 = \mathbf{J}_0 \tag{2.38}$$

with a good choice to compute $\mathbf{T}_0$ for arbitrary coil geometries is utilizing the Biot-Savart field

$$\mathbf{T}_0(\mathbf{r}) = \mathbf{H}_0(\mathbf{r}) = \frac{1}{4\pi}\int_{\Omega} \frac{\mathbf{J}_0(\mathbf{r}') \times (\mathbf{r} - \mathbf{r}')}{|\mathbf{r} - \mathbf{r}'|^3} d\Omega' \tag{2.39}$$

to describe the current density of the current driven coils, the resulting equation is

$$\nabla \times \mathbf{H} = \nabla \times (\mathbf{T} + \mathbf{T}_0) \tag{2.40}$$

where $\mathbf{T}$ represents the reduced current vector potential to describe the eddy currents in Ω_c. Taking advantage of the identity $\nabla \times (\nabla F) \equiv 0$ yields

$$\mathbf{H} = \mathbf{T} + \mathbf{T}_0 - \nabla\phi \text{ in } \Omega_c , \tag{2.41}$$

$$\mathbf{H} = \mathbf{T}_0 - \nabla\phi \text{ in } \Omega_n . \tag{2.42}$$

Writing Faraday´s law (2.2) and Gauss´ law of magnetism (2.3) along with the material relations, the set of partial differential equations of the problem are

$$\left.\begin{aligned} \nabla \times (\rho \nabla \times \mathbf{T}) + \mu\frac{\partial \mathbf{T}}{\partial t} - \mu\frac{\partial \phi}{\partial t} &= -\mu\frac{\partial \mathbf{T}_0}{\partial t}, \\ \nabla \cdot (\mu\mathbf{T} + \mu\nabla\phi) &= -\nabla \cdot (\mu\mathbf{T}_0) \end{aligned}\right\} \text{in } \Omega_c , \tag{2.43}$$

and

$$-\nabla \cdot (\mu\nabla\phi) = -\nabla \cdot (\mu\mathbf{T}_0) \text{ in } \Omega_n . \tag{2.44}$$

Transforming (2.43) and (2.44) into the frequency domain they can be written as

$$\left.\begin{aligned} \nabla\times\left(\rho\nabla\times\mathbf{T}\right)+\mu j\omega\mathbf{T}-\mu j\omega\phi &= -\mu j\omega\mathbf{T}_0, \\ \nabla\cdot\left(\mu\mathbf{T}+\mu\nabla\phi\right) &= -\nabla\cdot\left(\mu\mathbf{T}_0\right) \end{aligned}\right\} \text{ in } \Omega_c\,, \tag{2.45}$$

as well as

$$-\nabla\cdot\left(\mu\nabla\phi\right)=-\nabla\cdot\left(\mu\mathbf{T}_0\right) \text{ in } \Omega_n\,. \tag{2.46}$$

The corresponding boundary conditions to be satisfied by the potentials are

TABLE 2.4: Valid boundary conditions for the **T**,ϕ-ϕ-formulation

Boundary	Condition
Γ_{Hc}	$\mathbf{T}\times\mathbf{n}=\mathbf{T}_0\times\mathbf{n}=\mathbf{0}$ and $\phi=\phi_D=\text{constant}$
Γ_{Ec}	$\left(\rho\nabla\times\mathbf{T}\right)\times\mathbf{n}=\left(\rho\nabla\times\mathbf{T}_0\right)\times\mathbf{n}=0$ and $\mu\left(\mathbf{T}-\nabla\phi\right)\cdot\mathbf{n}=-\mu\mathbf{T}_0\cdot\mathbf{n}$
Γ_{Hn}	$\phi=\phi_D=\text{constant}$
Γ_{Bn}	$\mu\dfrac{\partial\phi}{\partial\mathbf{n}}=b+\mu\mathbf{T}_0\cdot\mathbf{n}$
Γ_{cn}	$\mathbf{T}\times\mathbf{n}=\mathbf{0}$ and $\left(\mu_c\mathbf{T}_0+\mu_c\mathbf{T}-\mu_c\nabla\phi\right)\cdot\mathbf{n}_c+\left(\mu_n\mathbf{T}_0-\mu_n\nabla\right)\cdot\mathbf{n}_n=0$

Using this formulation with holes present in the conducting domain (i.e. when this domain becomes multiply connected) results in a multivalued scalar potential in the non-conducting region. To solve such problems with the **T**,ϕ-ϕ-formulation additional constraints are required. This can be avoided by inserting a low conductivity material in the holes or coupling an electric circuit forcing an equivalent impressed current density around the hole.

2.1.3 Voltage driven coils

For simplicity, the previously discussed potential formulations of eddy current problems are defined as current driven, where a known current is impressed in the excitation coils. Since most practically relevant problems are excited by a given voltage, the potential formulations need to be adapted. Hence, additional constraints need to be enforced to determine the current of a voltage supply. An explicit derivation of including the voltage source into the FEM-formulations is given in [84, 85, 86, 87, 133].

Concerning the problems observed in this thesis the excited conductors are supposed to be free of skin effect appearance. This assumption is justified, when operating at low frequencies and contemplated measures in geometry design of the conductors are taken to avoid demeanor of the skin effect phenomena. Hence in this subsection the necessary terms of voltage excited coils without skin effect will be discussed.

With the magnetic scalar potential formulation introduced earlier in mind, we assume that the impressed current density $\mathbf{J}_0$ can be expressed by the curl of an impressed current vector potential $\mathbf{T}_0$ introduced in (2.38).

Since the winding current i is unknown, the current vector potential $\mathbf{T}_0$ can be expressed as the product of the unknown current and a unit current vector potential $\mathbf{t}_0$ [134] satisfying

$$\oint_{\partial\Gamma_i} \nabla\times\mathbf{t}_0\cdot d\mathbf{l} = \int_{\Gamma_i} \mathbf{t}_0\cdot d\boldsymbol{\Gamma} = 1 \tag{2.47}$$

as

$$\mathbf{T}_0 = \mathbf{t}_0 i\,, \tag{2.48}$$

with $\nabla\times\mathbf{t}_0$ being the turn density of the coil. Hence, the given voltage can be expressed as

$$u = Ri + \int_\Omega \nabla\times\mathbf{t}_0\cdot\mathbf{E}\,d\Omega = Ri - \int_\Omega \mathbf{t}_0\cdot\frac{\partial\mathbf{B}}{\partial t}d\Omega\,. \tag{2.49}$$

Utilizing the definitions of the $\mathbf{T}$,ϕ-ϕ-formulation one can obtain

$$u = Ri - \frac{d}{dt}\int_{\Omega} \mathbf{t}_0 \cdot \mu\left(\mathbf{T} + \mathbf{T}_0 + \mathbf{t}_0 i - \nabla\phi\right) d\Omega\,, \tag{2.50}$$

where the remaining $\mathbf{T}_0$ is a known quantity representing the possibility of current driven coils also being present. To solve a problem with given voltage excitation by the $\mathbf{T}$,ϕ-ϕ-formulation this equation has to be additionally taken into account.

Regarding the magnetic vector potential formulation, one can substitute (2.49) by (2.15) to yield

$$u = Ri - \frac{d}{dt}\int_{\Omega} \mathbf{t}_0 \cdot \nabla \times \mathbf{A} d\Omega\,, \tag{2.51}$$

as the additional equation to be satisfied in case of voltage driven coils in case of the $\mathbf{A}$,V-$\mathbf{A}$-formulation.

2.1.4 Loss computation

Many types of losses occur in electrical machines or transformers, such as iron or hysteretic losses, copper or resistive losses, stray losses and eddy current losses [3, 8, 14, 65, 95]. The focus of attention in this thesis is the improvement of FEM solution techniques. In comparing the accuracy of different approaches, the loss computation is a necessary tool.

The problems investigated in this thesis are excited by sinusoidal quantities; hence, the resulting magnetic field varies in time. Thus if any conductive material is present in the vicinity of the time varying magnetic field, eddy currents will be induced in the conductive object according to (2.2). As these eddy currents are induced by the presence of the magnetic field, they lead to additional losses. Concurrently, based on (2.1), the eddy-currents themselves give rise to a magnetic field exhibiting effects weakening the induction phenomenon. These effects manifest in a significant amount of the cumulative losses occurring in an electrical device. The losses due to eddy currents mostly exhibit distinctive non-linear characteristics in accordance with the material properties.

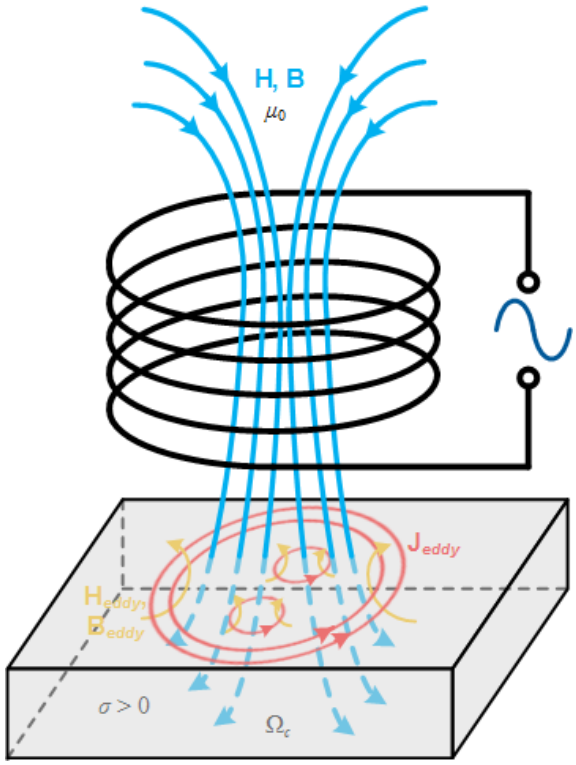

Fig. 2.6: Simplified design of induced eddy-currents.

Illustrated in Fig. 2.6 is a basic schematic procedure of eddy-currents being induced in a conductive domain Ω_c, situated adjacent to an alternating magnetic field **H**, **B**. The coil located in air is assumed to be driven by a time-varying, periodic quantity (e.g. a sinusoidal wave form).

The eddy current losses arising in the conductive material can be computed as

$$P_{eddy} = \frac{1}{T}\int_0^T \int_{\Omega_c} \frac{\left|\mathbf{J}_{eddy}\right|^2}{\sigma} d\Omega dt \,. \tag{2.52}$$

In (2.52) P_{eddy} corresponds to the eddy-current losses in a conductive region Ω_c, T represents a time-period and $\mathbf{J}_{eddy}$ is the eddy current density induced according to Faraday´s law in the conductive domain.

2.2 Finite Element Method

A brief introduction to the origin of this method was already given in sub-section 1.2.1. This section summarizes the underlying FEM strategy implemented in the solver used for the numerical investigations of electromagnetic field problems treated in this thesis. Fundamental discretization techniques as well as the shape of the finite elements and hence the resulting potential formulations as approximated solutions will be discussed. Furthermore, different approaches for the non-linear iteration procedures of eddy current problems will be discussed.

2.2.1 Finite element approximations

The FEM [22, 24, 26, 27, 28, 33] is used to obtain an approximate solution of boundary value problems in a domain Ω with boundary conditions given on the boundary limiting the domain $\Gamma=\partial\Omega$. Hence the field quantities become unique whether by defining constraints as Dirichlet boundary conditions prescribing the solution itself or Neumann boundary conditions regarding the derivative of the solution on the boundary. Such problems can be expressed as

$$Au = f\,, \tag{2.53}$$

where A is the differential operator, f represents the known excitation function and the unknown quantity u is to be solved for.

The distribution of the unknown quantity inside a finite element is interpolated based on the values at the nodes in case of nodal elements used for scalar variables or integrals over the edges using edge based vector elements. The so called basis (shape) functions need to be an entire set of polynomials. The approximate solution u_h with the corresponding coefficients c_j is written with the aid of N basis-functions n_j as

$$u \approx u_h = u_D + \sum_{j=1}^{N} c_j n_j\,, \tag{2.54}$$

where u_D denotes a function satisfying the inhomogeneous Dirichlet boundary conditions. The coefficients c_j are unknown, they have to be determined during the solution process. The solution is obtained after solving a system of equations. Setting

up such a system of equations for the BVP, first the system needs to be transformed into an algebraic equation system in the frequency domain or into an ordinary differential equation system in the time domain. This is achieved by using a weighted residual method, the Galerkin technique. Applying this procedure in each finite element an assembly of all elements yields a global matrix system.

The Galerkin technique will be highlighted in the following sub-section.

2.2.2 Weighted residual method (Galerkin technique)

A technique proposed by Boris G. Galerkin in 1915 is a variant of the method of weighted residuals [26, 33, 60, 135]. The idea is based on the minimization of the integral residual. Since u_h is the approximate solution of (2.53), substituting u_h for u in (2.53) will result in a non-zero residual

$$r = Au_h - f \neq 0. \tag{2.55}$$

The principle of the weighted residual states that the product of the residual and a set of weighting functions w_i should vanish when integrated over Ω:

$$\int_\Omega w_i r \, d\Omega = \int_\Omega w_i \left(Au_h - f \right) d\Omega = 0, \quad i = 1, 2, \ldots, N. \tag{2.56}$$

The Galerkin technique uses the same set of functions as weighting functions as expansion functions in the approximate solution. Hence, substituting (2.54) to (2.56) with $w_\mathrm{i} = n_\mathrm{i}$ yields the following equation system:

$$\sum_{j=1}^{N} c_j \int_\Omega n_i A n_j \, d\Omega = \int_\Omega n_i f \, d\Omega - \int_\Omega n_i A u_D \, d\Omega. \tag{2.57}$$

This can be rewritten as a matrix system

$$[A]\{u\} = \{b\}, \tag{2.58}$$

where the stiffness matrix $[A]$ consists of the coefficients

$$A_{ij} = \int_{\Omega} n_i A_j n_j \, d\Omega \,. \tag{2.59}$$

In case of a symmetric differential operator A, the stiffness matrix $[A]$ is symmetric as well. The vector $\{u\}$ gathers the unknown quantities u_j whereas the right hand side vector $\{b\}$ is composed of the known quantities

$$b_i = \int_{\Omega} n_i f \, d\Omega - \int_{\Omega} n_i A u_D \, d\Omega \,. \tag{2.60}$$

When using the method of finite elements to realize Galerkin´s technique, the continuous domain is replaced by subdomains where the unknown function is substituted by a linear combination of simple shape- or basis-functions (interpolation functions) with unknown coefficients. Hence the problem involving an infinite number of degrees of freedom (DOF) is transformed into a problem with a finite number of DOF resulting in an approximation of the original BVP. The equation system is obtained by applying Galerkin techniques. The basic recipe for solving such a problem includes the following points:

- Domain/space discretization using finite elements
- Find suitable interpolation functions (also known as shape or basis functions)
- Develop the corresponding equations for a single element
- Build the global matrix system by assembling all elements
- Enforce boundary conditions
- Solve the system of equations
- Post-process

The initial step when applying Galerkin´s technique to the FEM implies an appropriate space discretization of the problem domain assembling the finite element mesh, as discussed in the following sub-section.

2.2.3 Domain discretization using finite elements

The most significant step of the finite element approach is how to subdivide the problem domain to allow the use of simple basis functions to approximate the solution. The so called finite elements resulting from discretizing the domain of interest have immediate impact on storage requirements, computational costs and on

the accuracy of the numerical solution. The resulting mesh or grid, compromises line segments (Fig. 2.7(a)) for a single dimensional (1-D) domain, triangular or quadrilateral elements (Fig. 2.7(b) and Fig. 2.7(c)) in case of two dimensions (2-D) and, in case of three dimensional (3-D) space, one can expediently use tetrahedra (Fig. 2.8(a)), triangular prisms (Fig. 2.8(b)) or bricks (Fig. 2.8(c)).

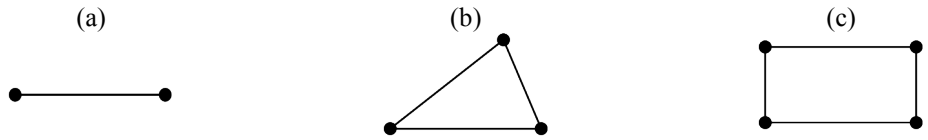

Fig. 2.7: Examples of 1-D and 2-D finite elements: (a) 1-D line element; (b) 2-D linear triangular element; (c) 2-D linear quadrilateral element.

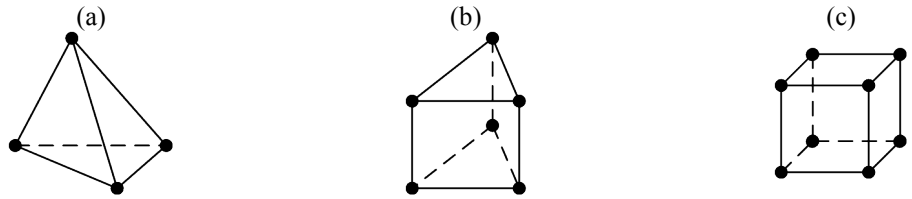

Fig. 2.8: Examples of 3-D finite elements: (a) linear tetrahedral element; (b) linear triangular prism element; (c) linear hexahedral element.

The samples of elements in Fig. 2.7 and Fig. 2.8 comprise several nodes and edges corresponding to the shape or basis functions. For the investigations in this thesis 2nd order hexahedral elements with edge and node based basis functions are used. A single element is defined by 20 nodes and 36 edges as shown in Fig. 2.9 [35, 43, 46, 48, 49, 50, 51, 136, 137].

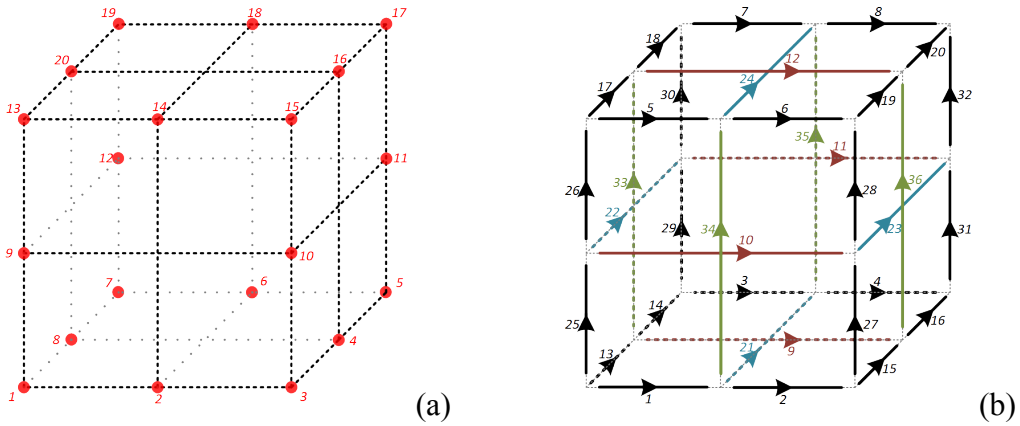

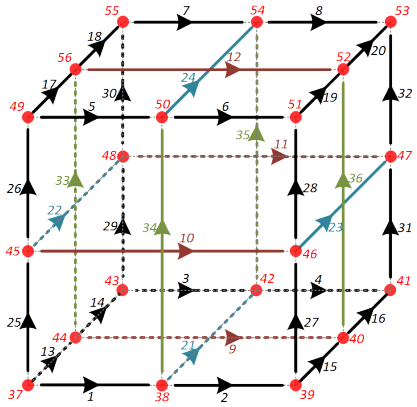

(c)

Fig. 2.9: Finite element applied to discretize the problem domains in this thesis. The quadratic hexahedral element comprises 20 nodes shown in (a) and 36 edges, as in (b). The numbering when merging nodes and edges together do define a single element is shown in (c).

In case of node based elements, the approximated unknown scalar functions are represented by their values in the nodes of the element. One can obtain an approximation using continuous and piecewise polynomial basis functions satisfying

$$n_j = \begin{cases} 1 & \text{at node } j, \\ 0 & \text{in all other nodes.} \end{cases} \tag{2.61}$$

The basis function can be expressed by transforming the geometry of an element into a local coordinate system. In other words, the local order number represents the position within the element, whereas the global order number indicates the position in the entire geometry. If the transformation between global coordinates (x_j,y_j,z_j) and local coordinates (ξ,η,ζ) is also expressed by the basis functions, the element is called isoparametric:

$$x = \sum_{j=1}^{N_n} x_j n_j(\xi,\eta,\zeta), \qquad y = \sum_{j=1}^{N_n} y_j n_j(\xi,\eta,\zeta), \qquad z = \sum_{j=1}^{N_n} z_j n_j(\xi,\eta,\zeta), \tag{2.62}$$

where N_n is the number of nodes in the element. The use of higher-order shape functions enables lower discretization errors when mapping curved boundaries.

As illustrated in Fig. 2.9, the elements used not only contain nodes but also involve edges forming a hybrid element. This is advantageous when approximating vector quantities. Indeed, nodal representations demand full continuity of the vector fields in both normal and tangential direction, bearing the risk of non-physical solutions. This can be prevented by using edge based elements for approximating the unknown vector functions. Hence the degrees of freedom are allocated to the edges

of the elements implying the continuity of the tangential component with the option of the normal component being discontinuous. The vector based basis or expansion function satisfies

$$\int_{edge_i} \mathbf{n}_j \cdot d\mathbf{l} = \begin{cases} 1 & \text{if } i = j, \\ 0 & \text{if } i \neq j. \end{cases} \tag{2.63}$$

Furthermore, the gradients of the node based basis functions should be representable as a linear combination of the edge based basis functions:

$$\nabla n_j = \sum_{k=1}^{N_e} c_{j,k} \mathbf{n}_k \quad \left(j = 1, 2, \ldots, N_n\right). \tag{2.64}$$

These expansion, basis or shape functions are commonly selected as polynomials of first order (linear), second order (quadratic) or even higher order. The latter ones are more accurate but may result in a more complex formulation than lower-order polynomials. Therefore, the linear interpolation is very popular and widely applied. The present solver uses second order elements as a compromise between precision and complexity.

Applying the basis functions as defined in (2.61), (2.63) and (2.64) yields sparse singular system matrices. Possible solving techniques for the linear equation systems obtained are direct or iterative procedures [138, 139]. Whereas direct methods are variants of Gaussian elimination and mostly applied to compact problems with a manageable number of degrees of freedom (DOF), the iterative methods as the conjugate gradient technique is universally applicable and preferably used for a large number of DOF. Since the availability of high-performance computers has developed considerably in recent years, also parallel direct solvers are increasingly being used for problem domains with a large number of DOF. Additionally, in case of iterative methods, suitable preconditioning techniques [140, 141, 142] can be applied to improve the convergence rate. Considering non-linear material characteristics the system of equations turns non-linear. Hence, non-linear matrix solving procedures have to be applied [29, 31, 63]. Such specific techniques are generally based on e.g. direct methods or the fixed-point iteration technique. The latter one will be briefly discussed in sub-section 2.3.3.

2.2.4 Finite element potential formulations

The potential formulations, discussed in sub-section 2.1.2 are used to describe the 3D electromagnetic field problems under investigation. The problems are solved with the aid of the finite element method utilizing the weak form of the Galerkin technique considering 2nd order hexahedral finite elements to discretize the problem domain, consisting of edge based vector basis functions $\mathbf{n}_j$ and node based scalar basis functions n_j as introduced in sub-section 2.2.2. Hence the potentials are approximated as

- Electric scalar potential

$$V(\mathbf{r},t) \approx V_h(\mathbf{r},t) = V_D + \sum_{j=1}^{N_n} V_j(t) n_j(\mathbf{r}) \tag{2.65}$$

- Modified electric scalar potential

$$\mathsf{V}(\mathbf{r},t) \approx \mathsf{V}_h(\mathbf{r},t) = \mathsf{V}_D + \sum_{j=1}^{N_n} \mathsf{V}_j(t) n_j(\mathbf{r}) \tag{2.66}$$

- Magnetic scalar potential

$$\phi(\mathbf{r},t) \approx \phi_h(\mathbf{r},t) = \phi_D + \sum_{j=1}^{N_n} \phi_j(t) n_j(\mathbf{r}) \tag{2.67}$$

- Magnetic vector potential

$$\mathbf{A}(\mathbf{r},t) \approx \mathbf{A}_h(\mathbf{r},t) = \mathbf{A}_D + \sum_{j=1}^{N_e} A_j(t) \mathbf{n}_j(\mathbf{r}) \tag{2.68}$$

- Reduced magnetic vector potential

$$\mathbf{A}_r(\mathbf{r},t) \approx \mathbf{A}_{rh}(\mathbf{r},t) = \mathbf{A}_{rD} + \sum_{j=1}^{N_e} A_{rj}(t) \mathbf{n}_j(\mathbf{r}) \tag{2.69}$$

- Unknown current vector potential

$$\mathbf{T}(\mathbf{r},t) \approx \mathbf{T}_h(\mathbf{r},t) = \mathbf{T}_D + \sum_{j=1}^{N_e} T_j(t) \mathbf{n}_j(\mathbf{r}) \tag{2.70}$$

- Impressed current vector potential

$$\mathbf{T}_0(\mathbf{r},t) \approx \mathbf{T}_{0h}(\mathbf{r},t) = \sum_{j=1}^{N_e} T_{0j}(t) \mathbf{n}_j(\mathbf{r}) \tag{2.71}$$

where in (2.65)-(2.71) **r** indicates the space coordinates and t represents time. In (2.71) the coefficients T_{0j} can be obtained by ensuring that

$$\oint_{\partial\Gamma_i} \mathbf{T}_0 \cdot d\mathbf{l} = \int_{\Gamma_i} \mathbf{J}_0 \cdot d\boldsymbol{\Gamma} \tag{2.72}$$

is satisfied for any closed path $\partial\Gamma_i$ in a set of loops in the graph with the cross-section Γ_i limited by the cycle of $\partial\Gamma_i$ as proposed in [143].

For the sake of simplicity, the notations of dependence on space and time will be omitted in the following.

2.2.4.1 Finite element approximation using the A,*V*-A-formulation

For the magnetic vector potential formulation presented in sub-section 2.1.2.1, the equations resulting when applying Galerkin techniques to (2.18) and (2.19) are [35, 144]:

$$\int_{\Omega_n \cup \Omega_c} \nabla \times \mathbf{n}_k \cdot \nu \nabla \times \mathbf{A}_h d\Omega + \frac{d}{dt} \int_{\Omega_c} \sigma \mathbf{n}_k \cdot \left(\mathbf{A}_h + \nabla v_h \right) d\Omega = \int_{\Omega_n \cup \Omega_c} \nabla \times \mathbf{n}_k \cdot \mathbf{T}_{0h} d\Omega, \tag{2.73}$$

with $k = 1,\ldots,N_e$ and

$$\frac{d}{dt} \int_{\Omega_c} \nabla n_k \cdot \sigma \left(\mathbf{A}_h + \nabla v_h \right) d\Omega = 0, \tag{2.74}$$

with $k = 1,\ldots,N_n$.

In case of voltage driven coils, the impressed current vector potential $\mathbf{T}_{0h}$ is substituted by the product of a unit current vector potential $\mathbf{t}_{0h}$ and the unknown current i as in (2.48). Hence the general equation taking account of both voltage and current excited coils can be written as

$$\int_{\Omega_n \cup \Omega_c} \nabla \times \mathbf{n}_k \cdot \nu \nabla \times \mathbf{A}_h - \nabla \times \mathbf{n}_k \cdot \left(\mathbf{t}_{0h} i + \mathbf{T}_{0h} \right) d\Omega + \frac{d}{dt} \int_{\Omega_c} \sigma \mathbf{n}_k \cdot \left(\mathbf{A}_h + \nabla v_h \right) d\Omega = 0, \tag{2.75}$$

with $k = 1,\ldots,N_e$, and the necessary additional equation (2.51) integrated over time to achieve symmetry is for approximate solution:

$$\int_t u dt = R \int_t i dt - \int_\Omega \mathbf{t}_{0h} \cdot \nabla \times \mathbf{A}_h d\Omega , \tag{2.76}$$

In this system of ordinary differential equations, the unknown coefficients A_j affiliated to the edge based basis functions and v_j corresponding to the node based basis functions as in (2.66) and (2.68) as well as the unknown current i are assembled in a vector $\mathbf{x}$ to facilitate writing (2.74)-(2.76) in a matrix form as

$$\mathbf{S}_\nu (\mathbf{x}) \mathbf{x} + \mathbf{M}_\sigma \frac{d\mathbf{x}}{dt} = \mathbf{f} . \tag{2.77}$$

Considering (2.64) and the fact that $\nabla \times \nabla n_j \equiv 0$, the obtained system of equations (2.77) is singular with a consistent right hand side. It is conspicuous that the so called stiffness matrix $\mathbf{S}_\nu$ depends on the reluctivity ν, dependent on $\mathbf{x}$ and t. The mass matrix $\mathbf{M}_\sigma$ depends on the conductivity σ and the right hand side vector $\mathbf{f}$ gathers the known values. The matrices can be partitioned as

$$\mathbf{S}_\nu = \begin{bmatrix} \mathbf{A}_\nu & \mathbf{0} & \mathbf{g} \\ \mathbf{0} & \mathbf{0} & \mathbf{0} \\ \mathbf{g}^T & \mathbf{0} & \mathbf{R}\int_t \end{bmatrix}, \quad \mathbf{A}_\nu = \left[\int_\Omega \nabla \times \mathbf{n}_k \cdot \nu \nabla \times \mathbf{n}_j d\Omega \right]_{k,j=1\ldots N_e}, \tag{2.78}$$

$$\mathbf{g} = \left[-\int_\Omega \nabla \times \mathbf{n}_k \cdot \mathbf{t}_{0h} d\Omega \right]_{N_e \times N_c}, \quad \mathbf{g}^T = \left[-\int_\Omega \mathbf{t}_{0h} \cdot \nabla \times \mathbf{n}_k d\Omega \right]_{N_c \times N_e}, \tag{2.79}$$

$$\mathbf{M}_\sigma = \begin{bmatrix} \mathbf{C}_\sigma & \mathbf{h} & \mathbf{0} \\ \mathbf{h}^T & \mathbf{V} & \mathbf{0} \\ \mathbf{0} & \mathbf{0} & \mathbf{0} \end{bmatrix}, \quad \mathbf{C}_\sigma = \left[\int_\Omega \mathbf{n}_k \cdot \sigma \mathbf{n}_j d\Omega \right]_{k,j=1\ldots N_e}, \tag{2.80}$$

$$\mathbf{h} = \left[\int_\Omega \mathbf{n}_k \cdot \sigma \nabla n_j d\Omega \right]_{k=1\ldots N_e, j=1\ldots N_n}, \quad \mathbf{h}^T = \left[\int_\Omega \nabla n_k \cdot \sigma \mathbf{n}_j d\Omega \right]_{k=1\ldots N_n, j=1\ldots N_e}, \tag{2.81}$$

$$\mathbf{V} = \left[\int_{\Omega} \nabla n_k \cdot \sigma \nabla n_j d\Omega \right]_{k,j=1\ldots N_n}, \tag{2.82}$$

$$\mathbf{x} = \begin{bmatrix} \boldsymbol{A} \\ \boldsymbol{v} \\ \mathbf{i} \end{bmatrix}, \quad \boldsymbol{A} = \left[A_1, \ldots, A_{N_e} \right]^T, \quad \boldsymbol{v} = \left[v_1, \ldots, v_{N_n} \right]^T, \quad \mathbf{i} = \left[i_1, \ldots, i_{N_c} \right]^T, \tag{2.83}$$

$$\mathbf{f} = \begin{bmatrix} \int_{\Omega} \nabla \times \mathbf{n}_k \cdot \mathbf{T}_{0h} - \nabla \times \mathbf{n}_k \cdot \nu \nabla \times \mathbf{A}_D d\Omega \\ -\int_{\Omega} \nabla n_k \cdot \sigma \left(\mathbf{A}_D + \nabla v_D \right) d\Omega \\ \int_t \mathbf{u} dt \end{bmatrix}_{N_e+N_n+N_c}. \tag{2.84}$$

Since the boundary conditions are homogeneous, the functions $\mathbf{A}_D$ and v_D vanish in (2.84).

In (2.78) **R** is a diagonal matrix built of the winding resistances. The unknown currents of each coil are gathered in the vector **i** as in (2.83) where N_c is the number of voltage excited coils, and in the same manner the prescribed voltages of the coils are written in the vector **u** as indicated in (2.84).

2.2.4.2 Finite element approximation using the $\mathbf{A}_r$,V-$\mathbf{A}_r$-formulation

As the reduced vector potential formulation has its origins in the total vector potential formulation with the unknown vector potential component reduced by a known source vector potential as introduced in sub-section 2.1.2.2, the finite element equations are similar to the previous one and hence not described in detail. Utilizing the Galerkin technique to realize a FE–approach and taking into consideration the boundary conditions as given in TABLE 2.3, (2.33) and (2.34) lead to [145, 146]

$$\begin{aligned} &\int_{\Omega_n \cup \Omega_c} \nabla \times \mathbf{n}_k \cdot \nu \nabla \times \mathbf{A}_{rh} d\Omega + \frac{d}{dt} \int_{\Omega_c} \mathbf{n}_k \cdot \sigma \left(\mathbf{A}_{rh} + \nabla v_h \right) d\Omega = \\ &\int_{\Omega_n \cup \Omega_c} \nabla \times \mathbf{n}_k \cdot \left(\mathbf{H}_s - \nu \mu_0 \mathbf{H}_s \right) d\Omega - \frac{d}{dt} \int_{\Omega_c} \nabla \times \mathbf{n}_k \cdot \sigma \mathbf{A}_s d\Omega, \end{aligned} \tag{2.85}$$

with $k = 1,\ldots,N_e$ and

$$\frac{d}{dt}\int_{\Omega_c} \nabla n_k \cdot \sigma\left(\mathbf{A}_{rh} + \nabla v_h\right) d\Omega = -\frac{d}{dt}\int_{\Omega_c} \nabla n_k \cdot \sigma \mathbf{A}_s d\Omega\,, \tag{2.86}$$

with $k = 1,\ldots,N_n$, where the impressed field intensity $\mathbf{H}_s$ on the right hand side in (2.85) is present in the ferromagnetic area only and vanishes inside the non-ferromagnetic domain. The left side of the equations (2.85) and (2.86) is equal to the left side of the equations obtained for the total vector potential. The right hand side is complemented by the impressed vector potential component $\mathbf{A}_s$ as well as $\mathbf{H}_s$. Hence the system of ordinary differential equations is analogous to (2.77).

2.2.4.3 Finite element approximation using the T,ϕ-ϕ-formulation

The current vector potential formulation [35] has been introduced in sub-section 2.1.2.3. The potentials in (2.43) and (2.44) are substituted by their approximations resulting in

$$\int_{\Omega_c} \nabla\times\mathbf{n}_k \cdot \rho\nabla\times\mathbf{T}_h d\Omega + \frac{d}{dt}\int_{\Omega_c} \mu\mathbf{n}_k \cdot\left(\mathbf{T}_h - \nabla\phi_h\right) d\Omega = -\frac{d}{dt}\int_{\Omega_c} \mu\mathbf{n}_k \cdot \mathbf{T}_{0h} d\Omega \tag{2.87}$$

with $k = 1,\ldots,N_e$ and

$$\frac{d}{dt}\int_{\Omega_n\cup\Omega_c} \mu\nabla n_k \cdot\left(\mathbf{T}_h - \nabla\phi_h\right) d\Omega = -\frac{d}{dt}\int_{\Omega_n\cup\Omega_c} \mu\nabla n_k \cdot \mathbf{T}_{0h} d\Omega \tag{2.88}$$

with $k = 1,\ldots,N_n$.

Additionally the voltage driven case is considered by (2.50) leading to

$$\int_{\Omega_c} \nabla\times\mathbf{n}_k \cdot \rho\nabla\times\mathbf{T}_h d\Omega + \frac{d}{dt}\int_{\Omega_c} \mathbf{n}_k \cdot \mu\left(\mathbf{T}_h + \mathbf{t}_{0h} i - \nabla\phi_h\right) d\Omega = -\frac{d}{dt}\int_{\Omega_c} \mathbf{n}_k \cdot \mu\mathbf{T}_{0h} d\Omega\,, \tag{2.89}$$

with $k = 1,\ldots,N_e$ and

$$-\frac{d}{dt}\int_{\Omega_n\cup\Omega_c}\nabla n_k\cdot\mu\left(\mathbf{T}_h+\mathbf{t}_{0h}i-\nabla\phi_h\right)d\Omega=\frac{d}{dt}\int_{\Omega_n\cup\Omega_c}\nabla n_k\cdot\mu\mathbf{T}_{0h}d\Omega\,, \tag{2.90}$$

with $k = 1,\ldots,N_n$. Equation (2.50) is formulated as

$$Ri+\frac{d}{dt}\int_{\Omega_n\cup\Omega_c}\mathbf{t}_{0h}\cdot\mu\left(\mathbf{T}_h+\mathbf{t}_{0h}i-\nabla\phi_h\right)d\Omega=u-\frac{d}{dt}\int_{\Omega_n\cup\Omega_c}\mathbf{t}_{0h}\cdot\mu\mathbf{T}_{0h}d\Omega\,. \tag{2.91}$$

Similarly to the **A**,V-**A**-formulation, (2.89)-(2.91) can be written in matrix form with the unknown vector **x** now constituted by the unknown coefficients T_j corresponding to edge based basis functions and ϕ_j affiliated with the node based basis functions, as well as the unknown currents i in presence of voltage excited coils as:

$$\mathbf{S}_\rho\mathbf{x}+\frac{d}{dt}\left(\mathbf{M}_\mu\left(\mathbf{x}\right)\mathbf{x}\right)=\mathbf{f}_\rho+\frac{d}{dt}\mathbf{f}_\mu\,. \tag{2.92}$$

The stiffness matrix $\mathbf{S}_\rho$ now depends on the resistivity ρ as indicated by the subscript. Hence $\mathbf{S}_\rho$ is independent of **x** and t. On the other hand the mass matrix $\mathbf{M}_\mu$ now depends on the magnetic permeability μ which varies with the magnetic field and time. With this formulation applied, the right hand side vector $\mathbf{f}_\mu$ contains the excitation functions but is also dependent of the permeability μ and the time derivative of the vector **x**. In the system of equations (2.92), the matrices and vectors are partitioned as

$$\mathbf{S}_\rho=\begin{bmatrix}\mathbf{A}_\rho & \mathbf{0} & \mathbf{0}\\ \mathbf{0} & \mathbf{0} & \mathbf{0}\\ \mathbf{0} & \mathbf{0} & \mathbf{R}\end{bmatrix},\quad \mathbf{A}_\rho=\left[\int_\Omega\nabla\times\mathbf{n}_k\cdot\rho\nabla\times\mathbf{n}_j d\Omega\right]_{k,j=1\ldots N_e}, \tag{2.93}$$

$$\mathbf{M}_\mu=\begin{bmatrix}\mathbf{C}_\mu & \mathbf{G}_\mu & \mathbf{g}_\mu\\ \mathbf{G}_\mu^T & \mathbf{L}_\mu & \mathbf{h}_\mu\\ \mathbf{g}_\mu^T & \mathbf{h}_\mu^T & \mathbf{V}_\mu\end{bmatrix},\quad \mathbf{C}_\mu=\left[\int_\Omega\mathbf{n}_k\cdot\mu\mathbf{n}_j d\Omega\right]_{k,j=1\ldots N_e}, \tag{2.94}$$

$$\mathbf{G}_\mu = \left[-\int_\Omega \mathbf{n}_k \cdot \mu \nabla n_j d\Omega \right]_{k=1\ldots N_e, j=1\ldots N_n}, \quad \mathbf{G}_\mu^T = \left[-\int_\Omega \nabla n_k \cdot \mu \mathbf{n}_j d\Omega \right]_{k=1\ldots N_n, j=1\ldots N_e}, \tag{2.95}$$

$$\mathbf{L}_\mu = \left[\int_\Omega \nabla n_k \cdot \mu \nabla n_j d\Omega \right]_{k,j=1\ldots N_n}, \tag{2.96}$$

$$\mathbf{g}_\mu = \left[\int_\Omega \mathbf{n}_k \cdot \mu \mathbf{t}_{0h} d\Omega \right]_{N_e \times N_c}, \quad \mathbf{g}_\mu^T = \left[\int_\Omega \mathbf{t}_{0h} \cdot \mu \mathbf{n}_j d\Omega \right]_{N_c \times N_e}, \tag{2.97}$$

$$\mathbf{h}_\mu = \left[-\int_\Omega \nabla n_k \cdot \mu \mathbf{t}_{0h} d\Omega \right]_{N_n \times N_c}, \quad \mathbf{h}_\mu^T = \left[-\int_\Omega \mathbf{t}_{0h} \cdot \mu \nabla n_j d\Omega \right]_{N_c \times N_n}, \tag{2.98}$$

$$\mathbf{V}_\mu = \left[\int_\Omega \mathbf{t}_{0h} \cdot \mu \mathbf{t}_{0h} d\Omega \right]_{N_c \times N_c}, \tag{2.99}$$

$$\mathbf{x} = \begin{bmatrix} \boldsymbol{T} \\ \boldsymbol{\phi} \\ \mathbf{i} \end{bmatrix}, \quad \boldsymbol{T} = \left[T_1, \ldots, T_{N_e} \right]^T, \quad \boldsymbol{\phi} = \left[\phi_1, \ldots, \phi_{N_n} \right]^T, \quad \mathbf{i} = \left[i_1, \ldots, i_{N_c} \right]^T, \tag{2.100}$$

$$\mathbf{f}_\rho = \begin{bmatrix} -\mathbf{A}_\rho \cdot \mathbf{T}_D \\ \mathbf{0} \\ \mathbf{u} \end{bmatrix}_{N_e+N_n+N_c}, \quad \mathbf{f}_\mu = \begin{bmatrix} -\left[\mathbf{C}_\mu \cdot \left(\mathbf{T}_{0h} + \mathbf{T}_D \right) \right] \\ -\left[\mathbf{G}_\mu^T \cdot \left(\mathbf{T}_{0h} + \mathbf{T}_D \right) + \mathbf{L}_\mu \phi_D \right] \\ -\left[\mathbf{g}_\mu^T \cdot \left(\mathbf{T}_{0h} + \mathbf{T}_D \right) + \mathbf{h}_\mu^T \phi_D \right] \end{bmatrix}_{N_e+N_n+N_c}. \tag{2.101}$$

In (2.101) it can be assumed that the functions $\mathbf{T}_D$ and ϕ_D vanish, as the Dirichlet boundary conditions are commonly homogenous.

R in (2.93) gathers the winding resistances as a diagonal matrix. Further the vector **i** in (2.100) comprises the unknown currents of the voltage driven coils and the vector **u** in (2.101) the given voltages.

2.3 Time-periodic steady-state solution

As the problems investigated in this thesis focus on steady-state solutions, it is assumed that the excitations whether voltage driven or excited by a given current are time-periodic with a time period $T = 1/f$ defined by the frequency f. Thus the right hand side vectors of the systems of ordinary differential equations, regardless of which potential formulation is used, are also time periodic i.e. $\mathbf{f}(t) = \mathbf{f}(t+T)$. To facilitate such investigations, harmonic decomposition methods as the harmonic balance method, as well as a time periodic approach are utilized to bypass a time-consuming transient solving approach.

2.3.1 Harmonic balance method

The fundamental idea of this method is a transformation from the time domain into the frequency domain [81, 82, 147].

Under the assumption that if the Fourier coefficients of two functions are equal, then, under appropriate conditions, these two functions are equal. Let us assume that the time average over a period is zero, then the solution approximated by a complex Fourier series with N harmonics results in

$$\mathbf{x}(t) \approx \mathbf{x}_N(t) = \mathrm{Re}\left(\sum_{m=1}^{N} \mathbf{X}_m e^{jm\omega t} \right), \tag{2.102}$$

where j represents the imaginary unit, $\omega = 2\pi f$ denotes the angular frequency of the excitation and $\mathbf{X}_\mathrm{m}$ is the complex Fourier coefficient of the m-th harmonic at the angular frequency $m\omega$ and can be obtained as

$$\mathbf{X}_m = \mathfrak{F}_m(\mathbf{x}) = \frac{1}{T}\int_0^T \mathbf{x}(t) e^{-jm\omega t}\, dt \tag{2.103}$$

where $\mathfrak{F}_\mathrm{m}$ denotes the m-th harmonic of the Fourier transform. This is executed by using a fast Fourier transformation [148]. Substituting (2.77) and (2.92) by this estimation and calculating the N Fourier coefficients, a system of equations with N times as many unknowns is acquired as there are degrees of freedom in $\mathbf{x}(t)$. Thus (2.77) yields

$$\mathcal{F}_m\left\{\mathbf{S}_\nu\left(\mathbf{x}_N\right)\mathbf{x}_N\right\}+jm\omega\mathbf{M}_\sigma\cdot\mathbf{X}_m=\mathcal{F}_m\left(\mathbf{f}\right),\qquad m=1,2,\ldots,N,\qquad(2.104)$$

as well as for (2.92)

$$\mathbf{S}_\rho\mathbf{X}_m+\mathcal{F}_m\left\{\frac{d}{dt}\left(\mathbf{M}_\mu\left(\mathbf{x}_N\right)\mathbf{x}_N\right)\right\}=\mathcal{F}_m\left(\mathbf{f}_\rho+\frac{d}{dt}\mathbf{f}_\mu\right),\qquad m=1,2,\ldots,N\,.\qquad(2.105)$$

As one can observe in (2.104) and (2.105) the nonlinear terms comprising the permeability or the reluctivity couple all Fourier coefficients to each other. Due to this coupling, a single harmonic solution cannot be achieved, a fact leading to a significant increase of the complexity of the problem. Thus the fixed-point technique is applied to achieve decoupled linear equation systems for each harmonic as described in 2.3.3.3.

2.3.2 Time periodic approach

Alternatively to the harmonic balance technique, a solution can also be obtained by a time domain approach. This can be realized by discretizing the time domain utilizing equidistant time steps within one time-period $\Delta t=T/N$. Hence the periodic time-function $\mathbf{x}(t)$ can be expressed as sequence $\mathbf{x}_k=\mathbf{x}\left(k\Delta t\right),\ k=1,2,\ldots,N$ with N equidistant time-steps Δt. Due to the underlying periodicity of $\mathbf{x}$, this sequence is cyclic $\mathbf{x}_0=\mathbf{x}_N$. Different discretization schemes for the time derivative can be employed as e.g. the finite difference scheme applied in [149, 150] or the implicit Euler scheme [79, 147], which will be focused on here. This discrete harmonic balance method [147] will later be termed as TPFP (time periodic fixed-pint) technique in combination with the fixed-point algorithm. The discretized systems of equations (2.77) and (2.92) obtained by the FEM approximations can then be written as:

$$\mathbf{S}_{\nu,m}\mathbf{x}_m+\mathbf{M}_\sigma\frac{\mathbf{x}_m-\mathbf{x}_{m-1}}{\Delta t}=\mathbf{f}_m,\qquad m=1,2,\ldots,N,\qquad(2.106)$$

and

$$\mathbf{S}_\rho \mathbf{x}_m + \frac{1}{\Delta t}\left(\mathbf{M}_{\mu,m}\mathbf{x}_m - \mathbf{M}_{\mu,m-1}\mathbf{x}_{m-1}\right) = \mathbf{f}_{\rho,m} + \frac{1}{\Delta t}\left(\mathbf{f}_{\mu,m} - \mathbf{f}_{\mu,m-1}\right),\ m = 1,2,\ldots,N \quad (2.107)$$

where in (2.107), the right hand side has to be considered for discretization as it depends on **x** and *t*, containing the time-derivatives, see (2.101). Proceeding with the huge block-structured equation systems (2.106) and (2.107) obtained, the following notations for the hyper-vectors shall be introduced:

$$\begin{aligned}
&\mathbf{x}[1] = \left[\mathbf{x}_1, \mathbf{x}_2, \cdots, \mathbf{x}_N\right]^T, \quad \mathbf{x}[0] = \left[\mathbf{x}_0, \mathbf{x}_1, \cdots, \mathbf{x}_{N-1}\right]^T, \\
&\mathbf{f}_\mu[1] = \left[\mathbf{f}_{\mu,1}, \mathbf{f}_{\mu,2}, \cdots, \mathbf{f}_{\mu,N}\right]^T, \\
&\mathbf{f}_\mu[0] = \left[\mathbf{f}_{\mu,0}, \mathbf{f}_{\mu,1}, \cdots, \mathbf{f}_{\mu,N-1}\right]^T, \\
&\mathbf{f}_\rho[1] = \left[\mathbf{f}_{\rho,1}, \mathbf{f}_{\rho,2}, \cdots, \mathbf{f}_{\rho,N}\right]^T,
\end{aligned} \quad (2.108)$$

as well as for the block-diagonal matrices

$$\begin{aligned}
&\left\langle \mathbf{S}_\nu[1] \right\rangle = \begin{bmatrix} \mathbf{S}_{\nu,1} & 0 & \cdots & 0 \\ 0 & \mathbf{S}_{\nu,2} & \cdots & 0 \\ \vdots & \vdots & \ddots & \vdots \\ 0 & 0 & \cdots & \mathbf{S}_{\nu,N} \end{bmatrix}, \quad \left\langle \mathbf{S}_\nu[0] \right\rangle = \begin{bmatrix} \mathbf{S}_{\nu,0} & 0 & \cdots & 0 \\ 0 & \mathbf{S}_{\nu,1} & \cdots & 0 \\ \vdots & \vdots & \ddots & \vdots \\ 0 & 0 & \cdots & \mathbf{S}_{\nu,N-1} \end{bmatrix}, \\
&\left\langle \mathbf{S}_\rho \right\rangle = \begin{bmatrix} \mathbf{S}_\rho & 0 & \cdots & 0 \\ 0 & \mathbf{S}_\rho & \cdots & 0 \\ \vdots & \vdots & \ddots & \vdots \\ 0 & 0 & \cdots & \mathbf{S}_\rho \end{bmatrix}, \quad \left\langle \mathbf{M}_\mu[1] \right\rangle = \begin{bmatrix} \mathbf{M}_{\mu,1} & 0 & \cdots & 0 \\ 0 & \mathbf{M}_{\mu,2} & \cdots & 0 \\ \vdots & \vdots & \ddots & \vdots \\ 0 & 0 & \cdots & \mathbf{M}_{\mu,N} \end{bmatrix}, \\
&\left\langle \mathbf{M}_\sigma \right\rangle = \begin{bmatrix} \mathbf{M}_\sigma & 0 & \cdots & 0 \\ 0 & \mathbf{M}_\sigma & \cdots & 0 \\ \vdots & \vdots & \ddots & \vdots \\ 0 & 0 & \cdots & \mathbf{M}_\sigma \end{bmatrix}, \left\langle \mathbf{M}_\mu[0] \right\rangle = \begin{bmatrix} \mathbf{M}_{\mu,0} & 0 & \cdots & 0 \\ 0 & \mathbf{M}_{\mu,1} & \cdots & 0 \\ \vdots & \vdots & \ddots & \vdots \\ 0 & 0 & \cdots & \mathbf{M}_{\mu,N-1} \end{bmatrix}.
\end{aligned} \quad (2.109)$$

With these notations, (2.106) and (2.107) can be written as

$$\left\langle \mathbf{S}_\nu[1] + \frac{1}{\Delta t}\mathbf{M}_\sigma \right\rangle \mathbf{x}[1] - \frac{1}{\Delta t}\left\langle \mathbf{M}_\sigma \right\rangle \mathbf{x}[0] = \mathbf{f}[1], \quad (2.110)$$

$$\left\langle \mathbf{S}_\rho + \frac{1}{\Delta t}\mathbf{M}_\mu[1] \right\rangle \mathbf{x}[1] - \frac{1}{\Delta t}\left\langle \mathbf{M}_\mu[0] \right\rangle \mathbf{x}[0] = \mathbf{f}_\rho[1] + \frac{1}{\Delta t}\left(\mathbf{f}_\mu[1] - \mathbf{f}_\mu[0]\right), \quad (2.111)$$

with [1] and [0] indicating the variation in time with respect to the matrices depending on the permeability or the reluctivity according to the definitions in (2.108).

To obtain a similar system of equations as in the harmonic balance approach, one can take advantage of the discrete Fourier transformation [148] applied to **x**[1]:

$$\hat{\mathbf{x}} = \mathcal{D}\left(\mathbf{x}[1]\right) = \left[\hat{\mathbf{x}}_1, \hat{\mathbf{x}}_2, \cdots, \hat{\mathbf{x}}_N\right]^T, \quad \hat{\mathbf{x}}_m = \mathcal{D}_m\left(\mathbf{x}[1]\right) = \sum_{k=1}^{N} \mathbf{x}_k e^{-j2\pi m\frac{k}{N}}, \quad m = 1, 2, \ldots, N, \quad (2.112)$$

and utilizing the shift theorem [148] for obtaining the discrete Fourier transform of **x**[0] as

$$\mathcal{D}\left(\mathbf{x}[0]\right) = \mathbf{P}\hat{\mathbf{x}}, \qquad \mathbf{P} = \begin{bmatrix} \mathbf{I}e^{-j2\pi\frac{1}{N}} & 0 & \cdots & 0 \\ 0 & \mathbf{I}e^{-j2\pi\frac{2}{N}} & \cdots & 0 \\ \vdots & \vdots & \ddots & \vdots \\ 0 & 0 & \cdots & \mathbf{I}e^{-j2\pi\frac{N}{N}} \end{bmatrix}, \quad (2.113)$$

with **I** representing the unit matrix. Hence the discrete Fourier transform of (2.110) and (2.111) yields a system of equations with N times as many unknowns as there are degrees of freedom in $\mathbf{x}_k$:

$$\mathcal{D}\left\{\left\langle \mathbf{S}_\nu[1] + \frac{1}{\Delta t}\mathbf{M}_\sigma \right\rangle \mathbf{x}[1]\right\} - \frac{1}{\Delta t}\left\langle \mathbf{M}_\sigma \right\rangle \mathbf{P}\hat{\mathbf{x}} = \mathcal{D}\left\{\mathbf{f}[1]\right\}, \quad (2.114)$$

$$\left\langle \mathbf{S}_\rho \right\rangle \hat{\mathbf{x}} + \frac{1}{\Delta t}\mathcal{D}\left\{\left\langle \mathbf{M}_\mu[1] \right\rangle \mathbf{x}[1] - \left\langle \mathbf{M}_\mu[0] \right\rangle \mathbf{x}[0]\right\} = \hat{\mathbf{f}}_\rho + \frac{1}{\Delta t}\mathcal{D}\left\{\mathbf{f}_\mu[1] - \mathbf{f}_\mu[0]\right\} \quad (2.115)$$

where the time-shift corresponds to a multiplication by the block diagonal matrix **P** in (2.114). Whereas in the linear case the elements of $\hat{\mathbf{x}}$, the discrete harmonics, are decoupled and the right hand side of (2.114) can be obtained directly from **f**[1], taking into account the nonlinear terms due to the dependence on μ or v of the unknown solution, all the discrete harmonics are coupled to each other. As, for computational reasons, decoupling the harmonics is highly desirable, the fixed-point technique is utilized to linearize the system of equations as introduced in the following sub-section.

2.3.3 Fixed-point technique

2.3.3.1 Introduction

A nonlinear solution strategy based on the linearization of the nonlinear equation systems is the so called fixed-point technique. This procedure is implemented in the solver and will be focused on in the upcoming explanations. In the literature, this method is sometimes called polarization method, successive substitution method [63] or the chord method [151]. The basic idea is finding the root of a nonlinear function by constructing an affine approximation corresponding to fixed points of some iteration function. Hence, for a mapping, e.g. $g:\mathbb{R}^n \mapsto \mathbb{R}^n$ every solution of the equation

$$x = g(x), \tag{2.116}$$

is a fixed point of the iteration function *g*. Several theorems guarantee the existence of fixed points. It can be postulated that any equation

$$f(x) = 0 \tag{2.117}$$

where *f* is a real function or an operator in the projected space can be rewritten as a fixed-point equation with α indicating a constant value for a possible improvement of the convergence behavior:

$$\alpha x = \alpha x + f(x). \tag{2.118}$$

In order to prove the existence of solutions of these equations, fixed-point theorems are a significant tool. The most important theorems are

- Banach fixed-point theorem, providing a generalization of the successive approximation technique on the use of contractive operators.
- Schauder fixed-point theorem, as a generalization of selection principles and compactness methods by the use of compact operators.
- Bourbaki-Kneser fixed-point theorem, applying set theoretic ordering principles.

These fundamental theorems are well formulated in literature [152, 153] and a detailed discussion would be beyond the scope of this thesis.

2.3.3.2 Basic approach

Based on the above theorems, a basic approach with dependence on a single variable can be established by recasting the initial equation (2.117) in the form of (2.116) with some iteration function g. Hence a solution x^* of this equation is a fixed point of g. With an initial guess x_0 a new approximation of x^* is computed by setting the iteration as

$$x_{n+1} = g\left(x_n\right). \tag{2.119}$$

The function g with the root x^* can then be replaced at some approximation x_n of x^* by a function

$$g\left(x\right) = x + \alpha^{-1} f\left(x\right), \tag{2.120}$$

with a suitable slope $\alpha \neq 0$. Furthermore, taking the obtained root $x_{\mathrm{n+1}}$ of g a new approximation to x^* and repeating this procedure with a fixed α, the iteration yields:

$$x_{n+1} = x_n - \alpha^{-1} f\left(x_n\right), \quad n = 0,1,\ldots. \tag{2.121}$$

Proceeding in this manner, the iterations will converge to the fixed point $x^* = g(x^*)$, if the mapping corresponding to the function $g(x)$ is a contraction, i.e. there exists a constant $k < 1$ so that for any x and y the inequality

$$\|g(x) - g(y)\| \le k\|x - y\|, \tag{2.122}$$

holds.

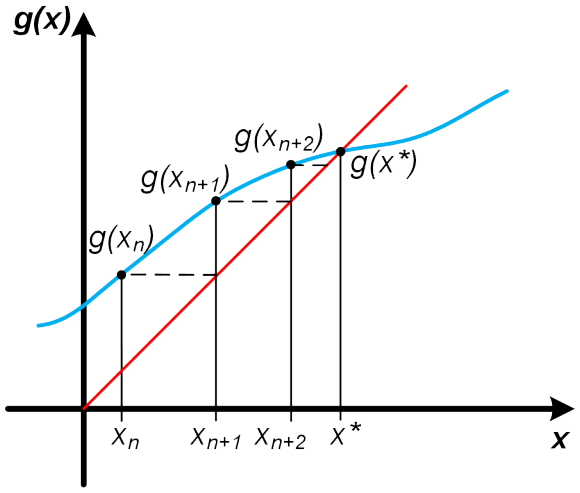

Fig. 2.10: Basic iteration scheme of of the function $g(x)$ using the fixed-point iteration procedure with an initial value x_n.

The solutions obtained for the root x^* of the nonlinear equation (2.116) are the intersections at x^* of the function $g(x)$ with the function x as illustrated in Fig. 2.10.

Replacing the values in (2.121) with vectors and vector functions, with the additional exchange of α with a suitable linear operator **A**, the method can easily be extended to an N-dimensional system as

$$\mathbf{x}_{n+1} = \mathbf{x}_n - \mathbf{A}^{-1}\mathbf{f}(\mathbf{x}_n), \quad n = 0,1,\ldots, \tag{2.123}$$

and hence the affine approximation at some iteration x_n is assumed to be

$$\mathbf{G}(\mathbf{x}) = \mathbf{x} + \mathbf{A}^{-1}\mathbf{f}(\mathbf{x}). \tag{2.124}$$

Convergence will be ensured for any initial value if **G** is a contraction fulfilling

$$\left\|\mathbf{G}(\mathbf{x})-\mathbf{G}(\mathbf{y})\right\| \le k\left\|\mathbf{x}-\mathbf{y}\right\|, \tag{2.125}$$

defined as in [63]: Let $S \subset \mathbb{R}$. A function $g : S \mapsto \mathbb{R}$ satisfies a Lipschitz condition on *S* if there exists a constant $k > 0$ such that, for any two points $x, y \in S$,

$$\left\|g(x)-g(y)\right\| \le k\left\|x-y\right\|. \tag{2.126}$$

The greatest lower bound for such constants is the Lipschitz constant for *g* on *S*. If *g* has Lipschitz constant $k < 1$ on *S*, then *g* is a contraction on *S*.

The advantages of the fixed-point technique are

- Convergence is guaranteed for contractive problems.
- The nonlinear function can be given as a piece-wise linear monotonous function.
- It will converge for any initial value.
- The system matrix is not needed to be updated in each iteration step.

A drawback can be found in the linear rate of convergence, reflecting a slow convergence behavior. Hence, additional measures to improve the convergence can be taken as e.g. preliminarily finding an optimal initial value for the fixed-point iteration procedure, applying an over-relaxation procedure as well as updating the linear operator **A** in each iteration-step. Employing the latter measure, (2.123) can be rewritten as

$$\mathbf{A}_n \cdot \mathbf{x}_{n+1} = \mathbf{A}_n \cdot \mathbf{x}_n + \mathbf{f}(\mathbf{x}_n) \tag{2.127}$$

where the subscript of **A** indicates its change in each iteration step.

Considering nonlinear eddy-current problems treated in this thesis, the nonlinearity is generated by the materials occurring in electro-magnetic applications [154, 155]. Hence, there exists a nonlinear correlation between the magnetic flux

density **B** and the magnetic field intensity **H** described by the so called *B-H* curve which is defined by the magnetic permeability μ or its inverse the magnetic reluctivity ν. Depending on the potential formulation used, the material dependencies can be written as

$$\mathbf{B} = \mu\left(\left|\mathbf{H}\right|\right)\mathbf{H} \quad \text{or} \quad \mathbf{H} = \nu\left(\left|\mathbf{B}\right|\right)\mathbf{B}\,. \tag{2.128}$$

It is straightforward to apply the linearization technique by defining a linear operator with respect to the magnetic permeability μ or the magnetic reluctivity ν to be set independent of the magnetic field. It should be mentioned that the fixed point values μ_{FP} or ν_{FP} are not necessarily independent of the space coordinates as the distributions may vary in the problem domain but are independent of the field and hence time. By the same manner as used for the linear operator **A** in (2.127), the fixed point permeability or reluctivity are updated in each iteration step. In the course of this procedure, the functions will be denoted as $\mu_{FP}^{(s)}$ or $\nu_{FP}^{(s)}$, where the superscript s indicates the iteration step. In order to accelerate the convergence of the fixed-point algorithm, an analysis of the optimal selection of $\mu_{FP}^{(s)}$ or $\nu_{FP}^{(s)}$ has been carried out in [149, 150, 156] and the result has been implemented in the 3D FEM solver used to investigate nonlinear eddy-current problems. The result of this work for finding an optimal choice is

$$\mu_{FP}^{(s)opt} = \max\left\{\begin{array}{l} \dfrac{\int_0^T \left(\mu^{(s)}\right)^2 dt}{\int_0^T \mu^{(s)} dt}, \\[2ex] \dfrac{\min\limits_{t\in[0,T]}\left(\mu^{(s)}\right) + \max\limits_{t\in[0,T]}\left(\mu^{(s)}\right)}{2}, \\[2ex] \max\limits_{t\in[0,T]}\left(\mu^{(s)}\left(1 - \dfrac{dH\left(B^{(s)}\right)}{dB}\mu^{(s)}\right)\right) \end{array}\right\}, \tag{2.129}$$

or

$$\nu_{FP}^{(s)opt} = \max\left\{\begin{array}{l} \dfrac{\int_0^T \left(\nu^{(s)}\right)^2 dt}{\int_0^T \nu^{(s)} dt}, \\ \dfrac{\min\limits_{t\in[0,T]}\left(\nu^{(s)}\right) + \max\limits_{t\in[0,T]}\left(\nu^{(s)}\right)}{2}, \\ \max\limits_{t\in[0,T]}\left(\nu^{(s)}\left(1 - \dfrac{dB\left(H^{(s)}\right)}{dH}\nu^{(s)}\right)\right) \end{array}\right\}, \tag{2.130}$$

where T is the time-period.

To illustrate the nonlinear iteration process of the fixed-point method with respect to the nonlinear behavior of the magnetic reluctivity ν, a simple example is given in Fig. 2.11 below.

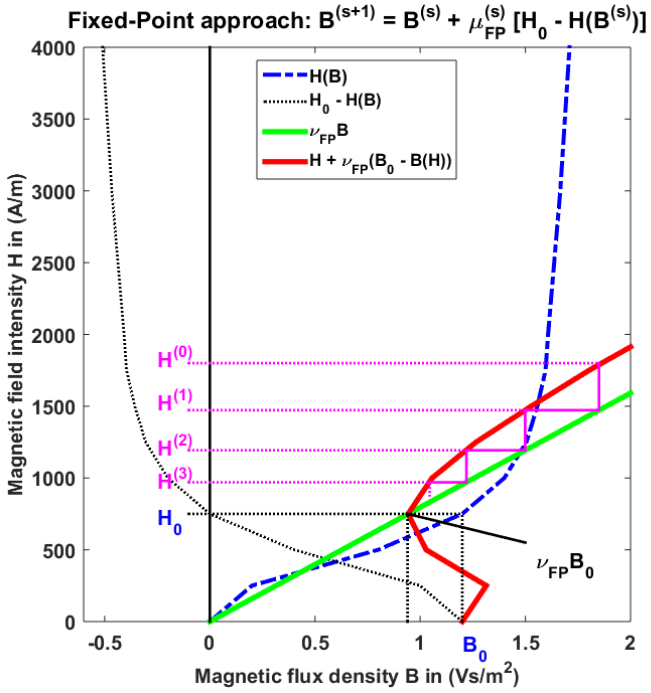

Fig. 2.11: Simplified iteration sequence of the fixed-point approach.

In this figure the value of the magnetic flux density B is iteratively determined. Assuming that H_0 is given, the solution for B_0 of $H\left(B_0\right)=H_0$ is sought. Convergence is achieved, once $H^{(s)}+\nu_{FP}^{(s)}\left[B_0-B\left(H^{(s)}\right)\right]=\nu_{FP}H_0$ is satisfied. Therefore, in each iteration step s, the magnetic flux density is updated as

$$B^{(s+1)}=B^{(s)}+\frac{H_0-H\left(B^{(s)}\right)}{\nu_{FP}^{(s)}}. \tag{2.131}$$

Applying the fixed-point technique, the obtained equation systems of the harmonic balance method as well as for the time periodic approach are linearized as described in the following sub-sections.

2.3.3.3 Harmonic balance fixed-point technique (HBFP)

For a fast solution of (2.104) and (2.105), it is preferable to decouple the harmonics, yielding N systems of equations, each containing as many unknowns as

there are degrees of freedom in the FEM approximation. This can be achieved by utilizing the fixed-point technique. The linearized ordinary differential equation systems obtained are then solved for the nonlinear iterations $s = 0,1,2,...$ as

$$\left[\mathbf{S}^{(s)}_{(\nu_{FP})} + jm\omega\mathbf{M}_{\sigma}\right]\mathbf{X}^{(s+1)}_{m} = \mathfrak{F}_{m}\left[\mathbf{S}^{(s)}_{(\nu_{FP}-\nu)}\mathbf{x}^{(s)} + \mathbf{f}\right], \qquad m = 1,2,...,N, \tag{2.132}$$

$$\left[\mathbf{S}_{\rho} + jm\omega\mathbf{M}^{(s)}_{(\mu_{FP})}\right]\mathbf{X}^{(s+1)}_{m} = jm\omega\mathfrak{F}_{m}\left[\mathbf{M}^{(s)}_{(\mu_{FP}-\mu)}\mathbf{x}^{(s)}\right] + \mathfrak{F}_{m}\left[\mathbf{f}_{\rho}\right] + jm\omega\mathfrak{F}_{m}\left[\mathbf{f}^{(s)}_{\mu}\right] \qquad m = 1,2,...,N, \tag{2.133}$$

where $\mathbf{x}^{(s)}$ is obtained as

$$\mathbf{x}^{(s)} = \mathrm{Re}\left(\sum_{k=1}^{N}\mathbf{X}^{(s)}_{k}e^{jk\omega t}\right). \tag{2.134}$$

The nonlinear iterations for solving the linear systems (2.132) and (2.133) are terminated once the alteration of $\mu^{(s)}$ or $\nu^{(s)}$ between two iteration steps will be less than an appropriate tolerance.

2.3.3.4 Time periodic fixed-point technique (TPFP)

The application of the fixed point technique is justified by the fact that some simplifications are valid if the permeability or the reluctivity are assumed to be linear. Indeed, in this case, the discrete Fourier transforms in (2.114) and (2.115) simplify to

$$\begin{aligned}
&\mathcal{D}\left\{\left\langle\mathbf{S}_{\nu}[1] + \frac{1}{\Delta t}\mathbf{M}_{\sigma}\right\rangle\mathbf{x}[1]\right\} = \left\langle\mathbf{S}_{\nu}[1] + \frac{1}{\Delta t}\mathbf{M}_{\sigma}\right\rangle\hat{\mathbf{x}},\\
&\mathcal{D}\left\{\left\langle\mathbf{M}_{\mu}\right\rangle\mathbf{x}[1] - \left\langle\mathbf{M}_{\mu}\right\rangle\mathbf{x}[0]\right\} = \left\langle\mathbf{M}_{\mu}\right\rangle(\mathbf{I}-\mathbf{P})\hat{\mathbf{x}},\\
&\mathcal{D}\left\{\mathbf{f}_{\mu}[1] - \mathbf{f}_{\mu}[0]\right\} = (\mathbf{I}-\mathbf{P})\mathcal{D}\left\{\mathbf{f}_{\mu}[1]\right\},
\end{aligned} \tag{2.135}$$

resulting in the harmonics being decoupled:

$$\left(\left\langle \mathbf{S}_{\nu}\right\rangle+\frac{1}{\Delta t}\left\langle \mathbf{M}_{\sigma}\right\rangle\left(\mathbf{I}-\mathbf{P}\right)\right)\hat{\mathbf{x}}=\mathcal{D}\left\{\mathbf{f}\left[1\right]\right\}, \tag{2.136}$$

$$\left(\left\langle \mathbf{S}_{\rho}\right\rangle+\frac{1}{\Delta t}\left\langle \mathbf{M}_{\mu}\right\rangle\left(\mathbf{I}-\mathbf{P}\right)\right)\hat{\mathbf{x}}=\hat{\mathbf{f}}_{\rho}+\left(\mathbf{I}-\mathbf{P}\right)\mathcal{D}\left\{\mathbf{f}_{\mu}\left[1\right]\right\}, \tag{2.137}$$

and can be rewritten as

$$\left[\mathbf{S}_{\nu}+\frac{1}{\Delta t}\mathbf{M}_{\sigma}\left(1-e^{-j2\pi\frac{m}{N}}\right)\right]\hat{\mathbf{x}}_{m}=\mathcal{D}_{m}\left\{\mathbf{f}\left[1\right]\right\},\qquad m=1,2,\ldots,N, \tag{2.138}$$

$$\left[\mathbf{S}_{\rho}+\frac{1}{\Delta t}\mathbf{M}_{\mu}\left(1-e^{-j2\pi\frac{m}{N}}\right)\right]\hat{\mathbf{x}}_{m}=\hat{\mathbf{f}}_{\rho,m}+\left(1-e^{-j2\pi\frac{m}{N}}\right)\mathcal{D}_{m}\left\{\mathbf{f}_{\mu}\left[1\right]\right\},\quad m=1,2,\ldots,N. \tag{2.139}$$

A great advantage here is that only $N/2$ linear systems have to be solved. Indeed, since the matrix $\mathbf{M}$ and the vector $\mathbf{f}_{\mu}$ are real, the m-th and the (m+ $N/2$)-th equations are complex conjugate to each other assuming that N is even. The right hand side vectors can directly be computed by discrete Fourier transformation and, having solved (2.138) or (2.139), the time values can be found by inverse discrete Fourier transformation:

$$\mathcal{D}^{-1}\left(\hat{\mathbf{x}}\right)=\mathbf{x}\left[1\right]=\left[\mathbf{x}_{1},\mathbf{x}_{2},\cdots,\mathbf{x}_{N}\right]^{T},\qquad \mathbf{x}_{m}=\frac{1}{N}\sum_{k=1}^{N}\hat{\mathbf{x}}_{k}e^{j2\pi m\frac{k}{N}}. \tag{2.140}$$

In the nonlinear case, this simplifies the use of the fixed-point algorithm necessary for linearizing the system of equations by making the permeability or the reluctivity constant. Thus, systems similar to (2.138) and (2.139) have to be solved with the TPFP-technique. For the **A**,V-**A**-formulation, in each nonlinear iteration $s=0,1,2,\ldots$ we have

$$\left[\mathbf{S}_{\nu_{FP}}^{(s)}+\frac{1}{\Delta t}\mathbf{M}_{\sigma}\left(1-e^{-j2\pi\frac{m}{N}}\right)\right]\hat{\mathbf{x}}_{m}^{(s+1)}=\mathcal{D}_{m}\left\{\left\langle \mathbf{S}_{\nu_{FP}-\nu}^{(s)}\left[1\right]\right\rangle\mathbf{x}^{(s)}\left[1\right]+\mathbf{f}\left[1\right]\right\},\qquad m=1,2,\ldots,N \tag{2.141}$$

and for the **T**,ϕ-ϕ-formulation, one obtains

$$\left[\mathbf{S}(\rho)+\frac{1}{\Delta t}\mathbf{M}^{(s)}_{\mu_{FP}}\left(1-e^{-j2\pi\frac{m}{N}}\right)\right]\hat{\mathbf{x}}^{(s+1)}_{m}=\hat{\mathbf{f}}_{\rho,m}+\frac{1}{\Delta t}\mathcal{D}_m\left[\left\langle\mathbf{M}^{(s)}_{\mu_{FP}-\mu}[1]\right\rangle\mathbf{x}^{(s)}[1]\right]$$
$$+\frac{1}{\Delta t}\mathcal{D}_m\left[\mathbf{f}^{(s)}_{\mu}[1]-\left\langle\mathbf{M}^{(s)}_{\mu_{FP}-\mu}[0]\right\rangle\mathbf{x}^{(s)}[0]-\mathbf{f}^{(s)}_{\mu}[0]\right], \qquad (2.142)$$
$$m=1,2,\ldots,N,$$

with $\mathbf{x}^{(s)}[1]$ computed from the discrete harmonics by inverse discrete Fourier transformation:

$$\mathbf{x}^{(s)}[1]=\left[\mathbf{x}^{(s)}_1,\mathbf{x}^{(s)}_2,\cdots,\mathbf{x}^{(s)}_N\right]^T,\qquad \mathbf{x}^{(s)}_m=\frac{1}{N}\sum_{k=1}^{N}\hat{\mathbf{x}}^{(s)}_k e^{j2\pi m\frac{k}{N}}, \qquad (2.143)$$

and a time shift back leads to $\mathbf{x}^{(s)}[0]$ as defined in (2.108).

In the same manner as for the HBFP-technique, the nonlinear iteration procedure is terminated, if the deviation of the permeability or the reluctivity between two iteration steps becomes less than a sufficient threshold to provide a suitably accurate result.

The most computational cost is necessary to solve the N linear equation systems in case of to the HBFP and $N/2$ ones when using the TPFP. Indeed, these are solved in parallel in such a way, that a single harmonic computation of $\mathbf{X}^{(s+1)}_m$ or $\hat{\mathbf{x}}^{(s+1)}_m$ is distributed to any accessible core of the CPU. With these computations being finished, the right hand side is updated for the next iteration by first determining the time function of the solution as in (2.134) or (2.143) followed by addressing the Fourier decompositions as indicated in (2.132) and (2.133) or (2.141) and (2.142).

2.3.4 Solution techniques for linear equation systems

In this sub-section, a brief introduction is given for treating linear systems of algebraic equations as derived in the previous sub-sections.

We present an overview of possibilities to solve linear equation systems, as described in pertinent literature such as e.g. [29, 31, 138, 139, 157, 158, 159], and

point out which strategy is embedded in the software used for the problem investigations in this thesis.

In general, the solution techniques can be categorized as direct or iterative methods. Usually, electromagnetic 3D-FEM problems result in a large set of algebraic equations. Depending on the underlying formulation used, the system matrices obtained can also be sparse, dense, symmetric or non-symmetric, and even singular.

A classical way to solve large systems of ordinary differential equations is an iterative approach by utilizing so called Krylov-subspace methods as e.g. conjugate gradient (CG) , biconjugate gradient (BiCG) [160], minimum residual (MINRES), quasi-minimal residual (QMR) and generalized minimum residual (GMR) techniques. These methods are applicable to positive semi-definite matrix structures except the BiCG method which is also usable for indefinite matrices. As an alternative, iterative methods like the Schur complement [63, 138, 161] or the Uzawa iteration technique [162, 163] can be applied for solving so called saddle point problems or indefinite systems. Since the CG has been introduced in 1952 it soon became very popular and has been improved ever since. As these solvers are very robust and suitable even for very large systems, drawbacks in terms of a poor convergence can emerge if an ill-conditioned, indefinite system is treated. To restore the attractiveness of the iterative procedures in view of this lack of robustness, appropriate preconditioning techniques can be applied. Simply speaking, preconditioning is a transformation of the original system into a system which is easier to solve by iterative methods but having the same solution. A good compilation of preconditioning techniques is given in [141] and very detailed explanations can be found in e.g. [31, 138]. The solver used for the computations in this thesis uses the so called Incomplete Cholesky Conjugate Gradient (ICCG) method [142, 164].

A possibility to avoid preconditioning in case of ill-conditioned matrices is the use of so called direct methods [165, 166] which are based on the principle to decompose the given system into directly solvable fractions. Among these factorization methods like the *Cholesky*- or *QR*-factorization, the *LU*-factorization is the oldest and the most commonly used one. The difference is in the formation of the decomposition of a matrix. Whereas the *Cholesky*-method factorizes a matrix $\mathbf{A}$ as $\mathbf{L}\mathbf{L}^T = \mathbf{A}$, where $\mathbf{L}$ is a lower triangular matrix, the *QR*-method utilizes the product $\mathbf{Q}\mathbf{R} = \mathbf{A}$, where $\mathbf{Q}$ is orthogonal and $\mathbf{R}$ is upper triangular and the *LU*-method factorizes as $\mathbf{L}\mathbf{U} = \mathbf{A}$, with $\mathbf{U}$ representing an upper triangular matrix. A drawback of these techniques is in their

incapability of solving singular systems. A well-established way to eliminate singularity is the procedure of tree gauging [167, 168] where the vector potential is set to zero within a spanning tree in the graph formed by the FE edges in the discretized domain. Compared to iterative approaches, the direct solving techniques require a larger amount of memory when treating sparse matrices. The demand of memory can be reduced by so called fill-in reduction algorithms as e.g. the minimum degree procedure [169] or the nested dissection technique as described in [170]. The latter one is also implemented in the software library PARDISO (Parallel Direct Solver) embedded in the Intel® Math Kernel Library (MKL) for thread-safe solving of large sparse linear systems of equations on shared-memory multicore architecture [157, 171, 172]. PARDISO is also integrated in the FEM-solver used in this thesis and can be applied as an alternative to the iterative solving procedure.

The solution techniques discussed are applicable to linear equation systems. Since nonlinearities are an inevitable attribute of material properties in electromagnetic field computations, the occurring nonlinear equation systems need to be processed to be treated with these linear solvers. Hence, the so called fixed-point linearization procedure as described earlier is applied.

3 Eddy-current losses in a steel grid in the vicinity of an air reactor

3.1 Introduction

The idea of this investigation was to determine the additional losses of a dry insulated current excited air reactor with the aid of the FEM. In such reactors no iron core or insulation fluid is present. Such reactors are used for example in distribution networks to compensate reactive power or capacitive currents in long low powered distribution lines, short circuit limiting reactors and, due to their linear behavior, in measurement setups. They can reach huge dimensions, and one has to guarantee that the seating of the reactor is capable to withstand its weight. To ensure this, the concrete seating is usually reinforced with a steel grid exposed to the time-varying magnetic field of the reactor. The results of this study have been published in [113].

3.1.1 Problem definition

Due to the time-varying magnetic field of the reactor, eddy currents are induced in the conducting, highly permeable grid in the vicinity of the reactor.

These eddy-currents cause additional losses and may heat up the grid structure, possibly leading to a burst of the surrounding concrete, and hence rendering the seating unable to withstand the reactor's weight any longer. Since the commonly used grid material features ferromagnetic behavior one has to deal with a nonlinear problem. The excitation is time-periodic and the steady state periodic solution is of interest. To solve the problem, a frequency domain approach has been chosen. At

first, a solution using a time-harmonic approximation has been generated. Later, the fixed point method introduced earlier in 2.3.3.3 as HBFP technique has been employed to take account of higher harmonics. The finite element method has been applied to the so called $\mathbf{A}_r$,V-$\mathbf{A}_r$ reduced vector potential formulation (see sub-sections 2.1.2.2 and 2.2.4.2).

3.1.2 FEM modelling

To assess the accuracy of the numerical solution, different FEM formulations have been used and the findings compared to measured results. As mentioned above, a time-harmonic approximation has been chosen in a first approach, and then, to consider higher harmonics in the FEM computation, the HBFP technique has been applied.

3.1.2.1 Time-harmonic approach

Using this method, the differential equation (2.77) is solved in the frequency domain [76]. Therefore, the time derivative of the ordinary system of equations is replaced by a multiplication by $j\omega$, resulting in a complex, nonlinear equation system in the frequency domain as

$$\left[\mathbf{S}_\nu + j\omega\mathbf{M}_\sigma\right]\mathbf{X} = \mathbf{F} \tag{3.1}$$

where the vector $\mathbf{X}$ gathers the unknown complex amplitudes of the vector and scalar potentials. The right hand side vector $\mathbf{F}$ contains the known quantities. This formulation has its benefits in yielding a fast computational result at the expense of accuracy due to not considering higher harmonics. The reluctivity is determined in each nonlinear-iteration by the peak values of B and H [173]. To solve the system of equations a parallel direct solver (PARDISO) was used as briefly introduced in sub-section 2.3.4.

3.1.2.2 Harmonic balance fixed-point technique

This method has been described in sub-section 2.3.3.3 and is applied here to consider higher harmonics. The system of equations to be solved is of the form (2.132)

$$\left[\mathbf{S}^{(s)}_{(\nu_{FP})} + jm\omega\mathbf{M}_{\sigma}\right]\mathbf{X}^{(s+1)}_{m} = \mathfrak{F}_{m}\left[\mathbf{S}^{(s)}_{(\nu_{FP}-\nu)}\mathbf{x}^{(s)} + \mathbf{f}\right], \qquad m = 1,2,\ldots,N, \tag{3.2}$$

with the superscript $s = 0,1,2,\ldots$ denoting the nonlinear iteration steps and the subscript m indicates the m-th harmonic of the Fourier transform $\mathfrak{F}_m$.

The nonlinear iterations have been carried out as described in sub-section 2.3.3.2. In the course of the nonlinear iteration process, the systems of linear equations have been solved by the conjugate gradient method using incomplete Cholesky factorization for preconditioning the system matrix.

3.2 Numerical investigations

To achieve a meaningful validation, the computational results of the proposed FEM formulations have been compared to measured values. The measurements have been carried out by TRENCH Austria Ltd. by measuring the losses of a specific air reactor at different values of the excitation current, first without a steel grid underneath it and then with the reactor placed on the grid (see Fig. 3.1). The difference between the two values represents the additional loss caused by the eddy-currents induced in the highly permeable steel grid. The investigated grid is a commercial standard for concrete reinforcements with a round cross-section and a diameter of 8 (mm) (CQS 80). Its conductivity has been measured to be $\sigma = 5.8\cdot 10^{6}\ \left(\mathrm{S/m}\right)$ at a reference temperature of 20° centigrade. The mesh width of the grid is 300 (mm) by 300 (mm) and the whole structure underneath the reactor spans an area of 4500 (mm) by 4500 (mm). The intersections of the bars are welded together. Based on this data, a FEM model has been designed with the symmetry of the test arrangement taken into account. Hence it is sufficient to model a quarter of the original domain as illustrated in Fig. 3.2. The current density of the coil is determined by the given current and the number of turns. The main parameters of the air reactor are given in TABLE 3.1.

TABLE 3.1: Main data of the air reactor test setup

Geometry data			Operational data		
Values	Unit	Quantity	Values	Unit	Quantity
Active winding height	mm	3133	Rated voltage	kV	35.5
Average winding diameter	mm	2803	Rated power	MVar	28.028
Radial winding width	mm	249	Rated current	A	1015
Number of turns	-	231.375	Rated reactance	Ω	27.206
Total mass	kg	6850	Rated frequency	Hz	50

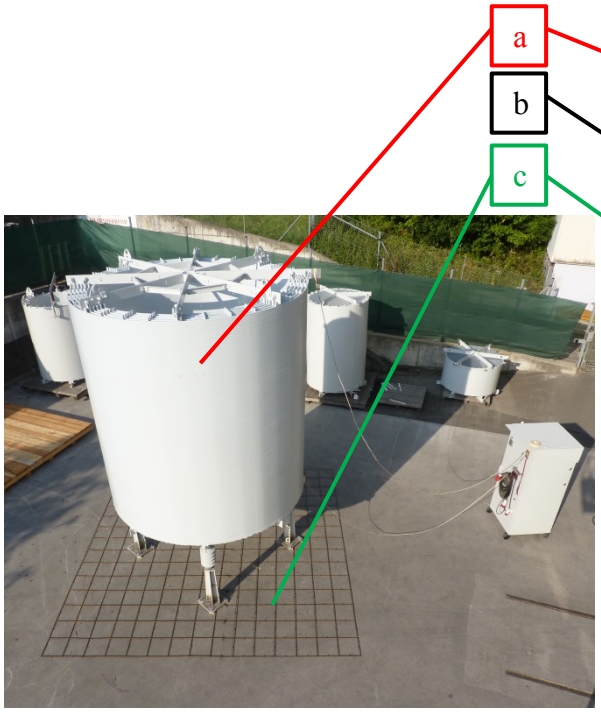

Fig. 3.1: Test setup of the loss measurement including the eddy-current losses.

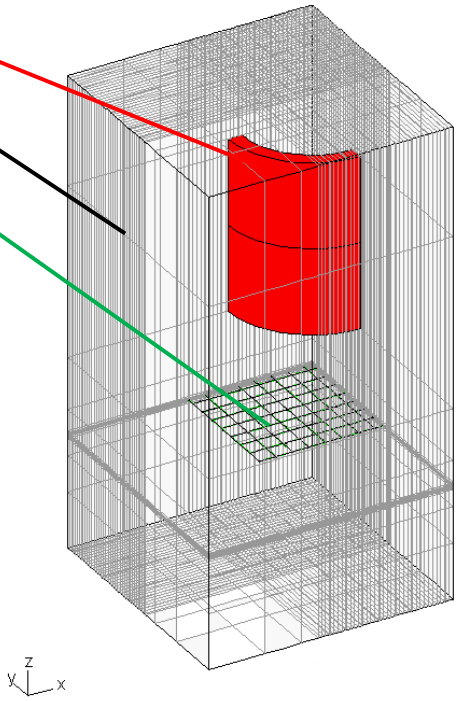

Fig. 3.2: Quarter-model of the problem domain applied in the FEM.

The coil of the air reactor marked with a) in Fig. 3.1 and colored red in Fig. 3.2 is assumed to be excited by a current source. It is hence advantageous to apply the reduced vector potential formulation, as it is then not necessary to model the coil in the finite element mesh. The steel grid where the eddy-currents are induced is indicated green and denoted with c). In Fig. 3.2 , the whole problem domain is shown including the finite element mesh marked with b).

The steel bars in the FEM model have a round cross section except at the welding point where the intersection of the bars has a conical shape. This is illustrated in the close up of the steel grid in Fig. 3.3.

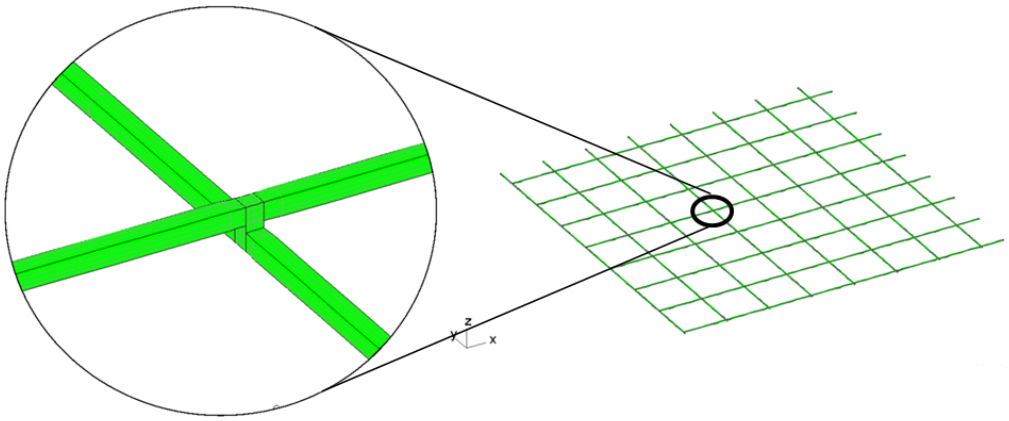

Fig. 3.3: Close up of an intersection of the steel grid.

The nonlinear material properties of the reinforcement steel are described by the appropriate *B*-*H* curve, provided by the manufacturer and shown in Fig. 3.4.

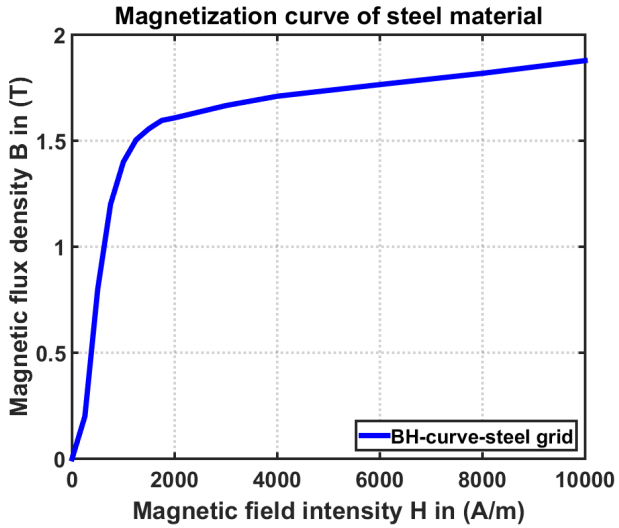

Fig. 3.4: Magnetization curve of the used steel bars.

The HBFP technique was used with up to the 11th harmonics considered. The numerical experiments show that considering higher harmonics affects the computational results marginally only, but increases the computational costs. The eddy-current losses were evaluated as presented in sub-section 2.1.4 evaluating a volume integral over the $\mathbf{A}_r, V$ domain averaging over a time-period as shown in (2.52).

3.2.1 Validation

The computational results of the two FEM formulations applied have been compared to the measurement results. The additional eddy-current losses have been evaluated for different excitation currents.

TABLE 3.2: Comparison of the measured and computed eddy-current losses

Value	Unit	Quantities					
I_{EXC}	A	50	100	300	500	700	1000
P_{eddy}^{m}	kW	0.074	0.272	2.777	10.106	20.158	43.364
P_{eddy}^{t-h}	kW	0.046	0.185	2.535	9.385	22.468	54.201
$P_{eddy}^{HBFP-11th}$	kW	0.048	0.183	2.389	8.751	20.680	50.140
$P_{eddy}^{HBFP-23rd}$	kW	0.048	0.183	2.389	8.750	20.680	50.110

In TABLE 3.2 the excitation current of the reactor is denoted by I_{EXC}, P_{eddy}^{m} represents the measured additional losses, P_{eddy}^{t-h} stands for the eddy-current losses obtained by the time-harmonic approximation and $P_{eddy}^{HBFP-11th}$ indicates the computed losses of the HBFP technique considering up to 11 harmonics and $P_{eddy}^{HBFP-23rd}$ represents the computed losses of the HBFP technique considering up to 23 harmonics. The results are summarized in Fig. 3.5 below with an appropriate interpolation of the data points.

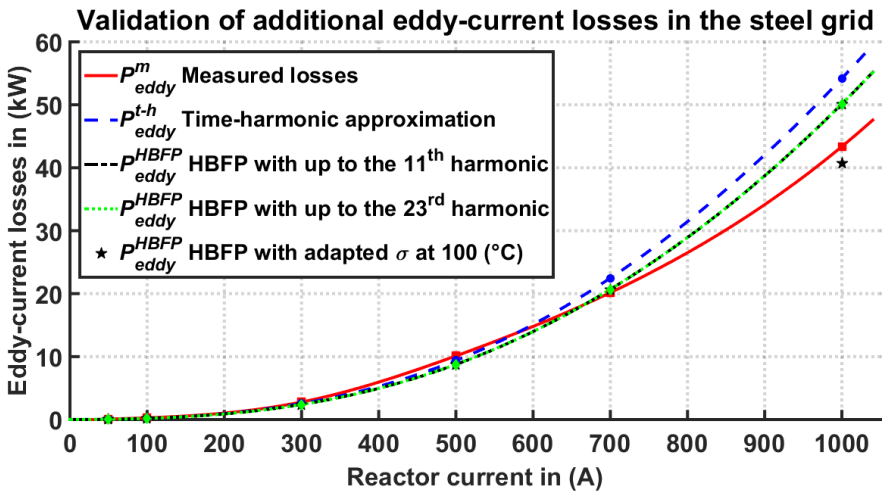

Fig. 3.5: Interpolated eddy-current losses as a function of the reactor excitation current.

As one can see in Fig. 3.5 the computed losses using the time-harmonic approximation differ considerably from the measured ones when the coil current rises. This is due to the fact that the saturation of the steel grid is more significant for higher currents. This error is less pronounced if higher harmonics are taken into account. Since the deviation of the losses at the highest excitation current level is still significantly high, a rise of the temperature in the steel grid was considered by adapting the electrical conductivity (see appendix B.3) as shown in TABLE 3.3.

TABLE 3.3: Computational losses in dependency of the electrical conductivity of the steel bars

Value	Unit	Quantities		
Conductivity σ	$\frac{S}{m}\cdot 10^6$	4.405	3.876	3.139
Temperature	°C	100	150	230
I_{EXC}	A		1000	
$P^{HBFP-11th}_{eddy}$	kW	40.067	37.522	31.817
P^{m}_{eddy}	kW		43.364	

In TABLE 3.3, it can be seen that considering a rise in the temperature of the steel grid by adapting the conductivity has a major impact on the computed eddy-current losses. Comparing the computed results to the measurement it can be concluded that the steel rods had an approximate temperature of about 90 (°C) to 100 (°C) during the measurement at an excitation current level of 1000 (A).

Regarding the computational costs, results for three different current levels have been summarized in TABLE 3.4. It is observable that the computational time increases significantly for high current values if higher harmonics are considered. This is due to the saturation effects in the steel bars and is even more dominant when higher numbers of harmonics are taken into account. Obviously, the computational costs bear no relation to the increase of accuracy if more than 11 harmonics are considered.

TABLE 3.4: Computational data

Value	Unit	Time-harmonic			HBFP		
CPU	-	2x Intel Xeon E5-2630 (6x2.00GHz – 12 Cores)					
approx. RAM usage	GB	30 (PARDISO)			14 (CG)		
No. of DOF	-	2,078,464					
I_{EXC}	A	50	500	1000	50	500	1000
Computational time	h	1.5	3.5	5.5	up to the 11th harm. 19.5	41.5	62.5
					up to the 23rd harm. 26	56.5	106

In addition to the loss validation, the induced currents have been measured and computed in several grid elements. For the measurement of the currents, a Rogowski coil was wound around the relevant steel bar.

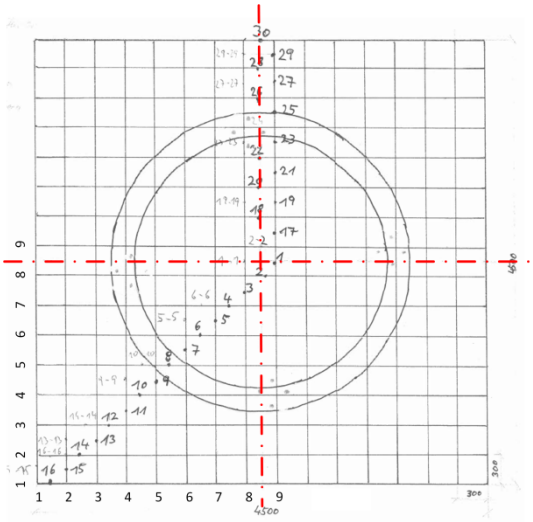

Fig. 3.6: Top view of the reactor and grid setup with the provided arrangement of the current measurement points.

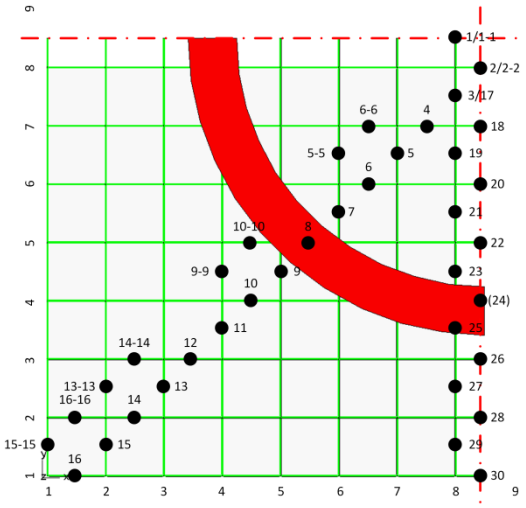

Fig. 3.7: Top view of the quarter FEM-model with the relocated distribution of the measurement points according to the symmetry planes.

Fig. 3.6 is a sketch of the current measurement points with the symmetry planes marked as red dash-dotted lines. In Fig. 3.7, the measurement points marked as black dots have been relocated to be within the quarter model. The currents at all indicated points have been calculated and compared to the measured values for each excitation current level. To summarize the findings, results for two current values are presented in this sub-section, but the complete data set is presented in the appendix B.2.

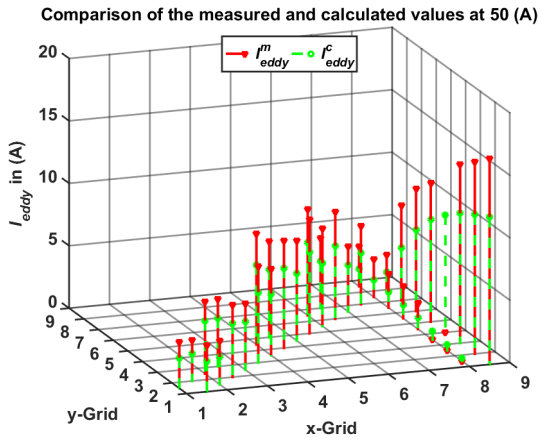

Fig. 3.8: Current distribution in the steel grid with an excitation current of the reactor of 50 (A).

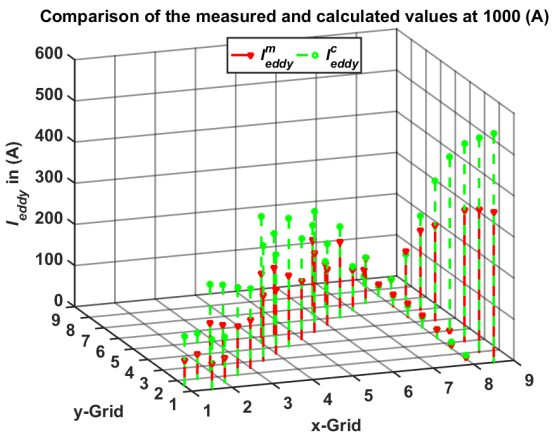

Fig. 3.9: Current distribution in the steel grid with an excitation current of the reactor of 1000 (A).

In Fig. 3.8 and Fig. 3.9 the magnitudes of measured and computed currents regarding the HBFP technique through the grid segments marked in Fig. 3.7 are plotted. The green stems indicate the calculated root mean square current values I^{c}_{eddy} , and the red plots represent the values of the measured currents I^{m}_{eddy} .

It is observable that when the reactor is energized with lower current levels the measured currents are higher than the computed ones and when the coil current becomes higher, the computed current values are higher than the measured ones. This effect may be attributed to the deviation of the conductivity varying with the temperature which is not considered in the computation.

To illustrate how the nonlinear material behavior affects the induced currents, the time response of the current in the segment marked 30 in Fig. 3.7 is shown in Fig. 3.10 with the coil energized with 50 (A) and in Fig. 3.11 with an excitation current of 1000 (A) applied. It is clearly visible that the deformation of the current response increases when the grid gets saturated at higher current levels.

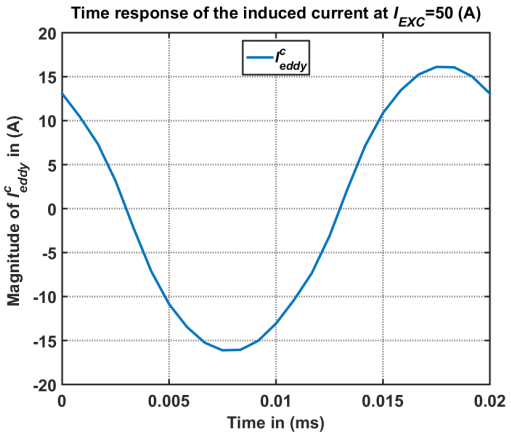

Fig. 3.10: Time response of the highest current amplitude in the grid at an exciting current of 50 (A)

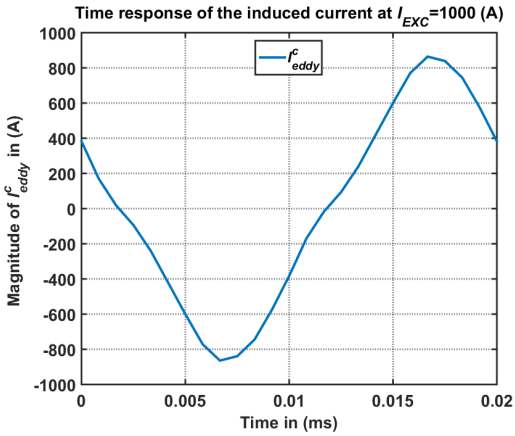

Fig. 3.11: Time response of the highest current amplitude in the grid at an exciting current of 1000 (A)

The additional losses caused by the induced eddy-currents can be lowered by using a grid made of stainless steel with low electrical conductivity. Indeed, stainless steel is barely affected by the time-varying magnetic field and the induced currents and hence the additional losses are negligibly low.

This has been observed in a further set of measurements and validated with FEM computations. The air reactor used as test object has not been the same but very

similar to the one investigated with the nonlinear steel grid (see appendix B.4 and B.5 for details). The measured and computed losses are summarized in TABLE 3.5.

TABLE 3.5: Comparison of the eddy-current losses in the stainless steel grid

Value	Unit	Quantities			
I_{EXC}	A	101.96	180.14	399.24	615.18
P_{eddy}^{m}	W	148	420	2040	4680
P_{eddy}^{FEM}	W	133	415	2039	4842

In TABLE 3.5, P_{eddy}^{m} indicates the mean value of the measured eddy-current losses and P_{eddy}^{FEM} denotes the losses computed with the aid of the FEM at different excitation current levels I_{EXC}.

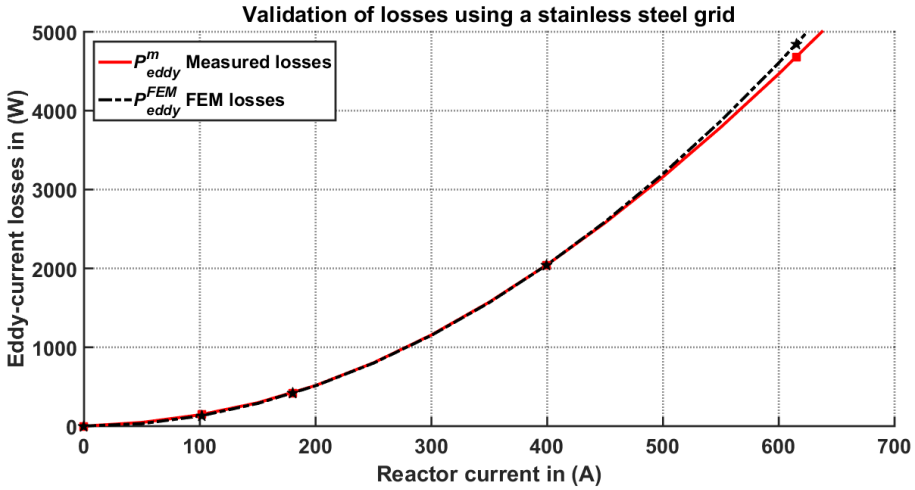

Fig. 3.12: Comparison of the occurring eddy-current losses in the stainless steel grid.

In Fig. 3.12, the computed and measured eddy-current losses are compared. It can be seen that the losses are in a very good agreement. This is due to the linear material behavior of the stainless steel grid. The losses are indeed very low compared to those occurring in the conventional steel grid, and are negligible compared to the losses of the reactor itself. Using a stainless steel material for concrete reinforcements is naturally expensive, the acquisition costs are four to eight times higher than the costs of conventional steel.

3.3 Conclusion

Concluding the results of these investigations, a FEM approximation with the time-harmonic approach is not acceptable due to its insufficient accuracy. For practical purposes, the results obtained by the HBFP method are close enough to measurements, but the deviations are significant, especially for high current levels. This is mainly due to the assumption of a constant electrical conductivity used in the computations for each excitation current level. At high currents, the steel rods heat up leading to a decrease of the electrical conductivity and hence lessen the induced current density and the additional losses. To improve the accuracy of the computed additional losses, the conductivity needs to be adjusted for higher excitation current levels.

Furthermore, the hysteresis losses of the steel grid have been neglected in the FEM investigation and this may also be a reason for the deviation in the losses especially at higher saturation levels.

It has been shown that increasing the number of harmonics taken into account over 11 does not improve the accuracy since their influence is negligible.

4 Design of nonlinear magnetic circuit models

4.1 Introduction

When aiming to improve the convergence of finite element method approaches for solving nonlinear, 3D, periodic, eddy-current problems, it is desirable to be able to carry out fast analyses in trying different alternative solution algorithms. The full FEM solutions are too time-consuming for this purpose. Hence, in order to facilitate a quick evaluation of different solving strategies to obtain the steady state solution of such problems, it is advantageous to develop simplified nonlinear magnetic circuit models governed by differential equations as close as possible to the 3D FEM partial differential equations discussed in the sub-section 2.2.4.1 for the magnetic vector potential formulation and in 2.2.4.3 for the current vector potential formulation. Since the focus of interest is in obtaining steady state solutions only, time periodic excitations are assumed and hence one can take advantage of the harmonic balance fixed-point technique (HBFP) introduced in sub-section 2.3.3.3.

4.2 Nonlinear magnetic circuit model

To generate an adequate planar nonlinear magnetic circuit model related to the equation systems obtained by the finite element formulations [86, 87, 174, 175, 176], one has to consider the iron parts, air gaps and also how to take account of the coils and eddy current regions. One has to define magnetic branches considering the

material behavior within a given region, nodes corresponding to a magnetic scalar potential, as well as magnetic branches forming loops related to a magnetic vector potential as indicated in Fig. 4.1 - Fig. 4.4.

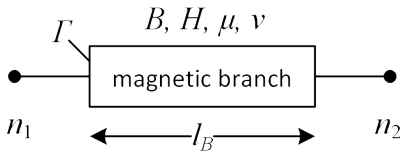

Fig. 4.1: Magnetic branch to consider material properties.

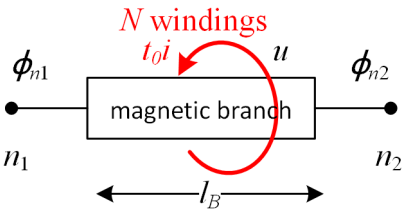

Fig. 4.2: Magnetic branch coupled with voltage excitation.

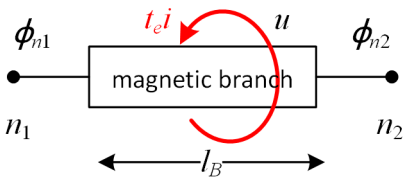

Fig. 4.3: Magnetic branch coupled with eddy-current domain.

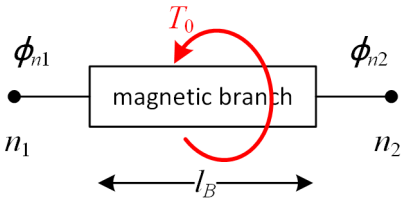

Fig. 4.4: Magnetic branch coupled with current excitation.

In the following notations, bold, symbols represent matrices or vectors of space coordinates as used in FEM formulations and non-bold, italic symbols correspond to concentrated quantities occurring in the circuit formulation. Furthermore, italic symbols with an arrow above are vectors consisting of concentrated quantities, and matrices are marked by an overline.

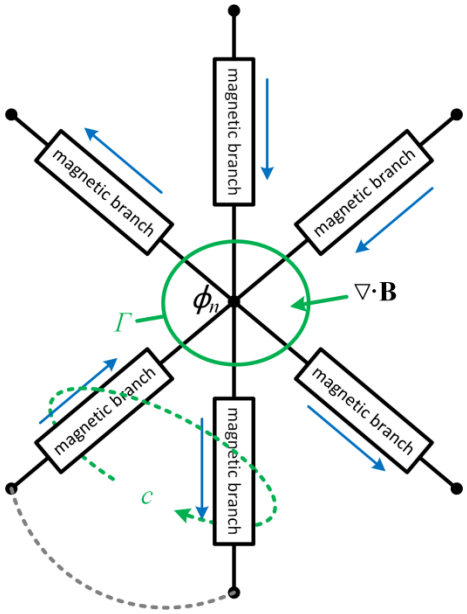

Fig. 4.5: Basic coupling of magnetic branches to a node. An exciting loop c is also indicated.

A basic coupling of magnetic branches to a node is shown in Fig. 4.5 where the magnetic scalar potential is denoted by ϕ_n and the subscript n represents the n-th node of the circuit. Similarly to an electrical circuit, one can apply Kirchhoff´s nodal law to the magnetic fluxes, obtaining

$$\nabla\cdot\mathbf{B}=0\Rightarrow\oint_{\Gamma}\mathbf{B}\cdot d\boldsymbol{\Gamma}=0\Rightarrow\sum_{k\in I_n}B_k\Gamma_k=0\,, \tag{4.1}$$

with $\mathbf{B}$ representing the magnetic flux density, Γ is the surface of the area where the branches are connected, thus $I_n=\{k\in[1\ldots nB]$: k-th magnetic branch connected to the n-th node$\}$ and nB denotes the number of the magnetic branches involved.

Further indicated in Fig. 4.5 is an excitation loop c to couple the magnetic branch with an electrical source. Here, one can derive

$$\nabla\times\mathbf{E}=-\frac{\partial\mathbf{B}}{\partial t}\Rightarrow\oint_{c}\mathbf{E}\cdot d\mathbf{s}=-\frac{d}{dt}\int_{\Gamma}\mathbf{B}\cdot d\boldsymbol{\Gamma}\Rightarrow u_T=-\frac{d}{dt}\sum_{i=I_u}B_i\Gamma_i\,, \tag{4.2}$$

where $\mathbf{E}$ is the electric field intensity, t is time, and u_T represent the turn voltage.

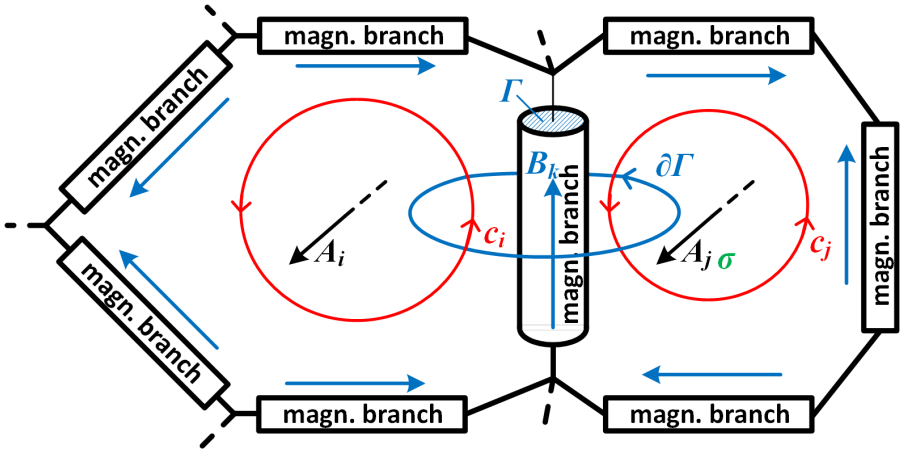

Fig. 4.6: Mesh of magnetic branches with indicated cycle basis and coupling between the loups.

Kirchhoff´s cycle law for the magnetic circuit formulation is illustrated in Fig. 4.6. One has

$$\nabla \times \mathbf{H} = \mathbf{J} \Rightarrow \oint_c \mathbf{H} \cdot d\mathbf{s} = I \Rightarrow \sum_{i=I_c} H_i l_i = I \,, \tag{4.3}$$

where **J** is the current density and I the exciting current and c is the closed path of magnetic branches as shown in Fig. 4.6. The excitation and eddy current domains are considered by appropriate coupling with electric loops and conductive materials as indicated in Fig. 4.1 - Fig. 4.6 instead of edge and nodal basis functions as in the FEM model.

The main goal in developing the magnetic circuit formulations is to be as close as possible to the FEM formulations to facilitate similar procedures to solve the ordinary differential equations as those used in the 3D FEM case to solve the partial differential equations. Therefore, we adapt mathematical expressions similar to those used in the FEM formulations to describe the magnetic circuit formulations.

Let us introduce two operators in the complex space $\mathbb{C}$, between the branch space and node space. The first one is $\nabla : \mathbb{C}^{nN} \rightarrow \mathbb{C}^{nB}$ to transform from node space to branch space. Here nN denotes the number of nodes and nB denotes the number of magnetic branches. $\mathbb{C}^{nN}$ represents the nN dimensional node space and $\mathbb{C}^{nB}$ the nB dimensional branch space. The operator is defined as

$$\nabla \triangleq \left[\gamma_{k,n}\right]_{nN\times nB};\quad \gamma_{k,n}=\begin{cases} 1/l_{B,k} & :k\in \mathbb{I}_{B_n},\\ -1/l_{B,k} & :-k\in \mathbb{I}_{B_n},\\ 0 & :\ else, \end{cases} \tag{4.4}$$

according to Fig. 4.1 - Fig. 4.4 and with $\mathbb{I}_{B_n}=\{k\in[1\ldots nB]$; if the k-th branch is incident with the n-th node and pointing towards the node$\}\cup\{-k\in[1\ldots nB]$; if the branch points away from the node$\}$. This operator will be called the discrete gradient operator due to its similarity to the continuous gradient operator.

The next operator transforms the branch space into node space and is denoted as $\nabla\cdot:\mathbb{C}^{nB}\to\mathbb{C}^{nN}$ and is defined as

$$\nabla\cdot \triangleq \left[\delta_{n,k}\right]_{nB\times nN};\quad \delta_{n,k}=\begin{cases} \Gamma_k & :k\in \mathbb{I}_{B_n},\\ -\Gamma_k & :-k\in \mathbb{I}_{B_n},\\ 0 & :\ else, \end{cases} \tag{4.5}$$

according to Fig. 4.5. This operator is called discrete divergence operator due to its analogy with the continuous divergence operator.

Two further operators are introduced between the branch and cycle spaces. Let us define the first operator from branch space to cycle space: $\nabla_B\times:\mathbb{C}^{nB}\to\mathbb{C}^{nC}$. Here nC denotes the number of cycles and $\mathbb{C}^{nC}$ denotes the nC dimensional cycle space. The operator is defined as

$$\nabla_B\times \triangleq \left[\beta_{j,k}\right]_{nC\times nB};\quad \beta_{j,k}=\begin{cases} l_{B,k} & :k\in \mathbb{I}_{C_j},\\ -l_{B,k} & :-k\in \mathbb{I}_{C_j},\\ 0 & :\ else, \end{cases} \tag{4.6}$$

according to Fig. 4.6 and $\mathbb{I}_{C_j}=\{k\in[1\ldots nB]$; if the k-th branch is incident with the j-th cycle and has the same orientation as the cycle$\}\cup\{-k\in[1\ldots nB]$; if it is incident with the j-th cycle and is counter-oriented to the cycle$\}$.

The last operator transforms the cycle space to the branch space and is denoted as $\nabla_C\times:\mathbb{C}^{nC}\to\mathbb{C}^{nB}$. This operator is defined as

$$\nabla_C \times \hat{=} \left[\alpha_{k,j}\right]_{nB\times nC};\quad \alpha_{k,j} = \begin{cases} 1/\Gamma_k & : k \in \mathbb{I}_{C_j}, \\ -1/\Gamma_k & : -k \in \mathbb{I}_{C_j}, \\ 0 & : \ else, \end{cases} \tag{4.7}$$

according to Fig. 4.6. These last two operators with the subscripts *B* and *C* denoting the difference in the affiliation, are called discrete curl operators due to their similarity to the continuous curl operators.

4.2.1 Nonlinear magnetic circuit model corresponding to the T,ϕ-ϕ-formulation

According to the **T**,ϕ-ϕ-formulation, each eddy current domain is represented by a magnetic branch with an additional unknown current vector potential $\vec{T} = \left[T_1 \cdots T_{nB}\right]^T$. Each node corresponds to a magnetic scalar potential $\vec{\phi} = \left[\phi_1 \cdots \phi_{nN}\right]^T$. The impressed current vector potentials $\vec{T}_0 = \left[T_{0,1} \cdots T_{0,nB}\right]^T$ represent the current excited windings. To take the voltage excited windings into account, the impressed current vector potentials $\overline{t}_0^w$ for unit currents are used as

$$\overline{t}_{0,i,j}^{w} = \begin{cases} \dfrac{1}{l_{B,i}} N_j & : i \in \mathbb{I}_{V_j}, \\ 0 & : \ else, \end{cases} \tag{4.8}$$

with $\mathbb{I}_{V_j} = \{ i \in \left[1 \ldots nB\right]$: *i*-th branch belongs to the *j*-th voltage excited coil$\}$, where the *j*-th coil has N_j electrical turns.

Expressing the concentrated magnetic field intensities in the magnetic branches as $\vec{H} = \left[H_1 \cdots H_{nB}\right]^T$, and using the discrete gradient operator one can obtain

$$\vec{H} = -\nabla\vec{\phi} + \vec{T} + \vec{T}_0 + \overline{t}_0^w \vec{i}^{\,w}, \tag{4.9}$$

where the vector $\vec{i}^{\,w}$ contains the unknown currents in the voltage excited windings.

Introducing the notations $\vec{i}_0$ for the unknown currents in the current excited windings, and $\vec{i}^{\,e}$ for the eddy currents, the current vector potentials can be expressed as follows

$$\vec{T}_0 = \overline{t}_0 \vec{i}_0 \text{ and } \vec{T} = \overline{t}^{\,e} \vec{i}^{\,e}, \tag{4.10}$$

with

$$\overline{t}_{0,i,j} = \begin{cases} \dfrac{1}{l_{B,i}} N_j & : i \in \mathbb{I}_{0,V_j}, \\ 0 & : \ else, \end{cases} \tag{4.11}$$

where $\mathbb{I}_{0,V_j} = \{ i \in [1 \ldots nB] :$ *i*-th branch belongs to the *j*-th current excited coil$\}$, where the *j*-th coil has N_j electrical turns, and

$$\overline{t}^{\,e}_{i,j} = \begin{cases} \dfrac{1}{l_{B,i}} & : i \in \mathbb{I}^{e}_{V_j}, \\ 0 & : \ else, \end{cases} \tag{4.12}$$

where $\mathbb{I}^{e}_{V_j} = \{ i \in [1 \ldots nB] :$ *i*-th branch belongs to the *j*-th eddy-current branch$\}$.

With this potential formulation, Kirchhoff´s cycle law written in (4.3) is automatically satisfied. The equations remaining to be solved are (4.1) and (4.2). Applying the discrete operators to the potentials in the circuit formulation, the equation for the excitations to be solved is

$$u_j - R_j i^w_j = -\frac{d}{dt} \sum_{i=1}^{nB} B_i \Gamma_i l_{B,i} t^w_{0,i,j}, \qquad j = 1, \ldots, nB, \tag{4.13}$$

and for the unknowns in the nodes

$$\nabla \cdot \vec{B} = \nabla \cdot \overline{\mu} \vec{H} = \nabla \cdot \left(-\nabla \vec{\phi} + \vec{T} + \vec{T}_0 + \overline{t}^{\,w}_0 \vec{i}^{\,w} \right) = 0, \tag{4.14}$$

where $\vec{B} = \left[B_1 \dots B_{nB}\right]^T$ contains the concentrated magnetic flux densities in the branches, $\overline{\mu}$ is a diagonal matrix of the size $\left[nB \times nB\right]$ of the magnetic permeabilities associated with the magnetic branches. Γ_i is the cross-section and $l_{B,i}$ is the length of the i-th magnetic branch. In (4.13) u_j is the voltage of the j-th winding with the resistance R_j.

Summarizing (4.13) and (4.14), the ordinary differential equation system to be solved has the form

$$\left(\underbrace{\begin{bmatrix} \overline{A}_\rho & 0 & 0 \\ 0 & 0 & 0 \\ 0 & 0 & \overline{R} \end{bmatrix}}_{\triangleq \mathbf{S}_\rho} + d/dt \underbrace{\begin{bmatrix} \overline{C}_\mu & \overline{G}_\mu & \overline{g}_\mu \\ \overline{G}_\mu^T & \overline{L}_\mu & \overline{h}_\mu \\ \overline{g}_\mu^T & \overline{h}_\mu^T & \overline{V}_\mu \end{bmatrix}}_{\triangleq \mathbf{M}_\mu} \right) \underbrace{\begin{bmatrix} \vec{i}^{\,e} \\ \vec{\phi} \\ \vec{i}^{\,w} \end{bmatrix}}_{\triangleq \mathbf{x}} = \underbrace{\begin{bmatrix} -d/dt\left(\overline{C}_\mu \vec{T}_0\right) \\ -d/dt\left(\overline{G}_\mu^T \vec{T}_0\right) \\ \vec{u} - d/dt\left(\overline{g}_\mu^T \vec{T}_0\right) \end{bmatrix}}_{\triangleq \mathbf{f}_\rho + \mathbf{f}_\mu}. \tag{4.15}$$

In (4.15) one can see the similarity to the FEM equation system (2.92) with the indicated vectors and matrices expressed by the concentrated circuit quantities and the values at the symmetry plane assumed to be zero. The circuit parameters are denoted as

$$\overline{A}_\rho = \left[diag\left(\vec{R}^e\right)\right]; \quad \overline{R} = \left[diag\left(\vec{R}^w\right)\right], \tag{4.16}$$

where $\overline{A}_\rho$ is a diagonal matrix of $\vec{R}^e$ denoting the resistances of the eddy-current branches, and $\overline{R}$ is a diagonal matrix of $\vec{R}^w$ representing the resistances of to the windings. Furthermore,

$$\overline{C}_\mu = \left[-\left(\overline{t}^{\,e}\right)^T \cdot \overline{\mu} l_B \Gamma \overline{t}^{\,e} \right]; \quad \overline{G}_\mu = \left[\overline{\mu} l_B \Gamma \left(\overline{t}^{\,e}\right)^T \nabla \right]; \quad \overline{G}_\mu^T = \left[\nabla \cdot \overline{\mu} \overline{t}^{\,e} \right], \tag{4.17}$$

$$\overline{L}_\mu = \left[-\nabla \cdot \overline{\mu} \nabla \right]; \quad \overline{h}_\mu = \left[\nabla \cdot \overline{\mu} \overline{t}_0^{\,w} \right]; \quad \overline{h}_\mu^T = \left[\overline{\mu} l_B \Gamma \left(\overline{t}_0^{\,w}\right)^T \nabla \right], \tag{4.18}$$

$$\overline{g}_\mu = \left[-\left(\overline{t}^{\,e}\right)^T \cdot \overline{\mu} l_B \Gamma \overline{t}_0^{\,w} \right]; \; \overline{g}_\mu^T = \left[-\left(\overline{t}_0^{\,w}\right)^T \cdot \overline{\mu} l_B \Gamma \overline{t}^{\,e} \right]; \; \overline{V}_\mu = \left[-\left(\overline{t}_0^{\,w}\right)^T \cdot \overline{\mu} \overline{t}_0^{\,w} l_B \Gamma \right]. \tag{4.19}$$

In order to simplify the notations, some vector and matrix parts are merged as highlighted in (4.20)

$$\left(\begin{bmatrix} \overline{A}_\rho & 0 & 0 \\ 0 & 0 & 0 \\ 0 & 0 & \overline{R} \end{bmatrix} + d/dt \begin{bmatrix} \overline{C}_\mu & \overline{G}_\mu & \overline{g}_\mu \\ \overline{G}_\mu^T & \overline{L}_\mu & \overline{h}_\mu \\ \overline{g}_\mu^T & \overline{h}_\mu^T & \overline{V}_\mu \end{bmatrix}\right) \begin{bmatrix} \vec{i}^{\,e} \\ \vec{\phi} \\ \vec{i}^{\,w} \end{bmatrix} = \begin{bmatrix} -\frac{d}{dt}\left(\overline{C}_\mu \vec{T}_0\right) \\ -\frac{d}{dt}\left(\overline{G}_\mu^T \vec{T}_0\right) \\ \vec{u} - \frac{d}{dt}\left(\overline{g}_\mu^T \vec{T}_0\right) \end{bmatrix}, \tag{4.20}$$

and hence

$$\underline{\overline{A}}_\rho = \begin{bmatrix} \overline{A}_\rho & 0 \\ 0 & 0 \end{bmatrix}; \quad \underline{\overline{C}}_\mu = \begin{bmatrix} \overline{C}_\mu & \overline{G}_\mu \\ \overline{G}_\mu^T & \overline{L}_\mu \end{bmatrix}; \quad \underline{\overline{g}}_\mu = \begin{bmatrix} \overline{g}_\mu \\ h_\mu \end{bmatrix}; \quad \underline{\overline{g}}_\mu^T = \begin{bmatrix} \overline{g}_\mu^T & \overline{h}_\mu^T \end{bmatrix}, \tag{4.21}$$

as well as for the vector of unknowns and the right hand side vector

$$\vec{x} = \begin{bmatrix} \vec{i}^{\,e} \\ \vec{\phi} \end{bmatrix}; \qquad \vec{f}_\mu = \begin{bmatrix} -\frac{d}{dt}\underline{\overline{C}}_\mu \underline{\vec{T}}_0 \\ \vec{u} - \frac{d}{dt}\underline{\overline{g}}_\mu^T \underline{\vec{T}}_0 \end{bmatrix}; \qquad \underline{\vec{T}}_0 = \begin{bmatrix} \vec{T}_0 \\ 0 \end{bmatrix}. \tag{4.22}$$

To solve the nonlinear equation system (4.15), the harmonic balance fixed-point technique is applied. Thus the equation system is linearized by the fixed-point method and the equations are decoupled using the harmonic balance procedure. One has to switch to the frequency domain by using a Fourier-transformation to compute the complex Fourier coefficient of the *m*-th harmonic at the angular frequency ω as

$$\begin{gathered} \hat{\vec{X}}_m = \mathfrak{F}_m\left(\vec{x}\right) = \frac{1}{T}\int_0^T \vec{x} \cdot e^{-jm\omega t} dt \\ \mathfrak{F}_m\left(\vec{x}\right) = \hat{\vec{X}}_m \qquad \mathfrak{F}_m\left(\frac{d}{dt}\vec{x}\right) = jm\omega \hat{\vec{X}}_m \qquad \forall m \in \mathbb{Z}. \end{gathered} \tag{4.23}$$

Since the nonlinearity in the HBFP is due to the dependence of C_μ on the solution, it is obvious to define a time independent fixed-point permeability μ_{FP}. Hence, one has to solve the given equation system in each iteration step s. The resulting equation system using (4.23) is obtained as

$$\begin{aligned}\left[\begin{bmatrix}\underline{A}_\rho & 0\\ 0 & \overline{R}\end{bmatrix}+jm\omega\begin{bmatrix}\overline{\underline{C}}^{(s)}_{\mu_{FP}} & \overline{\underline{g}}^{(s)}_{\mu_{FP}}\\ \left(\overline{\underline{g}}^{(s)}_{\mu_{FP}}\right)^T & \overline{V}^{(s)}_{\mu_{FP}}\end{bmatrix}\right]\begin{bmatrix}\hat{\vec{X}}_m\\ \hat{\vec{I}}^w_m\end{bmatrix}^{(s+1)} &= \begin{bmatrix}-jm\omega\mathfrak{F}_m\left(\overline{\underline{C}}^{(s)}_\mu\vec{\underline{T}}_0\right)\\ \vec{u}-jm\omega\mathfrak{F}_m\left(\left(\overline{\underline{g}}^{(s)}_\mu\right)^T\vec{\underline{T}}_0\right)\end{bmatrix}\\ &+\begin{bmatrix}\overline{\underline{C}}^{(s)}_{\mu_{FP}} & \overline{\underline{g}}^{(s)}_{\mu_{FP}}\\ \left(\overline{\underline{g}}^{(s)}_{\mu_{FP}}\right)^T & \overline{V}^{(s)}_{\mu_{FP}}\end{bmatrix}jm\omega\begin{bmatrix}\hat{\vec{X}}_m\\ \hat{\vec{I}}^w_m\end{bmatrix}^{(s)}-jm\omega\mathfrak{F}_k\left(\begin{bmatrix}\overline{\underline{C}}^{(s)}_\mu & \overline{\underline{g}}^{(s)}_\mu\\ \left(\overline{\underline{g}}^{(s)}_\mu\right)^T & \overline{V}^{(s)}_\mu\end{bmatrix}\begin{bmatrix}\vec{x}\\ \vec{i}^w\end{bmatrix}^{(s)}\right).\end{aligned} \tag{4.24}$$

The equation system in (4.24) is decoupled in each nonlinear iteration step and each harmonic solution can be solved parallel, a feature leading to a substantial saving of computational time.

4.2.2 Nonlinear magnetic circuit model corresponding to the A,V-formulation

Similarly to the **T**,ϕ-ϕ circuit-formulation, one can find an adequate equation system for the magnetic vector potential approach satisfying Kirchhoff´s nodal law applied to planar magnetic circuit problems. Thus, magnetic branches form loops corresponding to the magnetic vector potential and the coupling of these cycles result in the magnetic flux density as described below. To consider eddy current domains, one has to assign a conductivity σ to the relevant cycle. In case of the magnetic circuit formulation the electric scalar potentials are not explicitly needed.

As indicated in Fig. 4.1, each magnetic branch is described by geometry parameters as the cross section Γ and the length l_B, as well as by material properties as the magnetic permeability μ or the magnetic reluctivity ν to determine the relationship between the magnetic flux density B and the magnetic field intensity H. Fig. 4.6 (see page 71) shows a basic planar magnetic circuit mesh with a cycle basis c [177] corresponding to the unknown vector potential A. Assuming a planar graph circuit model, the magnetic flux density of a magnetic branch is determined by the adjacent cycles along the boundary of a magnetic branch $\partial\Gamma$ as

$$\int_{\Gamma} \mathbf{B} \cdot d\boldsymbol{\Gamma} = \oint_{\partial\Gamma} \mathbf{A} \cdot d\mathbf{s} \Rightarrow A_i - A_j = B_k \left| \Gamma_k \right|, \tag{4.25}$$

where the unknown vector potentials are denoted as $\vec{A} = \left[A_1 \ldots A_{nC} \right]^T$ and correspond to the cycles.

Due to (4.25) and using the discrete curl operators, the concentrated field quantity B can be written as

$$\vec{B} = \nabla_C \times \vec{A}. \tag{4.26}$$

According (4.2), using the discrete curl operator, the following equation is valid:

$$\nabla_C \times \vec{E} = -\frac{d}{dt} \vec{B} \Rightarrow \vec{E} = -\frac{d}{dt} \vec{A}. \tag{4.27}$$

Treating the eddy currents as short-circuit windings with only one turn, the concentrated current density results in the current $\vec{i}^{\,e}$ in the magnetic circuit formulation and is expressed as

$$\vec{i}^{\,e} := \overline{\sigma} \vec{E}, \tag{4.28}$$

with the conductivity $\overline{\sigma} = \left[diag\left(\vec{R}^e \right) \right]^{-1}$ in the eddy-current domains described by a diagonal matrix of the size $\left[nC \times nC \right]$. Thus equation (4.1) is automatically fulfilled and (4.2) and (4.3) remain to be solved for the excitation as

$$\int_t u_j - R_j \int_t i_j = -\sum_{i=1}^{nB} B_i \Gamma_i l_{B,i} t^w_{0,i,j}, \qquad j = 1, \ldots, nB, \tag{4.29}$$

and for the unknowns corresponding to the cycles

$$\nabla_B \times \vec{H} = \nabla_B \times \overline{\nu} \vec{B} = \nabla_B \times \overline{\nu} \nabla_C \times \vec{A} = \vec{i}_0 + \vec{i}^{\,w} + \vec{i}^{\,e} = \nabla_B \times \vec{T}_0 + \nabla_B \times \overline{t}_0^{\,w} \vec{i}^{\,w} - \overline{\sigma} \frac{d}{dt} \vec{A}. \tag{4.30}$$

The reluctivity $\overline{\nu}$ is represented by a diagonal matrix of the size $\left[nB \times nB\right]$. Summarizing (4.29) and (4.30), one obtains the following equation system

$$\left(\underbrace{\begin{bmatrix} \overline{S}_{\nu} & \overline{g} \\ \overline{g}^{T} & \overline{R}\int_{t} \end{bmatrix}}_{\hat{=}\mathbf{S}_{\nu}} + d/dt \underbrace{\begin{bmatrix} \overline{C}_{\sigma} & 0 \\ 0 & 0 \end{bmatrix}}_{\hat{=}\mathbf{M}_{\sigma}} \right) \underbrace{\begin{bmatrix} \vec{A} \\ \vec{i}^{\,w} \end{bmatrix}}_{\hat{=}\mathbf{x}} = \underbrace{\begin{bmatrix} \nabla_B \times \vec{T}_0 \\ \int \vec{u} dt \end{bmatrix}}_{\hat{=}\mathbf{f}}, \tag{4.31}$$

where

$$\begin{gathered} \overline{R} = \left[\vec{R}^{w} \right]; \quad \overline{S}_{\nu} = \nabla_B \times \overline{\nu} \nabla_C \times; \quad \overline{C}_{\sigma} = \overline{\sigma}; \\ \overline{g} = -\nabla_B \times \overline{t}_0; \quad \overline{g}^{T} = -\overline{t}_0^{T} l_B I \nabla_C \times. \end{gathered} \tag{4.32}$$

It can be observed that (4.31) has the same structure and properties as the 3D FEM equation system (2.77) when the electrical scalar potentials are zero.

For further reflection the vector of unknowns and the right hand side vector can be written as

$$\vec{x} = \vec{A}; \quad \vec{f} = \begin{bmatrix} \nabla_B \times \vec{T}_0 \\ \int \vec{u} dt \end{bmatrix}. \tag{4.33}$$

Applying the HBFP technique to (4.31) in the same manner as in case of the **T**,ϕ-ϕ-formulation in sub-section 4.2.1, one obtains the equation system

$$\begin{aligned} \left(\begin{bmatrix} \overline{S}_{\nu_{FP}}^{(s)} & \overline{g}^{T} \\ \overline{g} & \overline{R}/jm\omega \end{bmatrix} + jm\omega \begin{bmatrix} \overline{C}_{\sigma} & 0 \\ 0 & 0 \end{bmatrix} \right) \begin{bmatrix} \hat{\vec{X}}_m \\ \hat{\vec{I}}_m^{\,w} \end{bmatrix}^{(s+1)} = \\ = \mathfrak{F}_m \begin{bmatrix} \nabla_B \times \vec{T}_0 \\ \int \vec{u} dt \end{bmatrix} + \mathfrak{F}_m \left(\begin{bmatrix} \overline{S}_{\nu_{FP}}^{(s)} - \overline{S}_{\nu}^{(s)} & \overline{g}^{T} \\ \overline{g} & \overline{R}\int_{t} \end{bmatrix} \begin{bmatrix} \vec{x} \\ \vec{i}^{\,w} \end{bmatrix}^{(s)} \right). \end{aligned} \tag{4.34}$$

To ensure that these equation systems are regular, the chosen loops to determine the unknown magnetic vector potentials have to be independent of each other. Therefore, a proper cycle basis has to be chosen in the graph of the planar magnetic circuit model [177].

4.3 Numerical investigations

In the following sub-sections, the nonlinear magnetic circuit formulations presented previously are applied to an industrially relevant transformer model to enable a fast analysis of various solution procedures of the nonlinear equation systems and to examine their influence on the convergence of the nonlinear iterations and hence computational time. These fast nonlinear magnetic circuit investigations should establish the properties of the solution algorithms and help to decide which procedure is favorably to be used to solve 3D FEM problems.

4.3.1 Evaluation of two approaches for treating the voltage excitation in the T,ϕ-ϕ-formulation

The focus of this study is to investigate the impact of selecting various ways to treat the additional equations taking account of the voltage excitations. A 3D benchmark transformer model with sinusoidal voltage excitation has been simplified to a nonlinear magnetic circuit analysis problem. Two options for treating the system of equations are investigated: the so-called "*separated method*" and the "*combined method*", as published by the author in [119]. The motivation for the separated method, i.e. to treat the additional equations due to the voltage excitation separately from the remaining equation system during the nonlinear iterations is to ensure a better-conditioned system matrix. This is expected to lead to a faster convergence of the CG iteration process, a significant result, as the elapsed time for solving a problem by FEM is dominated by the CG iterations [106]. Since the fundamental solving strategy is the HBFP applied to the **T**,ϕ-ϕ-formulation presented in sub-section 4.2.1, the combined equation system was introduced in (4.24). Separating the voltage excitations,

$$\begin{aligned}\left(\left[\underline{\overline{A}}_{\rho}\right]+j\omega m\left[\underline{\overline{C}}_{\mu_{FP}}^{(s)}\right]\right)\left[\hat{\vec{X}}_{m}\right]^{(s+1)} &= \\ = j\omega m\Im_k\left(\left[-\underline{\overline{C}}_{\mu}^{(s)}\underline{\vec{T}}_0\right]+\left[\underline{\overline{C}}_{\mu_{FP}}^{(s)}-\underline{\overline{C}}_{\mu}^{(s)}\right]\left[\vec{x}\right]^{(s)}-\left[\underline{\overline{g}}_{\mu}^{(s)}\vec{i}^{\,w,(s)}\right]\right),\end{aligned} \tag{4.35}$$

as well as

$$\overline{R}\vec{i}^{\,w,(s+1)}+\frac{d}{dt}\left(\overline{V}_{\mu}^{(s)}\vec{i}^{\,w,(s+1)}\right)=\vec{u}-\frac{d}{dt}\left(\underline{\overline{g}}_{\mu}^{(s)}\right)^{T}\left(\vec{x}^{(s+1)}\underline{\vec{T}}_0\right), \tag{4.36}$$

emerge where, in (4.36) the unknown winding current due to a given voltage excitation is calculated separately, using the field solution determined in (4.35) from the current obtained in the previous iteration step.

The equation system of the combined method (4.24) as well as the equations of the separated method (4.35) and (4.36) have been implemented in a MathWorks®-MATLAB code to obtain solutions of the magnetic circuit problem. The input of this code consists of all known quantities and the connections, such as the cross-sections of the magnetic branches, the connection of the nodes, the current loops and the affected branches as well as the main parameters of the transformer. Based on these parameters the divergence and gradient matrices are assembled to solve the equation system. According to the nonlinearity, appropriate *B*-*H* curves have been implemented.

4.3.1.1 Magnetic circuit model of the transformer

Before starting the evaluation, one has to construct a magnetic circuit model of the transformer. The device is a basic transformer as drawn in Fig. 4.7. It is a single-phase transformer enclosed by a steel tank with the iron core and the steel exhibiting a nonlinear behavior. Both the primary and the secondary windings are split in two halves wound around each limb with the halves connected in series. In order to be as close to a practical problem as possible, the primary winding is assumed to be voltage-driven in this investigation. This transformer model will also be used as a benchmark in further 3D FEM investigations.

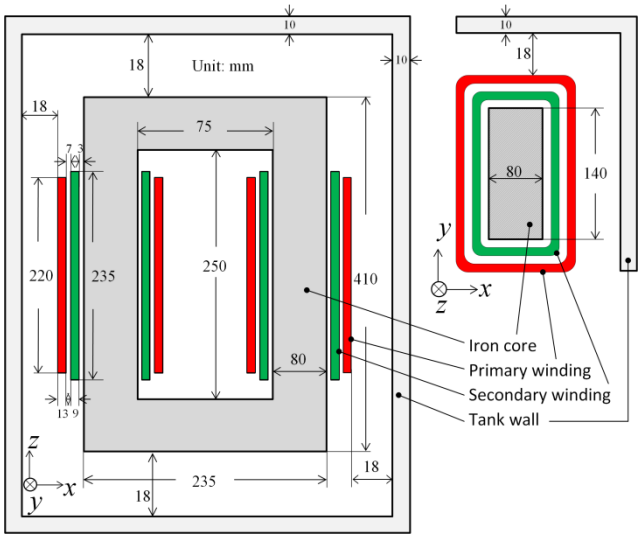

Fig. 4.7: Geometry of the basic transformer model.

The simplified equivalent magnetic circuit considering an appropriate assembly of the magnetic branches by applying the considerations in sub-section 4.2.1, as well as utilizing a symmetry plane corresponds to a half of the actual transformer model as drawn in Fig. 4.8.

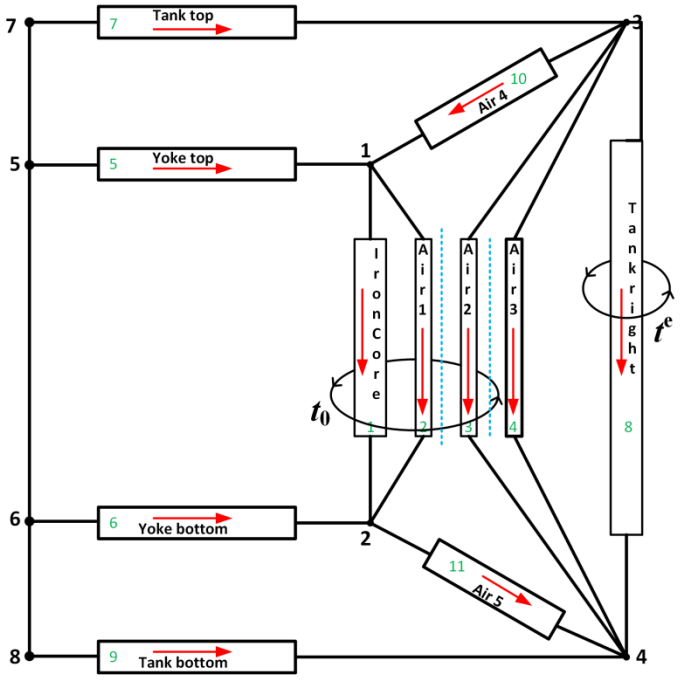

Fig. 4.8: Equivalent magnetic circuit model corresponding to the **T**,ϕ-ϕ-formulation.

In Fig. 4.8, the excitation of the coils and the eddy-current domain are represented by electrical loops denoted as t_0 and t^e. Here t_0 represents the excitation coil including one iron branch and two air branches and t^e includes one iron branch considered for the eddy-currents. The positions of the primary and secondary windings are indicated by dashed, blue lines between the magnetic branches representing the air domains “Air 1”-“Air 3”. The eddy-current domain is only considered in the right tank wall indicated in Fig. 4.8 as magnetic branch number 8. The iron core of the transformer is represented by the magnetic branches 1, 5 and 6. Analogously, the enclosing steel tank is considered by the branches 7, 8 and 9. With respect to the air volume between the iron core and the secondary winding the magnetic branch “Air 1” is introduced and further “Air 2” considering the air volume between the primary and secondary winding, as well as the branch “Air 3” characterizing the air domain between the primary winding and the right tank wall. The magnetic branches “Air 4” and “Air 5” correspond to the air regions flanked by the iron core and the tank at the top and the bottom of the model.

The dimensions of the magnetic branches are derived from the actual transformer model in Fig. 4.7. As for the investigation of the algorithms it is not necessary to generate an exact replication of the transformer, the focus was to map the transformer core and the air branches between the windings in detail and the tank structure and air volumes between the outer winding and the tank as approximated geometries as illustrated in Fig. 4.9 and Fig. 4.10. The dimensions of the magnetic branches in the circuit model are summarized in TABLE 4.1 and TABLE 4.2.

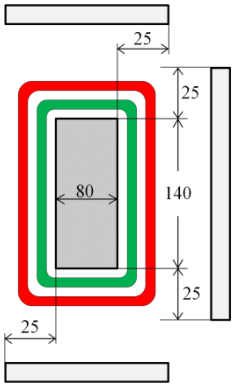

Fig. 4.9: Approximation of the circuit branch length of the right tank wall by considering relevant parts involved by the stray flux.

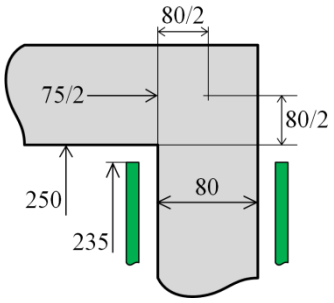

Fig. 4.10: Approximated dimensions for the top and bottom yoke circuit branches with indicated secondary winding marked green.

TABLE 4.1: Definitions of the geometry of the magnetic branches in the circuit model

nB	Labeling	Γ in mm^2	l_B in mm	Constitution
1	Iron core	11200	235	$\Gamma_1 = d_{cw} \cdot d_{cd}; \quad l_B = l_{hs}$
2	Air 1	3525	235	$\Gamma_2 = \left(d_{cw} + 2 \cdot \left(d_{a_1} + \frac{d_{ws}}{2} \right) \right) \cdot \left(d_{cd} + 2 \cdot \left(d_{a_1} + \frac{d_{ws}}{2} \right) \right) - \Gamma_1$
3	Air 2	10296	227.5	$\Gamma_3 = \left(d_{cw} + l_{wa} \right) \cdot \left(d_{cd} + l_{wa} \right) - \sum_{i=1}^{2} \Gamma_i; \quad l_B = \frac{l_{hs} + l_{hp}}{2}$
4	Air 3	15179	220	$\Gamma_4 = d_{ct} \cdot l_{st} - \sum_{i=1}^{3} \Gamma_i; \quad l_B = l_{hp}$
5/6	Yoke top / bottom	11200	125	$\Gamma_{5,6} = \Gamma_1; \quad l_B = \frac{l_y}{2} + \frac{l_{ww} - l_{hs}}{2} + \frac{d_{cw}}{2} + \frac{d_{cw}}{2}$ (see Fig. 4.10)
7/9	Tank top / bottom	150	100	$\Gamma_{7,9} = \delta \cdot d_{ttb}$, where δ is the estimated penetration depth of the induced eddy currents of the iron tank wall see (4.37). $l_B = l_{ttb}$
8	Tank right	450	250	$\Gamma_8 = \delta \cdot l_{sf}; \quad l_B = l_{ww}$
10/ 11	Air 4 Air 5	40500	20	$\Gamma_{10,11} = l_{sf} \cdot d_{ct}; \quad l_B = l_{yt}$

The penetration depth of the induced eddy-currents in the transformer tank wall is approximated as

$$\delta = \sqrt{\frac{2}{\sigma \cdot \mu_0 \cdot \mu_r \cdot f}} = \sqrt{\frac{2}{7.51 \cdot 10^6 \cdot 4 \cdot \pi \cdot 10^{-7} \cdot 5000 \cdot 50}} = 0.00092(\mathrm{m}), \qquad (4.37)$$
$$\delta \approx 0.001(\mathrm{m}) = 1(\mathrm{mm}).$$

TABLE 4.2: Estimated distances of the magnetic branches in the circuit model

Value	Distances in mm	Description
l_{hp}	$l_{hp} = 220$	Primary winding height.
l_{hs}	$l_{hs} = 235$	Secondary winding height.
l_{ww}	$l_{ww} = 250$	Height of the winding window.
l_y	$l_y = 75$	Yoke length.
d_{cw}	$d_{cw} = 80$	Iron core width.
d_{cd}	$d_{cd} = 140$	Iron core depth.
d_{a_1}	$d_{a_1} = 3$	Distance between core and secondary winding.
d_{ws}	$d_{ws} = 9$	Width of secondary winding.
d_{a_2}	$d_{a_2} = 7$	Distance between secondary and primary winding.
d_{wp}	$d_{wp} = 13$	Width of primary winding.
d_{wpt}	$d_{wpt} = 18$	Distance from primary winding to tank wall.
l_{wa}	$l_{wa} = 2 \cdot \left(d_{a_1} + d_{ws} + d_{a_2} + \frac{d_{wp}}{2} \right)$	Width of windings and air including half of the primary winding width.
d_{ct}	$d_{ct} = d_{cd} + 2 \cdot l_{ct}$	Width of core, windings and air to tank wall.
l_{ct}	$l_{ct} = \left(d_{a_1} + d_{ws} + d_{a_2} + d_{wp} + d_{wpt} \right)$	Distance from core to tank wall.
l_{st}	$l_{st} = \frac{l_y}{2} + d_{cw} + l_{ct}$	Distance from symmetry plane to tank wall.
d_{ttb}	$d_{ttb} = 150$	Estimated width of the top and bottom tank chosen as 10 mm larger than the core width.
l_{ttb}	$l_{ttb} = 100$	Approximated sufficient length of the considered top and bottom tank wall.
l_{sf}	$l_{sf} = 2 \cdot \left(25 + d_{cw} + 25 \right) + \left(25 + d_{cd} + 25 \right)$	Estimated length of the stray flux path summing parts of the rear and front tank wall as well as of the right tank wall (see Fig. 4.9).
d_{ct}	$d_{ct} = 90$	Estimated distance for the stray flux path between core and tank.
l_{yt}	$l_{yt} = 20$	Approximated distance form core yoke to tank wall.

For this investigation, the transformer is operating in no-load condition. Hence only the primary winding is energized by a given sinusoidal voltage whereas the secondary winding is open-circuited. The main parameters of the transformer are given in TABLE 4.3.

TABLE 4.3: Main parameters of the transformer

Values		Unit	Windings	
			Primary	Secondary
Voltage	U_{RMS}	V	6600	-
Resistance of the winding	R^w	Ω	21.7	-
Resistance of eddy-current domain	R^e	Ω	0.0006	-
No. of turns of the primary winding	N^w	-	1886	-
No. of turns of eddy-current domain	N^e	-	1	-
Frequency	f	Hz	50	

As illustrated in Fig. 4.8, the magnetic scalar potential has to be computed in the nodes 1-4. Additionally, two unknowns, one for the excitation and one for the eddy-current loop are to be considered when solving the equations as a combined system. Hence the number of equations to be solved in the system is six. Since the nodes 5-8 are on the symmetry plane, the scalar potential is set to zero here and hence these nodes can be eliminated from the computation. Thus, applying the discrete divergence operator results in a matrix of the size [6 x 11], and the discrete gradient operator yields a matrix of the size [11 x 6] as there are 11 magnetic branches to be considered. For this investigation 40 time-steps per period are taken into account. In the harmonic balance method, up to the 11^{th} odd harmonics are considered for this computation. This value has been empirically determined as a good compromise between computational time and sufficient accuracy of the solution.

To take into account the nonlinearity of the core and tank materials, two different *B-H* curves are utilized, where the values of μ are generated for each time step. The material behaviors are illustrated in Fig. 4.11 and Fig. 4.12.

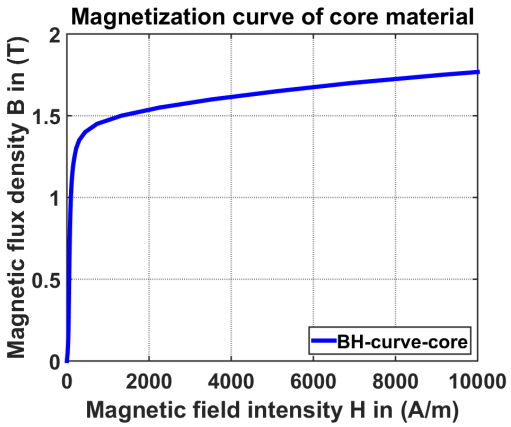

Fig. 4.11: Applied material properties for the transformer core.

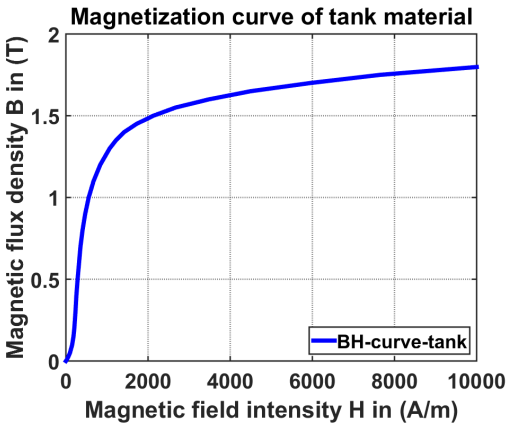

Fig. 4.12: Applied material properties for the transformer tank walls.

The assembly procedures of the separate and combined methods are identical. For the separate solution, the excitation equations are separated from the system matrix as in (4.36). The combined method is straightforward, simply solving (4.34) as a block matrix system in each nonlinear iteration step in the frequency domain.

Treating the voltage source equation separately, the initial step in the 0^{th}-iteration initializes a time independent constant for the permeability and subsequently obtains a solution of the combined equation system (4.34). Based on this result, μ is updated for the 1^{st}-iteration step where (4.35) is solved in the frequency domain by the means of the fixed-point technique to obtain the field quantities utilizing the current values of the previous solution. Thereafter, (4.36) is solved in the time domain with the previous computed field quantities to iteratively determine the new current values. Then, the fixed-point iteration process is started over again with the new current values until a sufficient stopping criterion for convergence is satisfied.

The exit criterion of the nonlinear iteration procedure is usually given by specifying the maximum and average deviation of the material values between the iteration steps [150]. For this investigation, however, the exit criterion is set to a limit of 4000 iterations to achieve fully converged results in order to get a meaningful comparison of the algorithms used.

4.3.1.2 Numerical results

Summarizing the results obtained in no-load condition of the two approaches, the computed magnetization currents and the eddy-currents are first presented to point out that both the separated and the combined method yield equally accurate results.

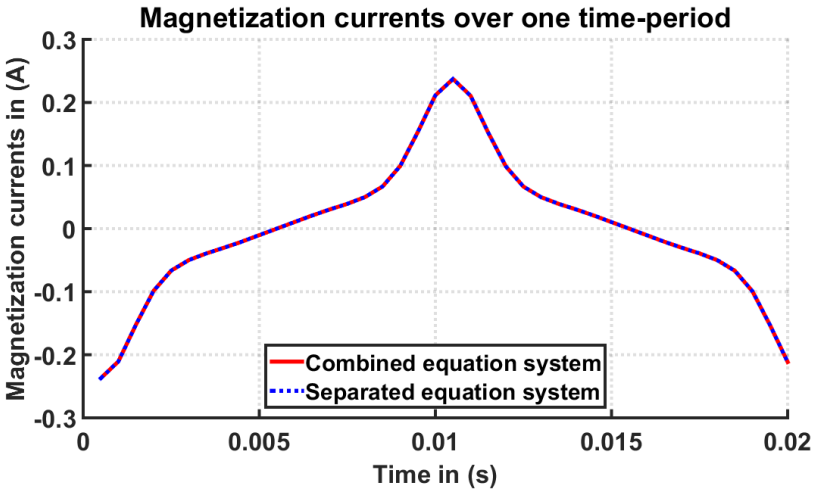

Fig. 4.13: Magnetization current in no-load condition over one time-period.

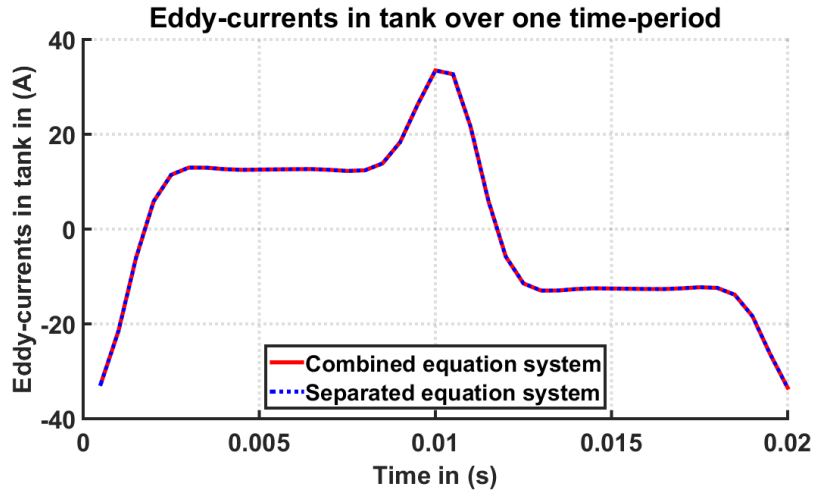

Fig. 4.14: Eddy-currents in the right tank wall in no-load condition over one time-period.

In Fig. 4.13, the magnetization currents computed by both methods with the transformer in no-load condition are plotted over one time-period. In Fig. 4.14 the eddy-currents occurring in the right tank wall are plotted over one time-period.

Comparing these results, it is observable that after a maximum of 4000 nonlinear iteration steps the solutions of the separated and combined approach are the same. Thus one can see that both methods converge to an identical result.

To arrive at a meaningful comparison, the relative error of the current in each nonlinear iteration step in the eddy-current domain, as well as the error of computed eddy-current losses in the right tank wall of both methods are evaluated.

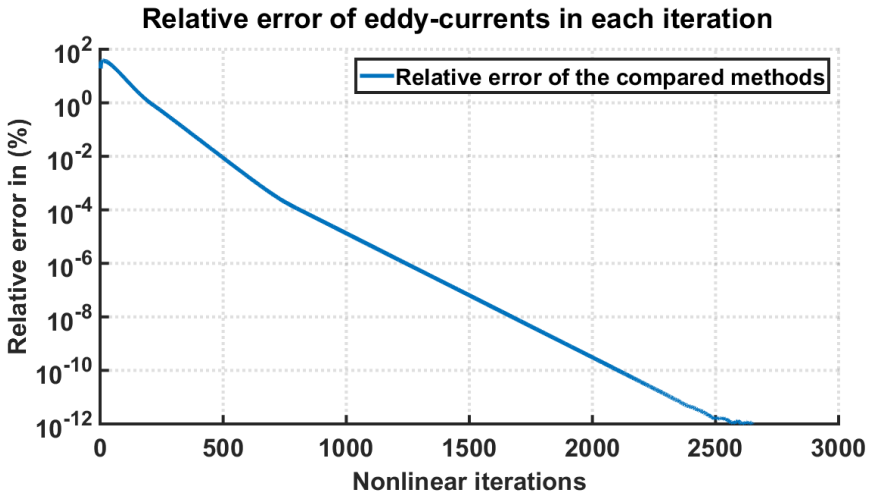

Fig. 4.15: Relative error of the deviation of combined and separated method in each iteration step.

The plotted graph in Fig. 4.15 shows the relative difference of the computed eddy-currents of the two methods in each nonlinear iteration step normalized to the last solution of the combined equation system. As it can be seen, in the first iteration steps the calculated currents are significantly different due to the disparity in the solving approaches. This discrepancy is getting less for a higher number of iterations due to the fact that both methods converge to the same results.

To establish the necessary number of iterations for convergence in the computed quantities in comparison of the two methods, the eddy-current losses in the right tank wall are monitored. This evaluation can be directly associated with the computational time consumption of the applied magnetic-circuit algorithms and hence hereinafter considered in the nonlinear 3D FEM formulation.

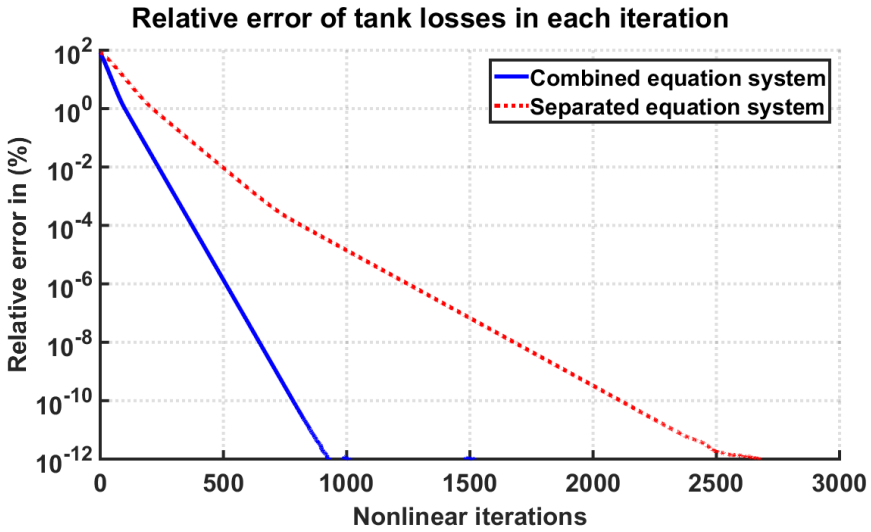

Fig. 4.16: Validation of the relative error of the eddy-current losses in the tank wall in each time-step.

The relative deviation of the eddy-current losses in the steel tank of the transformer are plotted in Fig. 4.16 in each nonlinear iteration step normalized to the last solution of the harmonic balance fixed-point iteration of the combined equation system. It is evident that the combined solution method needs approximately a third as many iterations to converge as the separated method. In practice, an accuracy of 10^{-2} (%) of error, would be acceptable for a meaningful result. With this assumption, the combined method needs about 250 iterations whereas the separated method needs 500 iterations to achieve this error value. Evaluating the condition number of the system matrix of the two algorithms, the condition number for the separated system of 940 and for the combined system the condition number is $2 \cdot 10^8$. The significantly better condition number of the separated equation system leads to the suspicion that, in case of a 3D FEM analysis, the computational costs due to the higher number of iteration steps of the separate method can be counterbalanced by the lower number of CG-iterations needed due to the better condition number. Hence further investigations will be done to assess the elapsed time of both approaches for the 3D FEM case. These results are summarized in chapter 6.

4.3.1.3 Conclusion

The motivation of this initial investigation by means of the magnetic circuit approach has been to compare two solution strategies of the nonlinear equation system. As it has been demonstrated, both methods are qualified for nonlinear computation and, comparing the final solutions, the methods are equally good. The idea of extracting the excitation equations from the system matrix is to arrive at a better conditioned matrix. However, in the combined method, the number of iterations to achieve a sufficiently accurate result is considerably less than in the separated method. As a matter of fact, this reveals a major benefit of using the combined method.

This study provides the basis of considering these formulations in the 3D FEM approach for further investigations (see chapter 6).

4.3.2 Comparison of two different potential formulations with respect to the fixed-point technique applied

The aim of this investigation is to compare the convergence behavior of a Finite-Element-Method approach for solving nonlinear three-dimensional periodic eddy current problems using the **T**,ϕ-ϕ-formulation and the **A**,V-**A**-formulation derived in sub-section 2.2.4. Hence, to facilitate a quick comparison, the formulations are adapted to a nonlinear magnetic circuit problem according to the previous definitions in section 4.2.

The problem setup for this investigation is the same benchmark transformer model as introduced in 4.3.1.1. For a meaningful comparison, two different ways to set up the equation system of the circuit model are considered: One for the analysis involving a magnetic vector potential (corresponding to the **A**,V-formulation see 4.2.2) and a second one using a current vector potential and a magnetic scalar potential (corresponding to the **T**,ϕ-ϕ-formulation see 4.2.1). The focus in developing the nonlinear magnetic circuit model was to derive differential equations as close as possible to the 3D FEM partial differential equations. Both formulations are evaluated using the HBFP. This comparison should point out the benefits of the two formulations. The results of this investigation have been presented at a conference, see [120].

4.3.2.1 Magnetic circuit models

The nonlinear circuit model according to the **T**,ϕ-ϕ-formulation has been derived in the previous sub-section 4.3.1.1 and is illustrated in Fig. 4.8. The equation system is solved in a combined way according to (4.24).

Analogously, based on the considerations in sub-section 4.2.2 the transformer model presented in 4.3.1.1 can be represented by a simplified equivalent nonlinear magnetic circuit model corresponding to the **A**,V–formulation. The circuit model obtained hence is drawn in Fig. 4.17.

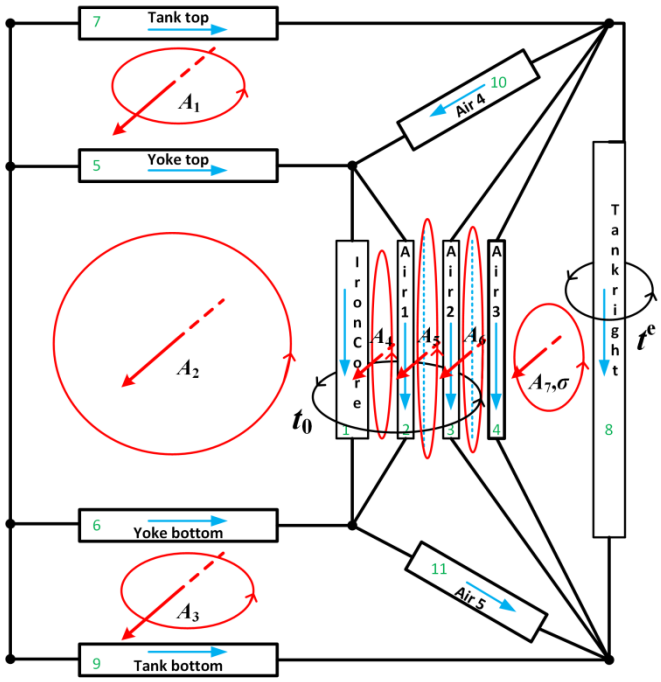

Fig. 4.17: Equivalent magnetic circuit model corresponding to the **A**,V-formulation.

The main difference to the **T**,ϕ-ϕ-formulation is that the field in the magnetic branches is determined by the adjacent cycle basis corresponding to the magnetic vector potentials. The conductivity has to be considered when the cycle basis includes eddy current domains.

Due to symmetry, one half of the transformer has been modeled only, and the coil energized includes the magnetic branches “Air1” and “Air2” and the magnetic branch for the iron core as shown in Fig. 4.17.

The assembly of the equation system using the **A**,V-formulation is identical to the **T**,ϕ-ϕ-formulation described earlier. The discrete curl operators (4.6) and (4.7) are

utilized to create a connection between the branch and the cycle spaces resulting in a matrix of the size [7 x 11] for the first discrete curl operator according to the length of the magnetic branches and [11 x 7] for the second operator summing up the inverse of the cross-sections of the corresponding magnetic branches as illustrated in Fig. 4.17. As the circuit model contains seven basic cycles corresponding to the unknown magnetic vector potentials A, this is also the number of equations to be solved.

The parameters of the magnetic branches are given in TABLE 4.1 and the main parameters of the transformer are given in TABLE 4.3. The exit criterion is again set to a number of 4000 nonlinear iterations to achieve fully converged results. In the HBFP technique, up to 11^{th} odd harmonics are again considered to obtain the computational results.

In accordance with the results of the investigations in 4.3.1, a combined equation system has been used in the present comparison. The equation systems of the simplified magnetic circuit formulations solved by the HBFP technique are (4.24) for the **T**,ϕ-ϕ-formulation and (4.34) for the **A**,V-formulation.

4.3.2.2 Presentation of the results

The computed currents are first investigated and compared. The final results for the magnetization current illustrated in Fig. 4.18 and the eddy-current in the right tank wall drawn in Fig. 4.19 after a maximum of 4000 iterations are the same for the two formulations. Thus one can see that both methods converge to identical results.

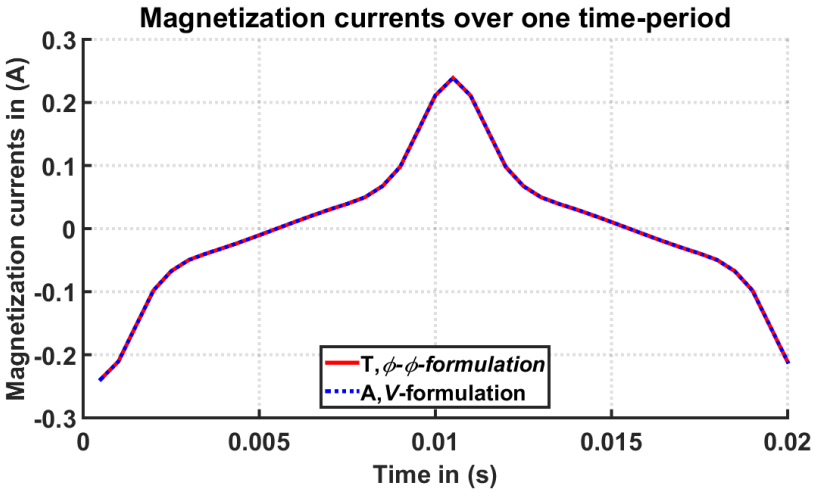

Fig. 4.18: Comparison of the magnetization currents corresponding to the **T**,ϕ-ϕ- and **A**,V-formulation after a maximum of 4000 iterations.

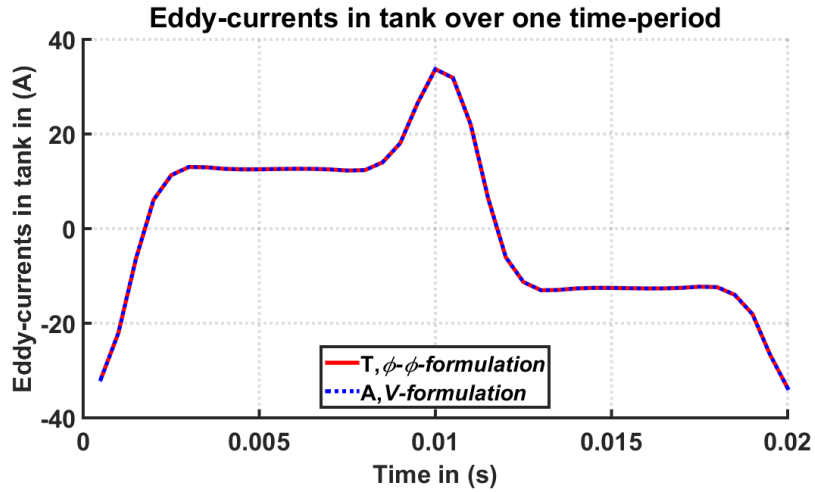

Fig. 4.19: Comparison of the eddy-currents of the **T**,ϕ-ϕ- and **A**,V-formulation after a maximum of 4000 iterations.

The relative deviation normalized to the converged solution of the fixed-point iteration of each formulation of the eddy-current in each iteration step has been investigated and plotted in Fig. 4.20. As one can see, both formulations lead to the same result but it is also obvious that in case of the **T**,ϕ-ϕ-formulation the current converges slower to the final solution than in the **A**,V-formulation.

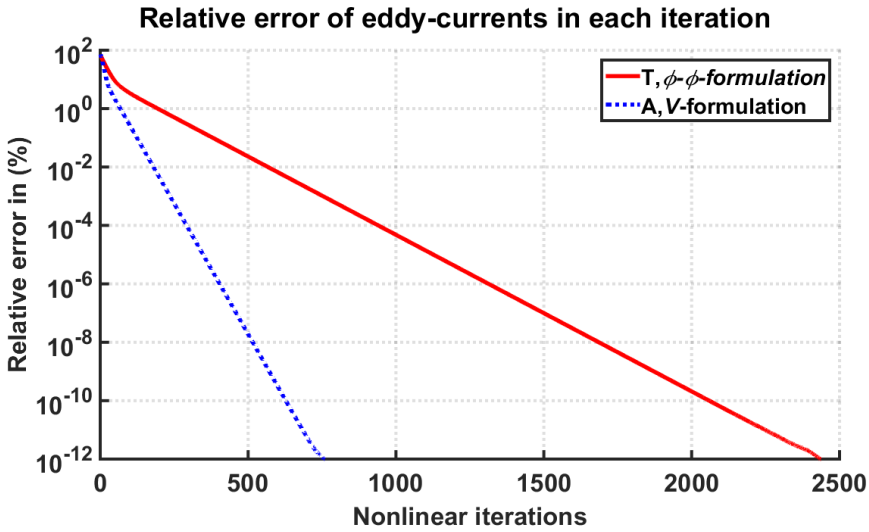

Fig. 4.20: Relative error of the eddy-currents in each iteration step normalized to the last solution of the fixed-point iteration for each formulation.

To compare the number of iterations necessary for convergence of the computed values, the eddy-current losses in the tank are also monitored.

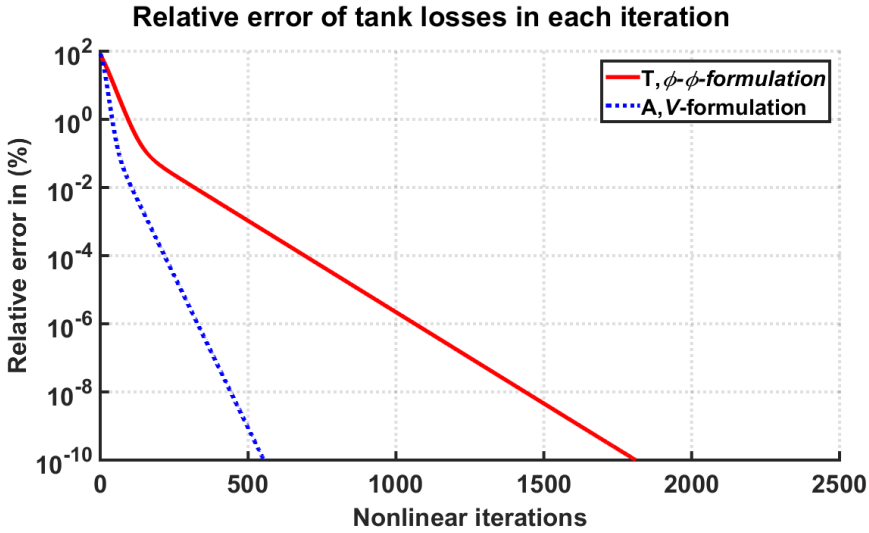

Fig. 4.21: Validation of the relative error of the eddy-current losses in the steel tank in each iteration step normalized to the last solution of the fixed-point iteration for each formulation.

The relative losses caused by the eddy-currents in the tank in each iteration step normalized to the converged solution of the fixed-point iteration are shown in

Fig. 4.21. One can see that the **A**,V-formulation needs approximately a third as many iterations to converge as the **T**,ϕ-ϕ-formulation. At the same time, the conditioning of the system matrix with a condition number of 943 is better for the latter formulation than the condition number of the **A**,V-formulation with a value of 29588. For an industrial problem an error threshold of 10^{-2} (%) would be enough to achieve a meaningful computational result for the losses.

4.3.2.3 Conclusion

The motivation of this study has been to compare two formulations for solving nonlinear periodic eddy-current problems. In fact, the solutions obtained by the methods are in good agreement. It turns out that the **A**,V-formulation as magnetic circuit problem needs less nonlinear iterations for convergence. This is an advantage for computation of magnetic circuit models.

It seems that the **A**,V-formulation has its benefits in the present case. In the 3D case one can expect that the advantage of faster convergence is overruled by the higher number of unknowns compared to using the **T**,ϕ-ϕ-formulation. In this case, the **T**,ϕ-ϕ-formulation is advantageous, since it uses a magnetic scalar potential in non-conducting domains and node based basis functions instead of a magnetic vector potential and edge based basis functions in the **A**,V-formulation resulting in a higher number of unknowns. In 3D real world problems, it is not possible to use direct solvers and, using iterative methods, the computational time is highly affected by the condition number of the equation system resulting from the used formulations. Due to this fact, the **T**,ϕ-ϕ-formulation can lead to a faster convergence in 3D problems.

5 Comparison of different solution techniques

5.1 Introduction

The focus of this investigation is to compare different finite element method approaches applied to nonlinear, 3-dimensional eddy-current problems. Hence, the techniques considered allow achieving steady-state without performing a transient procedure thus a quick field calculation considering higher harmonics is enabled. Such a procedure is highly recommended in case of transformer problems with the system reactance being much larger than the resistance resulting in time constants substantially exceeding the time period. Consequently it is important to avoid time stepping which would cost a lot of computational time [94] which will be pointed out in sub-section 5.3.3.2. With this issue in focus, a comparison of two techniques by solving a typical transformer problem with time-periodic conditions is executed.

An efficient technique known from the literature to solve nonlinear time-periodic eddy current problems is the so-called parallel time periodic finite element method (parallel TPFEM) [107, 109, 160, 178]. It has been proposed by the group of Professor Yasuhito Takahashi from the Doshisha University in Japan. A co-operation between this Japanese group and the Institute of Fundamentals and Theory in Electrical Engineering (IGTE) has made it possible to carry out investigations in order to compare the fixed-point techniques studied in this thesis with the parallel TPFEM.

Especially, the harmonic balance fixed-point technique (HBFP) [149, 156] presented in sub-section 2.3.3.3 and the time periodic fixed-point technique (TPFP) described in sub-section 2.3.3.4 [78, 82, 147] have been investigated in this comparison. Various excitation patterns of the transformer problem defined in sub-section 4.3.1.1 have been defined in order to explore the properties of the different approaches. The resulting problems have been solved by the parallel TPFEM as well as the two fixed-point techniques

Due to the differences in the established solvers of the Japanese and Austrian groups, the formulations used and the element orders are different. However, in order to achieve a meaningful comparison, the discretization has been selected to lead to an approximately same number of unknowns in both cases. The numerical results of the topic under investigation have been published in [115, 117].

5.2 FEM formulations

5.2.1 Parallel time-periodic finite element method (parallel TPFEM method)

The parallel TPFEM method [107, 109, 160, 178] uses the $\mathbf{A},V$-formulation to solve Maxwell's equations. Applying Galerkin techniques to the resulting 2nd order partial differential equations leads to the nonlinear ordinary differential equation system (2.77) derived in sub-section 2.2.4.1.

For simplicity, the backward Euler method is adopted for the time integration scheme applied to (2.77). 1st order finite elements are implemented in this technique since they lead to highly sparse system matrices and a relatively low number of degrees of freedom. Taking into account time periodic conditions for a full- or half-time-period, it is sufficient to discretize a full time-period or a half time-period into n time-steps and, taking advantage of $x_i = \pm x_{i+n}$, the nonlinear equations for a full- or half-period can be written as

$$\begin{cases} \mathbf{S}_{\nu_1}\mathbf{x}_1 + \dfrac{1}{\Delta t}\mathbf{M}_{\sigma_1}\left(\mathbf{x}_1 \mp \mathbf{x}_n\right) = \mathbf{f}_1 \\ \mathbf{S}_{\nu_2}\mathbf{x}_2 + \dfrac{1}{\Delta t}\mathbf{M}_{\sigma_2}\left(\mathbf{x}_2 \mp \mathbf{x}_1\right) = \mathbf{f}_2 \\ \vdots \\ \mathbf{S}_{\nu_n}\mathbf{x}_n + \dfrac{1}{\Delta t}\mathbf{M}_{\sigma_n}\left(\mathbf{x}_n \mp \mathbf{x}_{n-1}\right) = \mathbf{f}_n \end{cases}, \tag{5.1}$$

Δt is the time interval, the subscript indicates the time step, and the signs $-$ and $+$ in (5.1) correspond to either a full time-period condition or a half time-period condition. The large nonlinear system of equations (5.1) is solved by using parallel computing with pure message passing interface (MPI) programming.

Utilizing the Newton-Raphson (NR) method [31, 63, 151, 179] as linearization technique, the equation system can be written as

$$\begin{bmatrix} \tilde{\mathbf{T}}_1 & 0 & \cdots & 0 & \mp\tilde{\mathbf{M}}_n \\ -\tilde{\mathbf{M}}_1 & \tilde{\mathbf{T}}_2 & \cdots & 0 & 0 \\ 0 & -\tilde{\mathbf{M}}_2 & \ddots & \vdots & \vdots \\ \vdots & \vdots & \ddots & \ddots & 0 \\ 0 & 0 & \cdots & -\tilde{\mathbf{M}}_{n-1} & \tilde{\mathbf{T}}_n \end{bmatrix} \begin{Bmatrix} \Delta\mathbf{x}_1 \\ \vdots \\ \Delta\mathbf{x}_n \end{Bmatrix} = \begin{Bmatrix} -\mathbf{G}_1 \\ \vdots \\ -\mathbf{G}_n \end{Bmatrix}, \tag{5.2}$$

$$\tilde{\mathbf{T}}_i = \mathbf{S}_i + \frac{\mathbf{M}_{\sigma_i}}{\Delta t}, \quad \tilde{\mathbf{M}}_i = \frac{\mathbf{M}_{\sigma_i}}{\Delta t}, \quad \mathbf{S}_i = \frac{\partial \mathbf{S}_{\nu_i}\left(\mathbf{x}_i\right)}{\partial \mathbf{x}}, \tag{5.3}$$

where $\Delta\mathbf{x}_i$ is the increment of $\mathbf{x}_i$ and $\mathbf{G}_i$ denotes the residual. To solve the non-symmetric linearized system (5.2), the BiCGstab2 method is applied which has been found to be the fastest among several Krylov subspace methods tested [160] and the localized ILU(0) preconditioning where a preconditioner matrix is generated out of the block diagonal parts of the coefficient matrix [138, 140, 180]. To stabilize the convergence of the inexact NR method, the line search technique based on the minimization of an energy functional is applied [59, 181, 182]. A detailed explanation of the technique for solving (5.2) is given in [107]. Each block in the matrix system (5.2) has as many equations as degrees of freedom dictated by the geometry, hence each BiCGstab2-iteration is executed for all unknowns in space at

each time instant. A major benefit of this method is that the entries in the system matrices are real values.

5.2.2 Harmonic balance fixed-point technique (HBFP method)

In case of the harmonic balance fixed-point method, 2nd order finite elements are implemented (see 2.2.3) as a standard discretization of the FEM solver used. Applying Galerkin techniques to the differential equations resulting from the **T**,ϕ-ϕ-formulation, one obtains a system of nonlinear, ordinary differential equations (2.92) as introduced in sub-section 2.2.4.3.

Using the HBFP technique, the equation system to solve becomes

$$\left[\mathbf{S}_{\rho}+jm\omega\mathbf{M}_{(\mu_{FP})}^{(s)}\right]\mathbf{X}_{m}^{(s+1)}=jm\omega\mathfrak{F}_{m}\left[\mathbf{M}_{(\mu_{FP}-\mu)}^{(s)}\mathbf{x}^{(s)}\right]+\mathfrak{F}_{m}\left[\mathbf{f}_{\rho}\right]+jm\omega\mathfrak{F}_{m}\left[\mathbf{f}_{\mu}^{(s)}\right] \qquad m=1,2,\ldots,N, \tag{5.4}$$

as explicitly derived in sub-section 2.3.3.3. The equation system in (5.4) is decoupled in each nonlinear iteration step and each harmonic solution is solved parallel, a feature leading to a substantial saving of computational time.

5.2.3 Time periodic fixed-point technique (TPFP method)

Alternatively to the HBFP method, the time periodic fixed-point technique is implemented as a solution strategy in the FEM solver used. In these investigations, the TPFP method is applied to the **A**,V-**A**-formulation leading to a nonlinear ordinary differential system of equations. Linearization with the fixed-point technique and executing a discrete Fourier transformation developed in detail in sub-section 2.3.3.4 results in the system to be solved:

$$\left[\mathbf{S}_{\nu_{FP}}^{(s)}+\frac{1}{\Delta t}\mathbf{M}_{\sigma}\left(1-e^{-j2\pi\frac{m}{N}}\right)\right]\hat{\mathbf{x}}_{m}^{(s+1)}=\mathfrak{D}_{m}\left\{\left\langle\mathbf{S}_{\nu_{FP}-\nu}^{(s)}[1]\right\rangle\mathbf{x}^{(s)}[1]+\mathbf{f}[1]\right\} \qquad m=1,2,\ldots,N. \tag{5.5}$$

The system in (5.5) contains symmetric block diagonal matrices and block vectors relating to all time values indicated with the notation [1]. The equations in (5.5) are decoupled in each nonlinear iteration step and each harmonic solution is solved parallel.

For both the HBFP and the TPFP method, the nonlinear iterations for solving the linearized system of equations are terminated once the change of the permeability or the reluctivity within two iteration steps becomes less than a suitable limit. Once these parallel computations are completed, the right hand side of the next iteration can be determined by first computing the time-function and then carrying out the Fourier decompositions. The entries in the system matrices obtained are complex; hence the computational handling is somewhat more expensive than for the parallel TPFEM method.

5.3 Numerical investigations

The above finite element formulations are compared using the basic transformer benchmark problem introduced in sub-section 4.3.1.1.

In a first approach, the parallel TPFEM developed by the Japanese group of Professor Yasuhito Takahashi is compared to the HBFP technique. A major issue of this validation has been the difference in the adopted potential formulations since, at the time of these first investigations, voltage excitation was only implemented for the **T**,ϕ-ϕ-formulation but not for the magnetic vector potential formulation when realizing the TPFP or the HBFP technique. Nevertheless the numerical results are valuable in validating the techniques and therefore discussed in the sub-section 5.3.2.

Second, the parallel TPFEM has been compared to the TPFP technique. To eliminate the significant difference in the formulations used, the TPFP technique was adapted by implementing voltage excitation for the coils in the solver. A remaining disparity between the techniques is in the order of the finite elements: the parallel TPFEM uses 1^{st} order elements and the HBFP as well as the TPFP are utilizing 2^{nd} order elements. To enable a meaningful comparison, a compromise of the finite element meshes has been found. On the one hand, the aim was to construct the finite element meshes as close to each other as possible. On the other hand, the discretization of the problem domain shows some intended differences to guarantee an almost equal number of non-zero entries of the system matrices in the two cases.

5.3.1 Problem definition

The problem of interest is a single phase transformer modelled as a benchmark problem as earlier defined in the magnetic circuit evaluation in 4.3.1.1. By design, the transformer is enclosed by a highly permeable steel tank to ensure a nonlinear eddy- current problem.

Half of the primary and of the secondary winding are wound around each limb with the two halves connected in series. Inspired by practical applications, the transformer primary winding is voltage driven. The voltage excitation of the coils is a sine-function and implemented as described in 2.1.3 according to [85]. Nonlinearity is also taken into account in the highly permeable transformer core. The main parameters of the transformer are given in TABLE 5.1.

TABLE 5.1: Main parameters of the transformer

Values		Unit	Windings	
			Primary	Secondary
Voltage	U_{RMS}	V	6600	-
Resistance of the winding	R	Ω	21.7	0.0163
Load resistance	R_L	Ω	-	2.2
Number of turns	N	-	1886	60
Frequency	f	Hz	50	

The parameters in the table are U_{RMS}, the root mean square value of the excitation voltage, R denotes the resistance of the windings, R_L is the load resistance connected in series to the secondary winding. N represents the number of turns and f is the operating frequency.

Since the excitation of the coils is time dependent, the resulting time varying magnetic field causes eddy-currents in the highly permeable, conductive metal housing and hence additional losses. These eddy-current losses are to be investigated.

The materials of the iron core as well as of the tank walls are characterized by two different magnetization curves. These are shown in Fig. 4.11 and Fig. 4.12 (see page 87).

5.3.2 Parallel TPFEM technique compared to the HBFP method

In the first stage of the comparison, voltage excitation in the FEM solver used was only implemented in conjunction with the **T**,ϕ-ϕ-formulation in combination with the harmonic balance fixed-point technique. This investigation focuses on the performance of the parallel TPFEM technique adopting the Newton-Raphson linearization algorithm in comparison to the HBFP method utilizing the fixed-point linearization scheme. Due to the difference in the potential formulations used, the finite element mesh was modified to provide an almost equal number of unknowns and non-zero entries in the matrix-system. Hence a meaningful comparison has become feasible.

By taking symmetry planes into account, the FEM model can be reduced to an 8^{th} of the actual transformer. The FE-models used are drawn in Fig. 5.1 and Fig. 5.2.

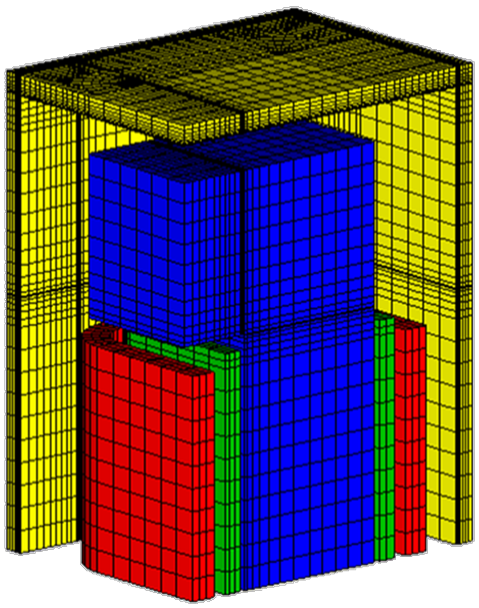

Fig. 5.1: Eighth of the FE transformer model for the parallel TPFEM.

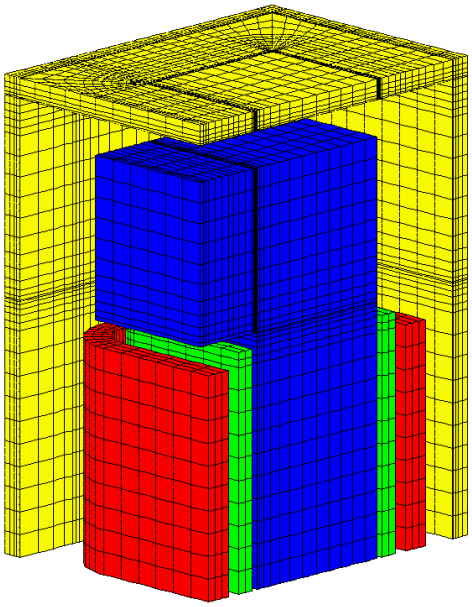

Fig. 5.2: Eighth of the FE transformer model for the HBFP.

With the **A**,V-formulation used, the coils have to be modelled by the finite elements whereas with the **T**,ϕ-ϕ-formulation, the coils need not to be included in the mesh. To be closer to the parallel TPFEM, the mesh was adapted in the HBFP as well to consider the coil geometry.

5.3.2.1 Comparison of the numerical results

The deviations of some quantities, i.e. the relative differences of the results obtained by the two methods have been investigated. Due to voltage excitation, the current of each winding has to be calculated numerically. The primary and the secondary currents of the transformer are practically sinusoidal as illustrated in Fig. 5.3.

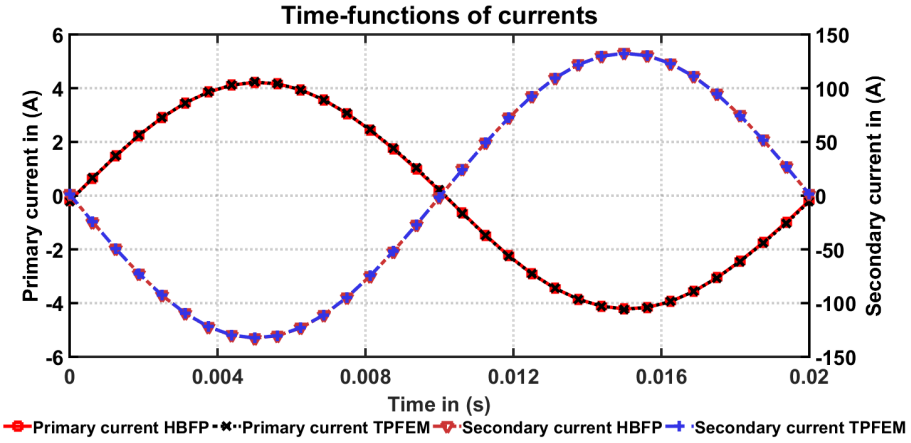

Fig. 5.3: Time-function of the computed currents over one time period.

The deviations normalized by the maximum of the current value of the HBFP method are shown in Fig. 5.4, plotted over one time period in logarithmic scale.

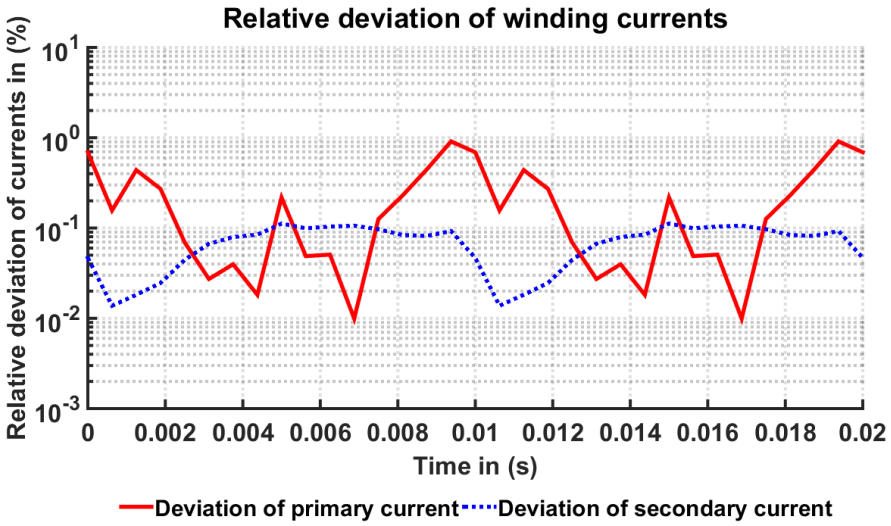

Fig. 5.4: Comparison of the deviation of the computed currents of the coils.

Further on, the losses in the housing of the transformer were investigated. In Fig. 5.5 the deviations of the losses are shown normalized with the maximum loss value of the HBFP method and plotted over one time-period.

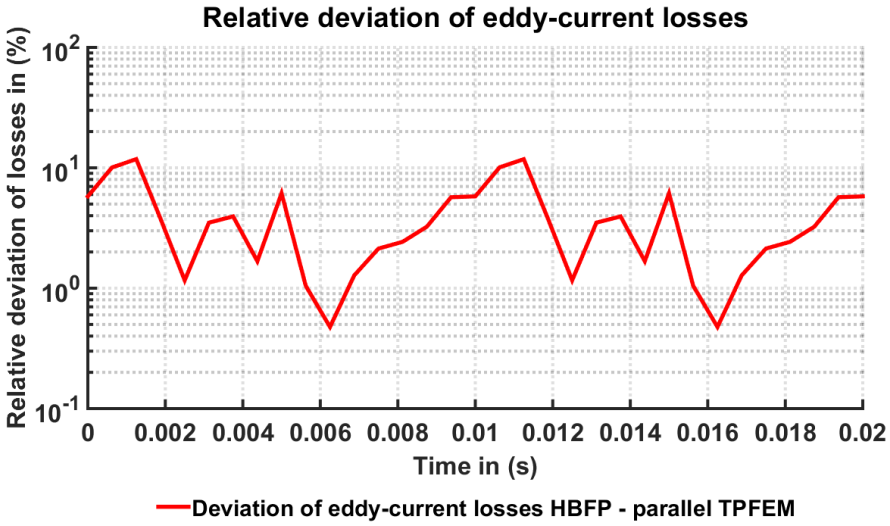

Fig. 5.5: Deviation of the computed eddy-current losses of the formulations in the tank.

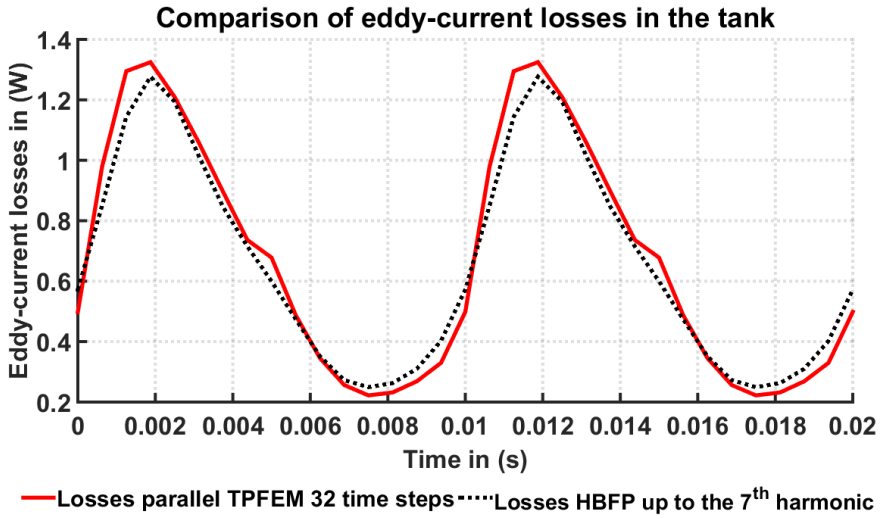

Fig. 5.6: Comparison of the time-functions of the computed eddy-current losses over one time-period.

In Fig. 5.6 the time-functions of the eddy-current losses are plotted over one time period. The effects of the even harmonics in the losses resulting from the odd harmonics in the current are clearly visible in the wave form.

For the computation with TPFEM, 32 time-steps were used for a full time-period T of 0.02 seconds. In case of the HBFP, odd harmonics up to the 7^{th} were considered as sufficiently accurate in this investigation. The deviation is mostly related to the number of time steps used and to the number of harmonics taken into account.

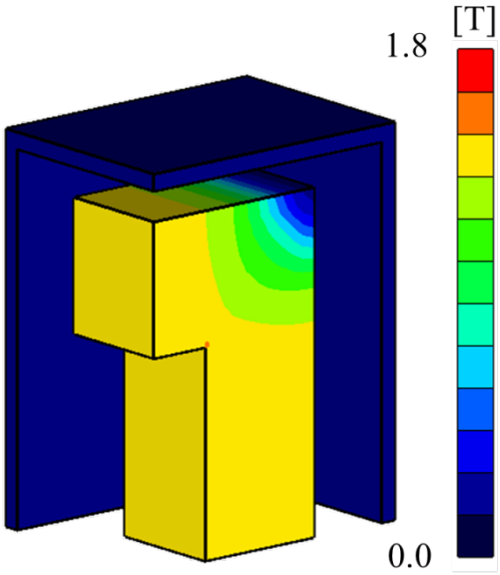

Fig. 5.7: Distribution of the magnetic flux density of the iron core and the tank wall according to the parallel TPFEM at time instance $t=T$.

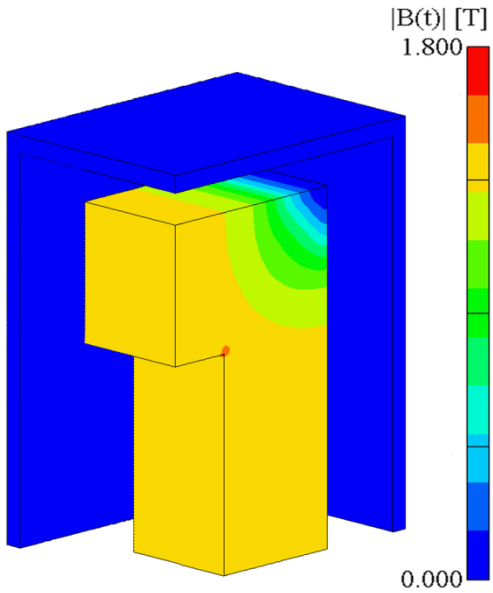

Fig. 5.8: Distribution of the magnetic flux density of the iron core and the tank wall according to the HBFP at time instance $t=T$.

Illustrated in Fig. 5.7 and Fig. 5.8 are the computed results of the magnetic flux density distribution in the iron core and the tank wall at the time $t=T$, where the load currents are almost zero, but due to the sinusoidal voltage excitation in the primary coil the peak flux in the core is present. The distributions obtained by the two methods agree well with the average flux density in the core being 1.388 (T) for the parallel TPFEM and 1.347 (T) according to the HBFP technique.

As a stopping criterion of the parallel TPFEM, the iteration is terminated when the normalized residual of the nonlinear equations is less than 10^{-2}.

As exit criterion for the BiCG, the tolerance was set to 10^{-4}. If the change in the flux density is less than 10^{-2} (T) for each element at every time step, the NR-iteration is terminated in the parallel TPFEM. In case of the HBFP the exit criterion of the

iteration is set to 1 (%) for the mean and 3 (%) for the maximum change of the permeability. The computation has been performed for the HBFP on an Intel Xeon E5-2687W using 16 CPU´s. In case of the TPFEM, the MPI was reduced to a single node that is similar to the system used for the HBFP computation. The computational data are given in TABLE 5.2.

TABLE 5.2: Overview of numerical data

Values	Parallel TPFEM	HBFP
No. of unknowns	350,141 per time-step	324,538 per harmonic
No. of non-zero coefficients	17,968,949 per time-step	19,439,494 per harmonic
No. of BiCGstab2 iterations	6,872	-
No. of BiCG iterations	-	14,898
Gaussian points in FE	3x3x3	3x3x3
Computational time in (s)	2,026.0	2,352.6
No. of nonlinear iterations	20	19
Order of finite elements	1^{st}	2^{nd}
No. of computed time-steps	16	odd harmonics up to the 7^{th}

As it is observable in TABLE 5.2, the number of unknowns and the number of non-zero entries in each time-step in the matrix system are adjusted to be as close as possible. Hence it was possible to provide a suitable basis for a meaningful evaluation of the computational costs of each formulation.

5.3.2.2 Conclusion

In this validation, the solutions obtained by the methods introduced agree well, validating both methods. However, the methods are too different for an exact comparison. For further investigation the methods have been extended by the missing formulations.

5.3.3 Parallel TPFEM technique compared to the TPFP method

To eliminate the major mismatch in the methods of the previous investigations due to the difference in the potential formulations used, the voltage excitation has been implemented in the $\mathbf{A},V$-formulation of the time periodic fixed-point technique introduced in sub-section 2.3.2. However, the discrepancy in the element orders has not been resolved due to the complexity of the solver source code. Nevertheless, to

assess a meaningful comparison, the discretization of the finite elements has been selected to obtain approximately the same number of non-zero entries in both cases.

The problem domain is the same as introduced in sub-section 5.3.1. Due to applying the $\mathbf{A},V$-formulation in case of the TPFP the finite element mesh has been adapted compared to the $\mathbf{T},\phi$-ϕ-formulation used in sub-section 5.3.2. Taking advantage of symmetry planes in assembling the FE models the resulting problem domains are illustrated in Fig. 5.9 and Fig. 5.10, respectively.

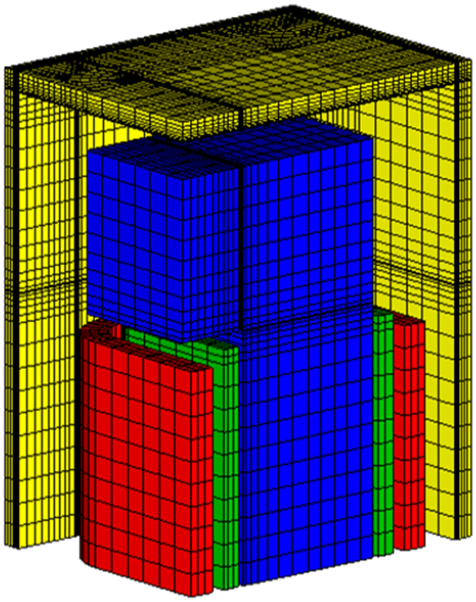

Fig. 5.9: Eighth of the transformer model utilized in the parallel TPFEM method.

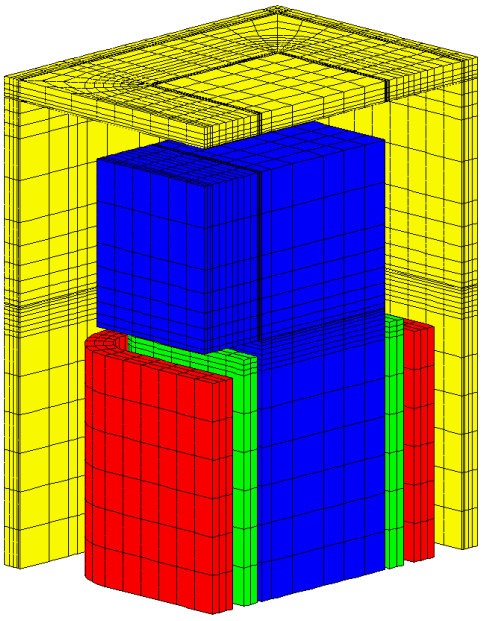

Fig. 5.10: Eighth of the transformer model utilized in the TPFP method.

5.3.3.1 Comparison of the numerical results

The results obtained are evaluated in the same manner as for the previous investigation, i.e. the deviations of some quantities of interests of the different solution algorithms are compared. The deviations of primary and secondary currents are illustrated in Fig. 5.11 where the results are normalized to the maximum current value obtained by the TPFP method and plotted over one time-period in logarithmic scale. The winding currents are practically sinusoidal and drawn in Fig. 5.12 for both methods and for the primary and secondary winding, respectively.

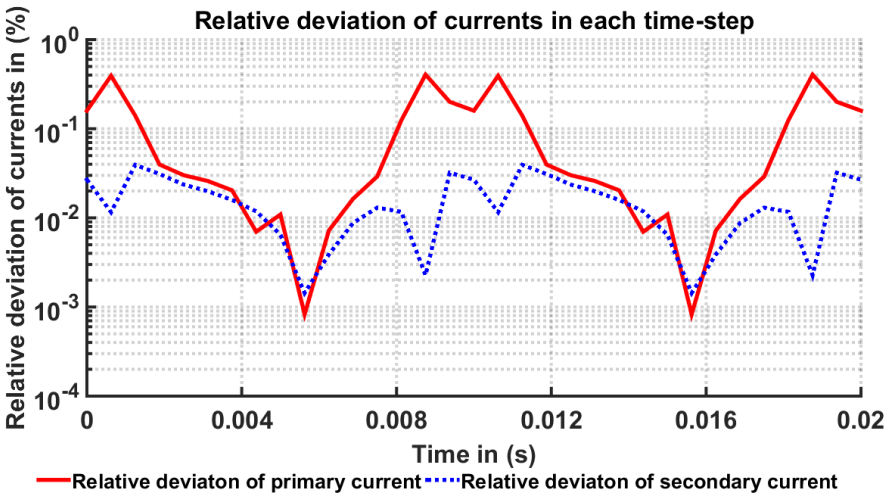

Fig. 5.11: Comparison of the relative deviation of the calculated currents normalized to the maximum current value of the TPFP method.

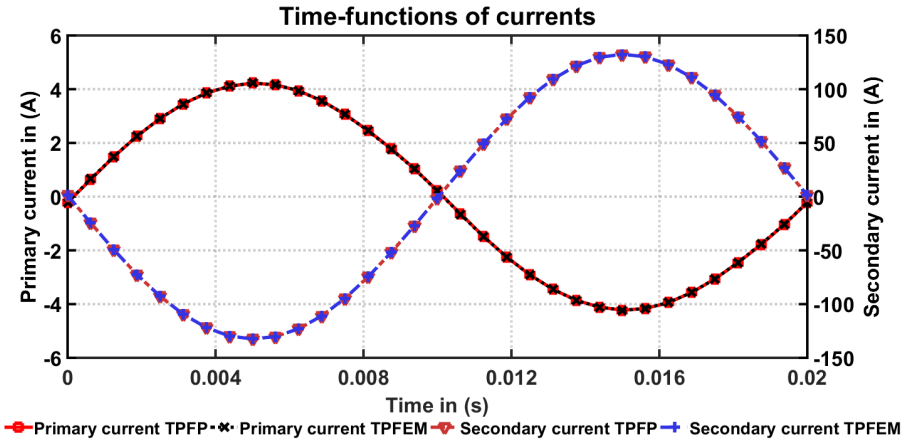

Fig. 5.12: Time-function of the computed currents over one time-period.

Furthermore, the additional losses due to the induced eddy-currents in the housing of the transformer have been investigated. Illustrated in Fig. 5.13 is the relative deviation of the computed losses in the tank normalized to the maximum loss value obtained by the TPFP method and plotted over one time-period.

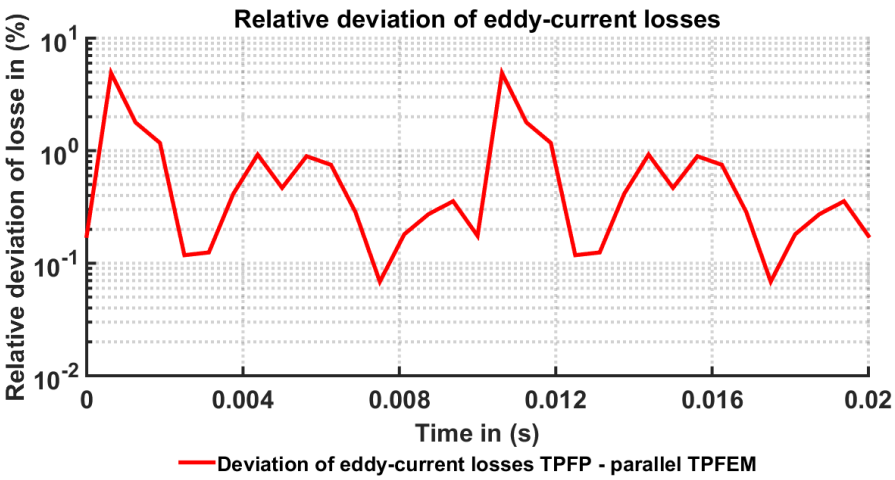

Fig. 5.13: Deviation of the computed eddy-current losses in the tank normalized to the maximum loss value according to the TPFP method.

In Fig. 5.14 the time-functions of the eddy-current losses of both formulations are plotted over one time-period. The effects of the even harmonics in the losses resulting from the odd harmonics in the current are clearly observable in the wave form. A full time-period T of 0.02 seconds was discretized in 32 time-steps in both the parallel TPFEM and the TPFP technique. The computed losses are in a good agreement for the two formulations.

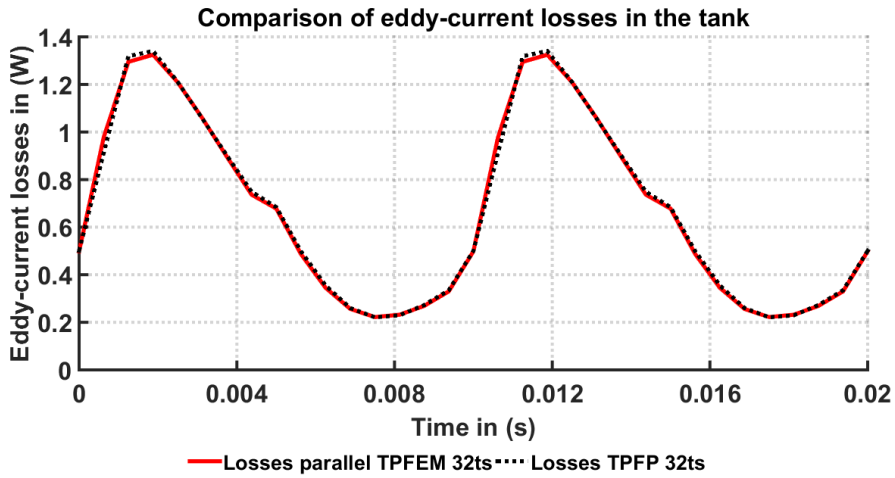

Fig. 5.14: Comparison of the time-functions of the computed eddy-current losses in the tank over one time-period.

Comparing the resulting magnetic flux density distribution, the formulations agree well as shown in Fig. 5.15 and Fig. 5.16. As the maximum core flux density occurs at the time instance $t=T$ due to the excitation voltage being a sine-function, this case has been chosen for illustration. An average flux density of 1.388 (T) has been computed in the core by both the parallel TPFEM and the TPFP, just the color scale is somewhat different.

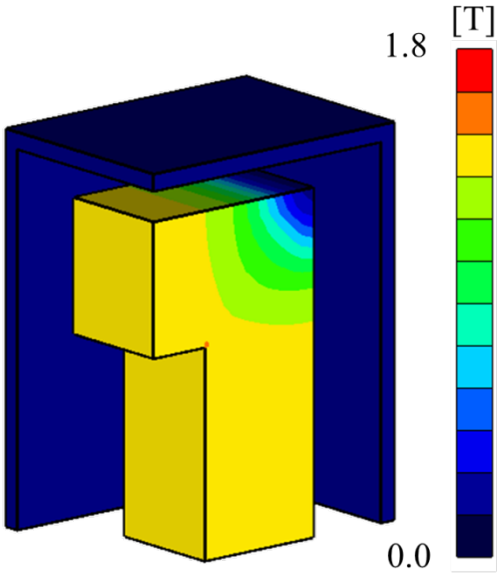

Fig. 5.15: Distribution of the magnetic flux density in the iron core and the tank wall according to the parallel TPFEM method at $t=T$.

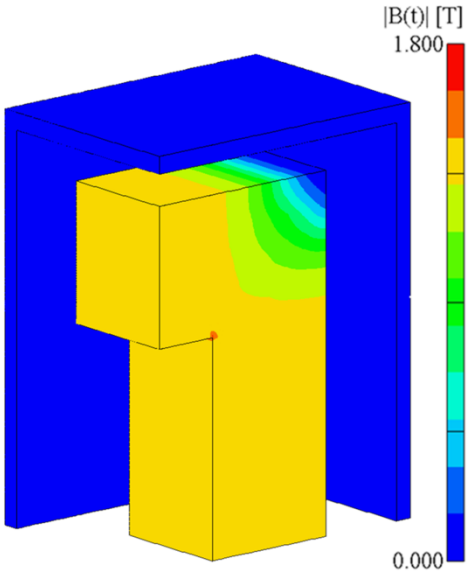

Fig. 5.16: Distribution of the magnetic flux density in the iron core and the tank wall according to the TPFP method at $t=T$.

TABLE 5.3: Overview of numerical results

Values	Parallel TPFEM	TPFP
No. of unknowns	350,141 per time-step	299,602 per discrete harmonic
No. of non-zero coefficients	17,968,949 per time-step	17,997,957 per discrete harmonic
No. of BiCGstab2 iterations	6,872	-
No. of BiCG iterations	-	25,161
Gaussian points in FE	3x3x3	3x3x3
Computational time in (s)	2,026.0	1,925.7
No. of nonlinear iterations	20	14
Order of finite elements	1st	2nd
No. of computed time-steps	16 time-steps	8 discrete harmonics

The computational results are summarized in TABLE 5.3. In case of the parallel TPFEM, the BiCGstab2 iteration method is applied and terminated if the normalized residual of the nonlinear equations is less than a threshold of 10^{-2}. Furthermore, the Newton-Raphson iteration is terminated if the change in the magnetic flux density is less than 10^{-2} (T) for each element at every time-step. Using the TPFP, the exit criterion for the BiCG method, was set to the value of 10^{-6}. The nonlinear iterations of the fixed-point technique are terminated once the mean change of the magnetic permeability is less than 1 (%). The computational hardware was the same as for the investigations in sub-section 5.3.2. The chosen exit criteria of the iteration methods are appropriate to yield a good agreement in the results.

5.3.3.2 Transient approach

To point out the necessity of the formulations introduced to obtain steady-state solutions without performing a step by step approach, a comparison to a transient computation has been carried. The transient computation was carried out for 20 time-periods, and still the results have not converged to the steady-state solution and the elapsed computational time is very high in comparison to the methods introduced. This transient evaluation has been performed by both groups leading to identical results. Hence the solutions obtained by the Austrian-group (IGTE) are presented as a comparison to the time-periodic result of the TPFP only.

TABLE 5.4: Overview of the results of the transient computation

Values	Austrian-group (IGTE)
Number of periods	20
Computational time in (s)	272808.8
Number of calculated time-steps	640

The most significant results of the transient computation are summarized in TABLE 5.4. Taking a look at the computational time of the transient solution in TABLE 5.4 compared to the elapsed time for the time-periodic solutions given in TABLE 5.2 and TABLE 5.3 the advantage of the presented methods is obvious. As mentioned before, after 20 computed time-periods resulting in 640 time-steps the eddy-current losses in the steel tank are still not converged as it can be seen in Fig. 5.17.

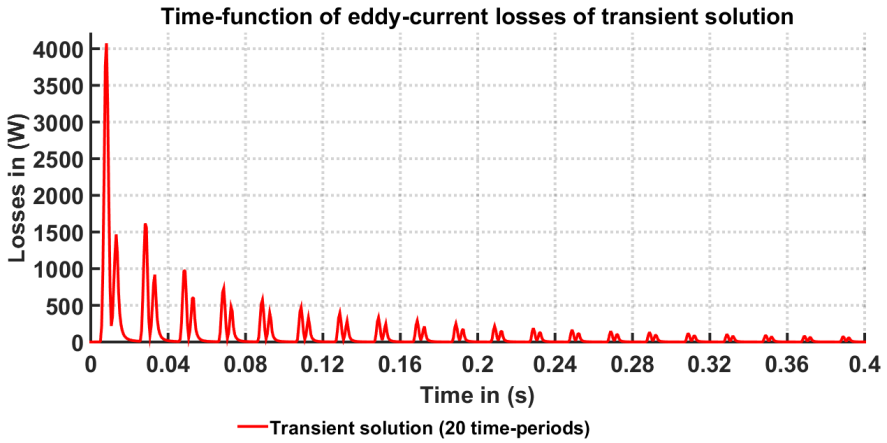

Fig. 5.17: Time-function of transient computed eddy-current losses after 20 time-periods.

To see that after 20 time-periods the losses are still not converged in the transient analysis, a close up of the last two time-periods is plotted in Fig. 5.18. It is clearly visible that the deviation to the time-periodic solution illustrated in Fig. 5.14 is significant. The result of the transient solution is practically not usable. Furthermore, it is observable that the deviation of the maximum loss value from the previous time-period to the next is about 10 (%). Thus it is evident that to achieve steady-state many more time-periods would have to be computed.

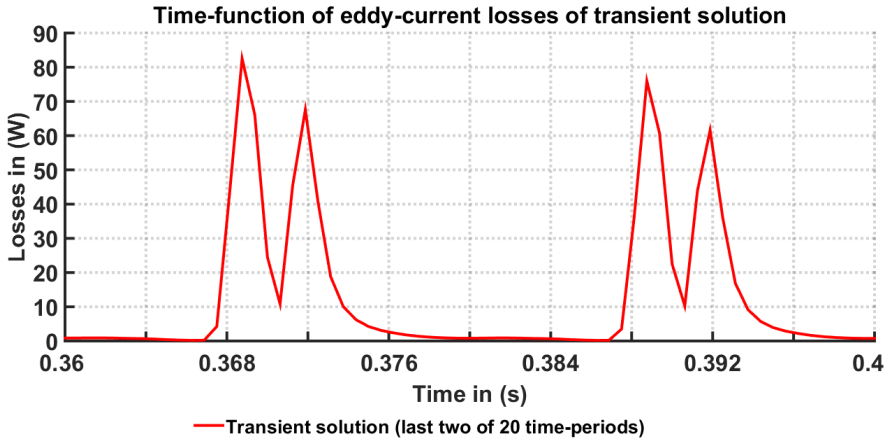

Fig. 5.18: Last two time-periods of the eddy-current losses of the transient analysis.

The time-function of the calculated primary current in the transient analysis is plotted over 20 time-periods in Fig. 5.19. Similarly to the losses, the primary current

is still not fully converged to the steady-state solution and it is clear that the convergence is very slow.

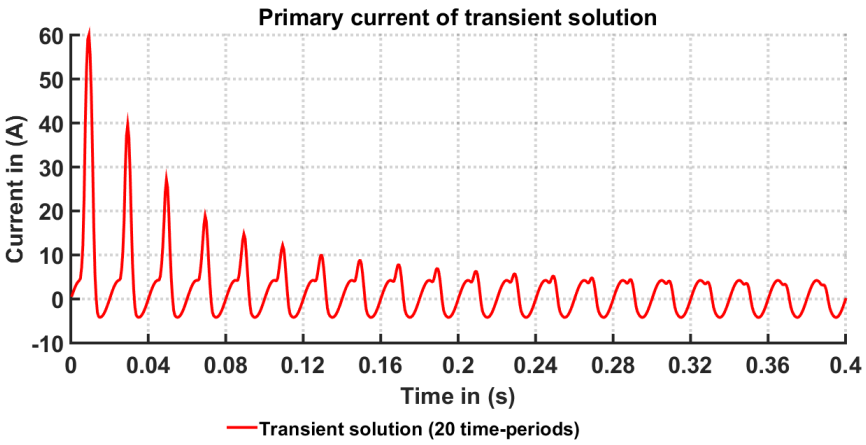

Fig. 5.19: Time-function of the transient primary current over 20 time-periods.

To point out the mismatch in the primary currents when comparing the last computed time-period of the transient solution to the steady-state solution of the TPFP, the current wave forms are illustrated in Fig. 5.20, where it can be seen that the inrush effect of the transient current is still present.

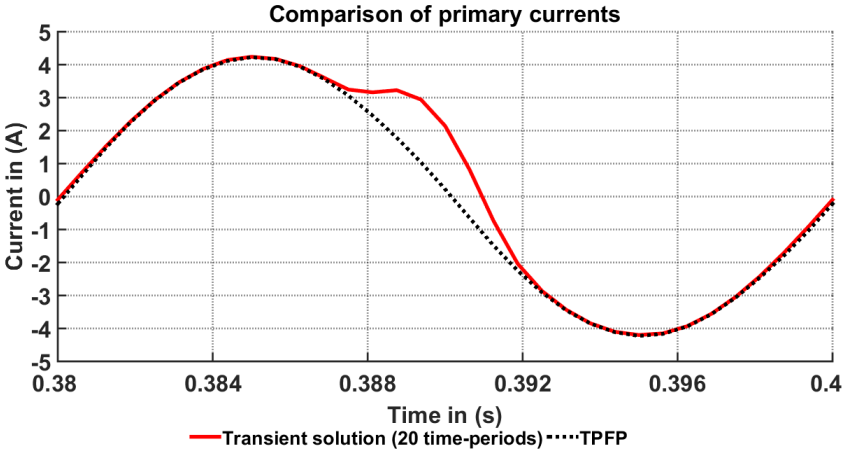

Fig. 5.20: Comparison of the computed primary currents of the last period in the transient solution and the steady-state solution in the TPFP.

Considering the current in the secondary winding in the step by step analysis, the result is drawn in Fig. 5.21. The secondary current has almost fully converged after 20 time-periods representing a sinusoidal behavior as expected.

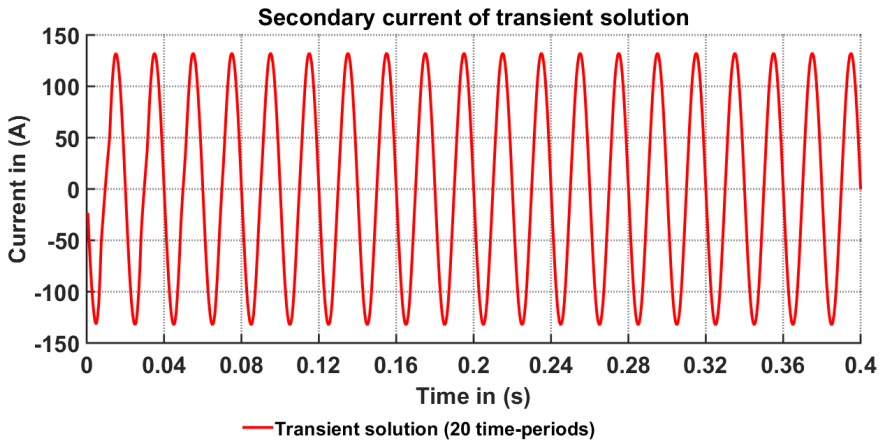

Fig. 5.21: Time-function of the secondary current in the transient case plotted over 20 time-periods.

The last computed time-period of the transient secondary current solution is compared to the steady-state solution of the TPFP and illustrated in Fig. 5.22. The calculated current values are almost matching.

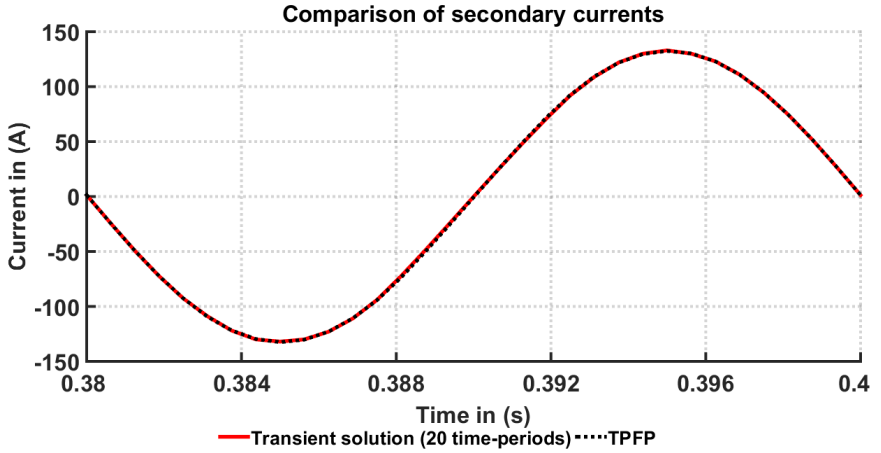

Fig. 5.22: Comparison of the last computed time-period of the computed secondary current in the transient approach and the steady-state solution of the TPFP.

Just as a remark, a transient computation considering 190 time-periods (6080 time-steps) was executed with the result that the primary current has almost

converged to a sinusoidal wave form but the eddy-current losses in the tank are still not converged to the steady-state solution. The elapsed time of this computation consumed 1,192,869 seconds.

5.3.3.3 Conclusion

Summarizing this investigation, the TPFP method utilizing the $\mathbf{A},V$-formulation was adapted by implementing the voltage excitation to obtain a better basis of validation. In case of the parallel TPFEM, all the nonlinear iterations for each time steps for a half-time-period are simultaneously solved. If using one process only, the computational cost is extremely high due to the large system of equations having to be treated. However, the parallel TPFEM can provide large granularity in parallel computing even in 2-D problems. Hence, for the purpose of fully exploiting the efficiency of the TPFEM it is essential to apply parallel computation environment. As nonlinear iteration method, the parallel TPFEM uses the Newton-Raphson (NR) technique. The convergence rate of the NR technique is theoretically superior to the fixed-point approach but, varying the fixed-point parameters, the convergence rate of the TPFP can be increased. A benefit of the parallel TPFEM lies in the entries in the system matrices being real values needing less numerical effort compared to the complex entries in the system matrices of the TPFP. However, the coefficient matrix of the parallel TPFEM is non-symmetric; therefore, a linear iterative solver for non-symmetric coefficient matrices has to be used. This is less efficient than the CG method. The TPFP technique is based on symmetric coefficient matrices hence the classical BiCG can be used. The results acquired by the formulations introduced agree well, validating both techniques for determining periodic steady-state solutions. When comparing the proposed methods to the step by step approach, the benefit is evident. In case of the transient method it would be necessary to consider many more time-periods to achieve convergence to the steady-state solution. The elapsed time of the transient method is not competitive to the time-periodic computations.

6 Comparison of FEM-techniques involving voltage driven coils

In order to be as close as possible to problems arising in practice, the FEM solver utilized has been adapted to enable voltage excitation as discussed in sub-section 2.1.3 for the time-periodic solution strategies HBFP and TPFP introduced in sub-sections 2.3.3.3 and 2.3.3.4. The additional equation to consider the voltage source has been implemented for the potential formulation involving a magnetic vector potential and electric scalar potential (**A**,V-**A**-formulation) as introduced in section 2.2.4.1 with the equation system detailed in (2.78)-(2.84) as well as for the potential formulation utilizing a current vector potential and a magnetic scalar potential (**T**,ϕ-ϕ-formulation) derived in section 2.2.4.3 with the resulting equation system written in (2.93)-(2.101). This chapter focuses on the numerical treatment of the equation systems under consideration of the fixed-point linearization technique. Convergence investigations of the methods have been executed by treating a 3D nonlinear periodic eddy-current problem. Furthermore, a comparison of the different fixed-point techniques using either the magnetic vector potential formulation or the current vector potential formulation has been carried out.

6.1 Treating the voltage equations with the T,ϕ-ϕ-formulation

To validate the results of the previous investigations on a nonlinear magnetic circuit model in sub-section 4.3.1.1, the scope of the research has been extended to a nonlinear 3D FEM problem. The aim of this study is to improve the convergence of techniques based on the finite element method for solving nonlinear 3D periodic eddy-current problems. The type of problem involves voltage-driven coils and the formulation applied uses a current vector potential and a magnetic scalar potential (**T**,ϕ-ϕ-formulation). The best way to treat the additional equations accounting for the voltage excitation is to be established. Two techniques are investigated: the so called "*separate method*" and the "*combined method*". When using FEM, the elapsed time for solving a problem is dominated by the process of iteratively solving the large linear equation systems arising. The motivation for treating the equations of the voltage excitations separately from the rest of the equation system is to achieve a better conditioned system matrix to determine the field quantities and hence a faster convergence of the CG process. However, preliminary investigations on the simplified magnetic circuit model indicate that the number of nonlinear iterations is significantly less using the combined method compared to the separated method. This is to be verified on a 3D transformer model with sinusoidal voltage excitation as formerly introduced in sub-sections 4.3.1.1 and 5.3.1. The outcome of this study has been presented at a conference, see [122].

6.1.1 Formulation of the "combined" and "separated" method

To investigate how to treat the additional equation of the voltage source necessary for the determination of the coil current, the equation system derived in 2.3.3.3 for the HBFP method involving the current vector potential formulation (2.133) is applied. This method includes the voltage equation and can be written according to (2.93)-(2.101) as

$$\left[\begin{bmatrix}\mathbf{A}_\rho & \mathbf{0} & \mathbf{0}\\ \mathbf{0} & \mathbf{0} & \mathbf{0}\\ \mathbf{0} & \mathbf{0} & \mathbf{R}\end{bmatrix} + jm\omega\begin{bmatrix}\mathbf{C}_{\mu_{FP}} & \mathbf{G}_{\mu_{FP}} & \mathbf{g}_{\mu_{FP}}\\ \mathbf{G}^T_{\mu_{FP}} & \mathbf{L}_{\mu_{FP}} & \mathbf{h}_{\mu_{FP}}\\ \mathbf{g}^T_{\mu_{FP}} & \mathbf{h}^T_{\mu_{FP}} & \mathbf{V}_{\mu_{FP}}\end{bmatrix}^{(s)}\right]\begin{bmatrix}\hat{\mathbf{T}}_m\\ \hat{\phi}_m\\ \hat{\mathbf{I}}_m\end{bmatrix}^{(s+1)} = \begin{bmatrix}-jm\omega\mathfrak{F}_m\left(\mathbf{C}_\mu\mathbf{T}_{0h}\right)\\ -jm\omega\mathfrak{F}_m\left(\mathbf{G}^T_\mu\mathbf{T}_{0h}\right)\\ \mathbf{u}-jm\omega\mathfrak{F}_m\left(\mathbf{g}^T_\mu\mathbf{T}_{0h}\right)\end{bmatrix}^{(s)}$$
$$+ jm\omega\mathfrak{F}_m\left\{\begin{bmatrix}\mathbf{C}_{\mu_{FP}-\mu} & \mathbf{G}_{\mu_{FP}-\mu} & \mathbf{g}_{\mu_{FP}-\mu}\\ \mathbf{G}^T_{\mu_{FP}-\mu} & \mathbf{L}_{\mu_{FP}-\mu} & \mathbf{h}_{\mu_{FP}-\mu}\\ \mathbf{g}^T_{\mu_{FP}-\mu} & \mathbf{h}^T_{\mu_{FP}-\mu} & \mathbf{V}_{\mu_{FP}-\mu}\end{bmatrix}^{(s)}\begin{bmatrix}\mathbf{T}\\ \phi\\ \mathbf{i}\end{bmatrix}^{(s)}\right\}, \qquad m=1,2,\ldots,N. \tag{6.1}$$

Solving the equations in this form corresponds to the combined method. An alternative is to solve for the field quantities in the *s*-th iteration step using the currents from the previous iteration as

$$\left[\begin{bmatrix}\mathbf{A}_\rho & \mathbf{0}\\ \mathbf{0} & \mathbf{0}\end{bmatrix} + jm\omega\begin{bmatrix}\mathbf{C}_{\mu_{FP}} & \mathbf{G}_{\mu_{FP}}\\ \mathbf{G}^T_{\mu_{FP}} & \mathbf{L}_{\mu_{FP}}\end{bmatrix}^{(s)}\right]\begin{bmatrix}\hat{\mathbf{T}}_m\\ \hat{\phi}_m\end{bmatrix}^{(s+1)} =$$
$$jm\omega\mathfrak{F}_m\left\{-\begin{bmatrix}\mathbf{C}_\mu\mathbf{T}_{0h}\\ \mathbf{G}^T_\mu\mathbf{T}_{0h}\end{bmatrix}^{(s)} + \begin{bmatrix}\mathbf{C}_{\mu_{FP}-\mu} & \mathbf{G}_{\mu_{FP}-\mu}\\ \mathbf{G}^T_{\mu_{FP}-\mu} & \mathbf{L}_{\mu_{FP}-\mu}\end{bmatrix}^{(s)}\begin{bmatrix}\mathbf{T}\\ \phi\end{bmatrix}^{(s)} - \begin{bmatrix}\mathbf{g}_\mu\mathbf{i}\\ \mathbf{h}_\mu\mathbf{i}\end{bmatrix}^{(s)}\right\}, \tag{6.2}$$

and excluding the excitation equations to update the current separately by solving

$$\left(\mathbf{R}+{}^{d}\!/_{dt}\,\mathbf{V}^{(s)}_\mu\right)\mathbf{i}^{(s+1)} = \mathbf{u}-{}^{d}\!/_{dt}\left(\mathbf{g}^{T,(s)}_\mu\mathbf{T}_{0h}+\mathbf{g}^{T,(s)}_\mu\mathbf{T}^{(s+1)}+\mathbf{h}^{T,(s)}_\mu\phi^{(s+1)}\right). \tag{6.3}$$

Equations (6.2) and (6.3) represent the separated method. The unknowns of the equation systems are approximated values with respect to the finite element method, constituting coefficients of edge based vector basis functions and node based scalar basis functions as defined in sub-section 2.2.1 in (2.65)-(2.71).

6.1.2 Numerical results

To assure a meaningful benchmarking of the formulations and comparison to the previous analysis, the applied problem of interest is not changed. The basic single-phase transformer introduced in 4.3.1.1 as a nonlinear magnetic circuit model as well as in 5.3.1 for the in comparison of different solution strategies is used again

to determine the convergence behavior of the combined and separated algorithms to solve nonlinear, periodic 3D FEM eddy-current problems.

The basic transformer design is drawn in Fig. 4.7 where the highly permeable core and tank materials are represented by two different *B-H* curves illustrated in Fig. 4.11 and Fig. 4.12. Due to symmetry, the finite element model incorporates one eighth of the actual transformer, as shown in Fig. 5.2.

When applying the separate method, the permeability is initialized as a constant independent of time and the combined equation system (6.1) is solved in the 0^{th} iteration step. With the results of this computation, the permeability μ is updated and used in the 1^{st} iteration step. Thereupon, (6.2) is solved using the fixed-point technique to obtain the field quantities in the frequency domain utilizing the current values obtained in the previous iteration step. With the field quantities computed, (6.3) is solved iteratively in the time-domain to determine the new current values. Once the current is computed, the fixed-point iteration process is started again, until an appropriate exit criterion for convergence is satisfied.

Alternatively, applying the combined method, the equation system in (6.1) is solved by means of the fixed-point technique for all harmonics in each nonlinear iteration step in the frequency domain, to acquire the unknown quantities.

TABLE 6.1: Main attributes of the 3D FEM computations

Values		Unit	HBFP **T**,ϕ-ϕ
Order of elements		-	2^{nd}
Gaussian points in FE		-	3x3x3
BiCG iteration exit criterion		-	10^{-7}
Nonlinear iteration exit criterion	avg. deviation of μ	%	0.1
	max. deviation of μ		0.1
Number of harmonics		-	Odd harmonics up to the 15^{th}

The attributes of the FEM computations are summarized in TABLE 6.1. The values of the exit criteria for the nonlinear iterations have been chosen to be extremely low to facilitate a better evaluation of the algorithms. For practical investigations it would not be necessary to define thresholds that low. Usually it is sufficient to set the normalized deviations of the permeability μ between two iteration steps to 1 (%) in average (avg.) and 5 (%) maximum (max.). The considered harmonics have been chosen to include odd harmonics up to the 15^{th}. To guarantee a meaningful comparison, all computations were executed on the same workstation

equipped with an Intel Xeon E5-2687W - 8x3.10 (GHz) with 16 cores / 32 threads. To investigate the combined and separated solving algorithms, different load conditions have been applied to the secondary winding of the transformer. The main transformer parameters for the different load conditions are given in TABLE 6.2. Note, that contrary to the investigations in section 5.3, the resistance of the primary winding has been taken to be 0, since this is a good approximation of the real situation.

TABLE 6.2: Main parameters of the transformer in different load-conditions

Values		Unit	Windings			
			Primary	Secondary		
				No-load	*R*-load	*I*-load
Voltage	U_{RMS}	V	6600	-	-	-
Current	I_{RMS}	A		-	-	95.2
Resistance of the winding	R	Ω	0	-	0.0163	-
Load resistance	R_L	Ω	-	-	2.2	-
Number of turns	N	-	1886	-	60	60
Frequency	f	Hz		50		

6.1.2.1 Transformer in no-load condition

In the first case, only the primary winding is excited with a sinusoidal voltage. The secondary winding is assumed to be open-circuited. The computational results are summarized in TABLE 6.3.

TABLE 6.3: Computational data in no-load condition

Values	Unit	HBFP using **T**,ϕ-ϕ formulation	
		Separated	Combined
Eddy-current losses	mW	116.832	123.304
Number of DOF	-	324,537	324,537
Overall BiCG iterations / average	-	532,595 / 372	435,448 / 260
BiCG it. 1st harm in 1st nlit / last nlit	-	772 / 383	710 / 151
BiCG it. 3rd harm in 1st nlit / last nlit	-	618 / 376	631 / 85
BiCG it. 15th harm in 1st nlit / last nlit	-	336 / 204	442 / 118
Nonlinear iterations (nlit)	-	179	210

As one can see, there is a deviation of about 5 (%) in the eddy-current losses. Comparing the BiCG iterations of the different harmonics indicates that the separated

method has not converged even though the given exit criterion of the material has been reached.

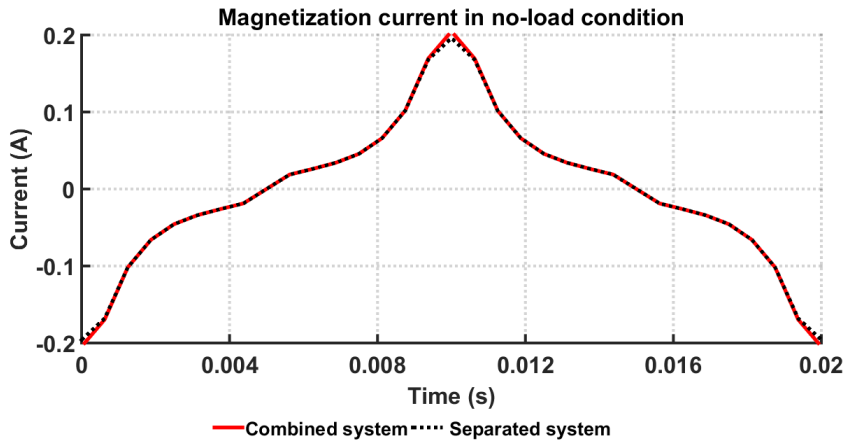

Fig. 6.1: Time-function of the computed magnetization current in no-load condition.

Illustrated in Fig. 6.1 is the computed magnetization current or the transformer. The currents are in good agreement.

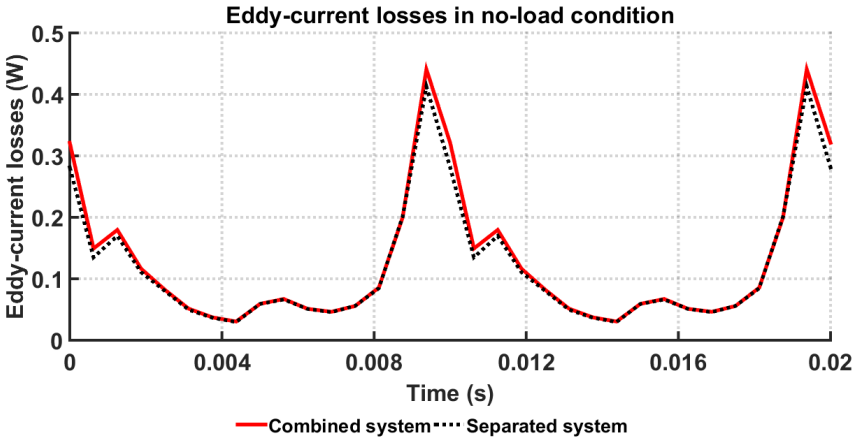

Fig. 6.2: Time-function of the eddy-current losses in the steel tank in no-load condition.

In Fig. 6.2, the time functions of the computed losses in the eddy-current domain are plotted over one time-period.

It can be seen that both methods converge to the same results but the deviation is clearly visible.

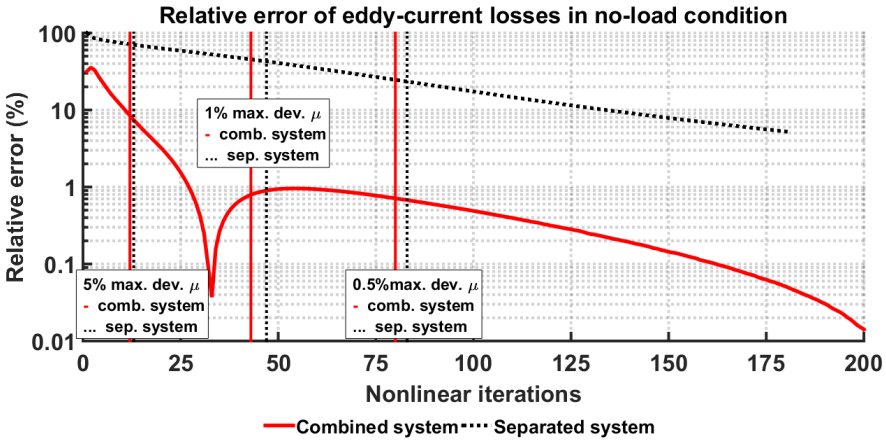

Fig. 6.3: Relative error of the eddy-current losses in no-load condition.

In Fig. 6.3 the computed eddy-current losses are normalized to the last solution of the fixed-point technique and plotted as an error function in each nonlinear iteration step. Also indicated with the vertical lines are the maximum material deviations for the permeability μ of 5 (%), 1 (%) and 0.5 (%) to illustrate the effect of the exit criterion on the error of the losses. In Fig. 6.3 it can be seen that the exit criterion in case of the separated method is not sufficient to obtain a converged result.

6.1.2.2 Transformer in resistive-load condition

In this load condition, a resistive load is attached to the secondary winding additionally to the secondary winding resistance. The results are summarized in TABLE 6.4.

TABLE 6.4: Computational data in resistive-load condition

Values	Unit	HBFP using **T**,ϕ-ϕ formulation	
		Separated	Combined
Eddy-current losses	mW	715.624	715.560
Number of DOF	-	324,538	324,538
Overall BiCG iterations / average	-	618,403 / 119	568,948 / 332
BiCG it. 1st harm in 1st nlit / last nlit	-	772 / 29	836 / 187
BiCG it. 3rd harm in 1st nlit / last nlit	-	473 / 82	710 / 178
BiCG it. 15th harm in 1st nlit / last nlit	-	175 / 69	630 / 123
Nonlinear iterations (nlit)	-	648	214

The computed primary current and secondary current of the transformer are practically sinusoidal as drawn in Fig. 6.4.

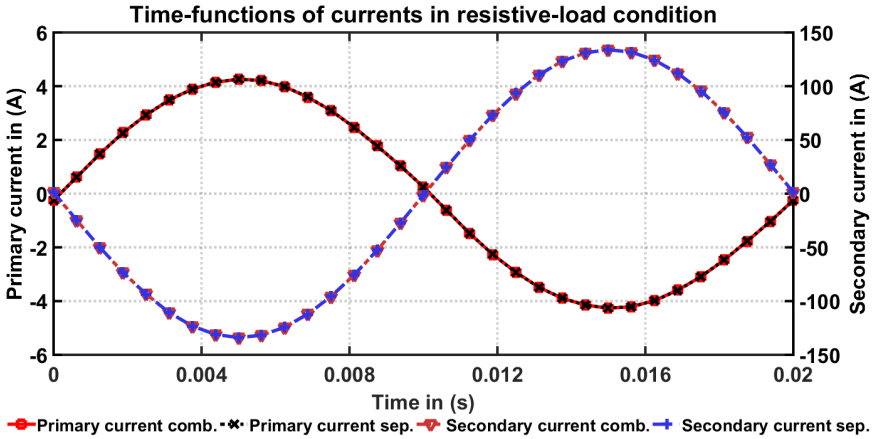

Fig. 6.4: Comparison of the computed current time-functions of both formulations.

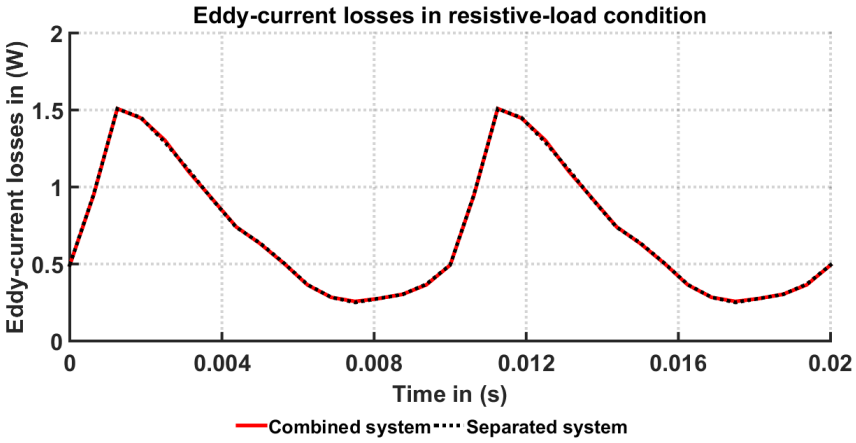

Fig. 6.5: Time-function of eddy-current losses in resistive-load condition.

In Fig. 6.5 the eddy-current losses are plotted over one time period. The effects of the even harmonics in the losses resulting from the odd harmonics in the current are clearly visible in the wave form. The relative error of the eddy-current losses is plotted in Fig. 6.6 with specific-material deviations indicated. The fact that the combined method converges faster to the computed losses with a suitable error is even more dominant than in the previous load scenario.

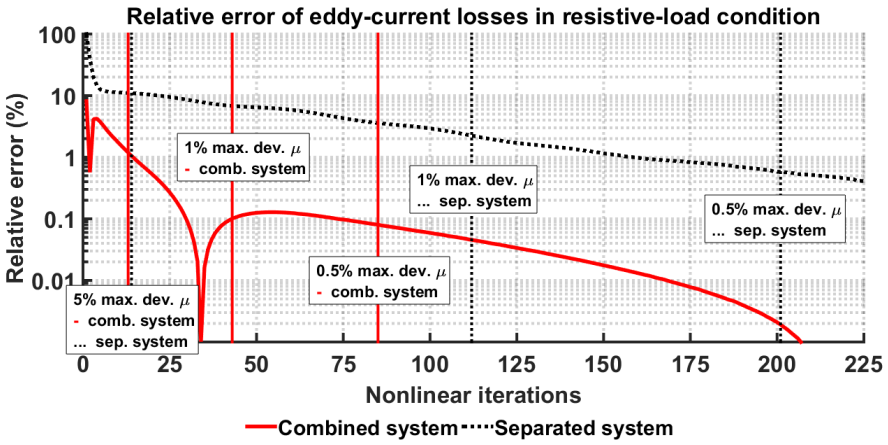

Fig. 6.6: Relative error of eddy-current losses in resistive-load condition.

Comparing the results of the CG iterations in TABLE 6.4 for the first and third harmonics in the first and last nonlinear iteration step, one can see the benefit of the better conditioned system matrix in the separate method but due to the slow nonlinear convergence this advantage is not effective in the overall solution.

6.1.2.3 Transformer in current-load condition

In this load condition, current excitation is applied to the secondary winding with the current derived in the previous simulation with a resistive-load. The results are given in TABLE 6.5.

TABLE 6.5: Computational data in current-load condition

Values	Unit	HBFP using **T**,ϕ-ϕ formulation	
		Separated	Combined
Eddy-current losses	mW	719.968	722.616
Number of DOF	-	324,537	324,537
Overall BiCG iterations / average	-	381,032 / 92	334,728 / 151
BiCG it. 1st harm in 1st nlit / last nlit	-	779 / 3	582 / 24
BiCG it. 3rd harm in 1st nlit / last nlit	-	443 / 3	553 / 78
BiCG it. 15th harm in 1st nlit / last nlit	-	131 / 1	455 / 67
Nonlinear iterations (nlit)	-	519	277

The computed primary currents due to voltage excitation of the primary winding are sinusoidal as expected and are identical for both separated method and combined method. The time-functions are compared in Fig. 6.7.

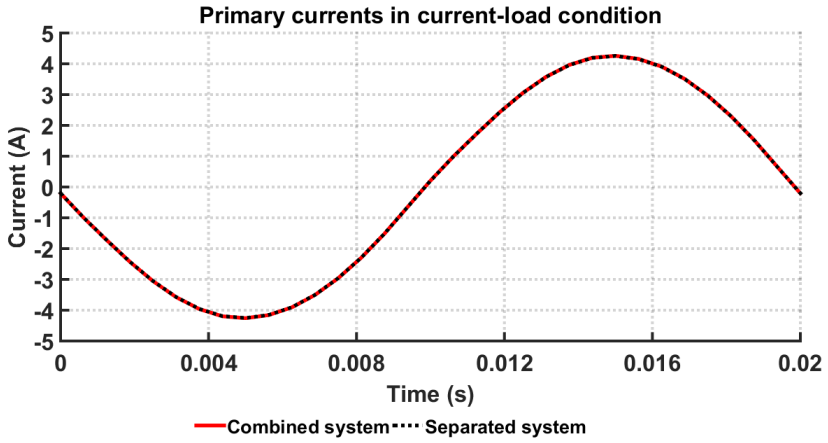

Fig. 6.7: Time-function of the calculated primary currents in current-load condition.

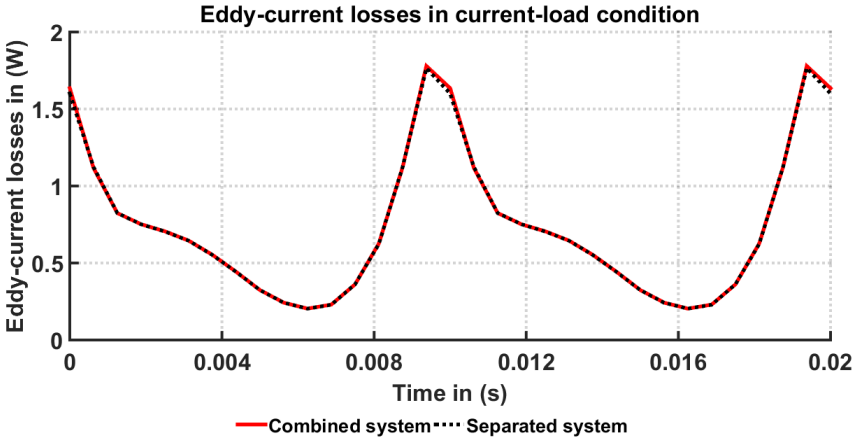

Fig. 6.8: Time-function of eddy-current losses in current-load condition.

In Fig. 6.8 and Fig. 6.9 the same effects as in the previous load condition can be observed. Both methods converge to the same results but the separated method has a very slow convergence of the computed losses.

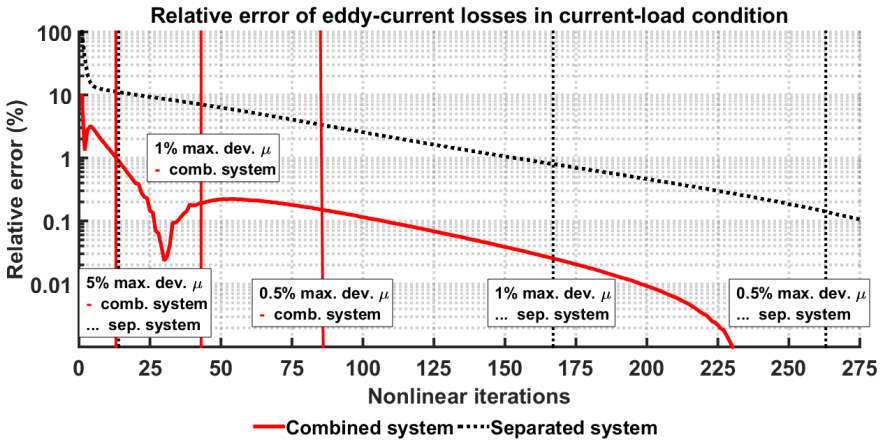

Fig. 6.9: Relative error of eddy-current losses in current-load condition.

6.1.3 Conclusion

Concluding this investigation, both methods converge to the same results. Indeed, the accuracy of the computational results could be increased by considering a higher number of the discrete time-steps in the Fourier transformation. However, increasing the number of discrete time-steps leads to a rise in the computational costs but doesn´t affect the conclusion that, in this application, the combined method shows clear benefits.

Compared to the investigations executed with a magnetic circuit model in sub-section 4.3.1, the better conditioned matrix of the separated method has less impact in the 3D FEM case than expected. However, the number of nonlinear iterations of the two methods shows similar relations as in the circuit investigations.

In conclusion, the combined method will be used as standard solution strategy for further evaluations.

6.2 Varying the FEM-formulations

To explore the benefits of different finite element formulations for solving nonlinear, three-dimensional periodic eddy-current problems with the focus on determining the steady-state solutions only, different potential formulations have been compared when utilizing either the harmonic balance fixed-point (HBFP) technique or the time periodic fixed-point (TPFP) technique.

The comparison involves voltage excited coils and different load conditions applied to the same benchmark model based on the 3D transformer model with sinusoidal excitation used earlier. The formulations for this investigation involve a magnetic vector potential and an electric scalar potential (**A**,V-**A**-formulation – see 2.2.4.1) on the one hand as well as a current vector potential and a magnetic scalar potential (**T**,ϕ-ϕ-formulation – see 2.2.4.3) on the other hand. Various operating conditions of the transformer model are simulated to get a meaningful comparison and to assess which formulation is preferable to be used for a 3D analysis at optimal computational cost. The equation system itself is solved by the combined method in accordance with the outcome of the investigation in section 6.1. The results of this validation have been presented at a conference, see [121].

6.2.1 Treating the voltage excitation in the A,V-A-formulation

Applying the fixed-point technique the approximated FEM equation systems are linearized by introducing the time-independent fixed-point reluctivity ν_{FP} and fixed-point permeability μ_{FP}. Thus one obtains a linear equation system. As presented in sub-section 2.3.3, either the harmonic balance technique utilizing a Fourier transformation to solve the linearized first order differential equation systems in the frequency domain can be applied or, as an alternative, the time-periodic technique by taking advantage of the discrete Fourier transformation for each time instance can be used. The equation systems have been presented in detail in sub-section 2.3.3.3 as (2.132) and (2.133) for the HBFP technique and in 2.3.3.4 (2.141) and (2.142) for the TPFP technique.

Hence the equation system for the HBFP, using the **A**,V-**A**-formulation is

$$\left[\mathbf{S}^{(s)}_{(\nu_{FP})} + jm\omega\mathbf{M}_{\sigma}\right]\mathbf{X}^{(s+1)}_{m} = \mathfrak{F}_{m}\left[\mathbf{S}^{(s)}_{(\nu_{FP}-\nu)}\mathbf{x}^{(s)} + \mathbf{f}\right], \qquad m = 1,2,\ldots,N\,, \tag{6.4}$$

and for the **T**,ϕ-ϕ formulation, we have

$$\left[\mathbf{S}_{\rho} + jm\omega\mathbf{M}^{(s)}_{(\mu_{FP})}\right]\mathbf{X}^{(s+1)}_{m} = jm\omega\mathfrak{F}_{m}\left[\mathbf{M}^{(s)}_{(\mu_{FP}-\mu)}\mathbf{x}^{(s)}\right] + \mathfrak{F}_{m}\left[\mathbf{f}_{\rho}\right] + jm\omega\mathfrak{F}_{m}\left[\mathbf{f}^{(s)}_{\mu}\right] \qquad m = 1,2,\ldots,N. \tag{6.5}$$

The equation system for the TPFP using the **A**,V-**A**-formulation is

$$\left[\mathbf{S}_{\nu_{FP}}^{(s)}+\frac{1}{\Delta t}\mathbf{M}_{\sigma}\left(1-e^{-j2\pi\frac{m}{N}}\right)\right]\hat{\mathbf{x}}_{m}^{(s+1)}=\mathcal{D}_{m}\left\{\left\langle\mathbf{S}_{\nu_{FP}-\nu}^{(s)}[1]\right\rangle\mathbf{x}^{(s)}[1]+\mathbf{f}[1]\right\},\qquad m=1,2,\ldots,N, \tag{6.6}$$

and, for the **T**,ϕ-ϕ-formulation, we have

$$\begin{aligned}\left[\mathbf{S}(\rho)+\frac{1}{\Delta t}\mathbf{M}_{\mu_{FP}}^{(s)}\left(1-e^{-j2\pi\frac{m}{N}}\right)\right]\hat{\mathbf{x}}_{m}^{(s+1)}&=\hat{\mathbf{f}}_{\rho,m}+\frac{1}{\Delta t}\mathcal{D}_{m}\left[\left\langle\mathbf{M}_{\mu_{FP}-\mu}^{(s)}[1]\right\rangle\mathbf{x}^{(s)}[1]\right]\\&+\frac{1}{\Delta t}\mathcal{D}_{m}\left[\mathbf{f}_{\mu}^{(s)}[1]-\left\langle\mathbf{M}_{\mu_{FP}-\mu}^{(s)}[0]\right\rangle\mathbf{x}^{(s)}[0]-\mathbf{f}_{\mu}^{(s)}[0]\right],\qquad m=1,2,\ldots,N.\end{aligned} \tag{6.7}$$

In (6.4)-(6.7), the superscript s denotes the nonlinear iteration step. $\mathcal{F}_m$ represents the m-th harmonic of the Fourier transform and $\mathcal{D}_m$ that of the discrete Fourier transform. Whereas the implementation of the voltage excitation is straightforward for the **T**,ϕ-ϕ-formulation as derived in sub-section 2.1.3 [85], it is not trivial for the **A**,V-**A**-formulation due to the resistance occurring in the stiffness matrix $\mathbf{S}_\nu$ also depending on the nonlinear material properties shown by the presence of ν. Using (2.76)-(2.84), the FEM system of equations is

$$\left[\underbrace{\begin{bmatrix}\mathbf{A}_{\nu}&\mathbf{0}&\mathbf{g}\\\mathbf{0}&\mathbf{0}&\mathbf{0}\\\mathbf{g}^{T}&\mathbf{0}&\mathbf{R}\int_{t}\end{bmatrix}}_{\mathbf{S}_{\nu}}+\frac{d}{dt}\underbrace{\begin{bmatrix}\mathbf{C}_{\sigma}&\mathbf{h}^{T}&\mathbf{0}\\\mathbf{h}&\mathbf{V}&\mathbf{0}\\\mathbf{0}&\mathbf{0}&\mathbf{0}\end{bmatrix}}_{\mathbf{M}_{\sigma}}\right]\underbrace{\begin{bmatrix}\boldsymbol{A}\\\boldsymbol{v}\\\mathbf{i}\end{bmatrix}}_{\mathbf{x}}=\underbrace{\begin{bmatrix}\int_{\Omega}\nabla\times\mathbf{n}_{k}\cdot\mathbf{T}_{0h}d\Omega\\\mathbf{0}\\\int_{t}\mathbf{u}dt\end{bmatrix}}_{\mathbf{f}}. \tag{6.8}$$

In order to represent this system of equations in a more compact form for the upcoming analysis, let us introduce some notations:

$$\underline{\mathbf{A}}_{\nu}=\begin{bmatrix}\mathbf{A}_{\nu}&\mathbf{0}\\\mathbf{0}&\mathbf{0}\end{bmatrix};\quad\underline{\mathbf{g}}=\begin{bmatrix}\mathbf{g}\\\mathbf{0}\end{bmatrix};\quad\underline{\mathbf{g}}^{T}=\begin{bmatrix}\mathbf{g}^{T}&\mathbf{0}\end{bmatrix};\quad\underline{\mathbf{M}}_{\sigma}=\begin{bmatrix}\mathbf{C}_{\sigma}&\mathbf{h}^{T}\\\mathbf{h}&\mathbf{V}\end{bmatrix}, \tag{6.9}$$

$$\underline{\mathbf{x}} = \begin{bmatrix} \boldsymbol{A} \\ \boldsymbol{v} \end{bmatrix}; \quad \mathbf{b} = \begin{bmatrix} \int_{\Omega} \nabla \times \mathbf{n}_k \cdot \mathbf{T}_{0h} d\Omega \\ \mathbf{0} \end{bmatrix}. \tag{6.10}$$

Transforming the system into the frequency domain, (6.8) can be hence rewritten as

$$\begin{bmatrix} \underline{\mathbf{A}}_{\nu} + jm\omega\underline{\mathbf{M}}_{\sigma} & \underline{\mathbf{g}} \\ \underline{\mathbf{g}}^{T} & \dfrac{1}{jm\omega}\mathbf{R} \end{bmatrix} \begin{bmatrix} \underline{\mathbf{x}} \\ \mathbf{i} \end{bmatrix} = \begin{bmatrix} \mathbf{b} \\ \dfrac{1}{jm\omega}\mathbf{u} \end{bmatrix}, \tag{6.11}$$

and applying the fixed-point technique yields

$$\begin{bmatrix} \underline{\mathbf{A}}^{(s)}_{\nu_{FP}} + jm\omega\underline{\mathbf{M}}_{\sigma} & \underline{\mathbf{g}} \\ \underline{\mathbf{g}}^{T} & \dfrac{1}{jm\omega}\mathbf{R} \end{bmatrix} \begin{bmatrix} \underline{\mathbf{x}} \\ \mathbf{i} \end{bmatrix}^{(s+1)} = \begin{bmatrix} \underline{\mathbf{A}}^{(s)}_{\nu_{FP}-\nu} + jm\omega\underline{\mathbf{M}}_{\sigma} & \underline{\mathbf{g}} \\ \underline{\mathbf{g}}^{T} & \dfrac{1}{jm\omega}\mathbf{R} \end{bmatrix} \begin{bmatrix} \underline{\mathbf{x}} \\ \mathbf{i} \end{bmatrix}^{(s)} + \begin{bmatrix} \mathbf{b} \\ \dfrac{1}{jm\omega}\mathbf{u} \end{bmatrix}^{(s)}. \tag{6.12}$$

For a transformer computation in no-load condition, it is practically reasonable to assume that the resistance of the excited winding is zero as it is usually significantly lower than its reactance. Thus, the entries in the main diagonal of the stiffness matrix containing the resistance values become zero and the matrix of the equation system to be solved by the CG iteration method is no more positive definite. Hence, the system of equations (6.12) results in a saddle-point problem not solvable by commonly applied CG iterations. Even if very low values for the resistance are considered, convergence may become very poor. In order to obtain a solvable system of equations independent of the resistive characteristics given, a Schur-complement method [138, 161] is adopted. In the system (6.11) the following notations are introduced:

$$\begin{aligned} \mathbf{D} &= \underline{\mathbf{A}}_\nu + jm\omega\underline{\mathbf{M}}_\sigma, \qquad \mathbf{a} = \mathbf{b}, \qquad \mathbf{B} = \underline{\mathbf{g}}, \\ \mathbf{P} &= \frac{1}{jm\omega}\mathbf{R}, \qquad \mathbf{c} = \frac{1}{jm\omega}\mathbf{u}, \end{aligned} \tag{6.13}$$

where the sizes of the matrices are $\mathbf{D} \in \mathbb{C}^{n\times n}$, $\mathbf{P} \in \mathbb{C}^{k\times k}$, $\mathbf{B} \in \mathbb{C}^{n\times k}$, $\mathbf{a} \in \mathbb{C}^{n\times 1}$, $\mathbf{c} \in \mathbb{C}^{k\times 1}$ and $n = N_e + N_n$ and $k = N_c$. With these notations, the equations have the form:

$$\begin{bmatrix} \mathbf{D} & \mathbf{B} \\ \mathbf{B}^T & \mathbf{P} \end{bmatrix} \begin{bmatrix} \underline{\mathbf{x}} \\ \mathbf{i} \end{bmatrix} = \begin{bmatrix} \mathbf{a} \\ \mathbf{c} \end{bmatrix}. \tag{6.14}$$

Eliminating **x** from the current equations leads to

$$\begin{bmatrix} \mathbf{I} & \mathbf{D}^{-1}\mathbf{B} \\ \mathbf{0} & \underbrace{\mathbf{P} - \mathbf{B}^T\mathbf{D}^{-1}\mathbf{B}}_{\mathbf{Q}} \end{bmatrix} \begin{bmatrix} \underline{\mathbf{x}} \\ \mathbf{i} \end{bmatrix} = \begin{bmatrix} \mathbf{D}^{-1}\mathbf{a} \\ \mathbf{c} - \mathbf{B}^T\mathbf{D}^{-1}\mathbf{a} \end{bmatrix} \tag{6.15}$$

where **I** is the identity matrix and in the second row in (6.15), **Q** is the Schur-complement of the block **D**. Eliminating **i** results in

$$\begin{bmatrix} \mathbf{I} & \mathbf{D}^{-1}\mathbf{B} \\ \mathbf{0} & \mathbf{I} \end{bmatrix} \begin{bmatrix} \underline{\mathbf{x}} \\ \mathbf{i} \end{bmatrix} = \begin{bmatrix} \mathbf{D}^{-1}\mathbf{a} \\ \mathbf{Q}^{-1}\left(\mathbf{c} - \mathbf{B}^T\mathbf{D}^{-1}\mathbf{a}\right) \end{bmatrix}, \tag{6.16}$$

$$\begin{bmatrix} \mathbf{I} & \mathbf{0} \\ \mathbf{0} & \mathbf{I} \end{bmatrix} \begin{bmatrix} \underline{\mathbf{x}} \\ \mathbf{i} \end{bmatrix} = \begin{bmatrix} \mathbf{D}^{-1}\mathbf{a} - \mathbf{D}^{-1}\mathbf{B}\mathbf{Q}^{-1}\left(\mathbf{c} - \mathbf{B}^T\mathbf{D}^{-1}\mathbf{a}\right) \\ \mathbf{Q}^{-1}\left(\mathbf{c} - \mathbf{B}^T\mathbf{D}^{-1}\mathbf{a}\right) \end{bmatrix} \tag{6.17}$$

$\mathbf{D}, \mathbf{P}, \mathbf{B}$ are covariance matrices [138, 161]. In (6.17) it is necessary to solve for

$$\mathbf{D}^{-1}\mathbf{a} \text{ and } \mathbf{D}^{-1}\mathbf{B}. \tag{6.18}$$

Obviously, **D** is a sparse system matrix (see (6.13)), hence it should not be inverted, but the equations are solved with $N_c + 1$ right hand sides corresponding to **a** and the columns of **B**.

Thus, this procedure leads to multiple right hand sides (RHS) when at least one coil with voltage excitation is involved. For each voltage-excited coil present, there will be a RHS to be considered in each CG iteration step. The system of equations is hence solved at an increase of the computational effort. This Schur-complement approach has been implemented in the solver for both, the HBFP technique and the TPFP technique when utilizing the **A**,V-**A**-formulation.

6.2.2 Numerical results

A comparison of the formulations applied to various load conditions of the transformer has been carried out. The common attributes of the 3D FEM model are summarized in TABLE 6.6.

TABLE 6.6: Attributes of the 3D FEM model

Values		Unit	TPFP	HBFP
			T,ϕ-ϕ / **A**,V-**A**	
Order of elements		-	2^{nd}	
Gaussian points in FE		-	3x3x3	
BiCG iteration exit criterion		-	10^{-7}	
Nonlinear iteration exit criterion	avg. deviation of μ / ν	%	0.1	
	max. deviation of μ / ν		0.1	
Number of computed time-steps		-	100	Odd harmonics up to the 50^{th}

The values chosen to terminate the nonlinear iteration process by an average (avg.) deviation and a maximum (max.) deviation of the permeability μ or the reluctivity ν between two iteration steps have been chosen extremely low. This is in order to ensure a sound evaluation of the formulations examined. For reasons of accuracy of the computed results the number of discrete time-steps as well as the number of considered harmonics has been increased in comparison to previous investigations in order to avoid deviations due to the different formulations used.

In order to provide meaningful comparisons for the no-load condition of the transformer, the computations were performed on the same computational unit with the specifications given in TABLE 6.7. The results for resistive-load and current-load were obtained on a different unit with the specifications given in TABLE 6.8.

TABLE 6.7: Specifications of the computational unit for the computations under no-load condition

Values	Unit	Computational unit
CPU architecture	-	Intel Xeon E5-2680V2
Number of CPU´s and clocking	-/GHz	10 / 2.8
Cores / Threads	-	20 / 40
RAM	GB	256
Operating system	-	Windows Server 2008 R2 x64

TABLE 6.8: Specifications of the computational unit for the computations under resistive- and current-load conditions

Values	Unit	Computational unit
CPU architecture	-	Intel Xeon X5690
Number of CPU´s and clocking	-/GHz	6 / 3.46
Cores / Threads	-	12 / 24
RAM	GB	192
Operating system	-	Windows Server 2008 R2 x64

6.2.2.1 Transformer in no-load condition

In the first case to be investigated, the transformer is operating in no-load condition, i.e. the primary winding is excited with a sinusoidal voltage and the secondary winding is assumed to be open-circuited. The main transformer parameters in this load condition are given in TABLE 6.2 (see page 121).

With the parameters and the geometrical data given in Fig. 4.7 (see page 82), the resulting maximum magnetic flux density B in the core is 1.4 (T) as illustrated in Fig. 6.10. According to the B-H curve in Fig. 4.11 (see page 87), the core material is saturated.

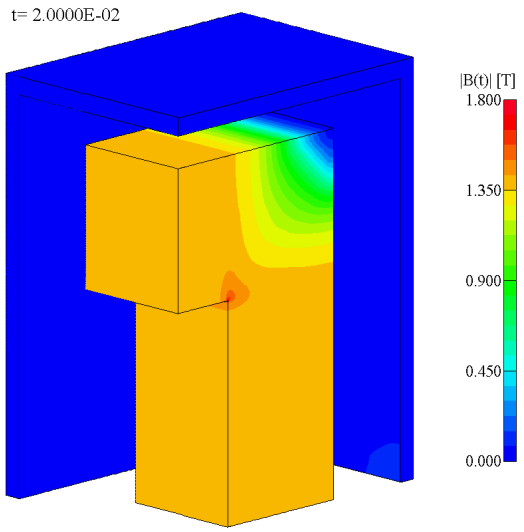

Fig. 6.10: Saturation of the core in no-load condition at time-instance $t=T$ with an maximum core flux density of 1.4 (T).

The nonlinear material behavior is also clearly reflected in the magnetization current shown in Fig. 6.11. The computational results are summarized in TABLE 6.9. It can be seen that the eddy-current losses obtained by the formulations agree well.

TABLE 6.9: Computational data in no-load condition

Values	Unit	TPFP		HBFP	
		A,V-**A**	**T**,ϕ-ϕ	**A**,V-**A**	**T**,ϕ-ϕ
Eddy-current losses	mW	117.94	117.74	123.04	122.84
No. of DOF	-	643,829	324,537	643,829	324,537
No. of non-zero coefficients	-	36,652,598	19,400,211	36,652,598	19,400,211
BiCG iterations	-	2,573,184	1,095,642	3,898,424	1,556,260
BiCG / nonlinear it.	-	27,969	3,445	38,598	4,498
Nonlinear iterations	-	92	318	101	346
Computational time	s	248,428.7	133,930.1	285,634.0	154,918.2

The marginal deviations between the losses obtained by the TPFP and the HBFP technique are due to the time shift caused by the differential scheme and the way the transformation into the frequency domain is executed by the Fourier transformation in the HBFP and the discrete Fourier transformation by the TPFP.

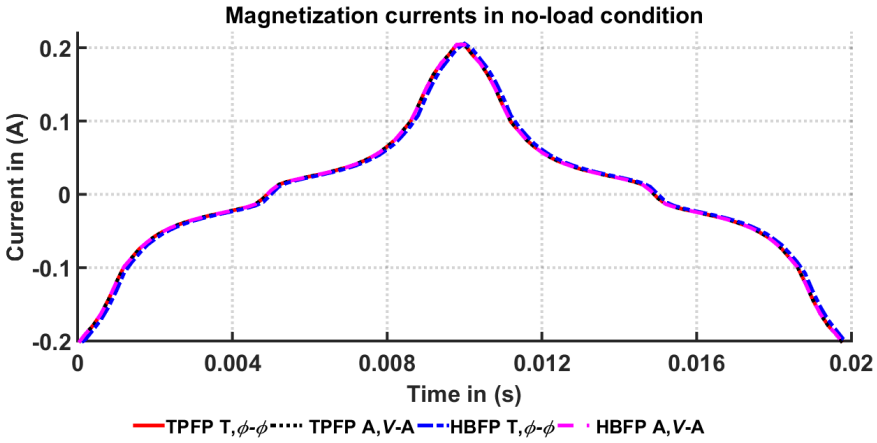

Fig. 6.11: Magnetization currents in no-load condition.

In Fig. 6.12, the eddy-current losses are plotted over one time-period. The resulting wave forms agree well. Due to the better time-discretization and higher number of harmonics considered in case of the HBFP, the deviation in the time-functions of the losses is marginal compared to the results obtained in previous investigations when validating the parallel TPFEM and the HBFP technique illustrated in Fig. 5.6 (see page 105).

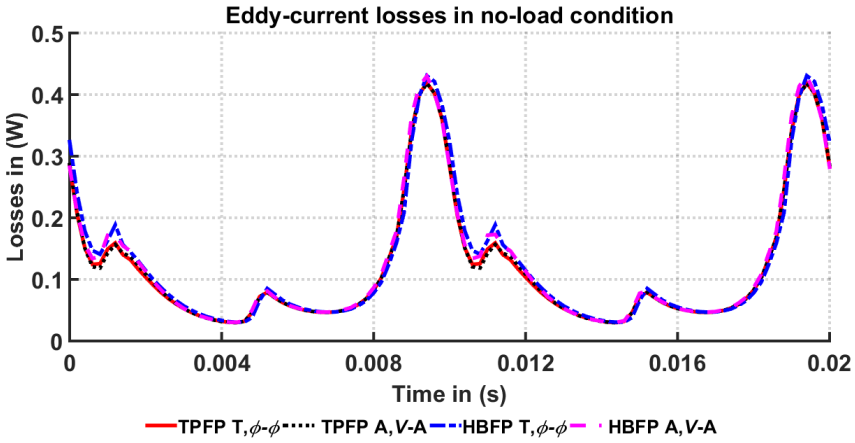

Fig. 6.12: Eddy-current losses in the transformer tank wall in no-load condition over one time-period.

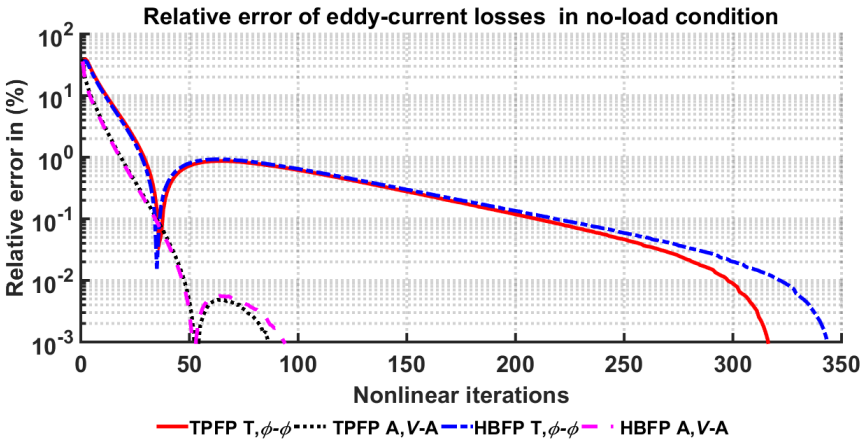

Fig. 6.13: Relative error of eddy-current losses in each iteration-step normalized to the last solution of the fixed-point iteration in no-load condition.

The relative error of the eddy-current losses in the tank normalized to the last solution of the fixed-point iteration is plotted in Fig. 6.13. The **A**,V-**A**-formulation needs less nonlinear iterations for convergence than the **T**,ϕ-ϕ-formulation regardless of the solution technique selected. This has also been pointed out in sub-section 4.3.2 devoted to the harmonic balance investigations on a simplified magnetic circuit model. Nevertheless, as seen in TABLE 6.9, the computational time using the **A**,V-**A**-formulation is considerably higher than that of the **T**,ϕ-ϕ-formulation. The main reason is the higher number of DOF due to using a magnetic vector potential in the air domain. A further point is that solving the equation system with zero resistivity resulting in multiple right hand sides needs more computational effort with the **A**,V-**A**-formulation than when applying the **T**,ϕ-ϕ-formulation.

6.2.2.2 Transformer in resistive-load condition

In this load condition, a resistive load attached to the secondary winding is considered additionally to the winding resistance. The primary winding is again excited with a sinusoidal voltage. The transformer parameters are again given in TABLE 6.2 (see page 121).

The computational results in resistive-load condition are summarized in TABLE 6.10.

TABLE 6.10: Computational data in resistive-load condition

Values	Unit	TPFP		HBFP	
		A,V-**A**	**T**,ϕ-ϕ	**A**,V-**A**	**T**,ϕ-ϕ
Eddy-current losses	mW	709.08	708.08	716.224	715.328
No. of DOF	-	643,830	324,538	643,830	324,538
No. of non-zero coefficients	-	36,652,598	19,439,494	36,652,598	19,439,494
BiCG iterations	-	3,935,040	1,496,468	5,761,739	2,227,609
BiCG / nonlinear it.		42,312	4,401	58,793	6,346
Nonlinear iterations	-	93	340	98	351
Computational time	s	582,308.2	213,978.4	833,399.9	260,582.2

Comparing the computational data in resistive-load condition to the data obtained in no-load condition similar conclusions can be drawn. The computed eddy-current losses agree well in the formulations applied. The number of non-zero coefficients in the equation system of the **A**,V-**A**-formulation is considerably higher than for the **T**,ϕ-ϕ-formulation. The number of degrees of freedom is increased by one due to the secondary winding considered now.

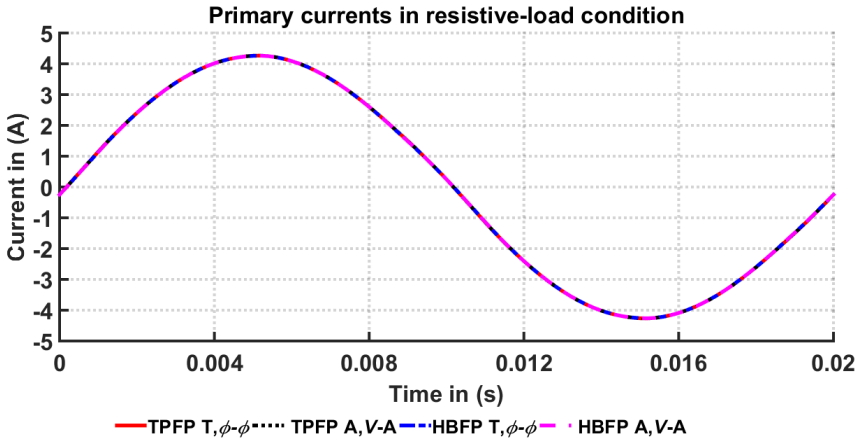

Fig. 6.14: Computed currents in the primary winding of the transformer in resistive-load condition.

Fig. 6.14 and Fig. 6.15 show that the numerically calculated currents of the primary and secondary winding are practically sinusoidal and overlapping regardless of the solution algorithm chosen.

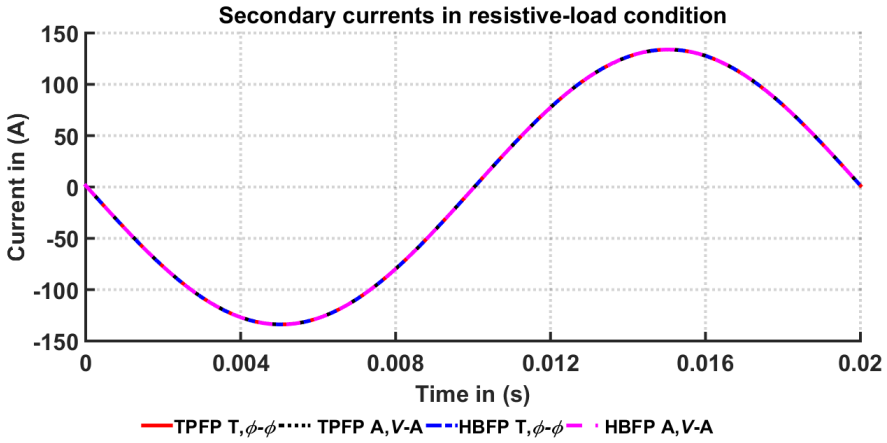

Fig. 6.15: Computed currents in the secondary winding of the transformer in resistive-load condition.

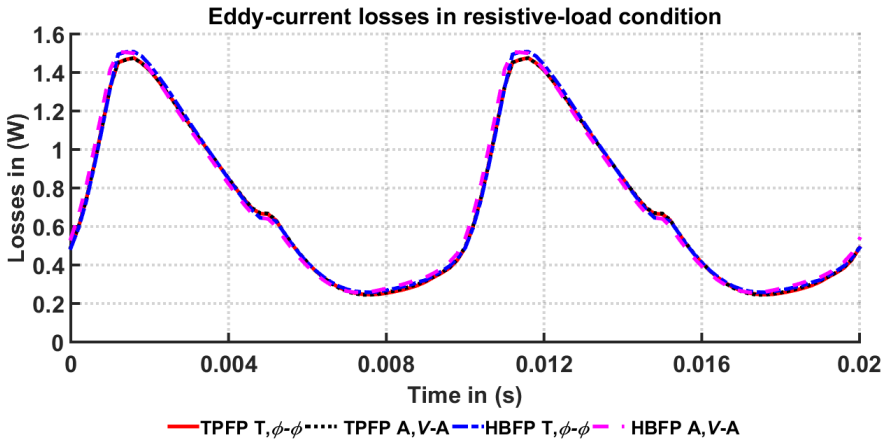

Fig. 6.16: Eddy-current losses in the tank of the transformer in resistive-load condition.

In Fig. 6.16, the time-function of the eddy-current losses occurring in the transformer tank in resistive-load condition are plotted over one time-period.

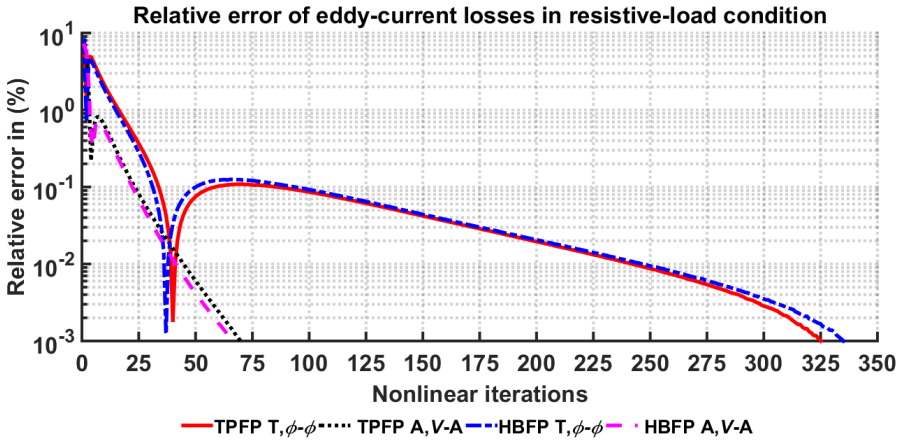

Fig. 6.17: Relative error of eddy-current losses in each iteration-step normalized to the last solution of the fixed-point iteration in resistive-load condition.

Illustrated in Fig. 6.17 is the relative error of the eddy-current losses in the tank in each iteration-step normalized to the last solution of the fixed-point iteration. Again it is clearly visible that the **A**,V-**A**-formulation needs less nonlinear iterations to obtain convergence than the **T**,ϕ-ϕ-formulation but comparing the computational time the **T**,ϕ-ϕ-formulation is advantageous.

6.2.2.3 Transformer in current-load condition

To conclude these investigations, the last load condition of the transformer is the so called current-load condition where the secondary winding is energized with an impressed current, given as the computed secondary currents of the previous resistive-load investigation. The main parameters are given in TABLE 6.2 (see page 121). The computational results are summarized in TABLE 6.11.

TABLE 6.11: Computational data in current-load condition

Values	Unit	TPFP		HBFP	
		A,V-**A**	**T**,ϕ-ϕ	**A**,V-**A**	**T**,ϕ-ϕ
Eddy-current losses	mW	699.792	698.216	713.296	711.872
No. of DOF	-	643,829	324,537	643,829	324,537
No. of non-zero coefficients	-	36,652,598	19,400,211	36,652,598	19,400,211
BiCG iterations	-	2,570,366	82,8019	3,695,789	1,092,423
BiCG / nonlinear it.		27,638	2,326	38,498	3,095
Nonlinear iterations	-	93	356	96	353
Computational time	s	433,689.2	178,470.8	580,980.3	191,058.7

For comparison of the computed currents only the primary winding currents will be observed as computed values due to the fact that regarding to the current-load condition the secondary winding current is impressed as a sinusoidal current function illustrated in Fig. 6.15. The computed primary currents are in a good agreement and result again as sinusoidal time-functions as expected, illustrated in Fig. 6.18.

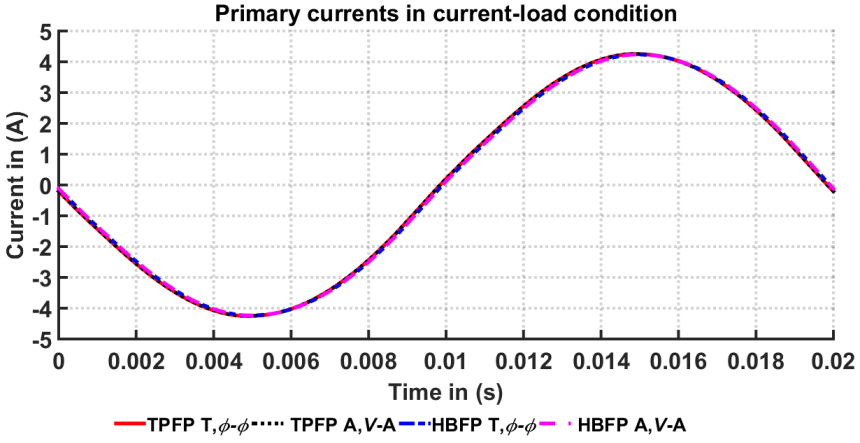

Fig. 6.18: Time-function of the computed primary currents in current-load condition.

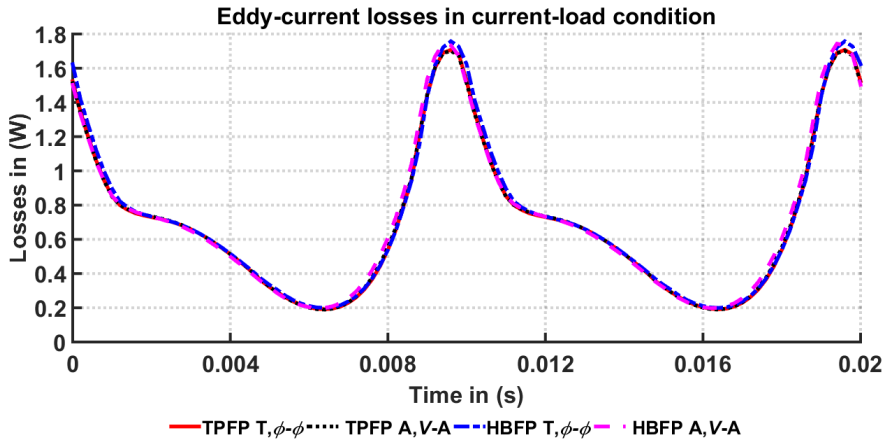

Fig. 6.19: Time-function of the computed eddy-current losses in current-load condition.

The computed eddy-current losses in the transformer housing of the applied formulations are compared in Fig. 6.19 and plotted over one time-period. It is observable that independent of the solving technique applied, the results are almost matching.

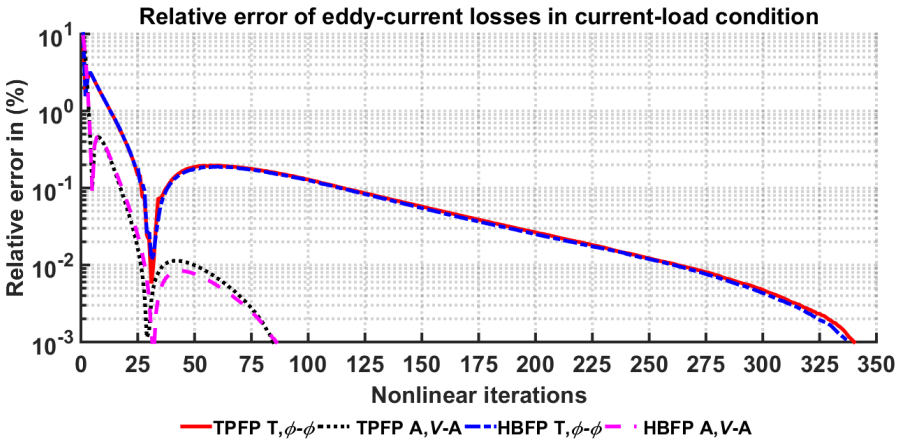

Fig. 6.20: Relative error of the eddy-current losses in each iteration step in current-load condition.

In Fig. 6.20 the relative error of the eddy-current losses in the transformer metal housing are illustrated in each time-step normalized to the value of the last solution of the nonlinear fixed-point iteration. Again it is evidently shown that the magnetic vector potential formulation needs less nonlinear iteration steps to achieve

convergence than the current vector potential formulation but still the computational time is much better than using the magnetic vector potential formulation.

6.2.3 Conclusion

The motivation of this investigation has been to compare two formulations of solving a nonlinear 3D FEM periodic eddy current problem in order to explore the advantages and disadvantages of the two approaches. Both methods are suitable for such computations and, comparing the results, they are equally good. As a matter of fact, the **A**,V-**A**-formulation needs much less nonlinear iterations for convergence. This is a great advantage when solving nonlinear 2D or magnetic circuit problems, as it has been pointed out in sub-section 4.3.2. In 3D real world problems using the **A**,V-**A**-formulation demands about double the number of DOF´s than when applying the **T**,ϕ-ϕ-formulation.

Due to the high number of equations occurring in these 3D problems, it is not possible to use direct solvers. Since one has to use iterative solvers, the computational time is highly affected by the condition number of the system matrix. As it has been seen for the magnetic circuit model in sub-section 4.3.2.2, the condition number of the **A**,V-**A** equation system is worse compared to the condition number of the **T**,ϕ-ϕ system hence the number of BiCG iterations necessary for convergence increases which is reflected in the computational results. Also, dealing with zero winding resistance causes additional computational costs when applying the **A**,V-**A**-formulation, since the system matrix is no more positive definite as discussed in sub-section 6.2.1. Utilizing the Schur-complement, the system has to be solved twice in case of no-load condition or current-load condition or even three times in resistive-load condition as the secondary winding is then also assumed to be voltage driven. Hence the significantly higher number of unknowns and non-zero coefficients of the **A**,V-**A**-formulation lead to a substantial increase in computational costs compared to the **T**,ϕ-ϕ-formulation. As a matter of fact this leads to the **A**,V-**A**-formulation being inferior regarding computational time even if the number of nonlinear iterations is less than when applying the **T**,ϕ-ϕ-formulation.

The results obtained using either HBFP or TPFP agree well. The number of harmonics considered in the HBFP formulation has been half of the discrete time-steps used in the TPFP. If the exact number of necessary harmonics to be considered is known to be less, e.g. it was determined via measurements, the computational costs when using the HBFP technique would be less.

7 Investigations under DC bias

7.1 Introduction

As detailed investigations using models as close to real world problems as possible are increasingly feasible, environmental influences can be taken into account more and more often. Considering transformer problems, the most significant environmental impact is generated by so called geo-magnetically induced currents (GIC) [16]. The currents can emerge due to sun flare activity [17, 18] interacting with the earth's magnetic field. Hence auroral currents influence the dormant magnetic field by varying the earth surface potential (ESP) generating the GIC traversing through the grounded neutral of transformers and along transmission lines. These GIC result in a direct current (DC) accompanying the exciting alternating source current or voltage of a transformer. Furthermore, adding a DC bias to the magnetization current of a transformer considerably affects its operational conditions by e.g. leading to a shift in the point of duty in the material hysteresis of the transformer iron core. Consequently, saturation effects of the core occur within the half-period in which the magnetization current and the DC bias are aligned in the same direction yielding an increase of the noise level, additional core losses as well as eddy-current losses due to the higher leakage flux resulting. As these effects are not negligible, numerical investigations involving such waveforms are mandatory.

Based on previous work [100, 101, 103, 106], the main goal of this investigation is to analyze different ways to predict the steady-state solution of 3D nonlinear eddy-current problems involving voltage driven coils with a DC bias present. Therefore, the simplified benchmark transformer problem introduced previously is adapted to a

three-phase transformer problem to be investigated by the means of a 3D FEM analysis. The analysis emphasizes different ways to treat the DC components in the equation system obtained by the time-periodic fixed-point technique applying the **T**,ϕ-ϕ-formulation.

The goal was to improve the fixed-point iteration strategy by providing a good initial solution yielding faster convergence by reducing the number of nonlinear iterations required. Considering transformer problems, the eddy-current regions are relatively small compared to the non-conducting domains, hence it is obvious to choose the initial solution by neglecting the eddy-currents, a procedure which will be called static initialization. The excitations of the magneto-static problem obtained are the winding fluxes with an unknown DC bias. As the coils are assumed to be voltage driven, the winding currents are unknown but their DC-component is given. Two solution strategies have been implemented in the time-periodic FEM solver to examine this special static problem. Early results of this work have been published by the author in [124].

7.2 FEM formulation

Direct currents form the vector of the time-invariant values defined as

$$\frac{1}{T}\int_0^T \mathbf{i}\,dt = \mathbf{i}_{DC}\,, \tag{7.1}$$

with T representing the length of one time-period and $\mathbf{i} = \left[i_1 \cdots i_{N_c} \right]^T$ is the vector of unknown currents containing the currents for each voltage driven coil present. Hence, it is necessary to consider the FEM formulations for the 0^{th} harmonic, i.e. a case with the time-derivative components of the equations vanishing. The equation system for the **A**,V-**A**-formulation is straightforward to establish, since the time derivative only occurs for the mass matrix and thus this term will vanish resulting in

$$\mathbf{S}^{(s)}_{\nu_{FP}} \mathcal{F}_0\left(\mathbf{x}^{(s+1)}\right) = \mathcal{F}_0\left(\mathbf{S}^{(s)}_{(\nu_{FP}-\nu)}\mathbf{x}^{(s)}\right) + \mathcal{F}_0\left(\mathbf{f}\right). \tag{7.2}$$

Note that in (7.2), the scalar potentials will also vanish as we are using the modified scalar potential represented by its time-derivative.

In case of the **T**,ϕ-ϕ-formulation, the time-derivatives are also present in parts of the right hand side and in the unknown variables to be iterated. Obtaining the system of equations is not that trivial then, due to the fact that the Maxwell´s equation $\nabla \cdot \mathbf{B} = 0$ has to be satisfied in the 0th harmonic, instead of its time-derivative (see (2.90)) Hence, let us start by introducing the divergence of **B** for the 0th harmonic (denoted by $\mathfrak{F}_0$) as

$$\mathfrak{F}_0\left(\nabla \cdot \mathbf{B}\right) = \mathfrak{F}_0\left(\nabla \cdot \mu\left(\mathbf{T} + \mathbf{T}_0 + \mathbf{t}_0\mathbf{i} - \nabla\phi\right)\right) = 0\,. \tag{7.3}$$

With the matrix notation introduced in (2.94), (7.3) can be rewritten as

$$\mathfrak{F}_0\left(\begin{bmatrix}\mathbf{G}_\mu^T & \mathbf{L}_\mu & \mathbf{h}_\mu\end{bmatrix}\begin{bmatrix}\mathbf{T}\\ \boldsymbol{\phi}\\ \mathbf{i}\end{bmatrix}\right) = \mathfrak{F}_0\left(\mathbf{f}_\mu\right), \tag{7.4}$$

and, applying the fixed-point linearization technique, the system becomes

$$\begin{aligned}\mathfrak{F}_0\left(\begin{bmatrix}\mathbf{G}_{\mu_{FP}}^T & \mathbf{L}_{\mu_{FP}} & \mathbf{h}_{\mu_{FP}}\end{bmatrix}\begin{bmatrix}\mathbf{T}^{(s+1)}\\ \boldsymbol{\phi}^{(s+1)}\\ \mathbf{i}^{(s+1)}\end{bmatrix}\right) &= \mathfrak{F}_0\left(\mathbf{f}_\mu\right)\\ +\mathfrak{F}_0\left(\begin{bmatrix}\mathbf{G}_{\mu_{FP}-\mu}^T & \mathbf{L}_{\mu_{FP}-\mu} & \mathbf{h}_{\mu_{FP}-\mu}\end{bmatrix}\begin{bmatrix}\mathbf{T}^{(s)}\\ \boldsymbol{\phi}^{(s)}\\ \mathbf{i}^{(s)}\end{bmatrix}\right).\end{aligned} \tag{7.5}$$

According to the relation (7.1), the currents corresponding to the 0th harmonic are defined as

$$\mathfrak{F}_0\left(\mathbf{i}^{(s)}\right) = \mathfrak{F}_0\left(\mathbf{i}^{(s+1)}\right) = \mathbf{i}_{DC}\,, \tag{7.6}$$

and as the direct components of the eddy currents vanish, the current vector potential can be assumed to be zero

$$\mathfrak{F}_0\left(\mathbf{T}^{(s)}\right)=\mathfrak{F}_0\left(\mathbf{T}^{(s+1)}\right)=\mathbf{0}\,. \tag{7.7}$$

Therefore the system in (7.5) can be simplified to

$$\mathbf{L}_{\mu_{FP}}\mathfrak{F}_0\left(\boldsymbol{\phi}^{(s+1)}\right)=\mathbf{L}_{\mu_{FP}}\mathfrak{F}_0\left(\boldsymbol{\phi}^{(s)}\right)+\mathfrak{F}_0\left(\mathbf{f}_\mu\right)-\mathfrak{F}_0\left(\mathbf{G}_\mu^T\mathbf{T}^{(s)}\right)-\mathfrak{F}_0\left(\mathbf{h}_\mu\mathbf{i}^{(s)}\right)-\mathfrak{F}_0\left(\mathbf{L}_\mu\boldsymbol{\phi}^{(s)}\right), \tag{7.8}$$

the resulting equation to be considered in case of a direct current bias present as the 0^{th} harmonic in addition to the systems derived in sub-sections 2.3.3.3 for the HBFP and 2.3.3.4 for the TPFP without DC bias.

The static initialization process has been implemented for the TPFP as well as for the HBFP technique utilizing the **T**,ϕ-ϕ-formulation only, hence the focus will be concentrated on this formulation.

7.3 Static initialization

As argued above, the basic idea of providing a good initial solution is to perform a static initialization procedure by neglecting the eddy-currents before starting the nonlinear iteration process fully considering the eddy current domains. Hence, with the assumption that for the 0^{th} harmonic the unknown current vector potential is zero: $\mathfrak{F}_0\{\mathbf{T}\}=\mathbf{0}$, and the eddy currents as well as the winding resistances are neglected, a magneto static problem results where $\mathbf{S}_\rho=\mathbf{0}$. The equation system (2.92) of the TPFP applying the **T**,ϕ-ϕ-formulation simplifies to

$$\frac{d}{dt}\left(\begin{bmatrix}\mathbf{L}_\mu & \mathbf{h}_\mu\\ \mathbf{h}_\mu^T & \mathbf{V}_\mu\end{bmatrix}\begin{bmatrix}\boldsymbol{\phi}\\ \mathbf{i}\end{bmatrix}\right)=\begin{bmatrix}\mathbf{0}\\ \mathbf{u}\end{bmatrix}-\frac{d}{dt}\begin{bmatrix}\mathbf{G}_\mu^T\mathbf{T}_{0h}\\ \mathbf{g}_\mu^T\mathbf{T}_{0h}\end{bmatrix}. \tag{7.9}$$

It is obvious that since **T** = **0**, the number of DOF in (7.9) is reduced dramatically in comparison to (2.92). The given voltages can be expressed with the time derivatives of the magnetic fluxes as

$$\mathbf{u}=\frac{d\boldsymbol{\Phi}}{dt}, \tag{7.10}$$

with

$$\mathbf{\Phi} = \int_t \mathbf{u} dt = \tilde{\mathbf{\Phi}} + \mathbf{\Phi}_0 \tag{7.11}$$

where $\mathbf{\Phi}_0$ represents an unknown vector of time independent constants containing the direct components of the magnetic fluxes and $\tilde{\mathbf{\Phi}}$ is given. Utilizing that no current driven coil is present, the impressed current vector potentials on the right hand side vanish and integrating (7.9) over time results in

$$\begin{bmatrix} \mathbf{L}_\mu & \mathbf{h}_\mu \\ \mathbf{h}_\mu^T & \mathbf{V}_\mu \end{bmatrix} \begin{bmatrix} \boldsymbol{\phi} \\ \mathbf{i} \end{bmatrix} = \begin{bmatrix} \mathbf{0} \\ \tilde{\mathbf{\Phi}} + \mathbf{\Phi}_0 \end{bmatrix}. \tag{7.12}$$

The system in (7.12) has to be solved in each time-step in a period. Due to the dependence on the permeability μ, the nonlinear equations are solved by updating μ in each iteration step and once the maximum relative change of the permeability in the integration points between two nonlinear iterations becomes less than a suitable threshold ε, the nonlinear iteration is terminated. Two approaches to obtain a static initial condition are investigated to solve (7.12) with (7.1) taken into account ($\mathbf{i}_{DC}$ is known).

7.3.1 Secant method

The first possibility investigated is based on the secant method [63] applied to iteratively obtain the direct components of the magnetic fluxes. This method has also been utilized in earlier work of our team [106]. It is assumed, that the DC flux Φ_{0j} of the j-th voltage driven coil depends on its DC current $i_{\mathrm{DC}j}$ only. Therefore the functions

$$i_{0j} = f\left(\Phi_{0j}\right) \tag{7.13}$$

can be introduced as obtained from the solution of (7.12) for each discretized and independent time-step with a fixed Φ_{0j} and

$$i_{0j} = \frac{1}{n}\sum_{k=1}^{n} i_j\left(t_k\right) \tag{7.14}$$

where n is the number of time-steps within one time-period. The secant method is applied to solve the equation $f\left(\Phi_{0j}\right) - i_{DCj} = 0$ by iteration of $\mathbf{\Phi}_0$ until $\left|i_{0j} - i_{DCj}\right| < \varepsilon_{i_{DC}} \cdot \left|i_{DCj}\right|$ as:

$$\Phi_{0j}^{(k+1)} = \Phi_{0j}^{(k)} - \left(f\left(\Phi_{0j}^{(k)}\right) - i_{DCj}\right)\frac{\Phi_{0j}^{(k)} - \Phi_{0j}^{(k-1)}}{i_{0j}^{(k)} - i_{0j}^{(k-1)}}, \tag{7.15}$$

with the initial value $\Phi_{0j}^{(0)} = 0$. This approach is a fast second order method, but numerical experiments demonstrate that its convergence is sensitive to the accuracy of evaluating the function f depending on $\varepsilon_{i_{DC}}$ and hence on the precision of the nonlinear material values in each time-step.

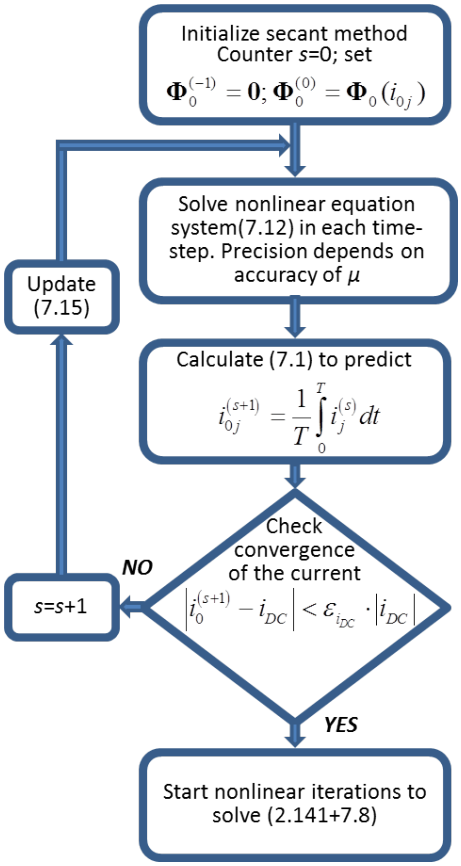

Fig. 7.1: Basic flow-chart of the secant method.

The basic flow-chart illustrated in Fig. 7.1 shows the static initialization process applying the secant method. Two initial guesses for the DC flux component $\mathbf{\Phi}_0$ have to be set in the beginning. The nonlinear iteration procedure approximately obtains $\mathbf{\Phi}_0$ and, as mentioned above, its precision is very sensitive to the choice of $\varepsilon_{i_{DC}}$.

7.3.2 Schur-complement

An alternative to obtain a static initial solution is to utilize a Schur-complement [138, 161] applied in sub-section 6.2.1 for treating voltage excited coils in the **A**,V-**A**-formulation. In this approach the Schur-complement is used to calculate the DC flux component $\mathbf{\Phi}_0$ in each nonlinear iteration-step to solve (7.12) in a way that (7.1) is approximately satisfied. According to the simplifications of the static initialization, a symmetric matrix system of the form

$$\begin{bmatrix} \begin{bmatrix} \mathbf{L}_{\mu,1} & \mathbf{h}_{\mu,1} \\ \mathbf{h}_{\mu,1}^T & \mathbf{V}_{\mu,1} \end{bmatrix} & & & \begin{bmatrix} \mathbf{0} \\ -\mathbf{I} \end{bmatrix} \\ & \ddots & & \vdots \\ & & \begin{bmatrix} \mathbf{L}_{\mu,n} & \mathbf{h}_{\mu,n} \\ \mathbf{h}_{\mu,n}^T & \mathbf{V}_{\mu,n} \end{bmatrix} & \begin{bmatrix} \mathbf{0} \\ -\mathbf{I} \end{bmatrix} \\ \begin{bmatrix} \mathbf{0} & -\mathbf{I} \end{bmatrix} & \cdots & \begin{bmatrix} \mathbf{0} & -\mathbf{I} \end{bmatrix} & \mathbf{0} \end{bmatrix} \begin{bmatrix} \begin{bmatrix} \boldsymbol{\phi}(t_1) \\ \mathbf{i}(t_1) \end{bmatrix} \\ \vdots \\ \begin{bmatrix} \boldsymbol{\phi}(t_n) \\ \mathbf{i}(t_n) \end{bmatrix} \\ \boldsymbol{\Phi}_0 \end{bmatrix} = - \begin{bmatrix} \begin{bmatrix} \mathbf{0} \\ \tilde{\boldsymbol{\Phi}}(t_1) \end{bmatrix} \\ \vdots \\ \begin{bmatrix} \mathbf{0} \\ \tilde{\boldsymbol{\Phi}}(t_n) \end{bmatrix} \\ n\mathbf{i}_{DC} \end{bmatrix}, \tag{7.16}$$

is obtained where $\mathbf{I}$ is the identity matrix of the size N_c. To determine the DC flux component, the Schur-complement is generated for eliminating the unknowns $\mathbf{i}(t_k)$ and $\boldsymbol{\phi}(t_k)$ yielding the equation system

$$\begin{aligned} \left(-\sum_{k=1}^{n} \begin{bmatrix} \mathbf{0} & -\mathbf{I} \end{bmatrix} \begin{bmatrix} \mathbf{L}_{\mu,k} & \mathbf{h}_{\mu,k} \\ \mathbf{h}_{\mu,k}^T & \mathbf{V}_{\mu,k} \end{bmatrix}^{-1} \begin{bmatrix} \mathbf{0} \\ -\mathbf{I} \end{bmatrix} \right) \boldsymbol{\Phi}_0 = \\ -n\mathbf{i}_{DC} - \sum_{k=1}^{n} \begin{bmatrix} \mathbf{0} & -\mathbf{I} \end{bmatrix} \begin{bmatrix} \mathbf{L}_{\mu,k} & \mathbf{h}_{\mu,k} \\ \mathbf{h}_{\mu,k}^T & \mathbf{V}_{\mu,k} \end{bmatrix}^{-1} \begin{bmatrix} \mathbf{0} \\ -\tilde{\boldsymbol{\Phi}}(t_k) \end{bmatrix} \end{aligned} \tag{7.17}$$

to be solved.

In order to optimize computational performance, the system in (7.17) can be split to calculate the components in each time-step in parallel. Indeed, using the notations

$$\mathbf{D}_k := \begin{bmatrix} \mathbf{L}_{\mu,k} & \mathbf{h}_{\mu,k} \\ \mathbf{h}_{\mu,k}^T & \mathbf{V}_{\mu,k} \end{bmatrix}^{-1} \begin{bmatrix} \mathbf{0} \\ -\mathbf{I} \end{bmatrix}, \quad \mathbf{E}_k := \begin{bmatrix} \mathbf{L}_{\mu,k} & \mathbf{h}_{\mu,k} \\ \mathbf{h}_{\mu,k}^T & \mathbf{V}_{\mu,k} \end{bmatrix}^{-1} \begin{bmatrix} \mathbf{0} \\ -\tilde{\boldsymbol{\Phi}}(t_k) \end{bmatrix} \tag{7.18}$$

where k represents a time-step between 1 and n, the Schur-complement solution is determined as

$$\mathbf{S} = \sum_{k=1}^{n} \begin{bmatrix} \mathbf{0} & -\mathbf{I} \end{bmatrix} \mathbf{D}_k \text{ and } \mathbf{r} = -n\mathbf{i}_{DC} - \sum_{k=1}^{n} \begin{bmatrix} \mathbf{0} & -\mathbf{I} \end{bmatrix} \mathbf{E}_k . \tag{7.19}$$

After $\mathbf{D}_k$ and $\mathbf{E}_k$ have been evaluated for each time-step by solving N_c+1 linear equation systems parallel with the sparse matrices in (7.18), the DC flux component of the magnetic flux can be determined as

$$\mathbf{\Phi}_0 = -\mathbf{S}^{-1}\mathbf{r}\,, \tag{7.20}$$

and finally, to obtain the unknown scalar potentials $\boldsymbol{\phi}$ and currents $\mathbf{i}$ for the static initialization,

$$\begin{bmatrix} \boldsymbol{\phi}(t_k) \\ \mathbf{i}(t_k) \end{bmatrix} = \mathbf{E}_k + \mathbf{D}_k\mathbf{\Phi}_0 \tag{7.21}$$

has to be evaluated for all time instances. The iteration procedure of the direct component of the magnetic flux $\mathbf{\Phi}_0$ is repeated until the change to the previous value of $\mathbf{\Phi}_0$ is less than a defined threshold $\varepsilon_{\mathbf{\Phi}_0}$. If so, $\mathbf{\Phi}_0$ is fixed and brought to the right hand side of (7.16) as $[\mathbf{I}]\mathbf{\Phi}_0$ and the system is solved in each time-step with a single RHS until the permeability converges or the deviation of the DC component is higher than a threshold $\varepsilon_{i_{DC}}$ of the defined DC value. If the DC component deviation will be higher than $\varepsilon_{i_{DC}}$ the Schur-complement iteration process has to be started over.

The final results obtained for the unknowns in the static iteration according to (7.21) provide the initial solution for starting the nonlinear iteration process including the eddy-currents.

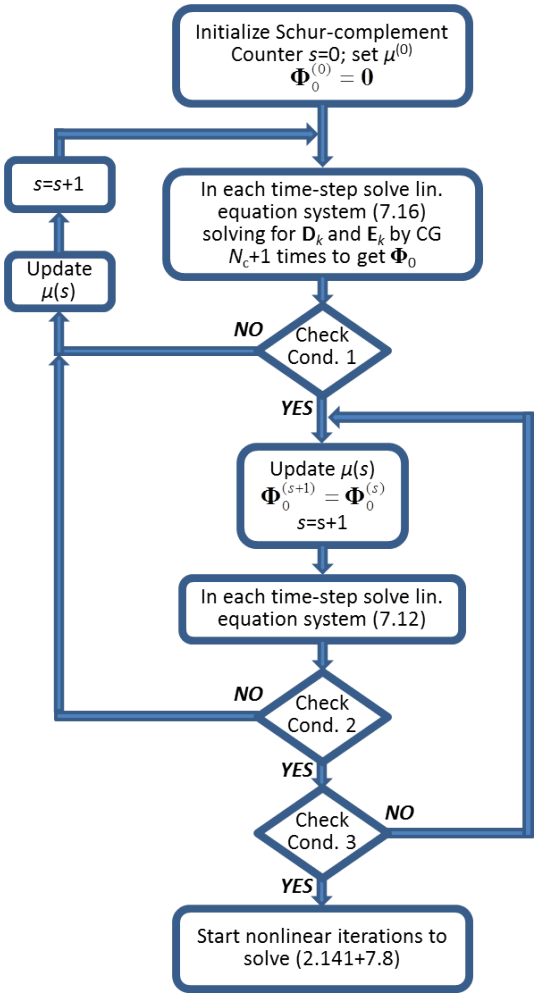

Fig. 7.2: Basic flow-chart of the Schur-complement method.

In Fig. 7.2 the basic process of the static initialization utilizing the Schur-complement is illustrated. The conditions to be checked are

Condition 1	$\left\|\boldsymbol{\Phi}_0^{(s+1)} - \boldsymbol{\Phi}_0^{(s)}\right\| \le \varepsilon_{\boldsymbol{\Phi}_0} \cdot \left\|\boldsymbol{\Phi}_0^{(s+1)}\right\|$
Condition 2	$\left\|\mathfrak{F}_0\left(i^{(s+1)}\right) - i_{DC}\right\| \le \varepsilon_{i_{DC}} \cdot \left\|i_{DC}\right\|$
Condition 3	Convergence of the material μ

This approach is insensitive to the choice of the exit criterion of the permeability due to the fact that $\boldsymbol{\Phi}_0$ can be determined exactly in each nonlinear static iteration-step where in every time-step, N_c+1 linear equation systems are to be solved.

7.4 Numerical results

To analyse the static iteration procedures, a two limb single-phase transformer used in earlier investigations (see chapter 4, 5 and 6) to benchmark several FEM solution methods is adopted and, in addition, the model is enhanced to a three-limb, three-phase transformer. To arrive at a nonlinear eddy-current problem, both models are enclosed by a highly permeable steel tank. The transformers are assumed to be in no-load condition, hence only the primary winding is modelled as a voltage excited coil with a sinusoidal wave form and an operational frequency of 50 (Hz). In addition to the previous investigations to guarantee saturation effects in the core material the exciting voltage was increased to achieve a maximum core flux density of 1.8 (T). The adapted *B*-*H* curves are illustrated in Fig. 7.3 and Fig. 7.4.

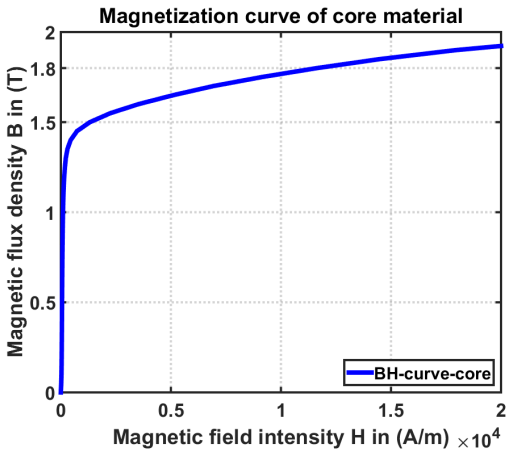

Fig. 7.3: Applied B-H curve for the core material in both transformer models.

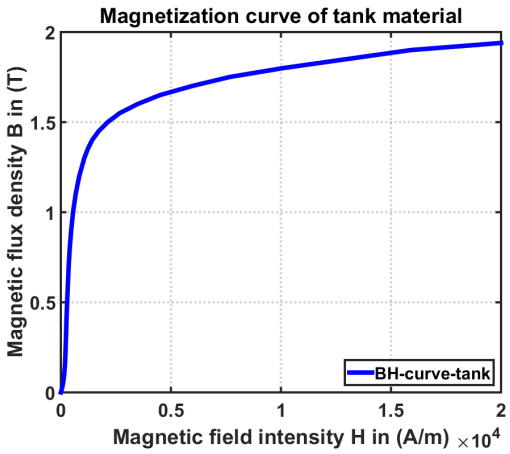

Fig. 7.4: Applied B-H curve for the tank material in both transformer models.

The geometry of the single-phase transformer has been shown in Fig. 4.7 (see page 82). In this case Fig. 7.5 illustrates the eighth of the transformer geometry applied as FEM model and its saturation, where the chosen time instance corresponds to the maximum flux in the iron core.

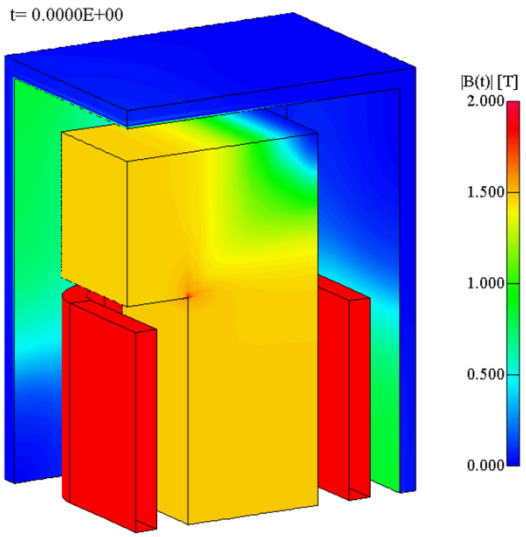

Fig. 7.5: 8th-FEM model of the single-phase transformer with indicated magnetic flux density distribution.

The geometry of the investigated three-phase transformer has been developed based on the single-phase model with the basic design drawn in Fig. 7.6.

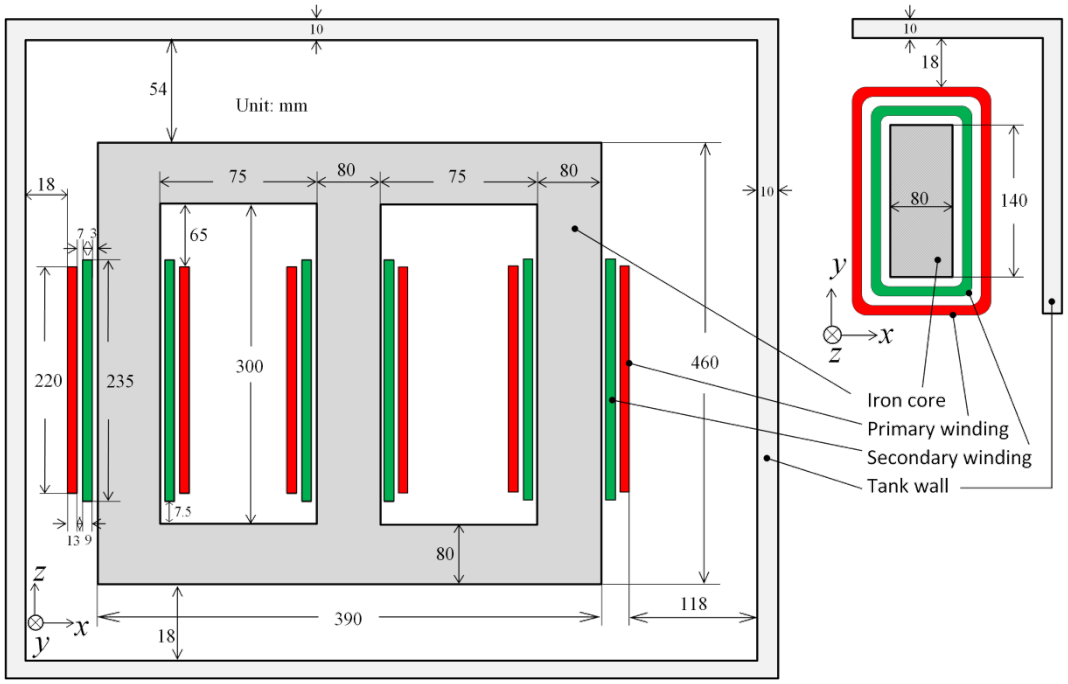

Fig. 7.6: Geometry of the basic three-phase transformer model.

The geometry has been chosen to be non-symmetric to be more close to a real world problem since the additional space is needed to include transmission gear switches and cable bushings. Hence, the distance to the right tank wall as well as to the top wall was extended and the coil window space was stretched at the top end. To construct a FEM-model only one symmetry-plane can be considered resulting in half of the actual problem domain to be included. The designed half-model implemented in the FEM is illustrated in Fig. 7.7. As the exciting voltages applied in each phase build a symmetric 3-phase system, the instant chosen for illustration provides a maximum flux density in the centre core limb.

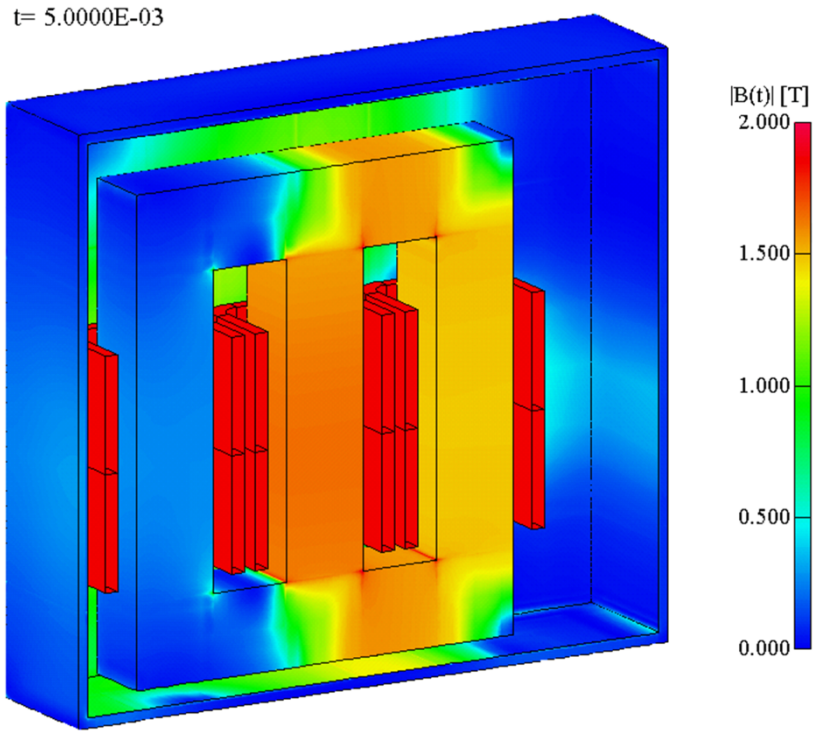

Fig. 7.7: Half-FEM model of the three-phase transformer problem with indicated magnetic flux density distribution.

The parameters for the computations with the aid of the finite element method are summarized in TABLE 7.1.

TABLE 7.1: Attributes of the 3D FEM computations

Values	Unit	TPFP **T**,ϕ-ϕ
Order of elements	-	2^{nd}
Gaussian points in FE	-	3x3x3
BiCG iteration exit criterion	-	10^{-9}
Number of computed time-steps	-	48

The exit criterion for the BiCG iteration has been chosen to be extremely low to assure convergence of the BiCG if the exit criterion of the nonlinear fixed-point iteration is chosen as a low value too, as it has been set in this investigation. To provide a meaningful validation of the obtained results, all the computations have been executed on the same workstation with the properties given in TABLE 7.2.

TABLE 7.2: Main parameters of the computational unit

Values	Unit	Computational unit
CPU architecture	-	Intel Xeon E5-2680V2
Number of CPU´s and clocking	-/GHz	10 / 2.8
Cores / Threads	-	20 / 40
RAM	GB	256
Operating system	-	Windows Server 2008 R2 x64

The computations have been carried out with a DC bias of 2 (A) present in each voltage-excited winding. To observe the effect of varying the threshold ε for the convergence of the material μ when utilizing the Schur-complement method, two different values, namely 5 (%) and 1 (%) have been set to terminate the static initialization process. Due to the fact that the secant-method is very sensitive to the precision of the permeability, a low value of 0.1 (%) in the deviation of the material has been selected. This has proved to be essential in order to ensure a stable iteration process. Furthermore, the convergence criterion for the current $\varepsilon_{i_{DC}}$ in case of the secant method is set to 1 (%) and in case of the Schur-complement to 5 (%), respectively. The threshold ε_{Φ_0} for the Schur-complement initialization has been set to a value of 1 (%).

In the fixed-point iterations considering the eddy-currents, the exit criterion value for ε has been chosen of 0.1 (%) in the maximum deviation of the permeability μ to achieve results as accurate as possible.

7.4.1 Symmetric single-phase transformer model

The computational results obtained for the symmetric single-phase transformer problem are summarized in TABLE 7.3.

TABLE 7.3: Computational data of the symmetric single-phase transformer model

Values		Unit	No Initialization	Schur-complement	Schur-complement	Secant
$\varepsilon_{i_{DC}}$		%	-	5	5	1
ε_{Φ_0}		%	-	1	1	-
ε	Static init.	%	-	5	1	0.1
	Fixed-point iteration	%	0.1	0.1	0.1	0.1
No. of static CG iterations		-	-	49,728	53,815	96,151
Comp. time of static initialization		s	-	890.1	1,144.1	692.4
No. of fixed-point CG iterations		-	15,069,345	12,238,075	11,762,599	11,248,076
Overall comp. time		s	325,807.1	205,896.5	206,238.9	202,192.1
Eddy-current losses in tank		W	115.14	100.32	99.82	100.27
No. of DOF overall		-	162,905			
No. of DOF in static initialization		-	-	95,569		

Comparing the results in the table above, the different applied static initialization procedures are in a good agreement. It turns out that the approximation of the current due to the secant method is slightly advantageous in terms of the computational time consumed for the static initialization procedure. It is demonstrated that varying the accuracy of the material deviation in the Schur-complement initialization has almost no influence on the precision of the losses obtained. It can lead to saving computational time if the threshold is set to a higher value. This would be even more dominant if, for practical reasons, the deviation of the material in case of the fixed-point iteration process considering the eddy-currents would not be set to a value that low as it has been adopted in case of the validation.

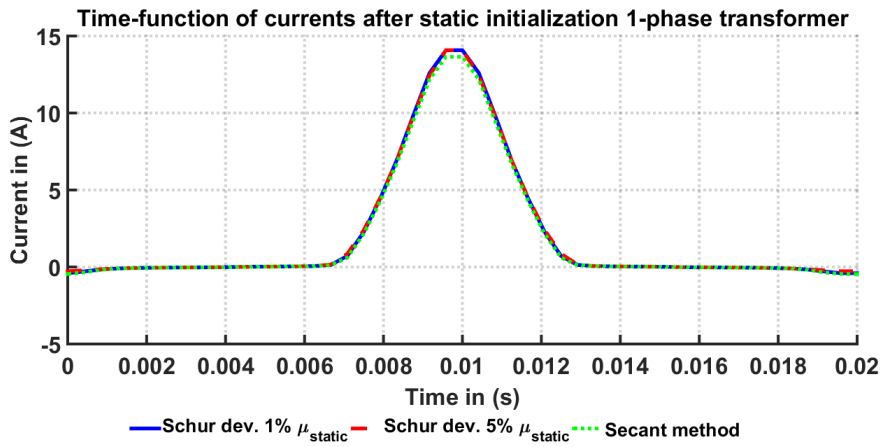

Fig. 7.8: Time-function of the computed currents after the static initialization procedure.

Fig. 7.8 shows the resulting currents after the static initialization process utilizing the Schur-complement and the secant-method. The nonlinearity and the effect of the DC bias are clearly visible. Furthermore, it can be seen that the computed current of the secant method has a marginal deviation compared to the Schur-complement currents due to its approximation procedure. This deviation needs then to be compensated in the nonlinear iterations considering the eddy-currents resulting in almost the same computational effort as for the Schur-complement solution.

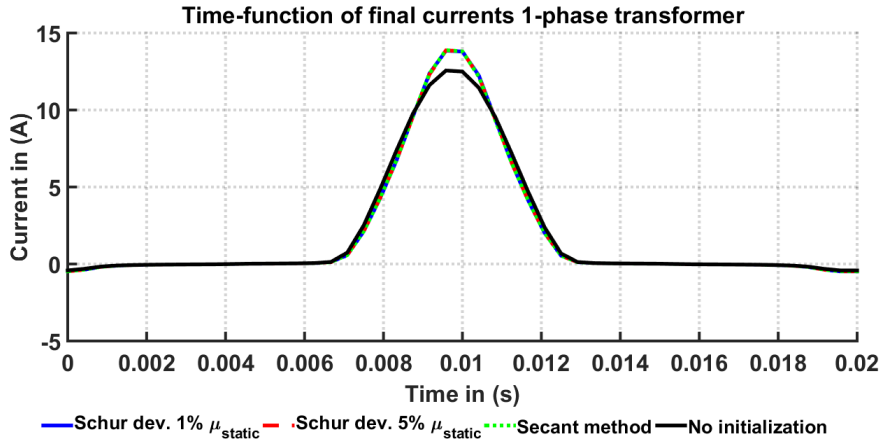

Fig. 7.9: Time-function of the currents after the last nonlinear iteration considering the eddy-currents.

Comparing the final results of the computed eddy-currents illustrated in Fig. 7.9, it is demonstrated that the solutions obtained utilizing the different static

initialization processes are equally good and in a perfect match. Furthermore, the computed current without initialization procedure is also shown and it is evident that the current waveform has still not converged. This is also reflected in the computed eddy-current losses listed in TABLE 7.3. To demonstrate the progress in the computational results of the eddy-current losses, these are illustrated in Fig. 7.10 in each nonlinear iteration step. It can be seen that the static initialization provides a good starting condition for the nonlinear fixed-point iteration considering the eddy-currents. For an industrial accuracy it would be sufficient to choose a limit of about 250 nonlinear iterations. However, the eddy-current losses obtained without an initialization procedure are not acceptable and show a considerably slower convergence behavior. To achieve fully converged results without static initialization, a lower threshold in the exit criterion of the material deviation has to be defined. Nevertheless, such a measure will evidently increase the computational time.

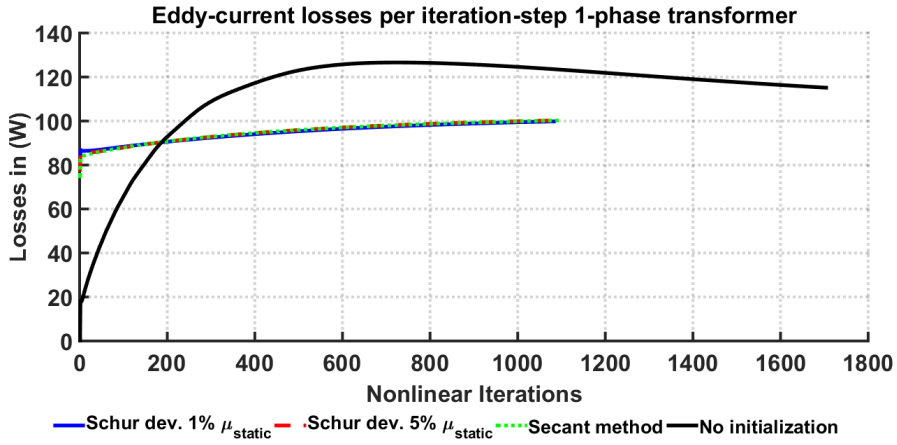

Fig. 7.10: Computed eddy-current losses in each nonlinear iteration-step.

The computed eddy-current losses in the transformer tank in no-load condition are plotted as a time-function over one time-period in Fig. 7.11. It is observable that the time responses of the static initialization solutions are matching whereas the solution obtained without initialization significantly differs in the peak values due to the results being not fully converged.

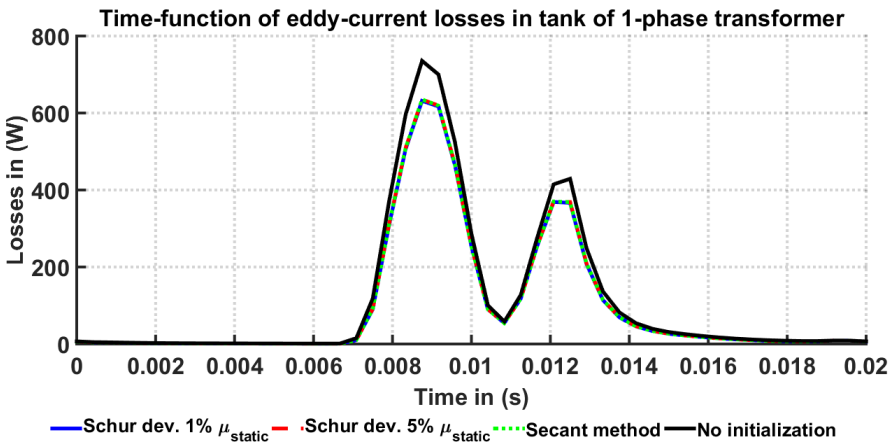

Fig. 7.11: Time-function of the computed eddy-current losses in the housing of the transformer.

7.4.2 Non-symmetric three-phase transformer model

The numerically obtained results for the non-symmetric three phase three-limb transformer model are summarized in TABLE 7.4.

TABLE 7.4: Computational data of the 3-phase non-symmetric transformer model

Vaules		Unit	No Initialization	Schur-complement	Schur-complement	Secant
$\varepsilon_{i_{DC}}$		%	-	5	5	1
ε_{Φ_0}		%	-	1	1	-
ε	Static init.	%	-	5	1	0.1
	Fixed-point iteration	%	0.1	0.1	0.1	0.1
No. of static CG iterations		-	-	1,442,499	1,495,219	2,251,618
Comp. time of static initialization		s	-	11,641.1	13,314.8	8,856.2
No. of fixed-point CG iterations		-	38,965,336	14,859,833	14,780,176	12,604,250
Overall comp. time		s	1,222,624	596,745.6	620,089.6	407,660.4
Eddy-current losses in tank		W	55.81	54.63	54.90	54.89
No. of DOF overall		-	340,747			
No. of DOF in static initialization		-	-	179,445		

Comparing the computed data in TABLE 7.4 with respect to the computational time, the benefit of the static initialization procedure is again evident. The consumed time without initialization is about double the time needed to achieve convergence utilizing the static initialization procedure. In the 3-phase case, the secant method turns out to be more advantageous than the Schur-complement as the static iteration procedure needs less computational time even if the number of CG iterations is higher than for the Schur-complement. This is also observable for the eddy-current fixed-point iteration process since N_c+1 CG solutions have to be computed for the Schur-complement iteration.

In Fig. 7.12, the computed currents after the static initialization process are plotted for each phase over one time-period. The results are in a good agreement

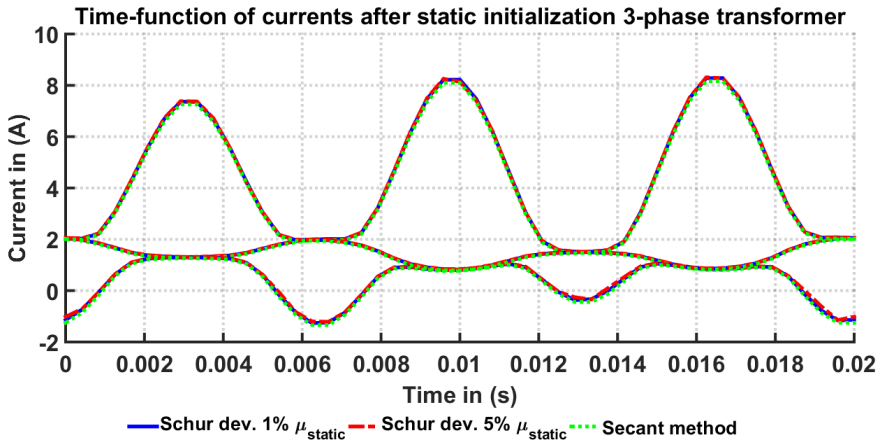

Fig. 7.12: Time-functions of the currents in each phase after the static initialization.

Comparing the final results of the computed currents in Fig. 7.13, the currents obtained applying the static iteration procedures are matching whereas the currents obtained without an initialization procedure have obviously still not converged. The slow convergence behavior without initialization process of the nonlinear eddy-current computations is also reflected in the computed eddy-current losses in the transformer tank wall illustrated in Fig. 7.14 in each nonlinear iteration step.

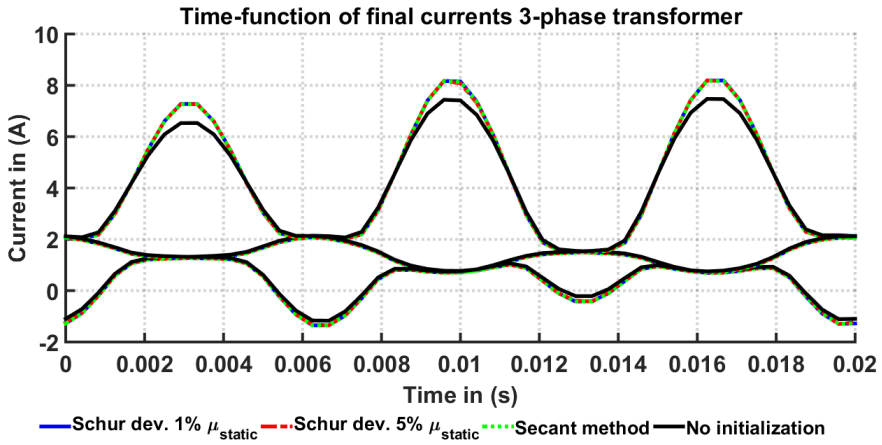

Fig. 7.13: Time-function of the currents after the last nonlinear iteration considering the eddy-currents.

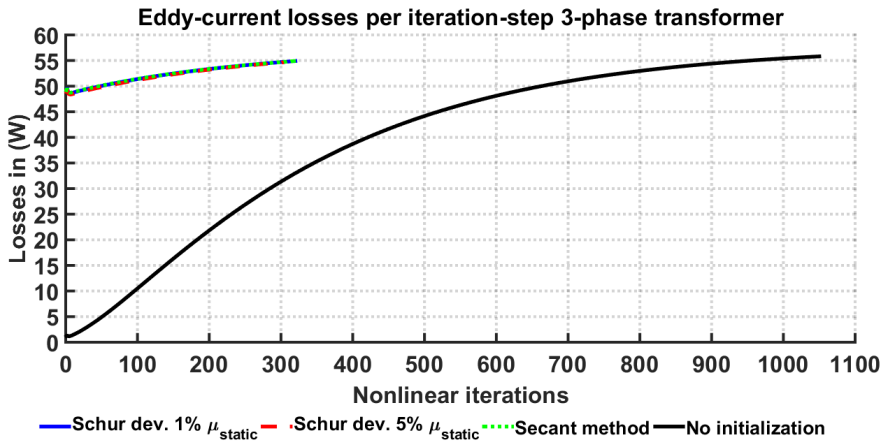

Fig. 7.14: Computed eddy-current losses in each nonlinear iteration-step.

Observing the computed eddy-current losses in Fig. 7.14 the benefit of the static initialization is evident. After about 300 nonlinear iterations the losses obtained by the Schur-complement and the secant initialization are already converged whereas the iteration procedure without initialization needs about 1000 iteration-steps. Nevertheless it can be seen that the methods converge to the same result. This can also be followed in Fig. 7.15 where the final computed eddy-current losses in the transformer tank wall are drawn as a time-function over one period. It can be seen that the results are matching except for some minor deviations in the peak values.

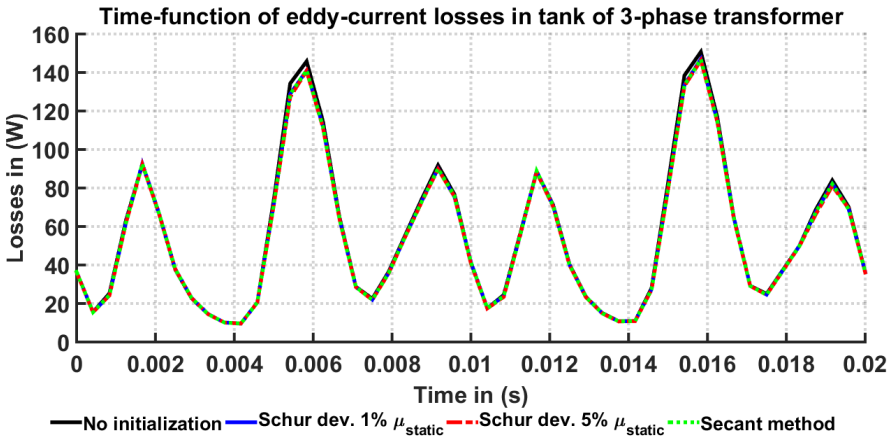

Fig. 7.15: Time-function of the computed eddy-current losses in the housing of the transformer.

7.5 Conclusion

Summarizing the numerical investigations, the static initialization procedures using the secant method, as well as using the Schur-complement technique, lead to the same computational results. Indeed both methods decrease the computational costs significantly compared to the calculations without an initialization process. In both cases investigated, the secant method turns out to be advantageous compared to the Schur-complement approach, provided the exit criterion for the static initialization process is chosen properly. Since the secant method is very sensitive to the accuracy of the permeability, this exit criterion has to be adjusted carefully for each new problem. As a benefit of using the Schur-complement method it turned out that the exit criterion of the static initialization is not needed to be defined as carefully as for the secant method. Opposing the robustness of the iteration procedure applying the Schur-complement is the fact that multiple right hand sides have to be solved in each iteration-step which leads to higher computational times compared to the secant method. It has been found that, when treating DC biased problems, the nonlinear iteration process of the fixed-point eddy-current losses converges very slowly in comparison to the problems investigated without DC bias. Therefore, it was necessary to define a low threshold in the material deviation as exit criterion. This in turn led to the fact that the BiCG accuracy had to be increased to guarantee a stable iteration process, as it has been set for this investigation.

8 Summary of scientific results

The aim of this thesis was to validate and adapt an existing numerical electromagnetic field analysis tool for treating three-dimensional, nonlinear, time-periodic, eddy-current problems. For this purpose, the computational results of the numerical solver were first compared to measured induced eddy-currents in a steel grid in the vicinity of a dry insulated air reactor to observe the influence of varying the number of the considered harmonics in the accuracy of the computational results. It has been shown that neither the impact of the higher harmonics nor the temperature-rise in the steel rods, influencing their conductivity were negligible for obtaining scientifically accurate results. A good agreement in the number of odd harmonics to be considered was found as up to the half of the used discrete time-steps.

Furthermore, a nonlinear, magnetic circuit model enabling fast analyses, based on the solution algorithm of the FEM has been developed to quickly validate adaptions of the numerical solution procedure. This has been successfully used to investigate treating the additional equations in presence of voltage-excited coils separately or combined to the system of equations of the field quantities. This magnetic circuit model was also utilized to assess the best way of applying voltage-excited coils in combination with the magnetic vector potential formulation. Based on these investigations, the 3D FEM solver was extended to take account of voltage excitation when using the magnetic vector potential formulation and has further been compared with the solution techniques of the Japanese group of Professor Yasuhito Takahashi from the Doshisha University in Japan. The numerically computed results of both teams are in a good agreement validating both techniques.

In the last section of this work, the numerical approach of solving 3D, nonlinear, time-periodic, eddy-current problems with a DC bias has been presented. A static

initialization process has been developed to enhance the performance of the solution algorithm. The idea was to first obtain a magneto-static solution by neglecting the eddy-currents and using the result as initial value to start the computation with the eddy-currents considered. Two different static solution procedures have been introduced. The validation of these techniques showed benefits and minor drawbacks in their application. Nevertheless, both methods provide equally good initial conditions resulting in a significant saving of computational costs.

In conclusion, the goals of validation have been fulfilled and hence improvements of the FEM solver have successfully been implemented. The findings have been processed in this thesis as well as published in various scientific journals.

Bibliography

[1] B. H. E. Bharat Heavy Electricals Limited, "Transformers, Second Edition," *Tata Mac Graw Hill,* 1987.

[2] J. Winders, "Power transformers: principles and applications," *CRC Press,* 2002.

[3] S. V. Kulkarni und S. A. Khaparde, „Transformer Engineering: Design and Practice," *CRC Press,* 2004.

[4] Y. Akiba, T. Futami and T. Suda, *Litz wire,* Google Patents, 1985.

[5] R. P. Wojda and M. K. Kazimierczuk, "Winding resistance of litz-wire and multi-strand inductors," *IET Power Electronics,* vol. 5, pp. 257-268, February 2012.

[6] D. D. Perco and P. V. Birke, *Multistranded component conductor continuously transposed cable,* Google Patents, 1984.

[7] P. Rabbia, *Continuously transposed conductor,* Google Patents, 2012.

[8] A. Roßkopf, E. Bär and C. Joffe, "Influence of Inner Skin- and Proximity Effects on Conduction in Litz Wires," *IEEE Transactions on Power Electronics,* vol. 29, no. 10, pp. 5454-5461, October 2014.

[9] C. R. Sullivan, "Optimal choice for number of strands in a litz-wire transformer winding," *IEEE Transactions on Power Electronics,* vol. 14, no. 2, pp. 283-291, March 1999.

[10] T. Trimmel and M. Trimmel, *Continuously transposed conductor,* Google Patents, 2014.

[11] T. Trimmel and M. Trimmel, *Continuously transposed conductor,* Google Patents, 2015.

[12] P. D. Agarwal, "Eddy-current losses in solid and laminated iron," *Transactions of the American Institute of Electrical Engineers, Part I: Communication and Electronics,* vol. 78, no. 2, pp. 169-181, May 1959.

[13] V. C. Silva, G. Meunier and A. Foggia, "A 3-D finite-element computation of eddy currents and losses in laminated iron cores allowing for electric and magnetic anisotropy," *IEEE Transactions on Magnetics,* vol. 31, no. 3, pp. 2139-2141, May 1995.

[14] J. H. Harlow, "Electric Power Transformer Engineering, Third Edition," *Taylor & Francis,* no. 2, 2012.

[15] B. H. E. Limited, "Transformers: Design, Manufacturing, and Materials," *McGraw-Hill Education,* 2005.

[16] A. Pulkkinen, A. Thomson, E. Clarke and A. McKay, "Geomagnetically induced currents," *HAL archives-ouvertes,* 2002.

[17] R. Pirjola, "Geomagnetically induced currents during magnetic storms," *IEEE Transactions on Plasma Science,* vol. 28, no. 6, pp. 1867-1873, December 2000.

[18] R. Pirjola, "Review On The Calculation Of Surface Electric And Magnetic Fields And Of Geomagnetically Induced Currents In Ground-Based Technological Systems," *Surveys in Geophysics,* vol. 23, no. 1, pp. 71-90, 2002.

[19] S. Arabi, M. M. Komaragiri and M. Z. Tarnawecky, "Effects of geomagnetically-induced currents in power transformers from power systems point of view," *Canadian Electrical Engineering Journal,* vol. 12, no. 4, pp. 165-170, October 1987.

[20] P. R. Price, "Geomagnetically induced current effects on transformers," *IEEE Transactions on Power Delivery,* vol. 17, no. 4, pp. 1002-1008, October 2002.

[21] B. Zhang, L. Liu, Y. Liu, M. McVey and R. M. Gardner, "Effect of geomagnetically induced current on the loss of transformer tank," *IET Electric Power Applications,* vol. 4, no. 5, pp. 373-379, May 2010.

[22] O. C. Zienkiewicz, R. L. Taylor and J. Z. Zhu, "The Finite Element Method: Its Basis and Fundamentals," *Elsevier Science,* 2013.

[23] J. T. Oden, "An Introduction to the Finite Element Method with Applications

to Nonlinear Problems (R. E. White)," *SIAM Review,* vol. 31, no. 3, pp. 512-512, 1989.

[24] R. T. Fenner, "Finite Element Methods for Engineers," *World Scientific Publishing Company,* 2013.

[25] B. Klein, "FEM: Grundlagen und Anwendungen der Finite-Element-Methode im Maschinen- und Fahrzeugbau," *Vieweg+Teubner Verlag,* 2010.

[26] A. C. Polycarpou, "Introduction to the Finite Element Method in Electromagnetics," *Morgan & Claypool Publishers,* 2006.

[27] J. N. Reddy, "An Introduction to the Finite Element Method," *McGraw-Hill, 3rd edition,* 2006.

[28] P. P. Silvester and R. L. Ferrari, "Finite Elements for Electrical Engineers," *Cambridge University Press,* 1996.

[29] K. J. Bathe and E. L. Wilson, "Numerical methods in finite element analysis," *Prentice-Hall,* 1976.

[30] D. A. H. Jacobs, "The state of the art in numerical analysis: proceedings of the Conference on the State of the Art in Numerical Analysis held at the University of York, April 12th-15th, 1976," *Academic Press,* 1977.

[31] S. Salon and M. V. K. Chari, "Numerical Methods in Electromagnetism," *Elsevier Science,* 1999.

[32] P. W. Gross and P. R. Kotiuga, "Electromagnetic Theory and Computation: A Topological Approach," *Cambridge University Press,* 2004.

[33] J. M. Jin, "The Finite Element Method in Electromagnetics," *Wiley,* 2002.

[34] J. P. A. Bastos and N. Sadowski, "Electromagnetic Modeling by Finite Element Methods," *CRC Press,* 2003.

[35] O. Bíró, "Edge element formulations of eddy current problems," *Computer Methods in Applied Mechanics and Engineering,* vol. 169, no. 3, pp. 391-405, 1999.

[36] O. Bíró and K. Preis, "Finite element analysis of 3-D eddy currents," *IEEE Transactions on Magnetics,* vol. 26, no. 2, pp. 418-423, March 1990.

[37] K. Preis, I. Bardi, O. Bíró, C. Magele, G. Vrisk and K. R. Richter, "Different finite element formulations of 3D magnetostatic fields," *IEEE Transactions on Magnetics,* vol. 28, no. 2, pp. 1056-1059, March 1992.

[38] M. Kuczmann, "Potential formulations in magnetics applying the finite

element method," *Lecture notes, Laboratory of Electromagnetic Fields,"Széchenyi István" University, Gyor, Hungary,* 2009.

[39] G. Meunier, "The Finite Element Method for Electromagnetic Modeling," *Wiley,* 2010.

[40] M. Chiampi, A. Negro and M. Tartaglia, "A finite element method to compute three-dimensional magnetic field distribution in transformer cores," *IEEE Transactions on Magnetics,* vol. 16, no. 6, pp. 1413-1419, November 1980.

[41] M. Chiampi, A. Negro and M. Tartaglia, "Finite elements computation of magnetic fields in multiply connected domains," *IEEE Transactions on Magnetics,* vol. 17, no. 4, pp. 1493-1497, July 1981.

[42] R. Albanese, E. Coccorese, R. Martone, G. Miano and G. Rubinacci, "On the numerical solution of the nonlinear three-dimensional eddy current problem," *IEEE Transactions on Magnetics,* vol. 27, no. 5, pp. 3990-3995, September 1991.

[43] A. Bossavit and I. D. Mayergoyz, "Computational Electromagnetism: Variational Formulations, Complementarity, Edge Elements," *Elsevier Science,* 1998.

[44] O. Bíró, K. Preis and K. R. Richter, "Various FEM formulations for the calculation of transient 3D eddy currents in nonlinear media," *IEEE Transactions on Magnetics,* vol. 31, no. 3, pp. 1307-1312, May 1995.

[45] O. Bíró, K. Preis and K. R. Richter, "On the use of the magnetic vector potential in the nodal and edge finite element analysis of 3D magnetostatic problems," *IEEE Transactions on Magnetics,* vol. 32, no. 3, pp. 651-654, May 1996.

[46] S. E. Benzley, E. Perry, K. Merkley, B. Clark and G. Sjaardama, "A comparison of all hexagonal and all tetrahedral finite element meshes for elastic and elasto-plastic analysis," in *Proceedings, 4th International Meshing Roundtable*, 1995.

[47] A. O. Cifuentes and A. Kalbag, "A performance study of tetrahedral and hexahedral elements in 3-D finite element structural analysis," *Finite Elements in Analysis and Design,* vol. 12, no. 3, pp. 313-318, 1992.

[48] E. Wang, T. Nelson and R. Rauch, "Back to elements-tetrahedra vs. hexahedra," in *Proceedings of the 2004 International ANSYS Conference*, 2004.

[49] J.-Y. Wu and R. Lee, "The advantages of triangular and tetrahedral edge elements for electromagnetic modeling with the finite-element method," *IEEE Transactions on Antennas and Propagation,* vol. 45, no. 9, pp. 1431-1437, September 1997.

[50] Z. Ren and N. Ida, "Solving 3D eddy current problems using second order nodal and edge elements," *IEEE Transactions on Magnetics,* vol. 36, no. 4, pp. 746-750, July 2000.

[51] P. Dular, J. Y. Hody, A. Nicolet, A. Genon and W. Legros, "Mixed finite elements associated with a collection of tetrahedra, hexahedra and prisms," *IEEE Transactions on Magnetics,* vol. 30, no. 5, pp. 2980-2983, September 1994.

[52] H. C. Lai, D. Rodger and P. J. Leonard, "Coupling meshes in 3D problems involving movements," *IEEE Transactions on Magnetics,* vol. 28, no. 2, pp. 1732-1734, March 1992.

[53] C. Golovanov, J. L. Coulomb, Y. Marechal and G. Meunier, "3D mesh connection techniques applied to movement simulation," *IEEE Transactions on Magnetics,* vol. 34, no. 5, pp. 3359-3362, September 1998.

[54] R. Becker, P. Hansbo and R. Stenberg, "A finite element method for domain decomposition with non-matching grids," *ESAIM: M2AN,* vol. 37, no. 2, pp. 209-225, 2003.

[55] S. Bohmer, E. Lange, M. Hafner, T. Cramer, C. Bischof and K. Hameyer, "Mesh Decomposition for Efficient Parallel Computing of Electrical Machines by Means of FEM Accounting for Motion," *IEEE Transactions on Magnetics,* vol. 48, no. 2, pp. 891-894, February 2012.

[56] Y. Takahashi, K. Fujiwara, T. Iwashita and H. Nakashima, "Parallel Finite-Element Analysis of Rotating Machines Based on Domain Decomposition Considering Nonconforming Mesh Connection," *IEEE Transactions on Magnetics,* vol. 52, no. 3, pp. 1-4, March 2016.

[57] G. J. Wallinger and O. Bíró, "3-D FE Method Analysis of Static Fields for Non-Conforming Meshes With Second-Order Node-Based Elements," *IEEE Transactions on Magnetics,* vol. 52, no. 3, pp. 1-4, March 2016.

[58] E. Kreyszig, "Introductory functional analysis with applications," *Wiley New York,* vol. 1, 1989.

[59] Y. Okamoto, K. Fujiwara and R. Himeno, "Exact Minimization of Energy

Functional for NR Method With Line-Search Technique," *IEEE Transactions on Magnetics,* vol. 45, no. 3, pp. 1288-1291, March 2009.

[60] M. Urabe, "Galerkin's procedure for nonlinear periodic systems," *Archive for Rational Mechanics and Analysis,* vol. 20, no. 2, pp. 120-152, 1965.

[61] C. P. Steinmetz, "On the Law of Hysteresis," *Transactions of the American Institute of Electrical Engineers,* vol. IX, no. 1, pp. 1-64, January 1892.

[62] A. G. Jack and B. C. Mecrow, "Methods for magnetically nonlinear problems involving significant hysteresis and eddy currents," *IEEE Transactions on Magnetics,* vol. 26, no. 2, pp. 424-429, March 1990.

[63] M. B. Allen and E. L. Isaacson, "Solution of Nonlinear Equations," in *Numerical Analysis for Applied Science*, John Wiley & Sons, Inc., 1997, pp. 161-219.

[64] G. Bertotti, "Hysteresis in Magnetism: For Physicists, Materials Scientists, and Engineers," *Elsevier Science,* 1998.

[65] S. V. Kulkarni and S. A. Khaparde, "Stray loss evaluation in power transformers-a review," in *2000 IEEE Power Engineering Society Winter Meeting. Conference Proceedings (Cat. No.00CH37077)*, 2000.

[66] P. J. Leonard and D. Rodger, "Finite element scheme for transient 3D eddy currents," *IEEE Transactions on Magnetics,* vol. 24, no. 1, pp. 90-93, January 1988.

[67] R. Albanese and G. Rubinacci, "Integral formulation for 3D eddy-current computation using edge elements," *IEE Proceedings A - Physical Science, Measurement and Instrumentation, Management and Education - Reviews,* vol. 135, no. 7, pp. 457-462, September 1988.

[68] A. Kameari, "Calculation of transient 3D eddy current using edge-elements," *IEEE Transactions on Magnetics,* vol. 26, no. 2, pp. 466-469, March 1990.

[69] R. Albanese and G. Rubinacci, "Formulation of the eddy-current problem," *IEE Proceedings A - Physical Science, Measurement and Instrumentation, Management and Education,* vol. 137, no. 1, pp. 16-22, January 1990.

[70] R. Albanese, G. Rubinacci, M. Canali, S. Stangherlin, A. Musolino and M. Raugi, "Analysis of a transient nonlinear 3-D eddy current problem with differential and integral methods," *IEEE Transactions on Magnetics,* vol. 32, no. 3, pp. 776-779, May 1996.

[71] T. Hara, T. Naito and J. Umoto, "Time-periodic finite element method for

nonlinear diffusion equations," *IEEE Transactions on Magnetics,* vol. 21, no. 6, pp. 2261-2264, November 1985.

[72] T. Nakata, N. Takahashi, K. Fujiwara and A. Ahagon, "3-D non-linear eddy current analysis using the time-periodic finite element method," *IEEE Transactions on Magnetics,* vol. 25, no. 5, pp. 4150-4152, September 1989.

[73] T. Nakata, N. Takahashi, K. Fujiwara, K. Muramatsu, H. Ohashi and H. L. Zhu, "Practical analysis of 3-D dynamic nonlinear magnetic field using time-periodic finite element method," *IEEE Transactions on Magnetics,* vol. 31, no. 3, pp. 1416-1419, May 1995.

[74] G. Paoli, O. Bíró and G. Buchgraber, "Complex representation in nonlinear time harmonic eddy current problems," *IEEE Transactions on Magnetics,* vol. 34, no. 5, pp. 2625-2628, September 1998.

[75] J. Weymann, P. Thomas and J. Gaombalet, "A new method for periodic solutions of nonlinear eddy current problems," *IEEE Transactions on Magnetics,* vol. 35, no. 3, pp. 1115-1118, May 1999.

[76] R. Albanese, E. Coccorese, R. Martone, G. Miano and G. Rubinacci, "Periodic solutions of nonlinear eddy current problems in three-dimensional geometries," *IEEE Transactions on Magnetics,* vol. 28, no. 2, pp. 1118-1121, March 1992.

[77] T. Matsuo and M. Shimasaki, "Time-periodic finite-element method for hysteretic eddy-current analysis," *IEEE Transactions on Magnetics,* vol. 38, no. 2, pp. 549-552, March 2002.

[78] O. Bíró and K. Preis, "An efficient time domain method for nonlinear periodic eddy current problems," *IEEE Transactions on Magnetics,* vol. 42, no. 4, pp. 695-698, April 2006.

[79] O. Bíró, G. Koczka and K. Preis, "Fast Time-Domain Finite Element Analysis of 3-D Nonlinear Time-Periodic Eddy Current Problems With T,Phi-Phi Formulation," *IEEE Transactions on Magnetics,* vol. 47, no. 5, pp. 1170-1173, May 2011.

[80] M. Nakhla and J. Vlach, "A piecewise harmonic balance technique for determination of periodic response of nonlinear systems," *IEEE Transactions on Circuits and Systems,* vol. 23, no. 2, pp. 85-91, February 1976.

[81] S. Yamada, K. Bessho and J. Lu, "Harmonic balance finite element method applied to nonlinear AC magnetic analysis," *IEEE Transactions on Magnetics,* vol. 25, no. 4, pp. 2971-2973, July 1989.

[82] S. Ausserhofer, O. Bíró and K. Preis, "An Efficient Harmonic Balance Method for Nonlinear Eddy-Current Problems," *IEEE Transactions on Magnetics,* vol. 43, no. 4, pp. 1229-1232, April 2007.

[83] I. R. Ciric and F. I. Hantila, "An Efficient Harmonic Method for Solving Nonlinear Time-Periodic Eddy-Current Problems," *IEEE Transactions on Magnetics,* vol. 43, no. 4, pp. 1185-1188, April 2007.

[84] P. J. Leonard and D. Rodger, "Voltage forced coils for 3D finite-element electromagnetic models," *IEEE Transactions on Magnetics,* vol. 24, no. 6, pp. 2579-2581, November 1988.

[85] O. Bíró, K. Preis, G. Buchgraber and I. Ticar, "Voltage-driven coils in finite-element formulations using a current vector and a magnetic scalar potential," *IEEE Transactions on Magnetics,* vol. 40, no. 2, pp. 1286-1289, March 2004.

[86] G. Meunier, H. T. Luong and Y. Marechal, "Computation of coupled problem of 3D eddy current and electrical circuit by using T0-T- phi; formulation," *IEEE Transactions on Magnetics,* vol. 34, no. 5, pp. 3074-3077, September 1998.

[87] P. Dular, C. Geuzaine and W. Legros, "A natural method for coupling magnetodynamic H-formulations and circuit equations," *IEEE Transactions on Magnetics,* vol. 35, no. 3, pp. 1626-1629, May 1999.

[88] W. W. Lewis, "Losses in transformers," *Proceedings of the American Institute of Electrical Engineers,* vol. 32, no. 2, pp. 477-504, February 1913.

[89] G. Bertotti, "General properties of power losses in soft ferromagnetic materials," *IEEE Transactions on Magnetics,* vol. 24, no. 1, pp. 621-630, January 1988.

[90] D. A. Koppikar, S. V. Kulkarni, S. A. Khaparde and S. K. Jha, "Evaluation of eddy losses due to high current leads in transformers," *IEE Proceedings - Science, Measurement and Technology,* vol. 144, no. 1, pp. 34-38(4), January 1997.

[91] D. A. Koppikar, S. V. Kulkarni, P. N. Srinivas, S. A. Khaparde and R. Jain, "Evaluation of flitch plate losses in power transformers," *IEEE Transactions on Power Delivery,* vol. 14, no. 3, pp. 996-1001, July 1999.

[92] E. Barbisio, F. Fiorillo and C. Ragusa, "Predicting loss in magnetic steels under arbitrary induction waveform and with minor hysteresis loops," *IEEE Transactions on Magnetics,* vol. 40, no. 4, pp. 1810-1819, July 2004.

[93] K. Preis, O. Bíró and I. Ticar, "FEM analysis of eddy current losses in nonlinear laminated iron cores," *IEEE Transactions on Magnetics,* vol. 41, no. 5, pp. 1412-1415, May 2005.

[94] M. Chiampi, A. Negro and M. Tartaglia, "Alternating electromagnetic field computation in laminated cores," *IEEE Transactions on Magnetics,* vol. 19, no. 4, pp. 1530-1536, July 1983.

[95] P. Handgruber, "Advanced Eddy Current and Hysteresis Loss Models for Steel Laminations of Rotating Electrical Machines," *PhD Thesis,* 2015.

[96] R. A. Walling and A. N. Khan, "Characteristics of transformer exciting-current during geomagnetic disturbances," *IEEE Transactions on Power Delivery,* vol. 6, no. 4, pp. 1707-1714, October 1991.

[97] F. S. Prabhakara, L. N. Hannett, R. I. Ringlee and J. Z. Ponder, "Geomagnetic effects modelling for the PJM interconnection system. II. Geomagnetically induced current study results," *IEEE Transactions on Power Systems,* vol. 7, no. 2, pp. 565-571, May 1992.

[98] S. Lu, Y. Liu and J. D. L. Ree, "Harmonics generated from a DC biased transformer," *IEEE Transactions on Power Delivery,* vol. 8, no. 2, pp. 725-731, April 1993.

[99] S. Lu and Y. Liu, "FEM analysis of DC saturation to assess transformer susceptibility to geomagnetically induced currents," *IEEE Transactions on Power Delivery,* vol. 8, no. 3, pp. 1367-1376, July 1993.

[100] O. Bíró, S. Außerhofer, G. Buchgraber, K. Preis and W. Seitlinger, "Prediction of magnetising current waveform in a single-phase power transformer under DC bias," *IET Science, Measurement & Technology,* vol. 1, pp. 2-5, January 2007.

[101] O. Biro, G. Buchgraber, G. Leber and K. Preis, "Prediction of Magnetizing Current Wave-Forms in a Three-Phase Power Transformer Under DC Bias," *IEEE Transactions on Magnetics,* vol. 44, no. 6, pp. 1554-1557, June 2008.

[102] X. Zhao, J. Lu, L. Li, Z. Cheng and T. Lu, "Analysis of the DC Bias Phenomenon by the Harmonic Balance Finite-Element Method," *IEEE Transactions on Power Delivery,* vol. 26, no. 1, pp. 475-485, January 2011.

[103] O. Bíró, Y. Chen, G. Koczka, G. Leber, K. Preis and B. Wagner, "Steady-State Analysis of Power Transformers Under DC-Bias by the Finite Element Method with Fixed-Point Technique," in *Compumag 2011*, 2011.

[104] X. Zhao, L. Li, J. Lu, Z. Cheng and T. Lu, "Analysis of the saturated electromagnetic devices under DC bias condition by the decomposed harmonic balance finite element method," *COMPEL - The international journal for computation and mathematics in electrical and electronic engineering,* vol. 31, no. 2, pp. 498-513, 2012.

[105] X. Zhao, L. Li, J. Lu, Z. Cheng and T. Lu, "Characteristics Analysis of the Square Laminated Core under dc-biased Magnetization by the Fixed-point Harmonic-balanced FEM," *IEEE Transactions on Magnetics,* vol. 48, no. 2, pp. 747-750, February 2012.

[106] O. Bíró, G. Koczka, G. Leber, K. Preis and B. Wagner, "Finite Element Analysis of Three-Phase Three-Limb Power Transformers Under DC Bias," *IEEE Transactions on Magnetics,* vol. 50, no. 2, pp. 565-568, February 2014.

[107] Y. Takahashi, T. Iwashita, H. Nakashima, T. Tokumasu, M. Fujita, S. Wakao, K. Fujiwara and Y. Ishihara, "Parallel Time-Periodic Finite-Element Method for Steady-State Analysis of Rotating Machines," *IEEE Transactions on Magnetics,* vol. 48, no. 2, pp. 1019-1022, February 2012.

[108] S. Boehmer, T. Cramer, M. Hafner, E. Lange, C. Bischof and K. Hameyer, "Numerical simulation of electrical machines by means of a hybrid parallelisation using MPI and OpenMP for finite-element method," *IET Science, Measurement Technology,* vol. 6, no. 5, pp. 339-343, September 2012.

[109] Y. Takahashi, T. Tokumasu, M. Fujita, T. Iwashita, H. Nakashima, S. Wakao and K. Fujiwara, "Time-Domain Parallel Finite-Element Method for Fast Magnetic Field Analysis of Induction Motors," *IEEE Transactions on Magnetics,* vol. 49, no. 5, pp. 2413-2416, May 2013.

[110] S. Rani, V. C. V. Rao, S. K. Maity and K. G. Gupta, "Parallelization of FDM/FEM computation for PDEs on PARAM YUVA-II cluster of Xeon Phi coprocessors," in *2014 Annual IEEE India Conference (INDICON)*, 2014.

[111] R. Plasser and O. Bíró, "Validation of Finite Element Solutions of Nonlinear Periodic Eddy Current Problems," in *9th PhD DLA Symposium*, Pécs, 2013.

[112] R. Plasser and O. Bíró, "Validation of finite element solutions of nonlinear, periodic eddy current problems," in *9th IET International Conference on Computation in Electromagnetics (CEM 2014)*, 2014.

[113] R. Plasser and O. Bíró, "Validation of finite element solutions of nonlinear, periodic eddy current problems," *Archives of Electrical Engineering,* vol. 63, no. 4, pp. 591-600, 2014.

[114] R. Plasser, Y. Takahashi and O. Bíró, "Comparison of various methods for the finite element analysis of nonlinear, periodic eddy-current problems.," in *16th IGTE Symposium 2014*, Graz, Austria, 2014.

[115] R. Plasser, Y. Takahashi, G. Koczka and O. Bíró, "Comparison of two methods for the finite element analysis of nonlinear 3D periodic eddy-current problems," in *20th International Conference on the Computation of Electromagnetic Fields (Compumag 2015)*, Montreal, Canada, 2015.

[116] R. Plasser, Y. Takahashi, G. Koczka and O. Bíró, "Comparison of two methods for the finite element analysis of nonlinear 3D periodic eddy-current problems," in *10th International Sympsium on Electric and Magnetic Fields (EMF 2016)*, Lyon, France, 2016.

[117] R. Plasser, Y. Takahashi, G. Koczka and O. Bíró, "Comparison of 2 methods for the finite element steady-state analysis of nonlinear 3D periodic eddy-current problems using the A,V− formulation," *International Journal of Numerical Modelling: Electronic Networks, Devices and Fields,* vol. 31, no. 2, pp. 1-9, August 2018.

[118] R. Plasser, G. Koczka and O. Bíró, "A nonlinear magnetic circuit model for periodic eddy current problems using T,Φ-Φ formulation," in *Symposium on Electromagnetic Phenomena in Nonlinear Circuits (EPNC)*, Helsinki, Finland, 2016.

[119] R. Plasser, G. Koczka and O. Bíró, "A nonlinear magnetic circuit model for periodic eddy current problems using T,Φ-Φ formulation," *COMPEL - The international journal for computation and mathematics in electrical and electronic engineering,* vol. 36, no. 3, pp. 649-664, 2017.

[120] R. Plasser, G. Koczka and O. Bíró, "Comparison of the Fixed-Point technique using T,ϕ-ϕ and A,V-A – formulations applied to a nonlinear magnetic circuit model," in *17th IGTE Symposium 2016*, Graz, Austria, 2016.

[121] R. Plasser, G. Koczka and O. Bíró, "Comparison of the Fixed-Point Technique using different FEM-Formulations applied to a 3D Nonlinear Periodic Eddy Current Problem," in *17th IGTE Symposium 2016*, Graz, Austria, 2016.

[122] R. Plasser, G. Koczka and O. Bíró, "Convergence investigation of finite element fixed-point techniques applied to 3D nonlinear periodic eddy current problems involving voltage-driven coils," in *2016 IEEE Conference on Electromagnetic Field Computation (CEFC)*, 2016.

[123] R. Plasser, G. Koczka and O. Bíró, "Improvement of the Finite Element

Analysis of 3-D, Nonlinear, Periodic Eddy Current Problems Involving Voltage Driven Coils under DC Bias," in *2017 21st International Conference on the Computation of Electromagnetic Fields (Compumag)*, 2017.

[124] R. Plasser, G. Koczka and O. Bíró, "Improvement of the Finite-Element Analysis of 3-D, Nonlinear, Periodic Eddy Current Problems Involving Voltage-Driven Coils Under DC Bias," *IEEE Transactions on Magnetics,* vol. 54, no. 3, pp. 1-4, 2018.

[125] K. Simonyi, "Foundations of Electrical Engineering: Fields-Networks-Waves," *Elsevier Science,* 2016.

[126] R. P. Feynman, R. B. Leighton and M. Sands, "The Feynman Lectures on Physics: The New Millennium Edition: Mainly Electromagnetism and Matter," *Basic Books,* no. 2, 2015.

[127] J. D. Jackson, K. Muellller and M. Diestelhorst, "Klassische Elektrodynamik," *de Gruyter,* 2013.

[128] E. Kreyszig, "Advanced engineering mathematics," *John Wiley & Sons,* 2010.

[129] O. Bíró and K. R. Richter, "CAD in electromagnetism," *Advances in electronics and electron physics,* vol. 82, pp. 1-96, 1991.

[130] K. Preis, I. Bardi, O. Bíró, C. Magele, W. Renhart, K. R. Richter and G. Vrisk, "Numerical analysis of 3D magnetostatic fields," *IEEE Transactions on Magnetics,* vol. 27, no. 5, pp. 3798-3803, September 1991.

[131] W. Renhart, "Calculating 3D eddy current problems using a reduced magnetic vector potential," in *Proceedings of the Eddy Current Seminar*, 1988, pp. 75-80.

[132] E. X. Xu and J. Simkin, "Total and reduced magnetic vector potentials and electrical scalar potential for eddy current calculation," *IEEE Transactions on Magnetics,* vol. 40, no. 2, pp. 938-940, March 2004.

[133] P. J. Leonard and D. Rodger, "Modelling voltage forced coils using the reduced scalar potential method," *IEEE Transactions on Magnetics,* vol. 28, no. 2, pp. 1615-1618, March 1992.

[134] O. Bíró and K. Preis, "Generating Source Field Functions With Limited Support for Edge Finite-Element Eddy Current Analysis," *IEEE Transactions on Magnetics,* vol. 43, no. 4, pp. 1165-1168, April 2007.

[135] R. G. Durán, "Galerkin Approximations and Finite Element Methods," in *Lecturing Notes*, Buenos Aires, 2005.

[136] A. Ahagon and K. Akihisa, "New Types of Second Order Edge Element by Reducing Edge Variables for Electromagnetic Field Analysis," *IEEE Transactions on Magnetics,* vol. 53, no. 6, pp. 1-4, 2017.

[137] Z. Ren and N. Ida, "Computation of magnetostatic field using second order edge elements in 3D," *COMPEL - The international journal for computation and mathematics in electrical and electronic engineering,* vol. 18, no. 3, pp. 361-371, 1999.

[138] Y. Saad, "Iterative Methods for Sparse Linear Systems," *Society for Industrial and Applied Mathematics,* 2003.

[139] O. Axelsson, "Iterative solution methods," *Cambridge university press,* 1996.

[140] C. Vollaire and L. Nicolas, "Preconditioning techniques for the conjugate gradient solver on a parallel distributed memory computer," *IEEE Transactions on Magnetics,* vol. 34, no. 5, pp. 3347-3350, September 1998.

[141] M. Benzi, "Preconditioning Techniques for Large Linear Systems: A Survey," *Journal of Computational Physics,* vol. 182, no. 2, pp. 418-477, 2002.

[142] D. S. Kershaw, "The incomplete Cholesky-conjugate gradient method for the iterative solution of systems of linear equations," *Journal of Computational Physics,* vol. 26, no. 1, pp. 43-65, 1978.

[143] O. Bíró, K. Preis, G. Vrisk, K. R. Richter and I. Ticar, "Computation of 3-D magnetostatic fields using a reduced scalar potential," *IEEE Transactions on Magnetics,* vol. 29, no. 2, pp. 1329-1332, March 1993.

[144] O. Bíró and K. Preis, "On the use of the magnetic vector potential in the finite-element analysis of three-dimensional eddy currents," *IEEE Transactions on Magnetics,* vol. 25, no. 4, pp. 3145-3159, July 1989.

[145] O. Bíró, C. Paul and K. Preis, "The use of a reduced vector potential Ar formulation for the calculation of iron induced field errors," *Technical report CERN,* 1999.

[146] O. Bíró and K. Preis, "An edge finite element eddy current formulation using a reduced magnetic and a current vector potential," *IEEE Transactions on Magnetics,* vol. 36, no. 5, pp. 3128-3130, September 2000.

[147] O. Bíró, G. Koczka and K. Preis, "Finite element solution of nonlinear eddy current problems with periodic excitation and its industrial applications," *Applied Numerical Mathematics,* vol. 79, pp. 3-17, 2014.

[148] E. O. Brigham, "The Fast Fourier Transform and Its Applications," *Prentice-*

Hall, Inc., 1988.

[149] G. Koczka, S. Außerhofer, O. Bíró and K. Preis, "Optimal fixed-point method for solving 3D nonlinear periodic eddy current problems," *COMPEL - The international journal for computation and mathematics in electrical and electronic engineering,* vol. 28, no. 4, pp. 1059-1067, 2009.

[150] G. Koczka, S. Auberhofer, O. Bíró and K. Preis, "Optimal Convergence of the Fixed-Point Method for Nonlinear Eddy Current Problems," *IEEE Transactions on Magnetics,* vol. 45, no. 3, pp. 948-951, March 2009.

[151] W. Rheinboldt, "Methods for Solving Systems of Nonlinear Equations," *Society for Industrial and Applied Mathematics,* pp. 35-44, 1998.

[152] E. Zeidler, "Nonlinear Functional Analysis and Its Applications: Fixed point theorems," *Springer-Verlag,* 1985.

[153] G. A. Anastassioua and I. K. Argyrosb, "A fixed point technique for some iterative algorithm with applications to generalized right fractional calculus," *JOURNAL OF NONLINEAR SCIENCES AND APPLICATIONS,* vol. 9, no. 2, pp. 493-505, 2016.

[154] W. Peterson, "Fixed-point technique in computing nonlinear eddy current problems," *COMPEL - The international journal for computation and mathematics in electrical and electronic engineering,* vol. 22, no. 2, pp. 231-252, 2003.

[155] E. Dlala, A. Belahcen and A. Arkkio, "A Fast Fixed-Point Method for Solving Magnetic Field Problems in Media of Hysteresis," *IEEE Transactions on Magnetics,* vol. 44, no. 6, pp. 1214-1217, June 2008.

[156] G. Koczka and O. Bíró, "Fixed-point method for solving non linear periodic eddy current problems with T, Φ-Φ formulation," *COMPEL - The international journal for computation and mathematics in electrical and electronic engineering,* vol. 29, no. 6, pp. 1444-1452, 2010.

[157] D. Padua, "Encyclopedia of parallel computing," *Springer Science & Business Media,* 2011.

[158] D. M. Young, "Iterative solution of large linear systems," *Elsevier,* 2014.

[159] L. Hogben, "Handbook of Linear Algebra, Second Edition," *Taylor & Francis,* 2013.

[160] M. H. Gutknecht, "Variants of BICGSTAB for Matrices with Complex Spectrum," *SIAM Journal on Scientific Computing,* vol. 14, no. 5, pp. 1020-

1033, 1993.

[161] R. Horn and F. Zhang, "Schur Complements," in *Handbook of Linear Algebra, Second Edition*, Chapman and Hall/CRC, 2013, pp. 175-193.

[162] C. Bacuta, "A unified approach for Uzawa algorithms," *SIAM Journal on Numerical Analysis,* vol. 44, no. 6, pp. 2633-2649, 2006.

[163] Q. Hu and J. Zou, "Nonlinear inexact Uzawa algorithms for linear and nonlinear saddle-point problems," *SIAM Journal on Optimization,* vol. 16, no. 3, pp. 798-825, 2006.

[164] A. Kameari and K. Koganezawa, "Convergence of ICCG method in FEM using edge elements without gauge condition," *IEEE Transactions on Magnetics,* vol. 33, no. 2, pp. 1223-1226, March 1997.

[165] T. A. Davis, "Direct methods for sparse linear systems," *SIAM,* 2006.

[166] N. I. M. Gould, J. A. Scott and Y. Hu, "A Numerical Evaluation of Sparse Direct Solvers for the Solution of Large Sparse Symmetric Linear Systems of Equations," *ACM Trans. Math. Softw.,* vol. 33, no. 2, June 2007.

[167] R. Albanese and G. Rubinacci, "Magnetostatic field computations in terms of two-component vector potentials," *International Journal for Numerical Methods in Engineering,* vol. 29, no. 3, pp. 515-532, 1990.

[168] I. Ticar, O. Bíró and K. Preis, "Vector potential expanded by edge basis functions associated with loops on finite-element facets," *IEEE Transactions on Magnetics,* vol. 38, no. 2, pp. 437-440, March 2002.

[169] X. S. Li and J. Demmel, "A Scalable Sparse Direct Solver Using Static Pivoting.," in *PPSC*, 1999.

[170] G. Karypis and V. Kumar, "A fast and high quality multilevel scheme for partitioning irregular graphs," *SIAM Journal on scientific Computing,* vol. 20, no. 1, pp. 359-392, 1998.

[171] O. Schenk and K. Gaertner, "Pardiso," in *Encyclopedia of Parallel Computing*, Springer, 2011, pp. 1458-1464.

[172] O. Schenk and K. Gaertner, "User Guide Version 5.0.0," *Journal of Future Generation Computer Systems,* vol. 20, no. 3, pp. 475-487, 2004.

[173] O. Bíró and K. Preis, "Finite element calculation of time-periodic 3D eddy currents in nonlinear media," *Adv. Computat. Electromagn. Selected Papers 3rd Japan-Hungary Joint Seminar Appl. Electromagn. Mater. Computat. Technol.,* vol. 9, no. 3, pp. 62-74, July 1994.

[174] G. Meunier, Y. L. Floch and C. Guerin, "A nonlinear circuit coupled t-t0- phi; formulation for solid conductors," *IEEE Transactions on Magnetics,* vol. 39, no. 3, pp. 1729-1732, May 2003.

[175] G. Meunier, C. Guerin and Y. L. Floch, "Circuit-Coupled t0-phi Formulation With Surface Impedance Condition," *IEEE Transactions on Magnetics,* vol. 44, no. 6, pp. 730-733, June 2008.

[176] Y. L. Floch, G. Meunier, C. Guerin, P. Labie, X. Brunotte and D. Boudaud, "Coupled problem computation of 3-D multiply connected magnetic circuits and electrical circuits," *IEEE Transactions on Magnetics,* vol. 39, no. 3, pp. 1725-1728, May 2003.

[177] J. L. Gross and J. Yellen, "Graph Theory and Its Applications, Second Edition (Discrete Mathematics and Its Applications)," *Chapman & Hall CRC,* pp. 197-207, 2005.

[178] Y. Takahashi, T. Tokumasu, A. Kameari, H. Kaimori, M. Fujita, T. Iwashita and S. Wakao, "Convergence Acceleration of Time-Periodic Electromagnetic Field Analysis by the Singularity Decomposition-Explicit Error Correction Method," *IEEE Transactions on Magnetics,* vol. 46, no. 8, pp. 2947-2950, August 2010.

[179] J. M. Ortega and W. C. Rheinboldt, "Iterative Solution of Nonlinear Equations in Several Variables," *SIAM,* pp. 181-239, 2000.

[180] Z. Badics and Z. J. Cendes, "A Newton-Raphson algorithm with adaptive accuracy control based on a block-preconditioned conjugate gradient technique," *IEEE Transactions on Magnetics,* vol. 41, no. 5, pp. 1652-1655, May 2005.

[181] Y. Okamoto, K. Fujiwara and A. Kameari, "Speedup of Nonlinear Iterative Scheme by Utilizing Convergence Characteristics of Newton-Raphson Method and ICCG Method," in *2006 12th Biennial IEEE Conference on Electromagnetic Field Computation*, 2006.

[182] K. Fujiwara, Y. Okamoto, A. Kameari and A. Ahagon, "The Newton-Raphson method accelerated by using a line search - comparison between energy functional and residual minimization," *IEEE Transactions on Magnetics,* vol. 41, no. 5, pp. 1724-1727, May 2005.

[183] D. Fink and H. W. Beaty, "Standard Handbook for Electrical Engineers," *Mcgraw-hill,* 2006.

[184] W. Hayt and J. Buck, "Engineering Electromagnetics," *MC GRAW HILL,* 1983.

[185] F. Richter, "The physical properties of steels - The 100 steels programme - Part I tables and figures," Mühlheim a.d. Ruhr, 1991.

Appendix

A Skin effect

The skin effect was generalized to conductors of any shape by Oliver Heaviside in 1885. This effect describes the inclination of an alternating electric current (AC) distributed within a conductor to exhibit the largest current density in the vicinity of the surface of the conductor and progressively decreasing current density in the inner regions of the conductor. This is due to an AC in a conductor generating an alternating magnetic field in the inside and around the conductor based on Ampère´s law (2.1). The change in the intensity of the current also alternates the magnetic field and this change, in turn, creates an electric field on the basis of Faraday´s law (2.2) counteracting the change in the current intensity.

This opposing electric field is the so-called counter-electromotive force or often referred to as “back EMF” which is most dominant in the center of the conductor and suppresses the current flow to the conductor boundaries. Hence, the electric current flows primarily at the "skin" of the conductor, between the outer surface and a level called the skin depth δ as illustrated in Fig. A.1. This provokes a rise in the effective resistance by reducing the actual cross-section of the conductor essentially at higher frequencies [125, 183, 184].

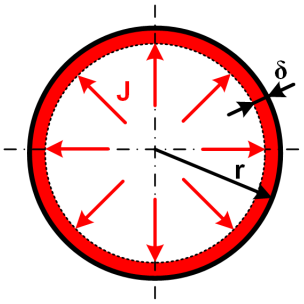

Fig. A.1: Illustration of the skin depth due to the displacement of the current density.

The skin depth δ can be computed as

$$\delta = \sqrt{\frac{2}{\sigma \cdot \mu_r \mu_0 \cdot \omega}}.$$

Thus the skin depth of a copper conductor with an electrical conductivity $\sigma = 5.7 \cdot 10^7$ (S/m) and the relative permeability $\mu_r \approx 1$, excited at a frequency of 50 (Hz) results in a $\delta \approx 10$ (mm). Hence, the skin effect is not negligible in AC electrical power and distribution applications, as the required conductor cross-section cannot be optimally used utilizing massive conductors. A counter measure is to replace massive conductors with continuously transposed litz-wires providing suitable cross-sections of each strand to guarantee a homogenous current density distribution in the strands [4, 5, 6, 7, 8, 9, 10, 11].

As an example of the skin effect, illustrated in Fig. A.2 is a round copper conductor with a radius of 1 (mm) and excited by a current of 1 (A) at a frequency of 50 (Hz). It can be seen that the current density has a homogeneous distribution. Whereas in Fig. A.3 the same conductor is excited with 1 (A) at a frequency of 50 (kHz) and the displacement of the current density to the conductor surface due to the skin effect is clearly visible.

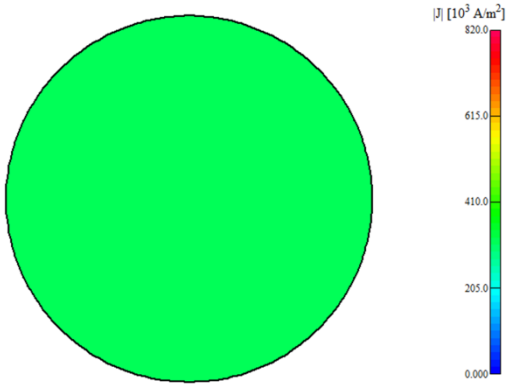

Fig. A.2: Current density distribution in a round conductor at a frequency of 50 (Hz).

Fig. A.3: Current density distribution in a round conductor at a frequency of 50 (kHz).

B Additional data of the dry insulated air-reactor

B.1 Technical data of the air reactor with standard commercial steel reinforcements underneath

The detailed technical data of the air-reactor under investigation with a standard commercial steel reinforcement underneath the reactor has been provided by the Trench Austria Ltd. who also provided the measurement results. Supplementary data for the air reactor investigated in section 3.2 is given in TABLE B.1

TABLE B.1: Additional technical data of the dry insulated air reactor

Technical data TCR 250/1177/86.6		
Values	Unit	Quantity
Insulation level (LIL)	kV	250
Rated Inductance	mH	86.6
Dynamic short circuit current (peak-value)	kA	3.6
Rated short time current (RMS-value) for 3.0 seconds	kA	1.4
Extension pole height	mm	750
Isolator height	mm	490
Distance from ground to winding	mm	1420

B.2 Comparison of the measured and computed results

TABLE B.2 contains the complete set of measured and computed current values in the given grid points as illustrated in Fig. 3.6 and Fig. 3.7 for different excitation current levels. The computed values refer to the HBFP technique with 11 harmonics considered.

TABLE B.2: Comparison of measured and computed current values

Grid point.	I^m_{eddy} in A	I^c_{eddy} in A	I^m_{eddy} in A	I^c_{eddy} in A	I^m_{eddy} in A	I^c_{eddy} in A	I^m_{eddy} in A	I^c_{eddy} in A	I^m_{eddy} in A	I^c_{eddy} in A	I^m_{eddy} in A	I^c_{eddy} in A
I_{EXC}	50A	50A	100A	100A	300A	300A	500 A	500A	700A	700A	1000A	1000A
1	3.3	1.42	6.0	2.87	10.0	7.55	15.6	11.01	27.6	14.75	35.0	21.47
1-1	3.2	1.42	6.6	2.87	13.3	7.55	17.1	11.01	25.0	14.75	37.6	21.47
2	2.8	1.44	4.1	2.87	8.1	7.62	12.8	11.35	14.9	15.45	22.5	22.89
2-2	3.6	1.44	6.9	2.87	15.0	7.62	16.5	11.35	25.6	15.45	43.8	22.89
3	2.7	1.38	4.5	2.77	8.7	6.90	12.6	10.82	17.8	15.39	34.0	23.49
4	6.3	4.12	9.6	7.36	21.0	19.32	44.4	36.57	64.4	60.88	107.8	109.78
5	5.2	3.73	9.3	6.67	22.8	18.79	37.3	35.87	58.0	59.51	97.5	106.22
5-5	8.5	5.81	14.2	9.84	38.2	32.15	66.8	69.45	102.3	121.44	179.0	215.55
6	8.6	5.84	13.2	9.90	37.6	32.91	74.9	71.38	112.0	124.50	183.0	219.97
6-6	5.6	3.76	9.3	6.67	20.9	19.30	43.8	37.28	60.0	62.13	103.0	110.56
7	7.8	5.04	12.6	8.84	36.6	30.42	60.7	65.35	89.6	112.81	135.0	195.68
8	9.1	6.52	14.1	11.40	47.3	43.76	88.7	99.64	124.0	170.85	191.0	292.37
9	8.0	5.38	13.6	9.67	40.1	37.42	70.0	84.06	99.0	144.48	140.0	244.14
9-9	8.9	6.38	15.1	11.38	49.1	46.64	85.7	107.72	123.0	183.73	168.0	307.40
10	8.6	6.41	14.9	11.48	50.9	47.39	92.7	109.14	124.7	185.45	172.0	309.69
10-10	7.7	5.42	12.7	9.77	40.9	38.28	74.6	85.92	102.5	146.99	165.0	247.66
11	6.9	4.94	11.7	8.98	37.9	36.97	67.9	84.55	93.0	144.39	155.0	240.11
12	7.7	5.63	12.3	10.16	44.1	42.86	78.8	99.42	108.3	168.48	159.5	279.39
13	5.3	3.85	9.0	6.99	31.6	29.34	52.9	67.94	74.0	115.84	116.6	191.76
13-13	5.8	4.26	9.9	7.70	31.9	31.80	58.1	74.38	80.8	127.46	118.4	211.83
14	5.8	4.29	9.7	7.75	32.7	32.26	61.1	75.29	85.5	128.54	118.0	213.04
14-14	5.4	3.87	9.3	7.07	29.4	29.93	51.3	68.92	75.0	116.94	96.0	193.06
15	3.5	2.19	5.1	3.97	17.3	16.38	29.5	38.09	41.2	65.42	58.0	108.92
15-15	3.7	2.44	5.8	4.43	18.0	17.77	31.8	41.66	43.7	71.86	62.5	120.46
16	3.7	2.44	5.8	4.43	18.0	17.77	31.8	41.66	44.0	71.85	62.0	120.46
16-16	3.3	2.22	5.3	4.01	17.3	16.84	32.0	39.00	44.5	66.49	59.5	110.12

17	3.0	1.38	5.4	2.77	10.4	6.90	12.4	10.82	16.4	15.39	28.0	23.49
18	7.6	4.24	11.4	7.64	25.0	19.62	42.3	36.17	70.0	59.73	116.0	107.50
19	2.8	1.26	4.7	2.48	8.5	6.60	10.9	11.23	15.1	16.56	39.0	25.99
19-19	2.7	1.26	4.6	2.48	8.6	6.60	16.4	11.23	23.9	16.56	28.0	25.99
20	9.8	6.54	14.9	11.01	39.9	33.88	72.4	72.50	118.0	126.88	193.0	227.45
21	2.6	1.09	4.0	2.16	7.1	6.30	14.3	11.15	13.4	16.65	32.0	26.05
22	11.1	8.18	17.7	13.94	52.3	49.39	100.7	111.92	153.0	194.05	230.0	337.66
23	2.1	0.90	2.9	1.80	5.2	5.72	12.3	10.33	10.0	15.42	28.5	24.02
25	0.0	0.69	2.3	1.39	4.3	4.80	8.2	8.83	10.7	13.08	21.0	20.11
26	14.3	10.39	23.0	18.68	76.6	73.74	138.3	167.75	195.6	286.71	318.0	479.99
27	0.0	0.47	0.0	0.95	3.7	3.54	4.9	6.69	6.5	9.87	8.5	14.93
27-27	0.0	0.47	0.0	0.95	4.8	3.54	6.0	6.69	8.6	9.87	9.5	14.93
28	15.4	11.17	26.8	20.50	84.0	82.09	150.7	184.64	204.0	312.83	346.0	520.14
29	0.0	0.24	0.0	0.49	3.4	1.92	3.5	3.78	4.0	5.67	9.4	8.51
29-29	0.0	0.24	0.0	0.49	4.2	1.92	3.9	3.78	3.5	5.67	4.2	8.51
30	16.5	11.81	29.2	22.11	90.7	90.36	159.2	201.23	207.6	337.30	366.0	556.07

B.3 Dependence of the electrical conductivity on temperature

Illustrated in Fig. B.1 is the change of the electrical conductivity of commercial steel in dependence on temperature [185] as an interpolated function of the values summarized in TABLE B.3.

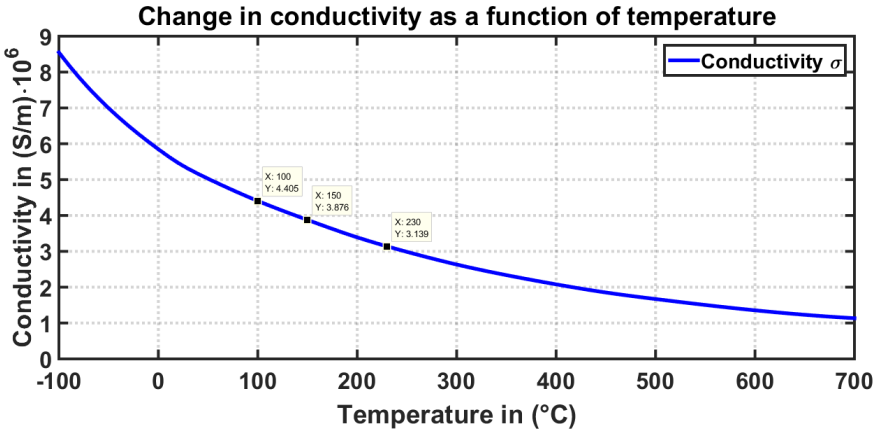

Fig. B.1: Dependency of the electrical conductivity of commercial steel on the temperature.

TABLE B.3: Dependence of the electrical conductivity of commercial steel on the temperature

Temp. °C	Cond. S/m·10^6	Temp. °C	Cond. S/m·10^6	Temp. °C	Cond. S/m·10^6
-100	8.547	150	3.876	450	1.852
-50	6.993	200	3.389	500	1.669
0	5.848	250	2.985	550	1.504
20	5.465	300	2.632	600	1.355
50	5.025	350	2.336	650	1.230
100	4.405	400	2.079		

In case of adapting the electrical conductivity in assumption of higher temperatures in the steel grid, the current evaluation in the given measurement points has again been performed with the HBFP considering 11 harmonics at an excitation current of 50 (A) and 1000 (A). The results are plotted in Fig. B.2 and Fig. B.3.

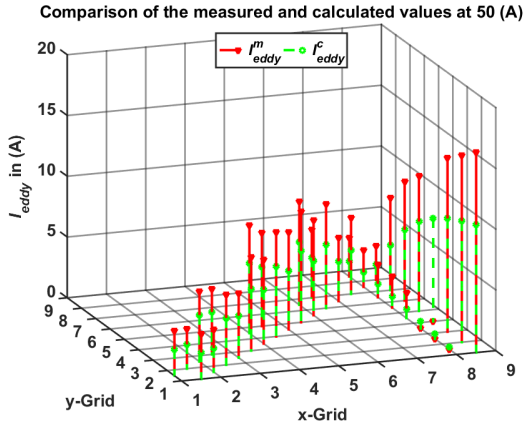

Fig. B.2: Current distribution in the steel grid with an adapted σ for 100 (°C) and an excitation current of the reactor of 50 (A).

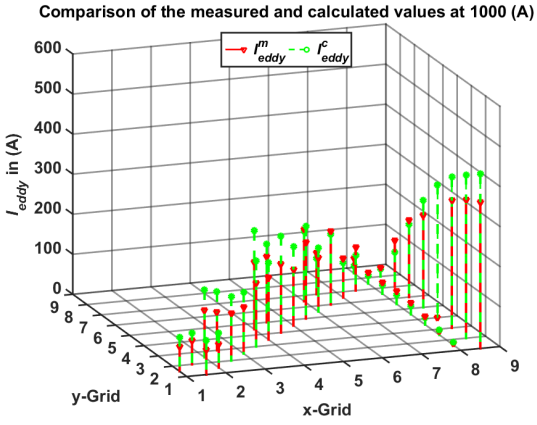

Fig. B.3: Current distribution in the steel grid with an adapted σ for 100 (°C) and an excitation current of the reactor of 1000 (A).

In case of an exciting current of 50 (A), the modification of the electrical conductivity leads to deterioration in the difference of measured and computed eddy-current values. Hence, the previously assumed value for the conductivity is a better match to the temperature in the steel grid at this excitation current level. However, when exciting with 1000 (A), the deviation between the measured and computed currents improved, leading to the assumption that the electrical conductivity at a temperature of about 100 (°C) is a good choice.

B.4 Technical data of the air reactor with stainless steel reinforcements underneath

TABLE B.4 concludes the fundamental data of the air-reactor when investigating the eddy-current losses with a present stainless steel grid underneath.

TABLE B.4: Main data of the air reactor test setup with stainless steel

Technical data FVR 125/634/27.5		
Values	Unit	Quantity
Active winding height	mm	1376
Average winding diameter	mm	2100
Radial winding width	mm	146
Number of turns	-	127.75
Rated voltage	kV	6.8
Rated power	MVar	3.269
Rated current	A	615.18
Rated reactance	Ω	8.639
Rated frequency	Hz	50
Insulation level (BIL)	kV	125
Rated inductance	mH	27.5
Isolator height	mm	490
Distance from ground to winding	mm	650

B.5 Comparison of the measured and computed results

Illustrated in the upcoming figures are the measured and computed eddy-current values in the stainless steel grid underneath the air-reactor.

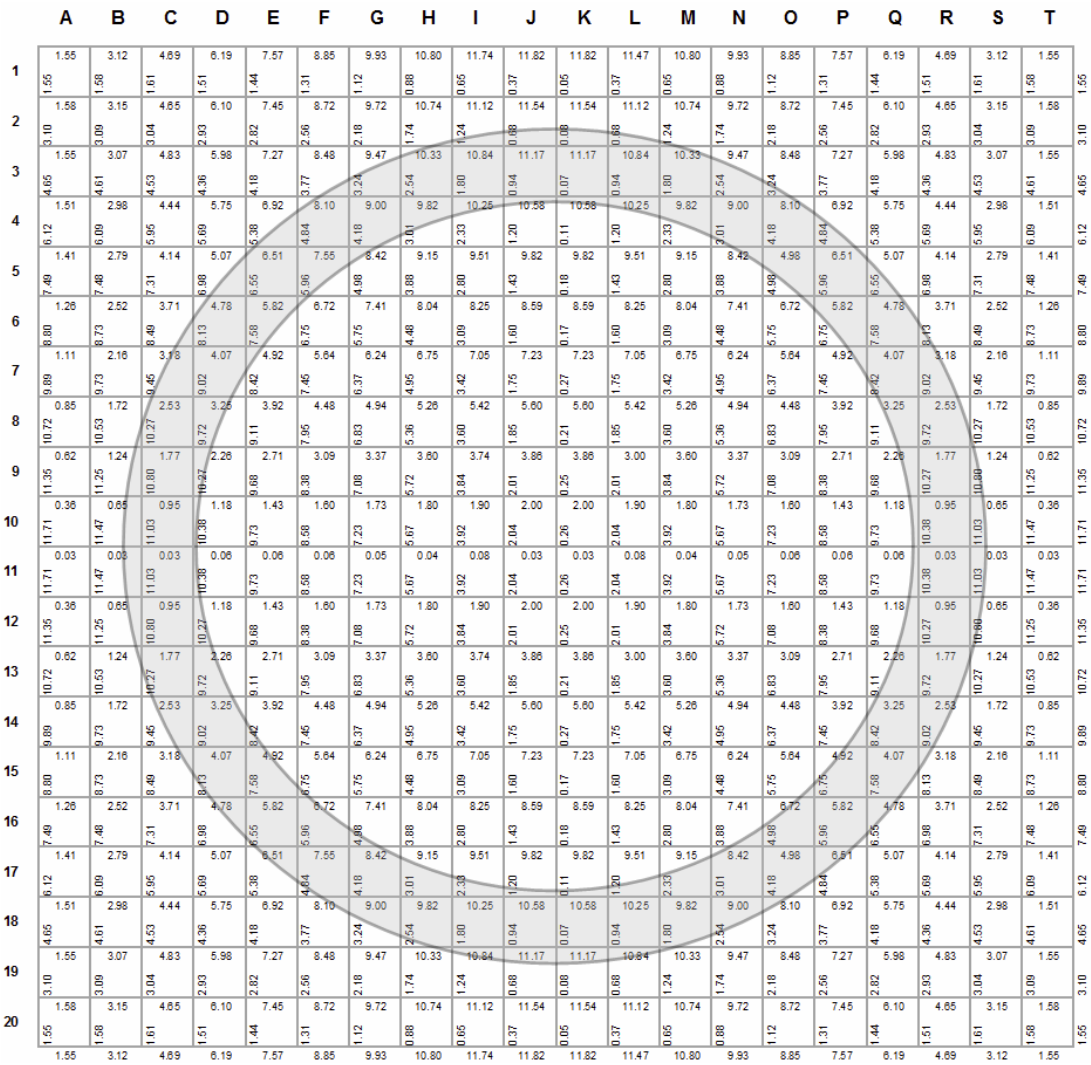

Fig. B.4: Provided measured eddy-currents in (A) in the stainless steel grid underneath the air-reactor with an excitation current of 101.96 (A).

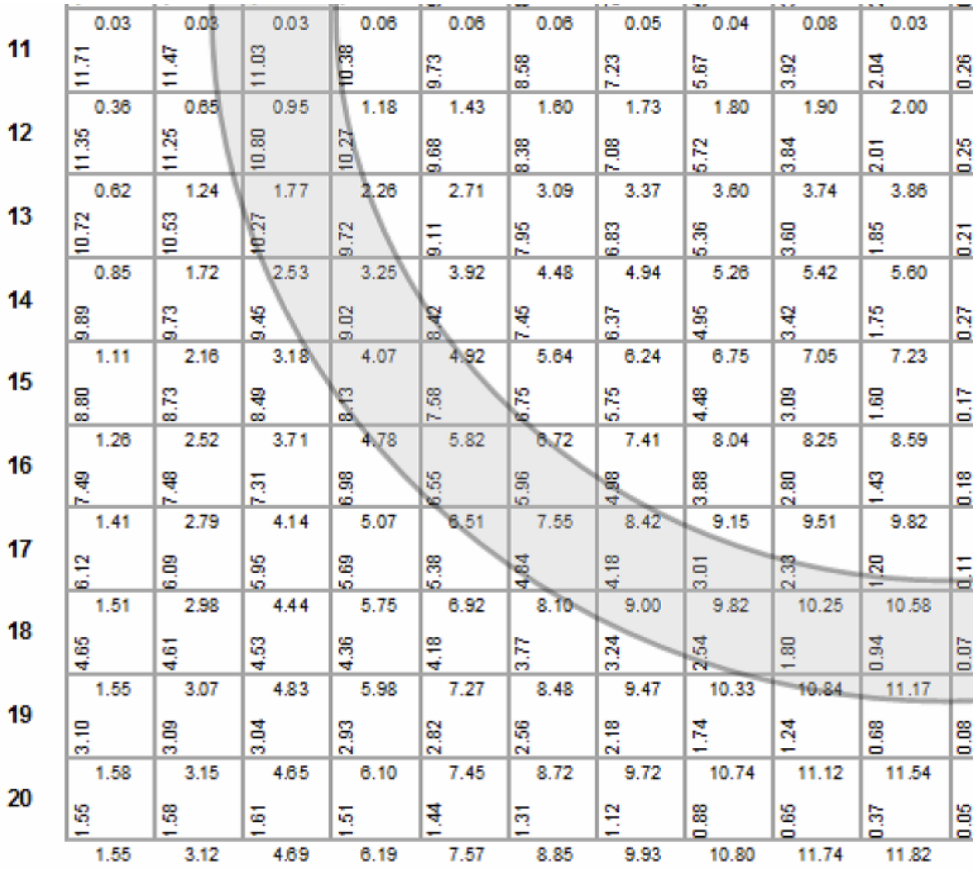

Fig. B.5: Measured eddy-current values in the stainless steel grid of the quarter-domain as considered for the FEM computation given in (A).

Illustrated in Fig. B.5 is the quarter-model domain with the measured eddy-current values in the stainless steel grid when the reactor is excited with a current of 101.96 (A).

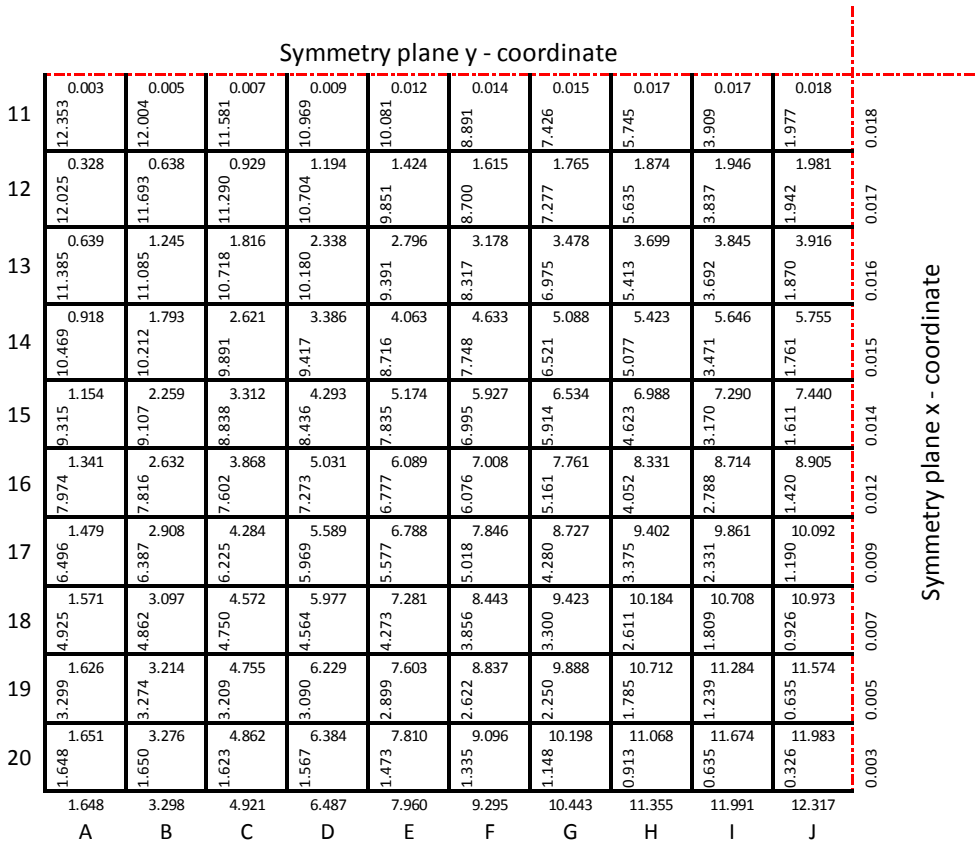

Fig. B.6: Computed eddy-current values in the stainless steel grid in (A).

Fig. B.6 shows the quarter FEM-model with the computed eddy-current values occurring in the stainless steel grid indicated when the reactor is excited with a current of 101.96 (A). The computed and measured values of the eddy-currents are in a good agreement.